LEABHARLANN CHOLÁISTE NA TRÍONÓIDE, BAILE ÁTHA CLIATH | TRINITY COLLEGE LIBRARY DUBLIN
Ollscoil Átha Cliath | The University of Dublin

Terms and Conditions of Use of Digitised Theses from Trinity College Library Dublin

Copyright statement

All material supplied by Trinity College Library is protected by copyright (under the Copyright and Related Rights Act, 2000 as amended) and other relevant Intellectual Property Rights. By accessing and using a Digitised Thesis from Trinity College Library you acknowledge that all Intellectual Property Rights in any Works supplied are the sole and exclusive property of the copyright and/or other IPR holder. Specific copyright holders may not be explicitly identified. Use of materials from other sources within a thesis should not be construed as a claim over them.

A non-exclusive, non-transferable licence is hereby granted to those using or reproducing, in whole or in part, the material for valid purposes, providing the copyright owners are acknowledged using the normal conventions. Where specific permission to use material is required, this is identified and such permission must be sought from the copyright holder or agency cited.

Liability statement

By using a Digitised Thesis, I accept that Trinity College Dublin bears no legal responsibility for the accuracy, legality or comprehensiveness of materials contained within the thesis, and that Trinity College Dublin accepts no liability for indirect, consequential, or incidental, damages or losses arising from use of the thesis for whatever reason. Information located in a thesis may be subject to specific use constraints, details of which may not be explicitly described. It is the responsibility of potential and actual users to be aware of such constraints and to abide by them. By making use of material from a digitised thesis, you accept these copyright and disclaimer provisions. Where it is brought to the attention of Trinity College Library that there may be a breach of copyright or other restraint, it is the policy to withdraw or take down access to a thesis while the issue is being resolved.

Access Agreement

By using a Digitised Thesis from Trinity College Library you are bound by the following Terms & Conditions. Please read them carefully.

I have read and I understand the following statement: All material supplied via a Digitised Thesis from Trinity College Library is protected by copyright and other intellectual property rights, and duplication or sale of all or part of any of a thesis is not permitted, except that material may be duplicated by you for your research use or for educational purposes in electronic or print form providing the copyright owners are acknowledged using the normal conventions. You must obtain permission for any other use. Electronic or print copies may not be offered, whether for sale or otherwise to anyone. This copy has been supplied on the understanding that it is copyright material and that no quotation from the thesis may be published without proper acknowledgement.

Electrochemistry of the Organic Molecule Methylene Blue

John Colleran
B.A. (Chem.)

A thesis submitted to the University of Dublin for the degree of Doctor of Philosophy.

Department of Chemistry
University of Dublin
2008

DECLARATION

This thesis has not been submitted as an exercise for a degree at any other university. Except where stated, the work described therein was carried out by me alone.

I give permission for the Library to lend or copy this thesis upon request.

Signed:

Declaration

This thesis has not been submitted as an exercise for a degree at any other University. Except where otherwise indicated, the work described herein has been carried out by the author alone. I, the undersigned, do also give permission to the Libraries of Trinity College, Dublin, to copy this thesis in whole or in part without further reference to me.

John Colleran

To Mam and Dad.

THESIS SUMMARY

The first Chapter deals with the general information about chemically modified electrodes, what they are, the development of fabrication techniques, and relevant applications of modified electrodes. This is followed by some background on the redox polymer, polymethylene blue, and closes with a description of magnetoelectrochemistry. In Chapter 2 the experimental procedures and theory used in this body of research are dealt with in good detail. The first part of Chapter 3 describes the solution phase electrochemistry of the organic phenothiazine dye, methylene blue, at a glassy carbon electrode. The effect that dimerisation has on the diffusion coefficients and electron transfer kinetics, is explored. Adsorption was observed at the glassy carbon electrode and an adsorption isotherm constructed. The maximum surface coverage for a MB monolayer was extracted from the isotherm data. The solid phase electrochemistry of MB was also investigated *via* electropolymerisation of the monomer onto the glassy carbon electrode. The charge carried by the polymer films was examined as a function of initial concentration of the monomeric solution and of the number of cyclic voltammetric polymer growth cycles applied. A value for the diffusional charge transfer coefficient was estimated using cyclic voltammetry. EQCM was employed to quantify the movement of counterions through the film and a stoichiometric expression for this redox process was proposed.

Introducing Chapter 4 is a brief description of the Andrieux-Saveant and Albery-Hillman models which describe the electrocatalytic oxidation/reduction of analytes at modified electrodes. The remainder of Chapter 4 deals with, in depth, the theoretical analysis of the steady state amperometric response of modified electrodes towards an electroactive analyte in terms of Michaelis-Menton kinetics. A derived model was fitted to experimental data in Chapter 5 to yield kinetic information about ascorbic acid and catecholamine oxidation at a polymethylene blue glassy carbon electrode. The Albery-Hillman and Andrieux-Saveant theoretical models were used to diagnose the rate limiting cases for the electrocatalytic oxidation of said analytes at the PMB/GC electrode. The

oxidation of the analytes at a bare and modified electrodes yielded diffusion coefficients for the analytes as well as kinetic data. The selectivity of the polymethylene blue glassy carbon towards the catecholamines over ascorbic acid using DVP was investigated.

The effect that an applied magnetic field has on solutions of ferri/ferrocyanide was quantitatively examined in Chapter 6, and relationships describing these effects were elucidated. Homogeneous catalytic oxidation of leucomethylene blue by Iron(III) was investigated using cyclic voltammetry and RDE, and the effect of the applied magnetic field on this reaction was examined. Finally, we return to polymethylene blue at the end of Chapter 6. The charge transport processes in a polymethylene blue modified electrode were studied in the magnetic field and the results presented.

ACKNOWLEDGEMENTS

First and foremost I offer my sincerest gratitude to my supervisor, Dr. Mike E. G. Lyons, for his guidance, support and especially his encouragement throughout the course of this work. Thanks for the pep-talks - there were times when I thought that the methylene blue would finish me, but I managed to stick at it. I would also like to thank Prof. Corish and Prof. Kelly for the use of the departmental facilities. In the various laboratories and workshops I have been aided for many years by three fine technicians, Martin, Patsy and Brendan, who were always helpful and in good form. Thanks to IRCSET for their financial support during the course of my work.

To all my fellow colleagues in the Electrochemistry Laboratory and in particular Ray, Brandon, Gar, Kinsella, Dee and Conchuir – my sincerest thanks. In the lab environment no holes were barred and disturbing home truths were constantly swapped – the 'Brandonisms' will remain with me always! On the flip side, physical chemistry theory was keenly discussed and innovation thus blossomed. Thank you to Aileen and Noelle who were particularly nice when they needn't have been. Many fond memories will remain with me from quality time spent with you all. Thank you to Mary, R.I.P., who had more of an influence on me than she knew. Possibly the most unfortunate person to have been in contact with me during my academic marathon is, of course, Eimear. Thank you for all the unconditional encouragement you gave me, which I hope to reciprocate when your time is near.

Finally, I want to extend my sincerest gratitude to Mam and Dad for the support throughout my tenure as a student, without which this research would not have been possible.

Table of Contents

1. General Introduction

---

2. Experimental Theory and Methodology

---

3. Electrochemistry of Solution Phase and Polymeric Methylene Blue

4. Theoretical Model

5. Redox Catalysis at the PMB/GC Electrode

6. The Magnetohydrodynamic Effect

7. Conclusions and Future Work

SYMBOLS AND ABBREVIATIONS

α	Saturation parameter.
α	Activity coefficient.
a_α/ a_β	activities of the species in the membrane/ solution.
A	Geometric area (cm^{-2}) of the support electrode.
AA	Ascorbic Acid.
B	Symmetry factor.
b	Tafel slope.
C	Catalyst species.
C’	Pre-catalyst species.
c_Σ	Total redox site concentration.
C^0	Bulk concentration of magnetic species in solution.
C.V.	Cyclic voltammetry.
δ	Diffusion layer thickness.
D	Diffusion coefficient of electroactive species in modification matrix.
D.C.	Direct current.
D.P.V.	Differential pulse voltammetry.
DA	Dopamine.
D	Diffusion coefficient.

D_{CT}	Charge transfer diffusion coefficient.
D_E	Diffusion coefficient of an electron.
D_F	Diffusional frequency of substrate within the modification film.
D_I	Counterion diffusion coefficient.
D_S	Diffusional frequency of substrate within the solution.
ρ	density.
E	Electrode potential.
E_m	Membrane potential.
E_q	Equilibrium potential.
E^0	Standard cell potential.
$E^o_{(O/R)}$	Standard redox potential of redox couple, O/R (V).
EP	Epinephrine
EQCM	Electrochemical quartz crystal microbalance
F	Faradays constant.
F_{mag}	Magnetic force.
F_P	paramagnetic gradient force.
F.I.D.	Flame ionisation detector.
FIA	Flow injection analysis.
θ	Geometrical factor.
ΔG^0	Standard Gibbs free energy.

Γ	Surface coverage of mediator sites in modification matrix.
GC	Glassy carbon electrode.
HRP	Horseradish Peroxidase
i_{ox}	Oxidative current response (A).
i_{RED}	Reductive current response (A).
I	Amperometric current response (A).
I_{EH}	Eadie Hofstee Intercept.
I_{LB}	Lineweaver Burk intercept.
j	Flux.
j_{Σ}	Net electron flux.
κ	Partition coefficient.
k	Second-order bimolecular rate constant (cm^{3} mol^{-1} s^{-1}).
k_{ME}	Heterogeneous electrochemical rate constant (cm s^{-1}).
k_{C}	Catalytic rate constant. (s^{-1})
K_{m}	Michaelis constant.
K-L	Koutecky-Levich.
L	Layer thickness (assumed to be uniform / cm).
LMB	Leucomethylene blue.
L.S.V.	Linear sweep voltammetry.
ν	Sweep rate (V s^{-1}).

MB	Methylene Blue.
MHD	Magnetohydrodynamic.
n	Number of electrons transferred in electrode reaction.
η	Absolute viscosity of electrolyte
NE	Norepinephrine.
NAD$^+$	Nicotinamide Adenine Dinucleotide.
NADH	Nicotinamide Adenine Dinucleotide Hydrogen.
NHE	Normal Hydrogen Electrode.
ω	Rotation speed of R.D.E. (Hz).
Φ	Thiele modulus ($= L/ X_k$)
μ_0	Permeability of free space.
PBS	Phosphate buffer solution.
PMB	Polymethylene blue.
PMB/GC	Polymethylene blue/Glassy Carbon electrode.
Pt	Platinum electrode.
PVC	Polyvinyl chloride.
Q	Charge.
R	Gas constant.
R.D.E.	Rotating disc electrode.
R-S	Randles-Sevcik.

rpm	Revolutions per minute.
s^{∞}	Bulk solution concentration.
SAM	Self assembled monolayer.
SCE	Saturated calomel electrode.
S_{HE}	Eadie Hofstee Slope.
S_{LB}	Lineweaver Burk Slope.
SP	Substrate Product complex.
$\tau_D-\tau$	Pulse duration time.
τ	Normalised time parameter.
T	Temperature. (K/ °C).
t	Time (seconds).
uv *vis*	Ultra violet visible spectroscopy.
V_M	Molecular volume.
X_{κ}	Reaction layer thickness.
χ_m	Molar susceptibility.
y	Normalised current response.
z	Valence of the ion.
θ	Surface fraction.
λ	Reorganizational energy.
Ψ	Normalised Current.

CHAPTER 1

GENERAL INTRODUCTION

1.1. Electrochemistry

In 1785 Luigi Galvani eluicidated, in a rather turbulent fashion, that the legs of a dead frog went into spasm when a pulse of electrical current was passed through its spinal chord. The birth of electrochemistry thus began with the belief that the dead could be restored to life by electrical means. This generated a great deal of excitement in the scientific community at the time, and vigorous experimentation thereafter paved the way to modern electrochemistry. Volta further developed Galvani's findings and by his death in 1827 had developed the first device that demonstrated chemical production of electric current, as well as the electrophore (a primitive capacitor), the condenstore (a device that detected weak electrical current), and the precursor to modern alkaline batteries, the voltaic pile.

The greatest pioneering work in electrochemistry though was carried out by Michael Faraday, the 'father' of electrochemistry. In 1834 he developed the First Law of Electrochemistry, which states: "The chemical power of a current of electricity is in direct proportion to the absolute quantity of electricity which passes". Faraday also developed the Second Law of Electrochemistry: "Electrochemical equivalents coincide, and are the same, with ordinary chemical equivalents". The discovery of electromagnetic induction, the development of the first transformer, electric motor and electric generator are just some of his many great achievements. Faraday also developed fundamental theory for electromagnetism and identified paramagnetism and diamagnetism.

With the discovery of the electron (J.J. Thompson, 1893) and the development of thermodynamics, electrochemical techniques such as potentiometry and polarography became important tools in the thermodynamic characterisation of solution properties. Equilibrium constants for a multitude of chemical reactions can be determined from relatively few standard reduction potentials, using the standard cell potential and Gibbs free energy relationship

$$\Delta G^0 = -nFE^0 \tag{1.1}$$

where ΔG^0 is the standard Gibbs free energy, F is Faraday's constant, n is the number of electrons transferred, and E^0 is the standard cell potential. Presently, powerful electrochemical techniques and data processing ability have improved electrochemical theory, giving a wealth of information on both thermodynamic and kinetic parameters.

The applications attributed to the ever advancing frontiers of electrochemical research are many, and continue to expand with new technologies. One of the most exciting areas is chemically modified electrodes from which a vast range of applications have sprouted. In particular, chemical sensor development has reached explosive proportions, from which environmental pollutants and constituents of bodily fluids can be monitored, even at the most dilute concentrations. Also stimulating the research into chemically modified electrodes is the drive to attain the goals of effective miniaturised computers, composite battery electrodes, fuel cells and more recently bio-fuel cells.

1.2 Chemically Modified Electrodes

1.2.1 Introduction

A chemically modified electrode [1-3] is an electrode whose surface has been deliberately altered with an aim to enhance or inhibit particular properties of the electrode. The term 'chemically modified electrodes' was first introduced by Murray and co-workers [4] in 1975, to describe electrodes that had foreign molecules deliberately immobilised onto their surfaces. The electrochemical reaction of species in solution takes place through the modifying layer and not directly at the electrode surface. Electron transfer occurs between the Fermi level of the electrode and the modifying layer, and redox groups in the latter then mediate the electron transfer to ions in solution. The redox groups in the modifying layer can catalyse or inhibit specific reactions. Electrodes can be modified to enhance its sensitivity, selectivity and response times.

Lane and Hubard [5,6], in 1973, were one of the pioneers of deliberately modifying electrodes. They used many different functionalised olefins to modify platinum electrodes by irreversible chemisorption, thus creating electrodes with a specific nature. Surface coverage measurements were used to elucidate that the loss of π-bonds and the formation of Pt-C σ-bonds had occurred. Olefin charge, dependent on applied potential, had a marked effect on the electron transfer reactions between the Pt surface and ions in solution. This was due to the effect of the olefin charge on the distribution of ions in the diffusion layer. Thus adsorption was a new technique of modifying electrode surfaces. As many compounds were known to adsorb strongly to electrodes, a diverse range of specifically modified electrodes was now possible, depending on the desired application of the electrode.

The authors, Miller *et al.* [7] in 1975, were one of the first research groups to report a functional modified electrode. An asymmetric reagent was used to modify a carbon electrode to develop a 'chiral electrode'. From a solution of optically inactive reagents, the electrode selectively favoured the production of one optical isomer over another. Racemic mixtures resulted when the unmodified electrode was used and so the possibility of selective electrode reactions was highlighted.

Further work by Murray *et al.* [4,8], used direct covalent bonding of the chosen modification molecule to the electrode surface, as a more permanent modification technique. The work consisted of attaching silanes to a SnO_2 electrode by reaction with surface hydroxide groups. This method of 'covalent-anchoring' results in either mono-layer or multi-layer coatings on the electrode surface. Electrode coverage depends on the solvent used as well as the functional groups of the silanes. In general, most metal electrodes, when treated with acidic media, form metal oxide layers which can then be derivatised [9]. Covalent anchoring is not specific to silanes and cyanuric chloride has been used to immobilise quinones and glucose oxidase at host electrode surfaces [10]. Oxide-free surfaces have also been modified [11,12] and mainly involve reactions with the surface atoms of carbon electrodes.

1.2.2 Development of Modifying Techniques

A variety of electrode modification techniques have been developed over the last five decades and since the early techniques of adsorption and covalent attachment, polymeric and plasma coating techniques have evolved. The adsorption of quinones and azines, electrocatalysts of NADH oxidation, has been used by Gorton and co-workers [13-16] to develop dehydrogenase based electrodes. The electrodes exhibited poor stability as adsorption has a general drawback in that slow desorption of the modifying layer can occur, leading to a loss in performance and function. The phenomenon of organised assemblies has lead to the formation of monolayer coated electrodes [17,18]. Surface active compounds, such as Langmuir-Blodgett films, can be transferred to an electrode surface from a liquid/air interface. Self-assembled monolayers occur *via* spontaneous coating of an electrode with the monomer, with lateral interactions between the molecules imposing order on the layer. Covalent attachment of specific moieties to an electrode surface is not always possible, so recent research has focused mainly on the use of polymers to modify electrode surfaces [1,10,19]. The advantages lie in the simplicity of synthesis of stable multi-layer films onto the electrodes surface and in retaining the inherent properties of the film, such as catalytic or selective properties. Films can also be functionalised, used to immobilise redox active molecules close to the electrode surface, and the layer thickness can be accurately controlled. Modification can be attained by deposition of a pre-formed polymer or by polymerisation of a redox active monomer, forming a film, onto the electrode surface. The pre-formed polymer deposition technique has an advantage in that the layer is complete prior to polymer characterisation and can be accomplished by dip or spin coating the electrode [1]. Spin coating results in a film of more uniform thickness and so is generally preferred to dip coating even though surface coverages are considered to be less reproducible. Direct polymerisation of the monomer can be produced by thermal, plasma, photochemical or electrochemical polymerisation [20]. The deposited polymer may then be functionalised, constructing electrodes with the desired characteristics.

Three main classes of polymer modified electrodes, ion-exchange, electronically conducting and redox polymers, have been made using these modifying techniques. Ion-exchange polymers(polyelectrolytes) contain charged sites that can bind ions form solution *via* an ion-exchange process, resulting in the dispersion of electrostatically bound redox active groups in the ionomer matrix. Charge percolation occurs via local electron hopping between neighbouring groups or by diffusion of the redox groups through the matrix. Uniform thick films, with a wide variety and controlled degree of ion loading species, are easily fabricated. The ion-exchange polymers protonated poly(4-vinylpyridine) and quaternised poly(4-vinylpyridine) have received a lot of attention to date. When neutral poly(4-vinylpyridine) is placed in an acidic medium, protonation of the pyridine occurs forming cations in the polymer matrix [21]. Highly charged anionic species in solution were then incorporated into the film due to the strong electrostatic attraction with these cations. The surface deposited microstructure was found to contain ca. 10^{-7} mol cm^{-2} of redox active material located in a 1μm thick layer corresponding to a catalyst/sensing element concentration of 0.1 mol dm^{-3}. This technique has been widely used to incorporate a large variety of anionic species [22-25] into cationic polymers. Cationic exchangers include the sulphonated flouroploymer, Nafion, and poly(styrenesulphonate). In particular, Nafion has shown a large affinity for hydrophobic cations [26] and exhibit selectivity coefficients typically of the order of 10^6 relative to sodium ions present in the polymer [27,28]. A variety of redox cations have been immobilized in Nafion and include $Ru(bpy)_3^{2+}$ [27], $Ru(NH_3)_6^{3+}$ [28], methyl viologen [29] and more recently, phenothiazine dyes [30-33].

Electronically conducting polymers can be fabricated *via* chemical synthesis or *via* electropolymerisation. In the former case the electrochemically conductive state is made by oxidative or reductive doping with chemical reagents such as Halogens (X_2), SbF_5, AsF_5, $FeCl_3$, or alkali metals. This method is extensively used in the case of polyacetylene and dopant transport within the polymer matrix has been examined by Benier and co-workers using radiotracer and gravimetric measurements [34-36]. The result is a structure that behaves as an extension of the electrode surface in the solution. Electronically conducting polymer modified electrodes have received huge attention since their discovery in the late 1960's by Dall'Olio *et al.* [37]. The group polymerised pyrrole onto a platinum electrode and the resulting film exhibited a conductivity of 8 mS cm^{-1}. Over a decade later Diaz and co-workers [38] successfully prepared continuous films of polypyrrole by anodic oxidation. A similar synthetic route was employed by Shirakawa *et al.* [39,40] when fabricating polyacetylene films. They reported that these films could be removed from the electrode surface, resulting in free standing films. The films were stable to air and had conductivities of up to 100 mS cm^{-1}. Other conducting polymers that have generated a great deal of interest include polyaniline and polythiophene. Due to π-conjugation, these materials have relatively delocalised electronic states, allowing this electronically conducting property. The electrochemical processes in conjugated polymers lead to a reorganisation of the bonds in the molecule itself, and is accompanied by ion-exchange between the polymer and the electrolyte. A comprehensive body of literature has been compiled by Skotheim [41] on the physics and chemistry of conducting polymers.

Spin and drop coating techniques have also been used to fabricate redox polymers. The authors Miller and Van De Mark [42-44] when modifying a platinum electrode with poly-*p*-nitrostyrene, dipped the electrode into a dilute solution of the polymer. The modified electrode nitro groups exhibited reversible redox behaviour and, when negatively charged, reduced the species in solution [43]. Typically, a redox polymer consists of a system where a redox-active transition metal group is covalently bound to, or immobilised within, some sort of polymer backbone which may or may not be electroactive. Immobilising electrocatalytic transition metal species in a polymer modified electrode matrix is a means to endow the electrode with the chemical, electrochemical, optical, and other properties of the immobilised molecule. Some of the advantages of this are; control of the reaction rate by the applied potential or current, co-operative effects stemming from the proximity of other catalyst sites, the electrocatalytic sites are relatively close, and in high concentration, to the electrode surface.

In plasma polymerisation the intended polymeric material is vapourised and active species for polymerisation are generated by an electromagnet. Extremely thin films ($<1 \mu m$) pinhole free can be prepared, and the plasma gas may be functionalised prior to electrode modification. Several groups have employed plasma polymerisation to make PVC electrodes [12,45,46]. A plasma discharge can also be used to activate a 'clean' carbon surface, initiating polymerization onto the electrode surface. Modified electrodes have been made using this technique [12,47] as the resulting film is of uniform thickness. The screen printing technique allows the application of films over the active areas with good resolution. They can also be mass produced at low cost and are readily adaptable for incorporation into disposable biosensors. A stencil is created on the electrode surface by photolithography or by etching. A thin slurry, liquefied mixture of the powdered material and suitable binder, is forced into the open regions of the etched electrode. After treatment in a furnace, a continuous film remains. Screen printed carbon electrodes with mediating organic dye molecules have been successfully used as sensors for H_2O_2 and NADH [48,49].

The polymers of interest in this thesis are redox polymers. Redox polymers are local state conductors, that is, electron transfer occurs via the process of sequential self exchange (electron hopping) between neighbouring groups attached to the polymer backbone. The electron transfer is accompanied by ion-exchange between the polymer and the electrolyte to maintain electroneutrality in the film. Electropolymerisation of suitable organic monomers, via irreversible potentiostatic or galvanostatic oxidation, is a technique that is now used extensively [15]. Suitable heteroaromatic monomers include phenothiazines [50-52], phenols [53], pyrroles [54,55], aromatic amines [56], vinyl based systems [57,58] and ruthenium co-ordinated bipyridine ligands [59]. The polymer backbone itself, as is the case with the phenothiazine dyes, may be the functioning mediator. The three dimentional distribution of the mediator make these types of modified electrodes ideal for electrocatalytic studies [60]. In this current body of work, the redox polymer polymethylene blue, was electropolymerised onto a glassy carbon electrode and the resultant properties of the electrode were investigated.

1.3 Chemically Modified Electrodes-Applications

The applications of chemically modified electrodes are numerous and new research adds to the list continuously. They include electrocatalysis, electrochemical sensors, photogalvanic cells, electroreleasing films, energy storage devices and display devises. Modification of host electrodes with dyes has been extensively researched for various applications, and specific examples of some dye modified electrodes (in particular phenothiazines) are discussed in this section. Polymerised phenothiazines, the family of which methylene blue is a member, are classed as redox polymers. Redox polymer modified electrodes are the focus of this thesis and the analysis of polymethylene blue modified glassy carbon electrodes is detailed in chapters 3 & 4. On a general level the applications both redox and conducting polymers are detailed in this section.

1.3.1 Electrocatalysis

The possibility of fabricating tailormade modified electrodes has promoted rigorous research in the area of electrocatalysis. Electrocatalysis serves to accelerate the heterogeneous electron transfer of the target analyte, which otherwise is slower at a bare electrode. It should not be confused with mediation which provides a source/sink of electrons for a target analyte, but electron transfer occurs at the same potential as it would at the bare electrode [61]. Of course mediation of electron transfer may be catalytic but not all mediators are catalysts. Catalytic moieties can be readily immobilised close to the electrode surface by a three dimentional polymer matrix. Thus the amount of catalyst required to provide a high concentration of catalytically active sites is minimised by immobilisation. This is a highly desirable feature since catalysts, such as platinum and palladium, can be expensive. For example, Stadler *et al.* [62] used a cobaltocenium redox polymer film containing particles of rhodium and palladium to catalyse the historically important hydrogen evolution reaction. The hydrogen evolution reaction is the cathode reaction in water electrolysis and some chlor-alkali cells, one of the reactions in corrosion, and a competing reaction in some organic reductions and metal deposition reactions [63].

The ability of an electrode to reduce O_2 is of huge importance to applications such as fuel cells and more recently biofuel cells. The main problems are that few catalytic metal materials are stable to anodic dissolution at potentials where oxygen reduction takes place, and the analysis of this reaction may be hampered by the oxidation/reduction of the metal catalyst itself. One way of overcoming this problem is to use organic molecules as the catalyst. The authors Seitz *et al.* [64] reported the reduction of O_2 to H_2O_2 by NAD^+ in the presence of methylene blue. Van De Mark and co-workers fabricated a poly-*p*-nitrostyrene modified platinum electrode capable of reducing O_2 at a potential 200mV less negative than at the bare platinum electrode [43]. More recently the enzyme laccase has been used for O_2 reduction in a membrane-less glucose/oxygen biofuel cell [65]. Oxidation of glucose is coupled to the reduction if dissolved O_2 *via* mediated electron transfer from glucose oxidase at the anode to laccase at the cathode.

Organic dyes, particularly phenoxazines [14,15,66], phenazines [16,67-69] and phenothiazines [52,70,71], have been used extensively to modify electrode surfaces for the catalytic electro-oxidation of NADH. Almost 500 known dehydrogenase enzymes depend on NADH/NAD^+ coenzymes as co-reactants. Rigorous electrochemical probing of this cofactor continues to yield exciting results. The phenazine dye poly(neutral red), when electropolymerised onto a glassy carbon, has been reported by Karyakin *et al.* [72] to electrocatalytically reduce NAD^+ to the enzymatically active NADH. In further research performed by the same author [52], glassy carbon electrodes were modified with the phenothiazine dyes methylene blue, methylene green, azur A, toluidine blue, and the phenoxazine dye, brilliant cresyl blue. The electrodes were modified via electropolymerisation from a 0.4mM monomer solution by potential cycling at a scan rate of 50mV s^{-1}. All modified electrodes exhibited high stability and a catalytic response to NADH oxidation. The overall conclusions, drawn from the results of each modified electrode, were that (i) ring substitution with only tertiary nitrogen atoms as ligands provides higher catalytic activity, and (ii) higher redox potential of the polymer also provides higher catalytic activity. The order of catalytic efficiency was found to be methylene green > methylene blue > azur A > brilliant cresyl blue > toluidine blue. The suggested reason for the smaller catalytic activity of the two latter dyes was due to the alkyl ligands that they possess.

Sol-gel ion exchange modified electrodes have also utilised methylene blue to catalyse the oxidation of NADH. The authors Zaitseva *et al.* [73] fabricated a SiO_2/ZrO_2 *via* a sol-gel processing method dispersed with the cation exchanger, Sb_2O_5, in the gel matrix. The $SiO_2/ZrO_2/Sb_2O_5$ was immersed in a solution of methylene blue and the redox cation was adsorbed into the matrix by an ion exchange reaction. The $SiO_2/ZrO_2/Sb_2O_5$/MB was mixed with graphite and mineral oil. The paste was then used to make a modified carbon paste electrode. The authors observed NADH oxidation at a potential ca. 500mV less negative than at a bare graphite electrode [16] and a detection limit of 36μM.

Later, the same author made carbon paste modified electrodes containing SiO_2/SbO_3 and the redox mediators methylene blue, toluidine blue, and medola's blue were immobilised in the sol-gel matrix [74]. The medola's blue carbon paste modified electrode exhibited the highest catalytic activity for NADH oxidation as it also has the highest E^0 value. Detection limits were 25, 42 and 7μM for the methylene blue, toluidine blue and medola's blue carbon paste electrodes respectively. The electrocatalytic ability of these organic dyes makes them ideal for NADH oxidation in the operation of successful sensors and biofuel cells. Moore *et al.* [75] have reported on the use of polymethylene green to electrocatalytically oxidise NADH in an ethanol/oxygen biofuel cell.

Ye and Baldwin were one of the first groups to use a methylene blue modified glassy carbon electrode for the electrocatalytic reduction of myoglobin and hemoglobin [76]. Myoglobin and hemoglobin are proteins found primarily in mammalian muscle tissue and are responsible for O_2 transport and storage. They contain heme moieties, one in myoglobin and four in hemoglobin, with variable oxidation states and which have generated a great deal of electrochemical research.

The methylene blue modified glassy carbon electrode was prepared by dip coating for 60s in a 0.01% m/v methylene blue solution and exhibited excellent stability and reproducibility. When used in flow injection experiments, the electrodes exhibited a linear current response to analyte concentration and yielded detection limits of 10 and 20pmol for myoglobin and hemoglobin respectively. The myoglobin oxidation currents were 100mV less negative at the modified electrode than at a bare glassy carbon electrode. Two other heme containing proteins catalase and cytochrome *c* were also electrocatalytically reduced at the methylene blue modified electrode. The authors also reported a hemoglobin and myoglobin reduction response at a thionine modified glassy carbon electrode. The two phenothiazine modifiers had very similar redox potentials but the electrocatalytic currents observed at the thionine modified electrode were significantly lower.

These selected examples of electrocatalysis using methylene blue highlight the versatility of the organic dye. The modifying techniques are numerous while the modified electrodes exhibit high stability and reproducibility. Methylene blue can be used to electrocatalytically oxidise and reduce molecules of major biological importance and so its use in applications based on electrocatalysis is ever growing.

1.3.2 Electrochemical Sensors

The detection and quantification of a vast range of chemical species is routinely required in a multitude of disciplines in the world today. The advances in sensor technology mirrors this phenomenon as research strives to keep abreast of increasing sensor demands. The fundamentally important requirement relating to sensors is the selectivity in detection of a specific analyte. Traditional methods of detection of a particular analyte use the combination of different analytical techniques. Firstly the analyte must be isolated and identified by gas or liquid chromatography, or mass or *ir* spectroscopy. The operation of such analytical tools requires highly skilled personnel and so chemically modified sensors offer a reliable and cost-effective alternative.

Advances in modified microelectrodes and ultramicroelectrodes have made it possible for *in vivo* analysis of analytes [77,78], though electrode fouling can be a problem [79]. Polymers modified electrodes can be a good solution to electrode fouling in that a particular polymer may be permselective towards a particular analyte *in situ*. Yacynych and co-workers [80] modified a platinised reticulated vitreous carbon electrode with glucose oxidase and electropolymerised 1,2-Diaminobenzene, for use as a glucose sensor in human serum. The 1,2-Diaminobenzene prevented interferents such as L-ascorbic acid, L-cysteine and urea from penetrating the film but was permselective towards H_2O_2. The H_2O_2, a bye-product of glucose oxidation, was detected at the electrode and accurately correlated to the amount of glucose present in the sample. Good summaries of the development of these type of sensors is presented in special editions of *The Analyst* [81,82].

Electrochemical sensors may be classified into two categories relating to the mode of operation, potentiometric and amperometric [83]. Potentiometric sensors operate under conditions of equilibrium in the sample. The potential difference across a membrane or solution/electrode interface is measured relative to a reference electrode, and is directly related to the analyte concentration. An example is an ion-selective electrode. The potential difference in these electrodes is created by the selective uptake of an ion from solution, from one phase to another. The membrane potential, E_m, analogous to the liquid junction Donnan potential, can be described as

$$E_m = \frac{RT}{nF}\ln\left(\frac{a_\alpha}{a_\beta}\right) \tag{1.2}$$

where a_α and a_β represent the activities of the species in the membrane and solution respectively, F is Faraday's constant, and n is the number of electrons lost or gained in the reaction of one mole of analyte, R is the gas constant, and T is the temperature [20,83]. If the activity of the ion in the membrane is constant, then the E_m varies in a Nernstian manner to the activity of the ion in solution. The analyte concentration varies logarithmically with the electrode potential. Fast electrode kinetics is a requirement of potentiometric sensors to ensure a stable local environment at the electrode surface. Potentiometric sensors are sensitive to noise and temperature due to the logarithmic relationship of current and potential.

Amperometric sensors operate by relating the current response, to a fixed potential, to analyte concentration. The potential effectively drives a reaction in the sample and a measurable charge is passed from electrode to the analyte or *vice versa*.

By use of Faraday's law, the amount of charge passed is related to the number of moles of electrons lost or gained in the electrochemical reaction

$$Q = nFAN \tag{1.3}$$

where Q is the number of coulombs used in converting N moles of analyte, F is Faraday's constant, A is electrode area, and n is the number of electrons lost or gained in the reaction of one mole of analyte. Differentiation of Q with respect to time gives a measure of the rate of conversion of analyte, the current

$$\frac{dQ}{dt} = i = nFA\frac{dN}{dt} \tag{1.4}$$

The current response to the applied potential is governed by the Butler-Volmer equation [84,85]. When the rate of electron transfer is slow, the reaction is said to under kinetic control. This is generally the case if the applied potential is close to the equilibrium potential of the analyte. For an applied potential that is significantly different from analyte equilibrium potential, the rate of electron transfer, and hence current response, increases until the reaction is under mass transport control. Slow kinetics can be a problem in amperometric sensors resulting in slow response times, so mediation of the charge transfer reaction is often required.

1.3.2.1 Specific Sensor Electrodes

In this section some specific examples of sensor electrodes will be described with an emphasis on redox polymer modified sensors. In particular the redox active Os(bipy)$_2$ and its derivatives are included due to the excellent redox properties they possess. Os(bipy)$_2$ and osmium derivatives have efficient electron shuttling properties and can be polymerised or incorporated into conducting polymers, making them ideal for important sensor applications. To close this section the redox polymer electrodes modified with phenazines, phenoxazines and phenothiazine dyes are discussed. Within this small group of modifying materials, a huge range of sensor types has been developed, due to the various properties that the dyes possess.

The most significant development in biosensors over the last twenty years is the glucose sensor. Diabetes is common but serious ailment and is on the increase due to the trends observed in the human diet. Convenience foods and lack of exercise can cause the onset of diabetes, as life becomes increasingly more hectic. The accurate detection of blood sugar levels is vital to diabetics and enables sufferers to enjoy a high quality of life, and consequently a huge market for glucose sensors has evolved.

Both O_2 and H_2O_2 levels can be used to correlate directly, the concentration of glucose in a sample, i.e., by monitoring the O_2 depletion or the increase in the by-product of glucose metabolism, H_2O_2, due to the glucose oxidase (GO_X) catalysed reaction:

$$\text{glucose} + O_2 \xrightarrow{\mathbf{GO_X}} \text{Gluconic acid} + H_2O_2$$

The evolution of the glucose sensors has evolved from; immobilisation of the enzyme glucose oxidase (GO_X) directly to an electrode surface [86], to immobilisation of both an electron mediator and GO_X to the electrode surface [87], to "wiring" the enzyme to the electrode surface [88, 89].

The first H_2O_2 sensor reported by Guillbault *et al.* [90] was an enzyme electrode for the determination of blood glucose based on amperometric (anodic) monitoring of the liberated hydrogen peroxide. Good precision and accuracy were obtained in connection to 100 μL blood samples.

In general, the main problem with enzyme electrodes is the effective and efficient mediation of electron transfer from the enzyme to the electrode surface. The redox enzyme active site, the flavin group, lies deep within the insulating protein shell of the enzyme, making electron transfer with the mediator difficult. Traditionally, communication between the flavin group and the electrode relied on diffusion of the ET mediator to the enzyme active site. This has been replaced in recent years by electrical "wiring" of the flavin site to the mediator using redox hydrogels. The authors Forster and Vos were the first to synthesise osmium and ruthenium modifed polyvinylimidazole (PVI) and poly(vinyl-pyridine) (PVP) redox hydrogels [91]. The use of these hydrogels facilitates enzyme "wiring" to the electrode surface and consequently properties of enzyme electrodes has vastly improved. Hydrogels are particularly relevant to electrochemical biosensors and biofuel cells. Both are very much linked as glucose and O_2 metabolising enzymes (e.g. GO_X and Laccase) may be used in both types of system.

Heller has been the most significant contributor to the area of enzyme "wiring" using these hydrogels, and indeed was the first to report on the "wiring" of glucose oxidase to an electrode surface [92]. Heller and co-workers have since reported numerous improved "wired" GO_X electrode systems [93-96]. These "wired" enzyme electrodes are constantly being improved and not only in sensitivity and selectivity. "Wired" glucose electrodes operate in the following way: redox centers of the glucose oxidase can be readily electrooxidized *via* a high molecular weight polycationic redox polymer. The enzyme is polyanionic and forms electrostatic complex with the polymer, thus reducing the electron-transfer distance. The redox polymer enzyme complex is preserved at high ionic strength if the polymer is covalently bound to the enzyme. Upon such bonding, the electrooxidation of glucose persists even at high ionic strength. The most efficient and utilised redox polymers are the aforementioned PVP-Os and PVI-Os complexes.

Recently Heller has also reported the on a PVP-Os GO_X carbon rotating disk and carbon fibre electrodes with an electron diffusion coefficient, D_E, of $5.8 \pm 0.5 \times 10^{-6}$ $cm^2\ s^{-1}$ [97]. This is an order of magnitude faster than previously reported and is attributed to the 13 atom spacer linking the osmium ligand to the PVP. A long spacer allows flexible movement of the electron mediating osmium ligand, thus enhancing electron diffusion through the hydrogel.

To date, the highest sensitivities for the bioelectrocatalytic determination of H_2O_2 were obtained with PVI-Os hydrogels, peroxidases and a cross-linker [98-100]. Prior to the enzyme-catalysed reduction of H_2O_2, the hydrogel-bound Os-centres provide a very efficient ET pathway from the electrode to the enzyme's prosthetic group, via an electron-hopping mechanism.

Glucose oxidase is not the only enzyme used in glucose sensors. The "wiring" of pyranose oxidase (PyOx) to graphite rod electrodes using a (PVP)-Os and (PVI)-Os hydrogels has been reported by Timur and co-workers [101]. PyOx is more suited to biofuel cells than GO_X because many sugars other than glucose can be oxidised for small scale energy production.

A bi-enzyme modified electrode, incorporating either poly(1-vinylimidazole)-Os or poly(vinyl-pyridine)-Os, has been reported by Nikitina *et al.* for the detection of the serious environmental pollutant, formaldehyde [102]. An inner ET mediating layer of [(PVI)-Os], or [(PVP)-Os] was coated with poly(ethylene glycol)(400) diglycidyl ether and then with diaphorase. The outer layer was comprised of a formaldehyde dehydrogenase (FDH) coat. The FDH-dependent NAD^+ and glutathione (GSH) were added to the electrolyte. The authors quote a sensitivity of 22 $Am^{-2}M^{-1}$, a detection limit of 32 μM, and a linear dynamic range of 50–500 μM for the sensor.

The authors Smutok *et al.* [103] used an osmium complex to mediate a bi-enzyme modified GC electrode. HRP and Alcohol Oxidase (AO_X) were immobilised onto a GC electrode using cathodic and anodic paints. The oxidation of ethanol to aldehyde was facilitated by the AO_X, which in turn was re-oxidised by O_2, forming H_2O_2 on contact with H_2O. H_2O_2 was rapidly broken down again by HRP, with the Os complex facilitating the re-reduction of the HRP. The sensors were stable and reproducible in the determination of ethanol content in wine, exhibiting rapid consumption of H_2O_2.

The future of important biological molecule detection is in the miniaturisation of biosensors which, hopefully, will pave the way for implantable biosensors for an ever growing number of applications. Subcutaneous (PVI)-Os redox hydrogel "wired" glucose sensors for real-time glucose monitoring in rats have been reported [104,105]. The size of implantable biosensors is currently governed by the power supply unit, i.e., the battery. It is desirable, therefore, to fabricate biosensors that can be powered by sugars found in abundance in the human body – biofuel cells. Heller reported on the first biofuel cell using PVI-Os GO_X "wired" to a carbon fibre anode and laccase "wired" to a carbon fibre cathode [106]. The anode is a glucose-oxidising, while the cathode is oxygen-reducing. The breakthrough for the development of miniature biofuel cells was made possible due to the discovery that O_2 could be reduced by (PVI)-Os "wired" laccase electrode at pH 5 [107]. A recent publication by the same author describes three different enzyme electrodes "wired" by (PVI)-Os hydrogels [108]. The cell consisted of anode immobilised GO_X and laccase and biliruben oxidase immobilised onto the cathode. The enzyme cathode is catalystic in the four electron O_2 – electroreduction to water generating current densities as high as 10^{-2} A cm^2. The glucose/O_2 biofuel cells had a current output of ~1mA cm^2 which is effective for a period of weeks. The authors found that the best redox hydrogel-GO_X

anode had an apparent electron diffusion coefficient of 6 x 10^{-6} cm^2 s^{-1}. The high apparent electron diffusion coefficient results from the 13 atom spacer arms separating the osmium ligand and the polymer backbone.

However, one disadvantage of using hydrogels is the manual deposition procedure which often results in poor reproducibility, making minaturisation of the sensors problematic. An attempt to address the problem of minaturisation has been reported using HRP and tobacco peroxidase (TOP) immobilised *via* polymerised pyrrole monomer functionalised with an osmium-complex [109]. The authors reported significantly higher sensitivities for the reduction of H_2O_2 for the HRP-based sensors as compared with the tobacco peroxidase-based ones, with 0.12 and 0.06 nA μM^{-1}, respectively. The authors attributed this to poor accessibility of the active site of TOP for the Os redox centres.

PVP-Os and PVI-Ru complexes have been used to fabricate sensors other than enzyme modified electrodes. For example a nitrite sensor has been reported by Vos and co-workers [110]. The sensor was stable, with good reproducibility and the authors quote a limit of detection of 0.1μg cm^{-3}. A poly(vinylimidazole-co-acrylamide) (PVIAA) partially imidazole-complexed with $[Ru(bpy)_2Cl]^+$ capable of detecting guanine [111] has been reported. The sensor boasts a detection limit of 5nM and has a linear concentration range of 8.0 nM–100 μM. The sensitivity of these sensors is testament to the remarkable qualities of these osmium and ruthenium complexes.

The redox polymer electrodes modified with phenazines, phenoxazines and phenothiazine dyes are discussed in this section. The wide range of special characteristics displayed by these materials is reflected in the vast and varied sensor electrodes that have been developed. One of the more important sensors to basic research is the pH electrode. The glass electrode is an amorphous solid that is permeable to hydrogen ions. This property makes it a suitable electrode for use as a potentiometric pH sensor. The membrane potential is created *via* ion exchange between the hydroxyl groups on the hydrated glass surface and the hydrogen ions in the sample, which is then related to hydrogen activity [112]. If the pH *versus* potential relationship is linear, a Nernstian response is obtained. A poly(neutral red) film, electropolymerised onto a indium-tin oxide electrode, was found to be suitable as a pH sensor [113]. Two distinct zones were assigned to the film, a redox active inner zone and an outer zone that behaved like a membrane. The membrane zone was permeable to H^+ and a linear relationship between pH and potential was found to exist, yielding a slope of -50mV dec^{-1}. This slope was deemed to be high enough for the potentiometric sensor to conduct pH measurements.

Amperometric sensor developments constitute the largest area of activity in sensor research due to the demands of biological molecule detection as described in the enzyme electrode section. The full range of successful modifying techniques has been utilised. Immobilisation of organic dyes at electrodes to mediate electron transfer reactions has been widely reported. The phenothiazines are particularly good mediators for the electron transfer reactions involving some enzymes, regenerating the enzyme activity towards the specific target molecule. This is of great importance as a particular enzyme to a specific target molecule, can be immobilised with the mediator to an electrode surface. This, of course, is not specific to glucose detection.

Adsorption is one mode of immobilisation, an example being the methylene blue mediated enzyme electrode, developed for the detection of trace mercury(II), mercury(I), methylmercury and a mercury-glutathione complex [114]. The accurate measurement of mercury(II) is very important in the food industry, environmental and clinical sample analysis, at concentrations usually in the ng ml^{-1} range or lower. A mixture of methylene blue, β-cyclodextrin, the enzyme horseradish peroxidase (HRP), and the polymer cellulose triacetate, was spin-coated onto a glassy carbon electrode at 3000rpm. The enzyme HRP catalyses the reduction of H_2O_2 to water, which is vital in biological systems as H_2O_2 attacks healthy tissue when scavenging for electrons. The electrode was placed in a solution of H_2O_2 and was reduced by HRP, which in turn was reduced in a methylene blue mediated reaction to produce a catalytic current. This catalytic current was correlated to the concentration of H_2O_2 and the HRP activity. The electrode was then immersed in a solution of the trace mercury compounds which inhibit the activity of HRP, towards H_2O_2, by binding to active sites in the enzyme. The decay in HRP activity was measured and calibration curves were constructed. The authors calculated detection limits in the ng ml^{-1} range for each inhibitor.

Ruan and co-workers [115] developed an amperometric sensor for H_2O_2 with the phenothiazine mediator, thionine, covalently attached to the HRP. A self assembled monolayer (SAM) electrode was prepared by immersion of an etched gold wire electrode in a deaerated 0.02M L-cysteine aqueous solution at room temperature for 12 hours. The electrode was then immersed in a glutaraldehyde solution for 20 minutes and then immersed in the HRP solution for 20 minutes. The amino groups of the L-cysteine tails can covalently bond to amino residues of the HRP, using glutaraldehyde as a bifunctional agent. Thus a HRP/SAM electrode was formed and on repetition of this step, enzyme mutilayers were attached to the SAM. The thionine mediator was attached to the HRP/SAM electrode by immersion in glutaraldehyde for 20 minutes, followed by immersion in a thionine solution for 20 minutes to fabricate the TH/HRP/SAM electrode. These steps were repeated to fabricate an electrode with a known amount of enzyme and thionine layers. The sensors displayed a rapid response to low concentrations of H_2O_2, in one case reaching 95% steady state current response in 4s. This novel method of fabrication opened up a new strategy in the construction reagentless enzyme biosensors.

Another HRP enzyme biosensor, this time methylene blue mediated, was reported by Xu *et al.* [116]. The methylene blue and HRP were immobilised onto multiwall carbon nanotube modified glassy carbon electrode *via* adsorption. HRP reduced the H_2O_2 to water and the methylene blue successfully mediated the regeneration of HRP *via* two separate electron transfers. The stability of the sensor was good with a 10% decrease in current response after 5 days. The authors also reported a detection limit of 1 μM and a Michaelis-Menton constant of 0.12mM indicative of the sensors high sensitivity.

Numerous amperometric sensors modified with ion-exchange films have been described in the literature [29, 33]. Nafion is a perfluorosulphonated ionomer, a type of ion-exchange film, capable of high selectivity in the intercalation of certain cations. This selectivity is due to the hydrophobic nature of the fluorocarbon phase of the film, and the relative size of the intercalating ion [27]. This partitioning towards interferent components in solution is highly desirable and has been used in the *in vivo* detection of dopamine [117]. The incorporation of methylene blue and thionine into Nafion and the subsequent electrochemical behaviour of the films has been described [30,118]. The dye/Nafion films displayed reversible, two electron transfer processes with good stability and reproducibility. A distinct advantage of Nafion is that the mediators are free to diffuse within the film. Chen and co-workers developed an amperometric sensor for the determination of hemoglobin [119]. They modified a carbon fiber electrode with methylene blue in a Nafion film, and reported the electrocatalytic oxidation of hemoglobin by the sensor. The sensor had a detection limit of 2 μM and standard deviation of 3.5% for six successive determinations at 6 μM. The amount of hemoglobin in normal human blood samples is between 2.2-2.6 mM. The sensor determined 2.4 mM from a real human blood sample, without any interference from other biological molecules. This was comparable to 2.5 mM obtained by spectrophotometry at a wavelength of 540 nm. The sensor exhibited good stability with a 4% drop in current response after 2 hours continual use.

An amperometric nitric oxide sensor based on a polythionine/Nafion film on glassy carbon has been reported by Chen and coworkers [33]. Nitric oxide is a neurotransmitter, whose release from cells is stimulated by L-arginine. The sensor was applied to monitor the nitric oxide release from rat kidney. Polythionine mediated the oxidation of nitric oxide, significantly increasing the current response, and the sensor detection limit of 7.2×10^{-8} M was determined.

A H_2O_2 amperometric sensor with methylene blue immobilised into the ion-exchanger α-zirconium phosphate has also been reported [120]. Intercalation of the methylene blue occurred spontaneously, in aqueous solution, to form an inclusion colloid. HRP and glutaraldehyde were added to this solution and drops of the composite were deposited onto a glassy carbon electrode to form the sensor. The authors recorded a 95% steady state current response within 20s and a detection limit of 3×10^{-7} M.

Sol-gels provide an attractive method of amperometric sensor fabrication and numerous methylene blue mediated enzyme electrodes have been reported [121,122]. A selective sol-gel sensor for the simultaneous determination of ascorbic acid and uric acid was developed by Khoo *et al.* [123]. The methylene blue electrocatalytically oxidises the biomolecules and the sensor exhibits separate current response peaks for the analytes using DPV. The detection limits were < 0.45 and < 0.25 mM for ascorbic acid and uric acid respectively, depending on the solution pH, with high sensitivity and stability observed.

Another biologically important molecule is pyridoxine hydrochloride(vitamin B_6), which plays an important role in amino acid synthesis, and may be converted to the metabolic coenzyme pyridoxal phosphate. An electropolymerised polymethylene blue modified glassy carbon electrode has been reported to electrocatalytically oxidise vitamin B_6 [124]. The authors concluded the electrode reaction to be quasi-reversible process, being diffusion controlled at low scan rates and adsorption controlled at high scan rates. The electrocatalytic current response to vitamin B_6 concentration was linear and the electrode had a detection limit of 1.34 μg mL^{-1}. Screen printed amperometric enzyme sensors have been developed using thionine and medola's blue [48,49].

1.3.3 Chromic Devices

Chromic materials possess the ability to undergo an induced colour change and the resultant chromism can be classified according to the type of applied stimulus. Electrochromism can be defined as a reversible and visible change in the transmittance of a material as a result of an electrochemical oxidation or reduction [125]. Methylene blue is an electrochromic material and is known to show a colour change from blue to colourless on reduction. Photochromic materials can reversibly change their chromatic properties upon exposure to both natural and artificial ultraviolet (UV) light [126]. While methylene blue may not change colour when subjected to the application of a light source, it is known to form a photoactive triplet state that can be photoreduced in solution by an appropriate electron donor [127]. This property has been harnessed in photochromic, electrochromic and colourimetric indicator devices. Potential targets for the applications of electrochromism and photochromism are curtainless smart windows for heat and daylight control, anti-dazzling rear-view mirrors for vehicles, and oxygen and humidity indicators [128].

The electrochromism of dye-adsorbed nafion coated glassy carbon and indium tin oxide electrodes has been reported by Ganesan *et al.* [129]. They fabricated the electrodes by casting a known volume of the dye-adsorbed nafion onto the electrodes and allowed the solvent to evaporate. The dyes used were thionine, methylene blue and phenosafranine, all of which possess electrochromic properties. The authors found that thionine leached from the nafion, while the methylene blue and phenosafranine remained bound to the nafion, after repetitive potential cycling. Mixed nafion films of methylene blue/phenosafranine were stable but thionine/phenosafranine films were not stable due to thionine leaching and being replaced by phenosafranine. The electrochromic properties of each film was spectroelectrochemically investigated and the progression of the colour changes with potential were recorded. The ITO/methylene blue/nafion film was oxidised at 0V *vs* SCE and after 300s was colourless due to the total reduction of methylene blue to leucomethylene blue in the film. The colour then changed back to blue on application of an oxidation potential of 0.6V for 300s, corresponding to the total re-oxidation of leucomethylene blue to methylene blue in the nafion film. The thionine/nafion film exhibited similar redox potentials, describing a colour change from colourless at 0V to violet at 0.5V, but leaching of the thionine cations was observed. The phenosafranine/nafion film experienced a colour change from colourless at -0.5V to red in its oxidised state, at 0V. The methylene blue/phenosafranine/nafion film was colourless at -0.5V to red at 0V to red-blue at 0.7V. All colour changes were reversible and the films, except thionine, were very stable. Methylene blue molecules have also been an immobilised in electronically conducting polymers [130,131], improving the electrochromic properties of the films over the non-mixed polymers. Modified graphite electrodes with adsorbed methylene blue have shown electrochromic properties [132].

A flexible spin coated nano-photo-electrochromic film, constructed with TiO_2 nanoparticles deposited on conductive poly(ethylene terephthalate), has been developed [133]. The TiO_2 nanoparticles were used anchor methylene blue molecules which inferred photo- and electrochromic properties to the electrode. The electrode was irradiated by red light, the methylene blue molecules were excited to a triplet state, and then photoreduced by electron donor triethylamine molecules present in the electrolyte. The film changed colour from blue to colourless in *ca.* 20 s. The re-colouring of the film, *via* electro-oxidation, was complete after application of a 1 s electrical impulse of 0.4V DC. The speed of re-oxidation was attributed to the immobilisation of the methylene blue molecules at the electrode surface. Also the presence of the TiO_2 nanoparticles served to greatly increase the surface area for oxidation of the methylene blue molecules. The re-oxidation response time was 16 times quicker than that of the authors previous publication [134] on a methylene blue/dipentaerythritol pentaacrylate based photoelectrochromic electrode.

An intelligent ink oxygen sensor has been reported based on the colorimetric properties of methylene blue [135]. This device is suitable for detecting oxygen in modified atmosphere packaging used primarily in the food industry. A dispersion of the semiconducting material TiO_2, methylene blue, and the mild electron donor triethanolamine, were encapsulated in hydroxyethyl cellulose polymer which was then spin coated on a glass cover slip. The TiO_2-MB-TEOA-HEC films were bleached *via* application of UV-A light, causing colour change of blue to colourless. The irradiation of TiO_2 semiconductor particles generates electron-hole pairs, and is reduced by the mild electron donor, to form TiO_2^-. This then reduces methylene blue causing bleaching of the film. The methylene blue re-oxidises on contact with oxygen and the film turns blue, indicating the presence of oxygen. The same authors [136] and the authors Gutierrez-Tauste *et al.* [137] have also reported similar films as colorimetric oxygen indicators.

Somani *et al.* [138] described the detection of humidity using changes in the absorption of methylene blue indicator incorporated in solid polymer electrolytes consisting of poly(vinyl alcohol)/H_3PO_4. These films, formed by dip-coating on a glass substrate, showed humidity-dependent absorbance changes that can be ascribed to either the association/dissociation complex that the dyes form with the polymer. The more humid the environment, the more acidic the local methylene blue environment became, and this caused a dissociation reaction of methylene blue from the film to occur. Humidity detection in the 20–80% RH range was reported.

1.3.4 Photogalvanic cells

A photogalvanic cell can be defined as: a galvanic cell in which significant current and voltage are simultaneously produced upon absorption of light by at least one of the electrodes. The conversion of light energy into chemical or electrical energy results from light in the visible region acting as an electron pump, injecting electrons into a semiconductor electrode material. This electrical energy can be stored or used to drive chemical reactions. Photogalvanic cells, therefore, are the basis for converting solar energy into electricity and chemical energy. The existing commercial devices used for solar energy conversion are expensive and they encounter technical problems, so interest has been directed towards photochemical and photoelectrochemical processes that utilise solar energy. Some semiconducting electrodes are not photoexcited by the visible region of the light spectrum, and so require a sensitiser to facilitate electron injection into the semiconductor. The sensitiser can absorb at the visible light frequency, thus promoting an electron form a lower energy orbital to a higher energy orbital. The result is an electron-hole (e^--h^+) pair corresponding to the excited-state. Recombination of this electron-hole pair can be a problem in photogalvanic cells. The photoexcited sensitiser species produced is capable of interfacial electron transfer at the semiconductor or it can be used to drive a chemical reaction.

Organic dyes, such as the phenothiazines, have been used in the sensitisation of semiconductor electrodes and a good review on the topic can be found in recent literature [139]. The absorption of a photon by the dye molecule at the electrode surface enables an injection of electrons into the semiconductor or can be used to drive a chemical reaction. In the former process, the oxidised sensitiser may be reduced by a suitable donor in solution, while the injected electron in the semiconductor can pass through an external circuit and used to reduce an acceptor at the counter electrode. This is the operation of a photogalvanic cell, where a chemical potential gradient drives the conversion of light into electricity. The chemical potential difference is generated by the presence of the acceptor and donor species. This chemical difference can be maintained by using two identical electrodes in separate cell compartments, and illuminating one compartment whilst keeping the other compartment in darkness.

A major factor that influences the electron injection yield is the proximity of the excited-state sensitiser to the semiconductor surface. Diffusion of the excited-state sensitiser to the electrode surface in solution would have to occur within the lifetime of the excited-state. Excited-state lifetimes are short when compared to solution phase diffusion and so it is generally accepted that sensitisers in solution are adsorbed onto the semiconductor surface [140,141] or are bound *via* electrostatic interactions [142].

The phenothiazine dyes have been deemed suitable sensitisers and thionine modified electrodes using Fe(III) as the electron acceptor have been used in photogalvanic cells [143-145] but have yielded low photovoltages and photocurrents. The azur's A, B and C were the dye sensitisers in a NaLS-ascorbic acid system reported by Genwa and Chouhan [146]. The cells constructed were cost effective and exhibited charge storage capacities of 110, 135, and 95 min for the azur A, B and C dyes, respectively. A system using methylene blue with NaLS-oxalic acid was used by Gangotri and Meena [147]. They reported a photogalvanic cell with a 35 min storage capacity. Gangotri and co-workers have also reported a number of mixed dye photogalvanic cells with EDTA as reductant. The authors quoted charge storage capacities of 46, 34, and 30 min for the methylene blue-azur B [148], methylene blue-toluidine [149], and methylene blue-thionine systems [150], respectively. In a paper by Somani and Radhakrishnan [151], a small concentration of methylene blue was used as a photosensitiser in a solid state photogalvanic cell. The cell was fabricated using doped and undoped polypyrrole coated electrodes sandwiched with a poly(vinyl alcohol) film doped with phosphoric acid. The polypyrrole transported the photogenerated charge carriers without recombination of the electron-hole pairs.

1.4 Polymethylene Blue

Organic dyes such as the phenazines, phenoxazines, and phenothiazines can electrochemically polymerised from a monomer solution onto electrode surfaces forming semiconductor films. They have received a great deal of attention for use in sensors as they exhibit high conductivity, high stability in air and show high redox reversibility. The main applications of such films are extensive-enzyme immobilisation at the electrode surface and the electron transfer mediation due to the properties of the polymer itself.

1.4.1 Electropolymerisation Process

The authors Lyons *et al.* [152] were the first to report the electropolymerisation of methylene blue. The electropolymerisation process is complicated with different polymerisation schemes proposed [152,153,156]. A glassy carbon working electrode was used by Lyons *et al.* [152], and they investigated the variation of the redox properties of the polymer with solution pH. This examination allowed the proposal of a detailed mechanism for film formation. The redox process within the polymer film was assumed to be reversible. They then applied the Nernst equation predicting that the modified electrode potential (for a known ratio of species in oxidised and reduced states) should vary linearly with the solution pH. The slope of this plot gave the ratio of electrons to protons for the redox process. From this information they proposed that electropolymerisation occurred via the coupling of oxidatively formed radical cations of monomeric methylene blue (Scheme 1.1). This results in the carbon-carbon coupling to produce the dimeric species. This proposed mechanism seems plausible as the electroactive heterocyclic nitrogen atoms are retained, thus the film retains its redox activity when deposited. Karyakin *et al.* [154,155] support this proposed carbon-carbon coupling scheme.

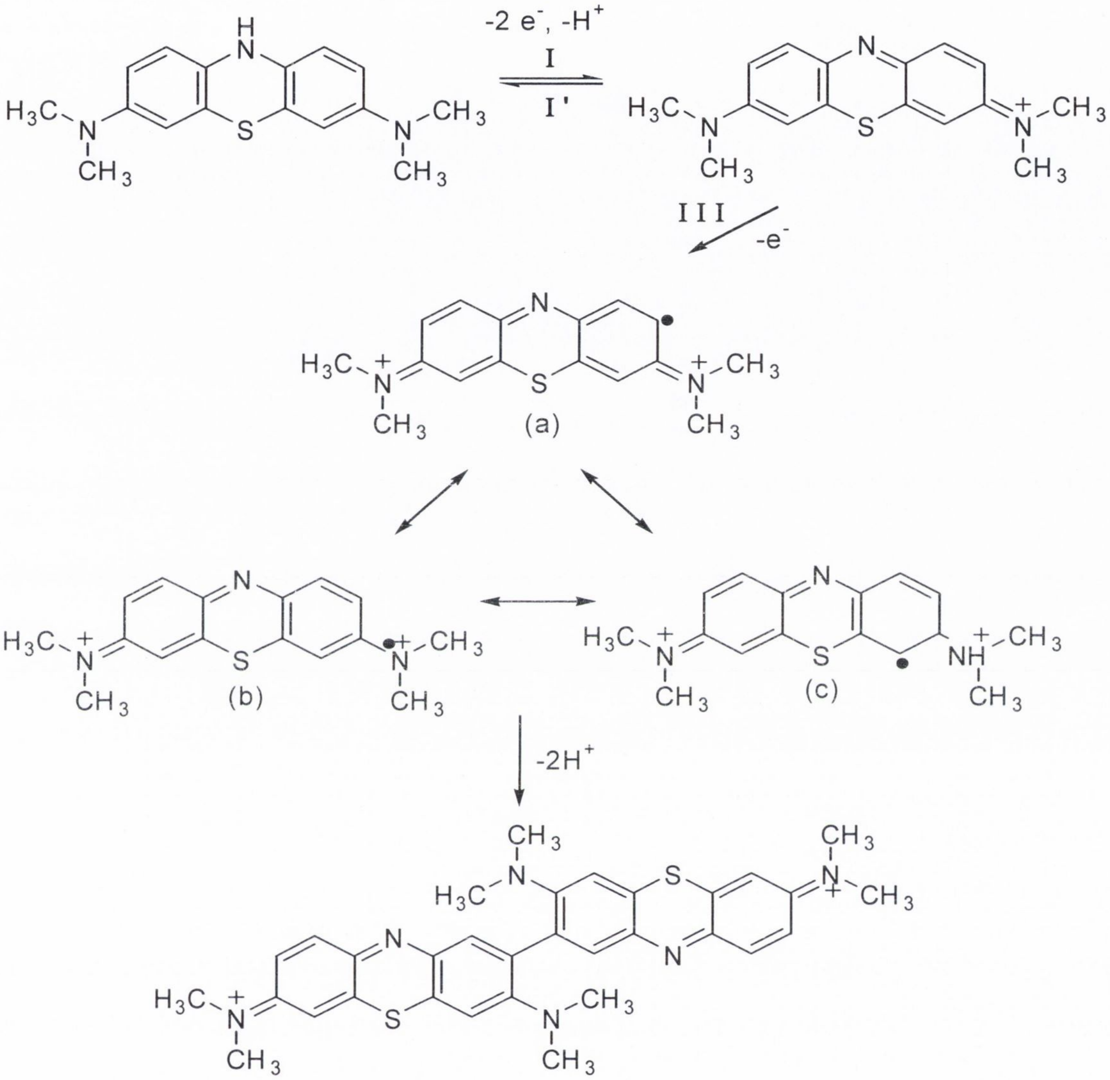

Scheme 1.1; The mechanism of electropolymerisation via carbon-carbon coupling.

In the paper published by Liu *et al.* [153], a different electropolymerisation mechanism (Scheme 1.2) was proposed. The authors suggested, using Raman spectra studies, that the dimeric species was nitrogen-nitrogen coupled. In scheme 1.2, the electroactive nitrogen atoms are present so the polymer has the redox sites required for electroactivity. Liu and co-workers quote Raman vibrational frequencies for N-CH_3 or N=$(CH_3)_2$ and –N$(CH_3)_2$ groups which are present in both proposed mechanisms, but it's not clear why specifically nitrogen-nitrogen coupling is thought to occur.

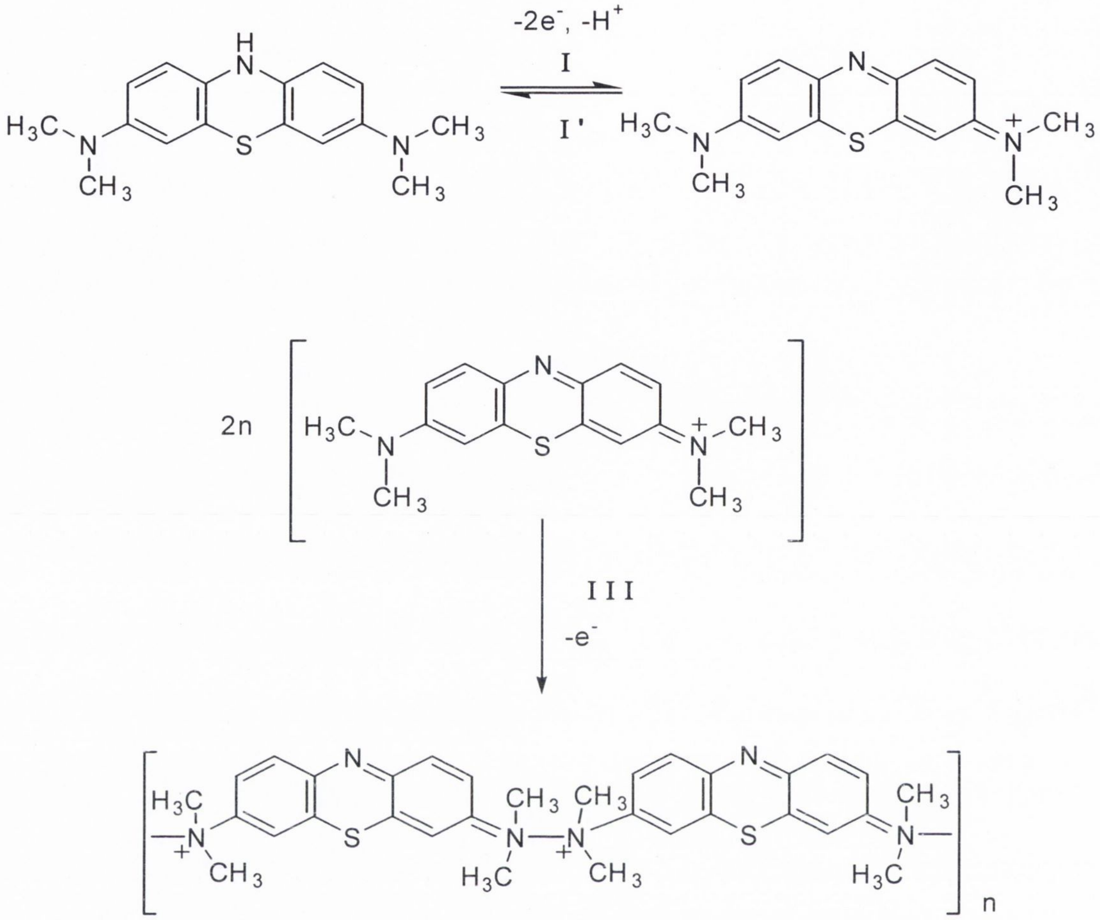

Scheme 1.2; Electropolymerisation of methylene blue via nitrogen-nitrogen coupling.

A third electropolymerisation scheme has been proposed by Kertesz and Van Berkel [156]. The authors used electrochemistry/electrospray mass spectrometry to investigate the polymerisation mechanism. The authors based their conclusions on the mass spectrometry results and proposed that electropolymerisation proceeds via nitrogen-carbon coupling.

Whichever mechanism is correct, the properties of the polymer film remain the same. A resolution to the polymerisation mechanism may be solved using labeling techniques, such as, radio tracing the nitrogen atoms.

1.4.2 *Charge Transport in Redox Polymers*

Electroactive redox polymers are characterised by the presence of redox sites distributed in a three dimensional manner throughout the film. Electroactivity in the redox polymer is localised as opposed to a reorganisation of the bonds in conjugated polymers. It is generally believed that redox polymers conduct *via* an electron hopping process or physical diffusion of the redox species themselves (Figure 1.1). Murray and co-workers [157] termed this type of charge transport "redox conduction". Electron hopping occurs between neighbouring redox species is driven by a concentration gradient of fixed oxidised and reduced sites and not by a potential gradient. The electrocatalytic site functions as a mediator, facilitating the transfer of electrons between the electrode and the substrate.

Redox polymers characteristically exhibit conductivity only over a very narrow potential range, with maximum conductivity occurring when the concentrations of the oxidised and reduced forms are equal in the film, *i.e.,* at the formal potential of the redox centers. The self-exchange rate reaches a maximum when the concentration of both species is equal, i.e., $C_{ox} = C_{red}$, hence maximum conductivity occurs at E^0.

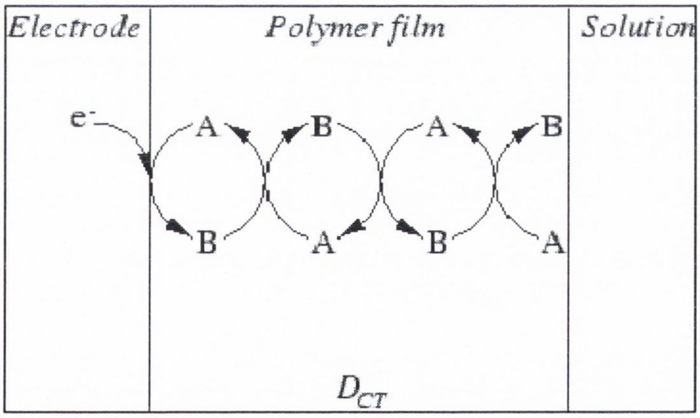

Figure 1.1; Charge transport between a polymer film and the underlying electrode, described as sequential self-exchange steps between adjacent redox groups.

The first step is charge injection at the polymer-electrode interface, which involves redox sites close (*ca.* 1 nm) to the surface. This is a potential-driven process and conforms to Butler-Volmer kinetics. The second process is the percolation of charge through the film, which is driven by concentration gradients and is quantifiable as a quasi-diffusional process (Equation 1.13). Electroneutrality in the film must be maintained and so the motion of the charge throughout the polymer is accompanied by the intake and motion of counterions. In cases where the redox sites within the film are mobile the ionic contribution may be disregarded, in which case the charge transport diffusion D_{CT} is just electron-hopping, D_{E}.

Lyons has published a detailed account of the concepts involved in charge percolation in redox polymers [158]. A few assumptions were made when deriving the model for the charge percolation process. The first assumption is that the redox sites A and B are evenly distributed throughout the film. The second assumption neglects local electric field effects between neighbouring sites. A and B are defined as an electron acceptor (oxidised sites) and electron donor (reduced species), respectively. The polymer layer may be represented by a series of slices, (1, 2, 3…, j-1, j.), each slice containing a redox site, between which the self-exchange of electrons occurs

$$\begin{array}{ccc} A_{j-1} & A_j & A_{j+1} \\ B_{j-1} & B_j & B_{j+1} \\ \leftarrow \delta \rightarrow & & \end{array} \tag{1.5}$$

where δ is the distance between neighbouring redox sites. The exchange reaction between slices j-1 and j can be described as

$$B_{j-1} + A_j \xrightarrow{k} A_{j-1} + B_j \tag{1.6}$$

where the electron exchange dynamics is quantified by k, the second-order bimolecular rate constant(cm^3 mol^{-1} s^{-1}). The net electron flux, j_Σ is given by

$$j_\Sigma = k\delta(b_{j-1}a_j - a_{j-1}b_j) \tag{1.7}$$

where a_j and b_j are the concentrations of the redox sites in slice j. Re-writing these quantities gives

$$b_j = b_{j-1} + \delta\frac{db_{j-1}}{dx} \text{ and } a_j = a_{j-1} + \delta\frac{da_{j-1}}{dx} \tag{1.8}$$

from which the flux expression may be obtained

$$j_{\Sigma} = k\delta^2 \left(b_{j-1} \frac{da_{j-1}}{dx} - a_{j-1} \frac{db_{j-1}}{dx} \right) \tag{1.9}$$

A general form of this equation may be written as it is valid for any slice in the polymer layer

$$j_{\Sigma} = k\delta^2 \left(b \frac{da}{dx} - a \frac{db}{dx} \right) \tag{1.10}$$

The sum of the oxidised and reduced sites in the polymer film describe the total redox site concentration, c_{Σ}, so equation 1.10 may be re-written as

$$j_{\Sigma} = k\delta^2 c_{\Sigma} \left(\frac{b}{c_{\Sigma}} \frac{da}{dx} - \frac{a}{c_{\Sigma}} \frac{db}{dx} \right) \tag{1.11}$$

This equation is now used to define the electron-hopping diffusion coefficient, D_E ($cm^2\ s^{-1}$)

$$D_E = k\delta^2 c_{\Sigma} \tag{1.12}$$

and substituting D_E into equation 1.11 we obtain

$$j_{\Sigma} = D_E \left(\frac{b}{c_{\Sigma}} \frac{da}{dx} - \frac{a}{c_{\Sigma}} \frac{db}{dx} \right) = D_E \left(\frac{a+b}{c_{\Sigma}} \frac{da}{dx} \right) = D_E \frac{da}{dx} = -D_E \frac{db}{dx} \tag{1.13}$$

where db/dx = -da/dx, and $a+b/c_{\Sigma} = 1$. This expression is the steady-state Fick diffusion equation and, thus, percolation of charge through the film is quantifiable as the aforementioned quasi-diffusional process.

We now must change equation 1.13 from steady-state to continuous, so the equation becomes

$$\frac{\partial a}{\partial t} = \frac{\partial j_\Sigma}{\partial x} = \frac{\partial}{\partial x}\left(D_E \frac{\partial a}{\partial x}\right) \tag{1.14}$$

which, on simplification, becomes Fick's time-dependent one-dimensional equation

$$\frac{\partial a}{\partial t} = D_E \frac{\partial^2 a}{\partial x^2} \tag{1.15}$$

Electron hopping may occur in one, two or three dimensions and so the geometrical factor θ must be included. θ has the values 1, 1/4, 1/6 for one, two and three dimensional electron-hopping, respectively.

$$D_E = \theta k \delta^2 c_\Sigma \tag{1.16}$$

This is the simplified model for electron-hopping occurring at fixed redox sites in the polymer layer. More complicated models that consider mobile redox sites, as well as long range hopping, have been developed and are described in detail by Lyons [158].

The modeling of the counterion motion through the polymer film can be described by the Nernst-Planck equation. The continuous form is utilised and yields

$$\frac{\partial c_{x-}}{\partial t} = -D_I \frac{\partial}{\partial x}\left(\frac{\partial c_{x-}}{\partial x} + \frac{zF}{RT} c_{x-} + \frac{\partial \Phi}{\partial x}\right) \tag{1.17}$$

and the counter ion flux is given by

$$j_x = -D_I\left(\frac{\partial c_{x-}}{\partial x} + \frac{zF}{RT} c_{x-} + \frac{\partial \Phi}{\partial x}\right) \tag{1.18}$$

where D_I is the counterion diffusion coefficient and z is the valence of the ion. Both the ion flux and electron-hopping flux are coupled due to the electroneutrality requirement. This mixed-conduction description of charge percolation through the polymer layer can be represented in terms of a simple equivalent circuit known as the transmission line. Again more complex models have been proposed and include other influencing phenomena such as ion-pairing in the film.

For the purpose of calculating charge transfer parameters in this body of work, the model derived by Aoki *et al.* [159,160] was used. Aoki proposed a theoretical approach in estimating charge transfer coefficients using cyclic voltammetry. EQCM investigations were also performed to monitor the counterion movement through the film throughout the polymer redox process, and during the electropolymerised film formation. The results and conclusions are presented in Chapter 3.

1.5 Magnetoelectrochemistry

The area of magnetoelectrochemistry is a relatively new field and has really only sparked research interest since Fahidy [161] submitted a review paper on the subject in 1983. Since then there has been a lot of research efforts in the quest to understand the effect of a magnetic field on electrochemical processes, an area of research now known as magnetoelectrochemistry. There have been a few notable review papers since 1983 [162-164] and these give concise, if not complete, explanations of the main areas of this exciting subject. Tacken *et al.* [162] classified the main areas of magnetoelectrochemistry into four parts, mass transport, reaction kinetics, cathodic metal deposition, and anodic metal dissolution. In the course of this body of work, magnetic field effects on mass transport and reaction kinetics were examined.

1.5.1 Mass Transport

The effect that a magnetic field has on the mass transport of an analyte to an electrode surface is known as the magneto-hydrodynamic (MHD) effect and is the most widely studied of magnetic field phenomena in electrochemistry. It is well known that the effect of the magnetic field is to cause convection in the electrolyte. Hinds *et al*. [164] found that the limiting current density, at a copper electrode in 0.75 M $CuSO_4$, increased in a field of 6 Tesla(T) to four times the value without the field.

This is due to the fact that the concentration of the analyte at the electrode surface was greater in the applied field, resulting from field induced convection of the electrolyte. The authors found the effect comparable to that of a rotating disk electrode at 100 rpm.

This convection arises from the interaction of velocity fields with electromagnetic fields. The unit volume element of the electrolytic conductor carrying a current density, i, is under the influence of the Lorentz force:

$$F_L = ixB \tag{1.19}$$

The region vacated by the moving ions is replaced by fresh electrolyte, which in turn experiences the Lorentz force, etc., and convection is observed on a macroscopic scale.

On a microscopic scale, Lorentz force can be described as the total force on a charged particle:

$$F_{\mathrm{L}} = \mathrm{q}[\mathrm{E} + \mathrm{v} \times \mathrm{B}] \tag{1.20}$$

where q is the charge of the moving particle, v is its velocity, E is the sum of the electric and electrostatic fields, and B is the magnetic induction. The summation (n_+ and n_-) of all the charged particles (both anions and cations) gives the expression for the total magnetic force:

$$F_{\mathrm{B}} = (\mathrm{n}_+\mathrm{q}_+\mathrm{v}_+ + \mathrm{n}_-\mathrm{q}_-\mathrm{v}_-) \times \mathrm{B} \tag{1.21}$$

where ($n_+q_+v_+ + n_-q_-v_-$) = the current density, i, which is parallel to the velocity of the ions. Substituting current density into equation 1.21:

$$F_{\mathrm{B}} = \mathrm{i} \times \mathrm{B} \tag{1.22}$$

Leventis *et al.* [165] have attempted to model field induced convection using Newton's second law (in the continuum) per unit volume, namely density x accelaration = sum of all forces per unit volume

$$\partial \mathbf{v}/\partial t + (\mathbf{v}\cdot\nabla)\mathbf{v} = -\frac{\nabla P}{\rho} + \nu\nabla^2\mathbf{v} \quad + F_{mag} \tag{1.23}$$

This is the Navier-Stokes equation for Newtonian fluids of constant density, ρ, and viscosity, where ν (= η/ρ) is the kinematic and η the absolute viscosity of the electrolyte [166]. Theoretical determination of the field dependence of the limiting current begins with the Navier-Stokes equation. The right hand side of the equation is the sum of the external forces on the element, with terms due to the pressure gradient, $\nabla\mathbf{P}$, and the magnetic force, $F_{mag.}$

The left hand side is the acceleration of the fluid element and solution of the equation yields the velocity profile $\mathbf{v}(\mathbf{r})$ in the fluid. This can be substituted into the convective-diffusion equation (equation 1.24) to obtain the concentration gradient, $\nabla\mathbf{c}$, near the electrode surface and hence the limiting current:

$$\partial c/\partial t = -\,\mathbf{v}\cdot\nabla\mathbf{c} + D\nabla^2 c \tag{1.24}$$

the gradient force

$$F_{\mathrm{mag}} = -\,\nabla E_{mag} \tag{1.25}$$

is the magnetic force exerted whenever there is a gradient in the magnetic energy,

$$E_{\mathrm{mag}} = -\,(1/2)\mathrm{MB} \tag{1.26}$$

where

$$\mathrm{M} = \chi_{\mathrm{m}} C_0 B / \mu_0 \tag{1.27}$$

is the local magnetization of the electrolyte induced by the field, χ_m, is the molar susceptibility, C_0 is the bulk concentration of magnetic species in solution and μ_0 is the permeability of free space. The gradient force is made up of two terms:

$$F_{mag} = \frac{\chi_m B^2 \nabla c}{2\mu_0} + \frac{\chi_m c_0 B \nabla B}{\mu_0} \qquad (1.28)$$

The first term is the paramagnetic gradient force, $\mathbf{F}_\mathrm{P}$, and describes how the paramagnetic susceptibility of the diffusion layer varies due to the concentration gradient of cations there. This force is usually negligible as the larger (10^6 times at room temperature) diffusional driving force acts in the same direction [164]. The second term is the field gradient force and is due to the field gradient, $\nabla\mathbf{B}$, in the solution when the field is non-uniform.

1.6 References

[1] R. W. Murray, in *'Electroanalytical Chemistry'*, ed. A.J. Bard, Dekker, New York, Vol. 13, 1984.

[2] W. J. Albery, A. R. Hilman, *Ann. Rep. Prog. Chem. Sect. C*, **78**, 377, 1981.

[3] K. D. Snell, A. G. Keenan, *Chem. Soc. Rev.*, **8**, 259, 1979.

[4] P. R. Moses, L. M. Weir, R. W. Murray, *Anal. Chem.*, **47**, 1982, 1975.

[5] R. F. Lane, A. T. Hubbard, *J. Phys. Chem.*, **77**, 1401, 1973.

[6] R. F. Lane, A. T. Hubbard, *J. Phys. Chem.*, **77**, 1411, 1973.

[7] B. F. Watkins, J. R. Behling, E. Kariv, L. L. Miller, *J. Am. Chem. Soc.*, **97**, 3549, 1975.

[8] P. R. Moses, R. W. Murray, *J. Am. Chem. Soc.*, **98**, 7435, 1976.

[9] J. R. Lenhard, R. W. Murray, *J. Electroanal. Chem.*, **78**, 195, 1977.

[10] M. A. Fox, F. J. Nobs, T. A. Voynick, *J. Am. Chem. Soc.*, **102**, 4029, 1980.

[11] S. Mazur, T. Matusinovic, K. Cammann, *J. Am. Chem. Soc.*, **99**, 3888, 1977.

[12] R. Nowak, F. A. Schultz, M. Umana, H. Abruna, R. W. Murray, *J. Electroanal. Chem.*, **94**, 219, 1978.

[13] L. Gorton, A. Torstensson, H. Jaegfeld, G. Johansson, *J. Electroanal. Chem.*, **161**, 103, 1984.

[14] L. Gorton, G. Johansson, A. Torstensson, *J. Electroanal. Chem.*, **196**, 81, 1985.

[15] L. Gorton, *J. Chem. Soc. Faraday Trans. I*, **82**, 1245, 1986.

[16] A. Torstensson, L. Gorton, *J. Electroanal. Chem.*, **130**, 199, 1981.

[17] C. W. Lee, A. J. Bard, *J. Electroanal. Chem.*, **239**, 441, 1988.

[18] H. O. Finklea, S. Avery, M. Lynch, T. G. Furtsch, *Langmuir*, **3**, 409, 1987.

[19] A. R. Hillman, in *"Electrochemical Science and Technology of Polymers"*, ed. R. Linford, Elsevier, London, Vol. 1, 1987.

[20] A. J. Bard, L. R. Faulkner, *"Electrochemical Methods-Fundamentals and Applications"*, 2nd ed., J. Wiley & Sons, NJ, 2001.

[21] N. Oyama, F. C. Anson, *J. Electrochem. Soc.*, **127**, 247, 1980.

[22] N. Oyama, S. Yamaguchi, Y. Nishiki, K. Tokuda, H. Matsuda, F. C. Anson, *J. Electroanal. Chem.*, **139**, 371, 1982.

[23] H. Braun, W. Storck, K. Doblhofer, *J. Electrochem. Soc.*, **130**, 807, 1983.

[24] I. Rubenstein, A. J. Bard, *J. Am. Chem. Soc.*, **102**, 6641, 1980.

[25] I. Rubenstein, A. J. Bard, *J. Am. Chem. Soc.*, **103**, 5007, 1981.

[26] C. R. Martin, H. Fraiser, *Anal. Chem.*, **53**, 902, 1981.

[27] M. W. Espenscheid, A. R. Ghatak-Roy, R. B. Moore III, R. M. Penner, M. N. Szentirmay, C. R. Martin, *J. Chem. Soc. Faraday Trans. I*, **82**, 1051, 1986.

[28] D. A. Buttry, K. A. Dollard, *J. Am. Chem. Soc.*, **105**, 685, 1983.

[29] M. N. Szentirmay, C. R. Martin, *Anal. Chem.*, **56**, 1898, 1984.

[30] S. A. John, R. Ramaraj, *J. Chem. Soc. Faraday Trans. I*, **90**(9), 1241, 1994.

[31] X. Chen, F. Wang, Y. Xu, S. Hu, *Chin. Chem. Letters*, **17**(4), 496, 2006.

[32] Q. Zhu, R. Yuan, Y. Chai, Y. Zhuo, Y. Zhang, X. Li, N. Wang, *Analytical Letters*, **39**(3), 483, 2006.

[33] X. Chen, P. Xie, Q. Tian, X. Li, S. Hu, *Analytical Letters*, **39**(7), 1321, 2006.

[34] F. Benier, S. Haridoss, J. P. Louboutin, A. Aldissi, J. M. Fabre, *J. Phys. Chem. Solids*, **42**, 649, 1981.

[35] J. P. Louboutin, F. Benier, *J. Phys. Chem. Solids*, **43**, 233, 1982.

[36] F. Benier, J. Corish, M. E. G. Lyons, T. McCabe, A. Morin, *J. Electrochem. Soc.*, **137**, 2181, 1990.

[37] A. Dall'Olio, Y. Dascola, V. Varacca, V. Bocchi, *Comples Rendus. C*, **267**, 433, 1968.

[38] A. Diaz, K. K. Kanazawa, G. P. Gardini, *J. Chem. Soc. Chem. Commun.*, 635, 1979.

[39] H. Skirakawa, A. G. MacDiarmaid, C. K. Heeger, E. J. Louis, C. K. Chang,

J. Chem. Soc. Chem. Commun., 578, 1977.

[40] H. Skirakawa,. Phys. Rev. Lett., **39**, 1098, 1977.

[41] T. A. Skotheim, *"Handbook on Conductive Polymers"*, Marcel Dekker, NY, Vols I and II, 1986.

[42] L. L. Miller, M. R. Van de Mark, *J. Am. Chem. Soc.*, **100**, 639, 1978.

[43] M. R. Van de Mark, L.L. Miller, *J. Am. Chem. Soc.*, **100**, 3223, 1978.

[44] L. L. Miller, M. R. Van de Mark, *J. Electroanal. Chem.*, **88**, 437, 1978.

[45] P. Daum, R. W. Murray, *J. Phys. Chem.*, **85**, 389, 1981.

[46] M. F. Dautartas, J. F. Evans, *J. Electroanal. Chem.*, **109**, 301, 1980.

[47] N. Oyama, A. P. Brown, F. C. Anson, *J. Electroanal. Chem.*, **87**, 435, 1978.

[48] R. Wedge, R. M. Pemberton, J. P. Hart, R. Luxton, *Biosensors,* **27**(7), 570, 1999.

[49] Q. Gao, F. Yang, Y. Ma, X. Yang, *Electroanalysis*, **16**(9), 730, 2004.

[50] R. J. Walton, J. Bargon, A. F. Diaz, *J. Phys. Chem.*, **87**, 2289, 1983.

[51] C.-X. Cai, K.-H. Xue, *J. Electroanal. Chem.*, **427**, 147, 1997.

[52] A. A. Karyakin, E. E. Karyakina, W. Schuhmann, H.-L. Schmidt, *Electroanalysis*, **11**(8), 553, 1999.

[53] M. C. Pham, J. E. Dubois, P. C. Lacaze, *J. Electroanal. Chem.*, **99**, 331, 1979.

[54] A. F. Diaz, J. J. Castillo, J. A. Logan, W. Y. Lee, *J. Electroanal. Chem.*, **129**, 115, 1981.

[55] E. M. Genis, G. Bidan, A. F. Diaz, *J. Phys. Chem.*, **87**, 1459, 1983.

[56] A. Volkov, G. Tourillon, P. C. Lacaze, J. E. Dubois, *J. Electroanal. Chem.*, **115**, 279, 1980.

[57] P. Denisevich, H. D. Abruna, C. R. Leidner, T. J. Meyer, R. W. Murray, *Inorg. Chem.*, **21**, 2153, 1982.

[58] R. R. Shaw, G. P. Haight, L. R. Faulkner, *J. Electroanal. Chem.*, **140**, 147, 1982.

[59] H. D. Abruna, P. Denisevich, M. Umana, T. J. Meyer, R. W. Murray, *J. Am. Chem. Soc.*, **102**, 2151, 1981.

[60] D.-M. Zhou, H.-Y. Chen, *Electroanalysis.*, **9**(5), 399, 1997.

[61] W. Kutner, J. Wang, M. L'Her, R. P. Buck, *Pure & Appl. Chem.*, **70**(6), 1301, 1998.

[62] C. J. Stadler, S. Chao, M. S. Wrighton, *J. Am. Chem. Soc.*, **106**, 3673, 1984.

[63] R. Greef, R. Peat, L. M. Peter, D. Pletcher, J. Robinson, *"Instrumental*

Methods in Electrochemistry", Southampton Electrochemistry Group, Ellis Horwood Ltd., 1985.

[64] D. C. Williams III, W. R. Seitz, *Anal. Chem.*, **48**(11), 1478, 1976.

[65] F. Barriere, Y. Ferry, D. Rochefort, D. Leech, *Electrochem. Comm.*, **6**, 237, 2004.

[66] S. Yabuki, H. Shinohara, Y. Ikariyama, M. Aizawa, *J. Electroanal. Chem.*, **277**, 179, 1990.

[67] G. Jonsson, L. Gorton, *Biosensors*, **1**, 335, 1985.

[68] T. Yao, Y. Matsumoto, T. Wasu, *Anal. Chim. Acta*, **218**, 129, 1989.

[69] K. Yokoyama, E. Tamiya, I. Karube, *J. Electroanal. Chem.*, **273**, 107, 1989.

[70] J. B. Persson, *J. Electroanal. Chem.*, **287**, 61, 1990.

[71] C.-X. Cai, K.-H. Xue, *J. Electroanal. Chem.*, **427**, 147, 1997.

[72] A. A. Karyakin, O. A. Bobrova, E. E. Karyakina, *J. Electroanal. Chem.*, **399**, 179, 1995.

[73] G. Zeitseva, Y. Gushikem, E. S. Ribeiro, S. S. Rosatto, *Electrochim. Acta*, **47**, 1469, 2002.

[74] E. S. Ribeiro, S. S. Rosatto, Y. Gushikem, L. T. Kubota, *J. Solid State Electrochem.*, **7**, 665, 2003.

[75] C. M. Moore, S. D. Minteer, R. S. Martin, *Lab. Chip*, **5**, 218, 2005.

[76] J. Ye, R. P. Baldwin, *Anal. Chem.*, **60**, 2263, 1988.

[77] S. Pons, M. Fleischman, *Anal. Chem.*, **59**, 1319A, 1987.

[78] M. E. Rice, C. Nicholson, *Anal. Chem.*, **61**, 1805, 1989.

[79] J. Wang, L. D. Hutchins, *Anal. Chem.*, **57**, 1536, 1985.

[80] S. V. Sasso, R. J. Pierce, R. Walla, A. M. Yacynych, *Anal. Chem.*, **62**, 1111, 1990.

[81] *"Analytical Applications of Chemically Modified Electrodes"*, Analyst, **117**, 1992.

[82] *"Sensors and Signals"*, Analyst, **118**, 1993.

[83] C. M. A. Brett, A. M. O. Brett, *"Electrochemistry - Principles, Methods and Applications"*, Oxford Science Publications, pp 294, 1993.

[84] J. A. V. Butler, *Trans. Faraday Soc.*, **19**, 729, 734, 1924.

[85] T. Erdey-Gruz, M. Volmer, *Z. Physik. Chem.*, **150A**, 203, 1930.

[86] L. Clark Jr., C. Lyons, *Ann. NY Acad. Sci.*, **102**, 29, 1962.

[87] S. Updike, G. Hicks; *Nature*, **214**, 986, 1967.

[88] Y. Degani, A. Heller.; *J. Am. Chem. Soc.*, **111,** 2357,1989.

[89] Y. Degani, A. Heller; *J. Phys. Chem.*, **91**,1285, 1987.

[90] G. Guilbault, G. Lubrano; *Anal. Chim. Acta*, **64**, 439, 1973.

[91] R. J. Forster, J. G. Vos; *Macromolecules*, **23**, 4372, 1990.

[92] Y. Degani, A. Heller; *J. Am. Chem. Soc.*, **111,** 2357, 1989.

[93] B. A. Gregg, A. Heller; *Anal. Chem.*, **62**, 258, 1990.

[94] A. Heller, A.; *Acc. Chem. Res.,* **23,** 128**,** 1990.

[95] A. Heller; *J. Phys. Chem.,* **96,** 3579, 1992.

[96] T. J. Ohara, R. Rajagopalan, A. Heller; *Anal. Chem.,* **66,** 2451, 1994.

[97] F. Mao, N. Mano, A. Heller; *J. Am. Chem. Soc.*, **125,** 4951, 2003

[98] S. Gaspar, I. C. Popescu, I. G. Gazaryan, A. G. Bautista, I. Y. Sakharov, B. Mattiasson, E. Csoregi; *Electrochim. Acta*, **46**, 255, 2000.,

[99] M. Vreeke, R. Maidan, A. Heller; *Anal. Chem.*, **64**, 3084, 1992.,

[100] T. J. Ohara, R. Rajagopalan, A. Heller; *Anal. Chem.,* **65**, 3512, 1993.

[101] S. Timur, Y. Yigzaw, L. Gorton, L.; *Sens. Actuators B,* **113,** 684, 2006.

[102] O. Nikitina, S. Shleev, G. Gayda, O. Demkiv, M. Gonchar, L. Gorton, E. Csoregi, M. Nistor; *Sens. Actuators B,* **125**, 1, 2007.

[103] O. Smutok, B. Ngounou, H. Pavlishko, G. Gayda, M. Gonchar, W. Schuhmann; *Sens. Actuators B*, **113**, 590, 2006.

[104] E. Csoregi, D.W. Schmidtke, A. Heller; *Anal. Chem.,* **67**, 1240, 1995.

[105] D. W. Schmidtke, A. Freeland, A. Heller, R. Bonnecaze; *Proc. Nat. Acad. Sci., USA*, **95**, 294, 1998.

[106] T. Chen, S. C. Barton, H.-H. Kim, G. Binyamin, Y. Zhang, Z. Gao, A. Heller; *J. Am. Chem. Soc.*, **123**, 8630, 2001.

[107] S. C. Barton, H.-H. Kim, G. Binyamin, Y. Zhang, A. Heller; *J. Am. Chem. Soc.*, **123**, 5802, 2001.

[108] A. Heller; *Phys. Chem. Chem. Phys.*, **6**, 209, 2004.

[109] S. Gaspar, K. Habermuller, E. Csoregi, W. Schuhmann; *Sens. Actuators B*, **72**, 63, 2001.

[110] M. M. Malone, A. P. Doherty, M. R. Smyth, J. G. Vos; *Analyst,* **117**, 1259, 1992.

[111] G. Goa; *Sens. Actuators B*, **123**, 293, 2003.

[112] D. T. Sawyer, J. L. Roberts jr., *"Experimental Electrochemistry for*

Chemists", Marcel Dekker, NY, pp 308, 1974.

[113] D. Benito, J. J. Garcia-Jareno, J. Navarro-Laboulais, F. Vicente, *J. Electroanal. Chem.*, **446**, 47, 1998.

[114] S. Han, M. Zhu, Z. Yuan, X. Li, *Biosens. & Bioelectron.*, **16**, 9, 2001.

[115] C. Ruan, F. Yang, C. Lei, J. Deng, *Anal. Chem.*, **70**, 1721, 1998.

[116] J.-Z. Xu, J.-J. Zhu, Q. Wu, Z. Hu, H.-Y. Chen, *Electroanalysis*, **15**(3), 219, 2003.

[117] G. Nagy, G. A. Gerhardt, A. F. Oke, M. E. Rice, R. N. Adams, R. B. Moore III, M. N. Szentirmay, C. R. Martin, *J. Electroanal. Chem.*, **188**, 85, 1985.

[118] Z. Lu, S. Dong, *J. Chem. Soc. Faraday Trans. I*, **84**(9), 2979, 1988.

[119] H.-Y. Chen, H.-X. Ju, Y.-G. Xun, *Anal. Chem.*, **66**, 4538, 1994.

[120] C. Ruan, F. Yang, J. Xu, C. Lei, J. Deng, *Electroanalysis*, **9**(15), 1180, 1997.

[121] H. Yao, N. Li, Y.-L. Wei, J.-J. Zhu, *Sensors*, **5**, 278, 2005.

[122] S. Cosnier, K. L. Lous, *J. Electroanal. Chem.*, **406**, 243, 1996.

[123] S. B. Khoo, F. Chen, *Anal. Chem.*, **74**, 5734, 2002.

[124] L. Tan, Q. Xie, S. Yao, *Electroanalysis*, **16**(19), 1592, 2004.

[125] H. Durr, H. Bouas-Laurent, *"Photochromism, Molecules and Systems"*, Elsevier: Amsterdam, Holland, 1990.

[126] P. M. S. Monk, R. J. Mortimer, D. R. Rosseinsky, *"Electrochromism: Fundamentals and Applications"*, Wiley-VCH: Weinheim, Germany, 1995.

[127] A. Mills, J. Wang, *J. Photochem. Photobiol. A*, **127**, 123, 1999.

[128] M. L. Hitchman, *"Measurement of Dissolved Oxygen"*, Wiley, York, **pp.**225, 1978.

[129] V. Ganesan, S. A. John, J. R. Ramaraj, *J. Electroanal. Chem.*, **502**, 167, 2001.

[130] S. Kuwabata, K. Mitsui and H. Yoneyama, *J. Electroanal. Chem.*, **281**, 97, 1990.

[131] R. M. Ion, F. Scarlat, Fl. Scarlet, V. I. R. Niculescu, *J. Optoelect. Adv. Mater.*, **5**, 109, 2003.

[132] R. O. Lezna, S. Juanto, J. H. Zagal, *J. Electroanal. Chem.*, **389**, 197, 1995.

[133] G. De Filipo, F. P. Nicoletta, G. Chidichimo, *Chem. Mater.*, **18**, 4662, 2006.

[134] M. Macchione, G. De Filipo, A. Mashin, F. P. Nicoletta, G. Chidichimo, *Adv. Mater.*, **15**, 327, 2003.

[135] S.-K. Lee, A. Mills, A. Lepre, *Chem. Comm.*, 1912, 2004.

[136] S.-K. Lee, A. Sheridan, A. Mills, *Chem. Mater.*, **17**, 2744, 2005

[137] D. Gutierrez-Tauste, X. Domenech, N. Casan-Pastor, J. A. Ayllon, *J. Photochem. Photobiol. A*, 2006, *In Press.*

[138] P. R. Somani, A. K. Viswanath, R. C. Aiyer, S. Radhakrishnan, *Sensors and Actuators B*, **80**, 141, 2001.

[139] D. F. Watson, G. J. Meyer, *Annu. Rev. Phys. Chem.*, **56**, 119, 2005.

[140] M. T. Spitler, M. Calvin, *J. Chem. Phys.*, **66**, 4294, 1977.

[141] M. T. Spitler, M. Calvin, *J. Chem. Phys.*, **67**, 5193, 1977.

[142] L. P. Sonntag, M. T. Spitler, *J. Phys. Chem.*, **89**, 1453, 1985.

[143] W. J. Albery, W. R. Bowen, F. S. Fisher, A. W. Foulds, K. J. Hall, A. R. Hillman, R. G. Egdell, A. F. Orchard, *J. Electroanal. Chem.*, **107**, 37, 1980.

[144] M. D. Archer, M. I. C. Ferreira, *J. Electroanal. Chem.*, **111**, 295, 1980.

[145] W. J. Albery, A. W. Foulds, K. J. Hall, A. R. Hillman, *J. Electrochem. Soc.*, **127**, 654, 1980.

[146] K. R. Genwa, A. Chouhan, *J. Chem. Sci.*, **116**, 339, 2004.

[147] K. M. Gangotri, R. C. Meena, *J. Photochem. Photobiol. A*, **141**, 175, 2001.

[148] K. M. Gangotri, C. Lal, *Energy Sources*, **23**, 267, 2001.

[149] K. M. Gangotri, C. Lal, *Int. J. Energy Res.*, **24**, 365, 2000.

[150] K. M. Gangotri, C. Lal, *Proc. I MECH E Part A J. Power & Energy*, **219**, 315, 2005.

[151] P. R. Somani. S. Radhakrishnan, Chem. Phys. Lett., **379**, 401, 2003.

[152] M. E. G. Lyons, H. J. Fay, C. Mitchel, D. E. McCormack, *Electrochem., Sens. and Anal.*, Proc. Int. Conf. on Electroanalysis, Dublin, June 10-12, Amsterdam, 285, 1986.

[153] J. Liu, S. Mu, *Synthetic Metals*, **107,** 159, 1999.

[154] A. A. Karyakin, A. K. Strakhova, E. E. Karyakina, S. D. Varfolomeyev, A. K. Yatsimirsky, *Bioelectrochem. & Bioenerg.*, **32,** 35, 1993.

[155] A. A. Karyakin, E. E. Karyakina, H.-L. Schmidt, *Electroanalysis*, **11**, 149, 1999.

[156] V. Kertesz, G. V. Van Berkel, *Electroanalysis*, **13**(17), 1425, 2001.

[157] P. G. Pickup, R. W. Murray, *J. Am. Chem. Soc.*,105, 4510, 1983.

[158] M. E. G. Lyons, *"Transport and Kinetics in Electroactive Polymers; Part 1"*, Wiley, 1994.

[159] K. Aoki, K. Tokuda, H. Matsuda, *J. Electroanal. Chem.*, **146**, 417, 1983.

[160] K. Aoki, K. Tokuda, H. Matsuda, *J. Electroanal. Chem.*, **160**, 33, 1984.

[161] T. Z. Fahidy, *J. Appl. Electrochem.*, **25**, 553, 1983

[162] R. A. Tacken, L. J. J. Janssen, *Applications of magnetoelectrolysis. J. Appl. Electrochem.*, **25,** 1, 1995.

[163] R. Aogaki, *Magnetic fields effects in electrochemistry. Proc. 4th Annual Pamir Conference 4.*, 321, 2000.

[164] G. Hinds, J. M. D. Coey, M. E. G. Lyons, *Electrochem. Comm.*, **3,** 215, 2001.

[165] N. Leventis, M. Chen, X. Gao, M. Canalas, P. Zhang, *J. Phys. Chem.*, **102**, 3512,1998.

[166] J. S. Newman, "*Electrochemical Systems*", 2nd ed.; Prentice Hall: Englewood Cliffs, NJ, 1991.

CHAPTER 2

EXPERIMENTAL THEORY AND METHODOLOGY

2.1 Introduction

The instrumentation and experimental techniques employed during the course of this work will shall be described in this chapter. An initial discussion of the mathematical basis of electrochemistry shall be followed by a description of the instrumentation, electrochemical cell and its components, used in this thesis. Finally the experimental applications as well as the relevant theoretical foundations of the principal techniques used in his study, Cyclic Voltammetry, Rotating Disc Voltammetry and Differential Pulse Voltammetry [1-3].

A typical electrochemical reaction consists of several steps; diffusion of reactant species to the electrode surface, rearrangement of the ionic atmosphere, adsorption onto the electrode, electron transfer and diffusion of the product species from the electrode. The dependence of the current on the applied potential is simplified if one of these steps is rate determining. In a sequential electrochemical process in which the transfer of n electrons occur, the steady-state current density, *j*, is given by:

$$j = \frac{nFk_c k_D[O]}{k_c + k_D} - \frac{nFk_a k_D[R]}{k_a + k_D} \tag{2.1}$$

where F is the Faraday constant (96,480 C/mol), k_c (m/s) is the rate constant for the cathodic (reduction) reaction, k_a (m/s) is the rate constant for the anodic (oxidation) reaction, k_D is the diffusional rate constant and [O] and [R] are the surface concentrations (mol/dm^3) of oxidised and reduced species. The first term on the right hand side of equation 2.1 is the cathodic (reduction) current while the second term is the anodic (oxidation) current. The current ratio will be close to unity when the reaction is close to equilibrium.

The magnitude of applied potential, E, will determine whether the reaction is under activation (electrode kinetics) or mass transport (diffusional) control. At equilibrium the potential at which the net current is zero is called the equilibrium potential, E_{eq}. The difference between the applied potential and equilibrium potential is called the overpotential, η;

$$\eta = \mathrm{E} - \mathrm{E}_{eq} \tag{2.2}$$

In Section 2.1.1, the heterogeneous electrode kinetics are explained while mass transport is dealt with in Section 2.1.2

2.1.1 Heterogeneous Electron Transfer kinetics

The electrical double layer is the interfacial region between the electrode and the electrolyte. This region of charge separation behaves like a capacitor in that when a potential difference is applied across it, a charging current flows at short times. It is in this region that the electron transfer process occurs. The first models for this region were proposed by Helmholtz (1879), Gouy-Chapman (1910-1913), Stern (1924), and Grahame (1947). The most sophisticated models propose a rigid ordering of adsorbed ions at the electrode surface followed by a diffuse layer of ions extending into the bulk solution.

The electron transfer kinetics in this double layer are highly sensitive to the overpotential. At high overpotentials electrode kinetics are rapid but at low overpotentials mass transport is rate determining ($k_c, k_a << k_D$) and equation 2.1 reduces to:

$$j = \mathrm{nFk_c[O]} - \mathrm{nFk_a[R]} \tag{2.3}$$

Diffusion of the reactants to the electrode surface is rapid relative to the rate of electron transfer and so the reaction kinetics is under activation control.

Activated complex theory can be used to determine the dependence of the rate constants k_c and k_a on the overpotential:

$$\mathrm{k_c} = \mathrm{k_0}\exp\left\{-\alpha_C nF\frac{\left(E - E^{0'}\right)}{RT}\right\} \tag{2.4}$$

$$\mathrm{k_a} = \mathrm{k_0} \exp\left\{\alpha_a nF \frac{\left(E - E^{0'}\right)}{RT}\right\} \tag{2.5}$$

where k_0 (m/s) is the standard electrochemical rate constant for the reaction, $E^{0'}$ (V) is the formal standard potential, R is the gas constant (8.314 JK^{-1} mol^{-1}) and α_c and α_a are the cathodic and anodic charge transfer coefficients. At equilibrium $k_0 = \alpha_c = \alpha_a$.

Substituting equations 2.4 and 2.5 into equation 2.1 we get the following equation:

$$\mathrm{j} = \mathrm{nFk_0}\left\{[\mathrm{O}]\exp\left(-\alpha_C nF \frac{\left(E - E^{0'}\right)}{RT}\right) - [R]\exp\left(\alpha_a nF \frac{\left(E - E^{0'}\right)}{RT}\right)\right\} \tag{2.6}$$

k_0 should not be mistaken for the actual rate of electron transfer which is an adiabatic process according to the Franck-Condon principle, with a timescale of the order of 10^{-16} s. It is however, a measure of the time taken for rearrangement of the reactant species and their ionic atmospheres so that electron transfer can occur. Thus the ease of which electron transfer takes place can be quantified. Large values of k_0 indicate facile electron transfer-a typical value for a simple electron transfer being that for the reduction of aromatic hydrocarbons ($k_0 \sim 0.1$ m/s). Equation 2.6 describes the current-potential characteristic of a given electrochemical reaction and can be used to determine kinetic parameters from data using a wide range of experimental techniques.

At equilibrium, the anodic and cathodic currents are equal and equation 2.6 can be rearranged to yield:

$$\exp\left\{nF \frac{\left(E_{eq} - E^{0'}\right)}{RT}\right\} = \frac{[O]}{[R]} \tag{2.7}$$

And since [O] and [R] are equal to the bulk concentrations $[O]_\infty$ and $[R]_\infty$ Equation 2.6 becomes the Nernst equation:

$$E_{eq} = E^{0'} + \frac{RT}{nF} \ln \frac{[O]}{[R]} \tag{2.8}$$

The Nernst equation describes how the equilibrium potential varies with the concentration of the oxidised and reduced species in solution. Combining equations 2.1, 2.6 and 2.7 gives the current density-overpotential equation:

$$j = j_0 \left\{ \frac{[O]}{[O]_\infty} \exp\left(\frac{-\alpha_C nF\eta}{RT} \right) - \frac{[R]}{[R]_\infty} \exp\left(\frac{\alpha_a nF\eta}{RT} \right) \right\} \tag{2.9}$$

The exchange current density, j_0, is the magnitude of either the cathodic or anodic current density at equilibrium. The first term on the right hand side is the cathodic current density as a function of η and the second term is the dependence of the anodic current density on η. If the surface concentrations do not drop below the bulk values (if the solution is well stirred), we obtain the Butler-Volmer equation:

$$j = j_0 \left\{ \exp\left(\frac{-\alpha_C nF\eta}{RT} \right) - \exp\left(\frac{\alpha_a nF\eta}{RT} \right) \right\} \tag{2.10}$$

The Butler-Volmer equation is very useful as the overpotential can be measured, thus the current density can be obtained. As previously stated, the cathodic and anodic currents are close to unity at equilibrium, but the reaction can be driven in either direction depending on the polarity of the applied overpotential. Applying a large positive overpotential the cathodic current becomes negligible and we have:

$$j = j_0 \exp\left(\frac{\alpha_a nF\eta}{RT} \right) \tag{2.11}$$

Taking logarithms of both sides we obtain the Tafel relation:

$$\log j = \log j_0 + \left(\frac{\alpha_a nF\eta}{2.3RT} \right) \tag{2.12}$$

Conversely when η is large and negative, the anodic current is negligible:

$$\log j = \log j_0 - \left(\frac{\alpha_C nF\eta}{2.3RT} \right) \tag{2.13}$$

A plot of log j versus η is known as a Tafel plot with slopes of the lines equal to $\alpha_a nF/2.3RT$ and $-\alpha_c nF/2.3RT$. The exchange current, I_0, can be obtained from the intercept $E = E_{eq}$ (since $I_0 = j_0A$), α_a and α_c can be determined from the slopes. Close to $E = E_{eq}$ there are deviations from straight lines since reactions occur in both directions. At values far from $E = E_{eq}$ the lines level off due to mass transport effects dealt with in Section 2.1.2. The same theory can be applied to homogeneous electron transfer kinetics except the reaction site is the point where two ions meet in the solution, not at the electrode surface.

2.1.2 Mass Transport processes

In electrochemical processes at the electrode surface, the reactant is transported to the electrode surface and then converted to the product. The reactant concentration at the electrode surface needs to be replenished from the bulk solution if the reaction is to continue taking place. If the rate of electron transfer is rapid then the rate limiting step is the mass transport of reactant to the electrode surface, i.e., the reaction is mass transport controlled. Mass transport occurs in three ways; diffusion, migration and convection.

Migration is defined as the movement of charged species in an electric field. This effect can be rendered negligible by addition of, to the bulk solution, an excess of inert dissolved salt known as the supporting electrolyte. The supporting electrolyte increases the conductivity of the solution and ensures that most of the current is carried by species that are not involved in the electron transfer process. The concentration of supporting electrolyte is typically ~ 0.1 M.

Diffusion is defined as thermal movement of particles down a concentration gradient, while convection is transport of the species through the motion of the fluid itself. Mass transport control can be divided into two main parts; systems under total diffusional control (quiescent systems) and those where convection is significant (hydrodynamic systems).

Fick's first law of diffusion describes the movement of ionic species in solution:

$$J = -D\nabla c - \frac{z[C]_\infty F}{RT}\nabla V \tag{2.14}$$

where J is the number flux of species, D is the diffusion coefficient of the species (m^2/s), ∇c is the concentration gradient, z is the charge on the ion and ∇V is the potential gradient. The first term on the right hand side of the equation is flux due to diffusion while the second term is that due to migration. With the addition of supporting electrolyte the migration term is negligible and we obtain the expression - Fick's second law of diffusion:

$$\frac{\partial c}{\partial t} = \mathrm{D}\nabla^2 \mathrm{c} \tag{2.15}$$

The solution of this equation, assuming the fact that a concentration gradient is being imposed at the electrode surface, gives the variation of diffusion-limited current (for the reduction process) with time:

$$I = -\,\mathrm{nFAD}\nabla\mathrm{c} \tag{2.16}$$

and

$$j = -\,\mathrm{nFD}\nabla\mathrm{c} \tag{2.17}$$

where j is the current density.

The concentration gradient tends asymptotically to zero at large distances from the electrode and the concentration gradient is not linear. It is convenient to define the diffusion layer as the region between the electrode surface and the bulk solution where the concentration gradient is linear. This is obtained by extrapolation of the concentration gradient at the electrode surface until the bulk concentration is attained. Nernst developed this relation:

$$D\nabla c = \frac{D([C]_\infty - [C]_0)}{\delta} \tag{2.18}$$

where δ is the diffusion layer thickness. Hence substituting into equation 2.17 we obtain for the current density:

$$j = -\frac{nFD([C]_\infty - [C]_0)}{\delta} \tag{2.19}$$

At sufficiently high overpotentials, the surface concentration of reactant species, $[C]_0$, will become so small that it is negligible and the current density now becomes the limiting current density, j_L, and can be expressed as:

$$j_L = -\frac{nFD[C]_\infty}{\delta} \tag{2.20}$$

This equation describes the situation where are all the reactant species reaching the electrode surface are immediately reduced. But equation 2.15 can be solved to show that the diffusion layer thickness increases with $t^{1/2}$, hence at large values of t, natural convection (due to species of different densities present) manifests itself and is a problem.

Hydrodynamic techniques are a solution to this problem. The diffusion layer thickness can be controlled due to forced convection keeping the bulk concentration at a fixed distance from the electrode surface. The diffusion layer thickness at a rotating disk electrode is given by [1]:

$$\delta = 1.61\mathrm{D}^{1/3}\nu^{1/6}\omega^{-1/2} \tag{2.21}$$

where ω is the angular frequency of rotation of the electrode (rad/s) and ν is the kinematic viscosity of the solution (m^2/s). If the rotation speed is constant, δ is fixed.

2.2 Instrumentation

2.2.1 CH Instruments Workstation

All experimental work was conducted using the CH Instruments electrochemical workstation. The three main components being the PC, potentiostat and electrochemical cell. All the experimental/control parameters are entered through the CH Instruments/Windows interface. This information is transferred to the CH instruments microprocessor where optimum hardware settings are calculated for the specified technique. These values are then loaded automatically and after the experiment is run the data is collected and transmitted to the PC where it is displayed in virtual real-time. The data may subsequently be processed using options such as peak height determination or transformations e.g. Cotrell or Anson transforms.

2.2.2 Potentiostat

The potentiostat is a device for monitoring and controlling cell potentials between the working and the reference electrodes. The basic building block in the construction of a potentiostat device is called an operational amplifier. This component comes in the form of an integrated circuit, often with different characteristics, depending on its destined application or requirement. A more comprehensive discussion of the device can be found in many electrochemical texts [1-3].

2.2.3 C2 Cell Stand

The C2 cell stand is used for completely isolating the electrochemical cell during experimentation. The cell is enclosed in a Faraday cage to shield the cell from external electrical interference, this being an important factor when working with microelectrodes were the measured currents are at submicroampere level. Another advantage of the cell stand is that the cell is completely isolated from light during experimentation therefore facilitating work with light sensitive chemicals. The cell also features manual and computer controlled gas purging and stirring of solutions.

2.2.4 Rotating Disc Electrode

The rotating disc electrode was used upon conducting hydrodynamic techniques. Purging of the solution and the acceleration/deceleration of the electrode were computer and manually controlled. The electrodes rotation speed varies from 0-10,000 rpm. in single increments, where the proprierty electrode contact system ensure that the electrodes are held securely so as to provide low-noise performance.

2.3 The Electrochemical Cell

The electrochemical cell (volume: Rotating Disc Electrode (R.D.E.) = $50cm^3$, C2 Cell Stand = $25cm^3$) consists primarily of a working vessel, electrodes and an electrolyte solution. A cell top sealed the vessel at all times with inlets for the electrodes and for the gas purger. Solutions were purged with nitrogen gas for 15 minutes before experimentation ensuring saturation and during experimentation a blanket of the inert gas was maintained above the solution. All work was conducted at 20°C ±1°C. A standard three electrode electrochemical cell was used at all times consisting of a working electrode, which defines the interface under study, a reference electrode, which maintains the reference potential and an auxiliary (counter) electrode which allows the passage of current. Figure 2.1 illustrates the experimental cell set up.

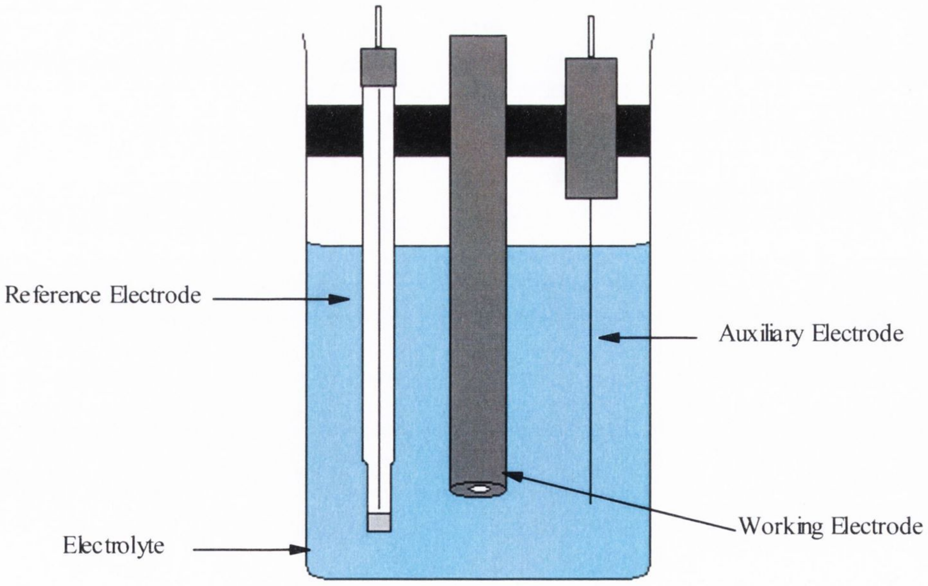

Figure 2.1; Three electrode electrochemical cell.

2.3.1 Working Electrode

The working electrode material is usually chosen to complement the requirements of a particular experiment. An essential feature is that the electrode should not react chemically with the solvent or solution components. Another consideration is that the electrode works correctly in the desired potential range. The working electrode range in terms of accessible potentials is limited by a number of processes such as electrolyte and solvent decomposition, hydrogen and oxygen evolution and oxide formation on the electrode surface [1,2]. To minimise the effects of these phenomena and to maximise electrode reliability, various different solid materials may be used in these electrodes. Materials such as platinum, carbon, mercury and gold have all been used. In order to ensure uniform current and potential distribution the area of the working electrode should be smaller than the auxiliary/counter electrode.

In this body of work several working electrodes were used. A glassy carbon macroelectrode was used when conducting experiments using both the C2 Cell Stand and the Rotating Disc Electrode. The glassy carbon rotating disc electrode and the stationary glassy carbon electrode had surface areas of 0.0707 cm^2 while the stationary platinum electrode area was 0.0314 cm^2. All electrodes were produced by embedding the disc of glassy carbon or platinum into a PTFE plastic rod. The electrodes before use were polished (section 2.4.1) to a mirror finish to ensure that a reproducible state of oxidation, surface morphology and freedom from adsorbed impurities was achieved.

2.3.2 Reference Electrode

The purpose of a reference electrode is to provide a fixed potential which is invariant with respect to time during the experiment. The potential of the reference electrode is in turn related to other scales, for example, to the normal hydrogen electrode (NHE). Hence any change in applied potential in the cell appears at the working electrode/solution interface. Ideally, if a small current passes through the reference electrode, the potential change should be negligible and should return to its initial value when the current ceases.

Although a little dated now, Janz and Ives [4] have comprehensively reviewed the theory and characteristics of a wide variety of reference electrode systems. The most commonly used reference electrode for aqueous systems are the saturated calomel (mercury/mercurous chloride) electrode and the silver/silver chloride electrode. In the case of the Ag/AgCl electrode, the electrolyte is usually saturated KCl or NaCl. The reference potential is dependent on the concentrations of the chloride concentration in the electrolyte as well as the standard redox potential of the electrochemical reaction. It should also be noted that any changes in the salt concentration within the reference electrode will effect its potential. Hence a porous Vycor barrier is normally placed between the internal solution of the electrode and the electrolyte. This allows contact between the two solutions but minimises effective mixing thereby keeping the salt concentration within the reference electrode virtually constant. The Ag/AgCl, 3M KCl electrode (sat.) was used in this body of work.

2.3.3 Auxiliary Electrode

The purpose of the counter electrode is to supply the current required by the working electrode thereby preventing the polarisation of the reference electrode due to the passage of current. It should be insoluble and inert in the supporting electrolyte solution and should not impose its characteristics upon the measured cell response. The size, shape and position of the auxiliary electrode are important considerations since these factors determine whether the working electrode is an equipotential surface. In this work a platinum wire (Area RDE= 3.1 cm^2, C2 Cell Stand = 1.3 cm^2) was used as a counter electrode. This was positioned close to the working electrode to minimise overall cell resistance. The surface area of the counter electrode is deliberately kept high to minimise polarisation on the electrode thus avoiding unwanted contributions to the cell response.

2.3.4 Electrolyte Solutions

All electrode reactions are conducted in solutions containing a high concentration of inert electrolyte called a supporting electrolyte. The reason for using this solution is to minimise the phenomenon of migration of the electroactive ions caused by the electric field and to confine the interfacial potential difference to the distance of closest approach of solvated ions to the electrode.

The supporting electrolyte is the principle source of electrically conducting ionic species and has a concentration of at least 100 times that of the electroactive species, typically 0.1 M in this body of work. The supporting electrolyte must truly be inert in the potential range of the experiment, not reacting with the electrode or with the products of the electrode reaction. It is for this same reason that the reagent used for preparing the electrolyte must be of a high purification grade.

As mentioned previously dissolved oxygen in the electrolyte solution is an undesirable impurity in electrochemical experiments. Some problems which might arise due to the presence of oxygen include: oxygen reduction at cathodic potentials, oxide formation on the electrode surface and reaction with intermediates formed during electrode reactions. As a result degassing of the working solution with a fine stream of Nitrogen gas was conducted for approximately fifteen minutes before experimentation and during experimentation a blanket of the inert gas was maintained over the solution.

2.4 Electrode Modification Techniques

2.4.1 Electrode pre-treatment

All electrodes were pre-treated to ensure a reproducible surface morphology and freedom from adsorbed impurities. However due to the different nature of the electrode materials employed slightly differing regimes were engaged.

The glassy carbon electrodes used were initially polished on a cloth pad with diamond lapping compounds of 15, 3 and 1 micrometre dimensions. Following this treatment the electrode was polished with an alumina oxide paste in distilled water on a fine grit pad so as to remove any solid polishing residues. However due to the nature of the metal the platinum electrodes were polished using only the alumina oxide paste on the fine grit pad. The electrodes were sonicated for 15 minutes and re-polished. In all cases the polishing resulted in reproducible, uniform electrode surfaces.

The polymer modified electrodes were prepared by immersing the electrodes in a methylene blue solution with 0.1 M phosphate buffer, pH $\approx$ 7, and 0.1 M KCl as supporting electrolyte and cycling in the potential range –0.4 V to 1.2V. The polymer thickness varied as a function of polymer deposition cycles.

2.5 *Experimental Techniques*

2.5.1 Potential Sweep Techniques

Cyclic voltammetry has taken over from polarography as being the best-known classical measuring method in electro-analytical chemistry [5-9]. Simple diagnostic criteria and relatively easy measuring techniques hastened the development of the procedure. The technique essentially involves applying a time dependent potential to the working electrode of an electrochemical cell (as described in section 2.3). The potential is swept cyclically between two pre-determined voltage limits E_1 and E_2 at a known scan rate, v. This triangular waveform is illustrated in figure 2.2. The resulting voltammogram, often termed the electrochemical spectrum, records the measured cell current as a function of applied potential where the current peaks represent the initiated redox activity of the substrate due to the applied potential. Upon analysis of the voltammograms the exact nature of the redox couple is elucidated i.e. determining the role of diffusion and homogeneous chemical reactions in a particular redox system.

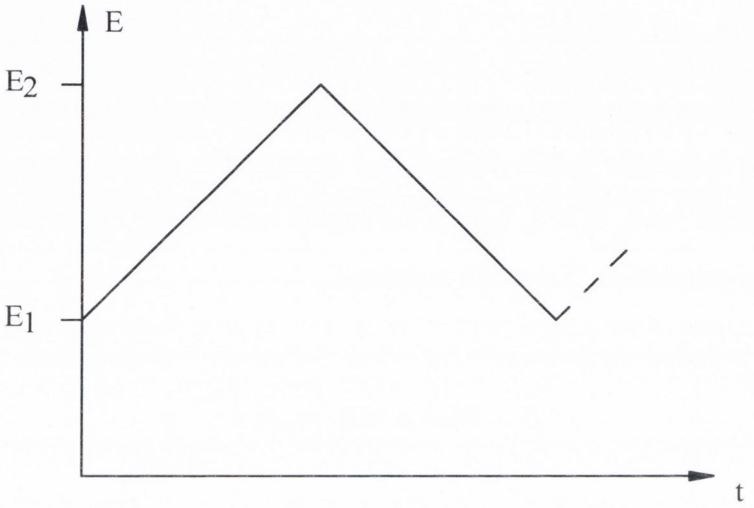

Figure 2.2; Illustration of the linear potential sweep with a triangular waveform, which is applied to the working electrode. This excitation signal scans the electrode between two potentials E_1 and E_2

Electrochemical systems may be divided into three categories; reversible, irreversible and quasi-reversible systems. The magnitude of the electrode transfer rate constant for a particular system decides the subsequent allocation of type. The current response is dependent on two steps, the transport of electroactive species to the electrode and secondly, the transfer reaction between the species and the electrode. If the electrochemical kinetics of the electron transfer process are so fast that the transport of the species to the interface is the rate controlling step, the reactions are said to be mass transport controlled and are referred to as reversible reactions. For this process it is useful to consider a simple n electron reversible electrode reaction

$$R \Leftrightarrow O + ne^- \qquad (2.22)$$

where R and O represent the reduced and oxidised forms respectively.

For a reversible redox process, the ratio of the concentration of the oxidised form to reduced form, C_o/C_R, within the region next to the electrode surface follows the applied potential in a Nernstian manner,

$$E = E^0 + 2.303\left(\frac{RT}{nF}\right) ln\left(\frac{C_0}{C_R}\right) \qquad (2.23)$$

where E^0 is the formal potential of the redox couple. The current I, is proportional to the concentration gradient near the electrode surface according to Fick's first law

$$I = nFAD\left(\frac{dC_0}{dx}\right) \qquad (2.24)$$

where D is the diffusion coefficient, F is the Faraday constant and A is the geometric area of the electrode.

The shape of the cyclic voltammogram may be explained in terms of the concentration profiles shown in figure 2.3. Initially at cathodic potentials there is no cell current produced however as the potential is swept anodically towards E^0 the electrode becomes a sufficiently strong oxidant converting R to O (figure 2.3 a), resulting in a small anodic current flowing. At E^0, the ratio of concentrations, C_o/C_R is always unity. As the potential is swept further the current continues to rise, past E^0, until the concentration gradient reaches a maximum resulting in a peak current, i_{pa}.

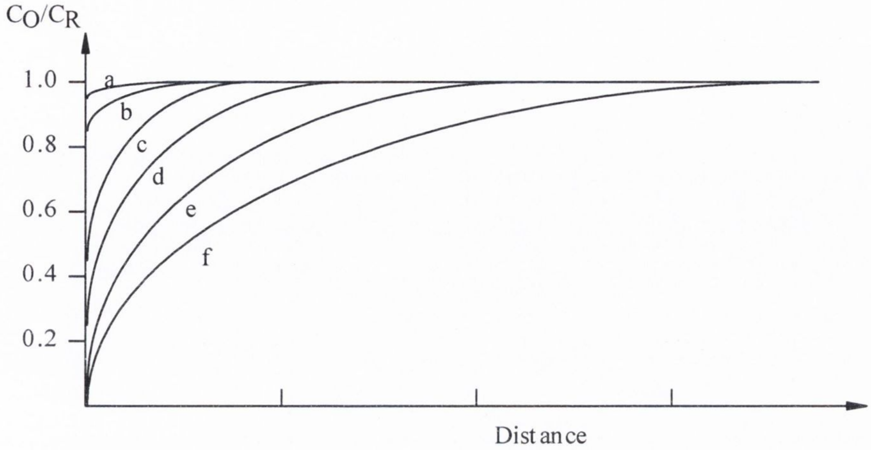

Figure 2.3; The concentration-distance profiles for an electroactive species, R, during linear sweep voltammetry. The overall reaction sequence is R ⇔ O + ne^-.. The curves correspond to the following approximate potentials; (a) E^0 –90mV; (a) E^0 –90mV; (b) E^0 –50mV; (c) E^0 ;(d) E^0 +30mV; (e) E^0 +130mV; (f) E^0 +280mV.

Further increasing of the potential leads to the consumption of the reduced form of the electroactive species at the electrode surface resulting in the depletion of the R species concentration to almost zero. On reverse scanning the described series of events is repeated for the generation of O, the oxidised form of the electroactive species which now predominates at the electrode surface. This opposite process results in the generation of a reduction peak on the reverse scan, the net process producing a current/potential trace similar to that illustrated in figure 2.4.

The redox species diffuses to the electrode surface due to the generation of an interfacial concentration gradient. Migration effects are eliminated ensuring there is a presence of a relatively large amount of electro-inactive ions, while convection is avoided by working with unstirred solutions.

Under the conditions of semi-infinite linear diffusion, the peak current i_p, is given [10-12].

$$i_p = 0.4663nFA\left(\frac{nF}{RT}\right)^{\frac{1}{2}} C_0^{\infty} D^{\frac{1}{2}} \upsilon^{\frac{1}{2}} \tag{2.25}$$

This is known as the Randles-Sevcik equation and shows that the peak current is proportional to the square root of the scan rate. It should be noted, however, that the diffusion characteristics of the system may only hold for a short time, as thermal and concentration gradients may induce random convection processes, resulting in fluctuations of the resulting current. For this reason, only data obtained from analysis of the first sweep is normally used to deduce kinetic parameters.

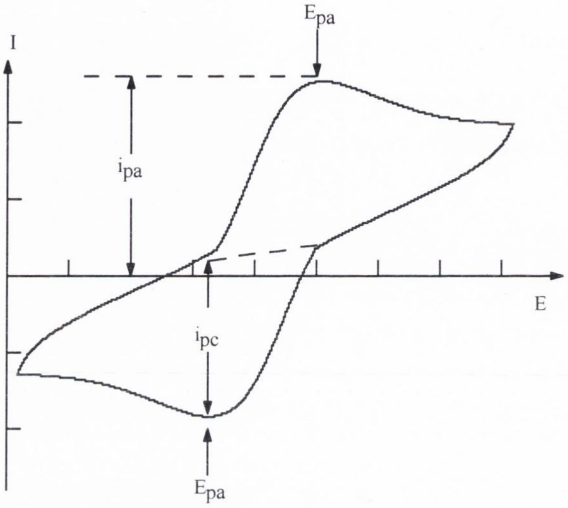

Figure 2.4; Cyclic Voltammogram for a model reversible process, R $\Leftrightarrow$ O + ne$^-$.

In the case of irreversible systems, the electron transfer rates at all potentials are significantly less than the rate of mass transfer. As a result, Nernstian equilibrium is not maintained at the electrode surface. When the rate of electron transfer is insufficient to maintain this surface equilibrium, then a modification of the shape of the cyclic voltammogram is observed. Probably the most marked feature of a cyclic voltammogram recorded for a totally irreversible system, is total absence of a reverse peak, however this alone is not conclusive evidence of a reversible system and other diagnostic tests are necessary for verification [1,13]. Frequently, processes under cyclic voltammetric examination appear reversible at low values of scan rate, but appear to become irreversible at higher values of sweep rate. This scan dependence is illustrated in figure 2.5. This type of system is mathematically complex as it necessitates simultaneous consideration of the kinetics of both the oxidation and the reduction reactions and the rate of material transport to the electrode surface.

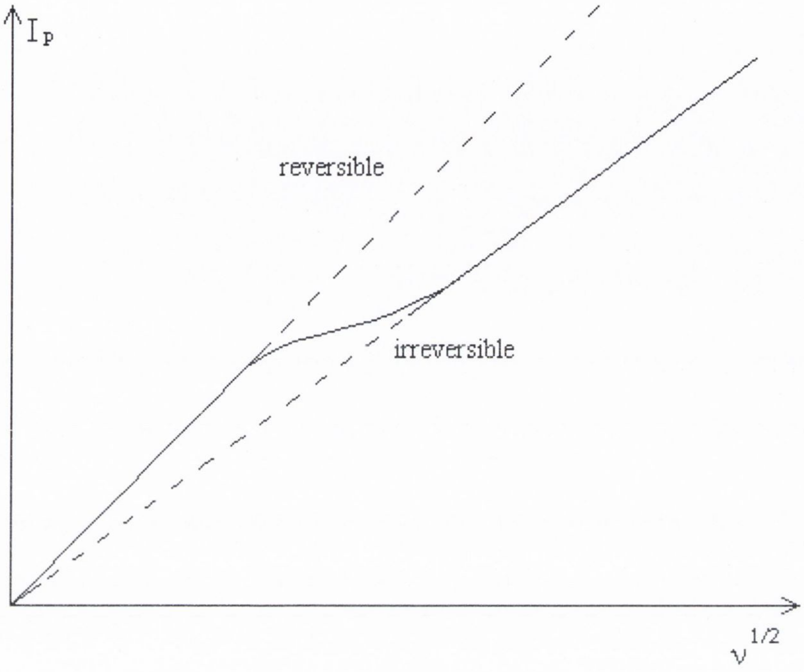

Figure 2.5; Transition from reversible to irreversible behaviour of the redox couple due to change of scan rate.

2.5.2 Hydrodynamic Electrodes

Hydrodynamic electrodes are electrodes which function in a controlled convection environment [1,2]. Rotating disc electrodes are hydrodynamic since transport of electroactive species can be controlled and varied quantitatively over a wide range. The primary advantage of these electrodes is the increased transport of electroactive species to the electrode, leading to higher currents and consequently greater sensitivity and reproducibility. The thickness of the diffusion layer may simply be controlled by altering the rotation speed of the electrode and may be quantitatively calculated for a specific geometry, while at the same time the hydrodynamics of the liquid flow are solvable, and the associated kinetic equations relatively simple. This is a marked advantage over cyclic voltammetry where the diffusion layer is time dependent. The disc shape of the electrode ensures that the electrode surface has uniform current density across the entire surface.

The hydrodynamic technique involves rotating the electrode surface at a known frequency, f. The angular velocity i.e. the parameter of interest is subsequently obtained from $\omega = 2\pi f/60$. A well defined flow pattern is obtained, figure 2.6, where the rotating electrode acts as a 'pump', pulling the solution vertically upwards towards the disc, and then throwing it out centrifugally. The flow patterns have been quantitatively analysed and defined streamline flow patterns in terms of cylindrical polar co-ordinates determined [14,15]. The rotation of the electrode must not be so fast as to cause turbulence in the solution, therefore ensuring laminar flow of the substrate to the electrode surface.

The layer of liquid immediately adjacent to the electrode surface is considered to be stagnant with respect to movement towards the rotating disc, and is said to rotate with the disc at the same angular velocity. The electroactive species in bulk solution flows rapidly to the edge of this boundary layer (signified δ) and therefore, the concentration of the electroactive species attains its bulk value at all distances greater than δ from the electrode surface. The local geography near the electrode surface can be regarded as comprising of two distinct regions; a well stirred region with convection being the means of mass transport and a stagnant diffusion layer of thickness δ, where the mass transport occurs solely by diffusion. The resulting concentration profile may be described using the Nernst diffusion layer model as seen in figure 2. 7. However it should be noted that the transition between the diffusion layer and the outer hydrodynamic layer is not sharply defined in reality. Levich proposed a quantitative relationship which describes the dependence of the diffusion thickness on angular rotation rate ω [16]. This is outlined in the following expression

$$\delta = 1.61\upsilon^{1/6} D^{1/3} \omega^{-1/2} \qquad (2.26)$$

where D is the diffusion coefficient and υ is the kinematic viscosity of the solution. Typically υ has a value of 0.01 $cm^2\, s^{-1}$ for dilute aqueous solutions.

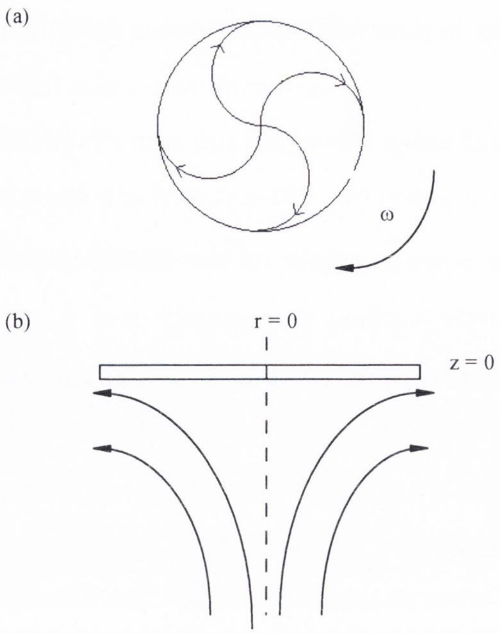

Figure 2.6; The patterns of flow to a rotating disc electrode (a) viewed from below the electrode face and (b) across its surface as viewed from the side. Laminar flow is assumed.

This result predicts that the faster the rotation rates the narrower the stagnant diffusion layer. This narrower layer results in a steeper concentration gradient across the diffusion layer and increases the rate of mass transport of the species to the electrode surface. The observed current should increase with the increase in ω, since the current is proportional to the interfacial concentration gradient.

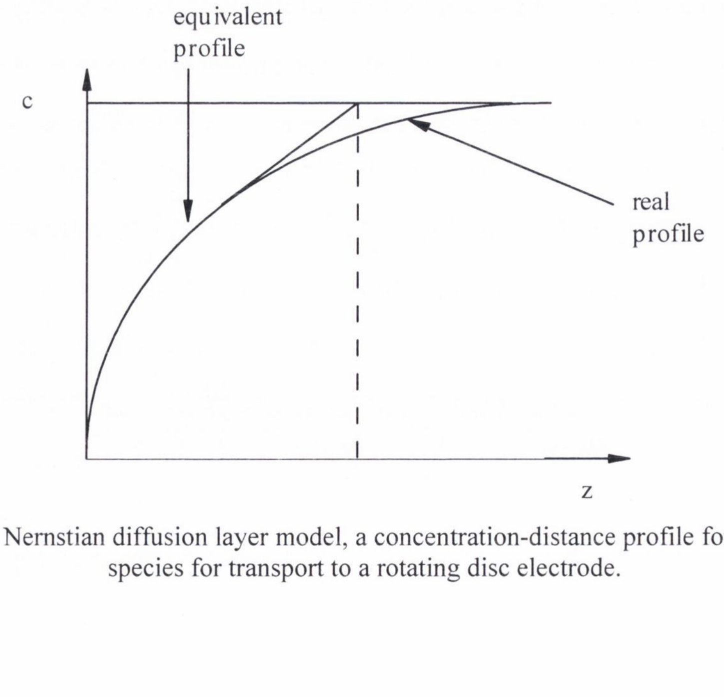

Figure 2.7; The Nernstian diffusion layer model, a concentration-distance profile for an electroactive species for transport to a rotating disc electrode.

The diffusional flux, J, to the surface of the electrode is described by the expression:

$$J = k_m(C^{\infty} - C^{\sigma}) \tag{2.27}$$

where C^{∞} and C^{σ} are the concentrations of the electroactive species in the bulk solution and at the electrode surface respectively and k_m is the mass transport coefficient (D/δ). The flux may then be related to the current as indicated by the following expression

$$J = \frac{i}{nFA} \tag{2.28}$$

where n, F and A have there usual meanings. When the electrode potential attains a value such that C^{σ} is zero the current is then said to be mass transport limited. Combining 2.26, 2.27 and 2.28 yields an expression for the limited current, i_L:

$$i_L = 0.62nFA\nu^{-1/6}D^{2/3}C\omega^{1/2} \tag{2.29}$$

This is known as the Levich equation. The limiting current is directly proportional to the square root of the rotation speed with the elucidated plot yielding a straight line through the origin whose slope can be used to estimate the diffusion coefficient. A linear Levich plot implies the absence of kinetic complications. If the redox system is not strictly reversible and interfacial electron transfer is the rate-limiting step then a non-linear Levich plot is obtained. Non linearity indicates that the Levich equation cannot be applied to anything other than strictly reversible redox systems. This means modifying the Levich equation. The Koutecky-Levich [17] equation is just that

$$\frac{1}{i_{LIM}} = \frac{1}{nFAD^{2/3}k_{ME}C^{\infty}} + \frac{1.61}{nFA\nu^{-1/6}D^{2/3}C^{\infty}\omega^{1/2}} \tag{2.30}$$

where k_{ME} is the heterogeneous rate constant in the forward reaction. A plot of $1/i_L$ against $1/\omega^{1/2}$ should be linear for an irreversible reaction, the slope being independent of the applied potential. The plot intercept however, is potential dependent since it contains the rate constant expression term k_{ME}.

If quasi-reversible electron transfer exists at the interface, the kinetics of both the forward and backward electron transfer processes must be considered. A more complicated expression is obtained [17]

$$\frac{1}{i_{LIM}} = \frac{1}{nFAD^{2/3}\left(k_b C_R^{\infty} - k_f C_0^{\infty}\right)} + \frac{1.61}{nFA\upsilon^{-1/6} D^{2/3}\left(k_b C_R^{\infty} - k_f C_0^{\infty}\right)\omega^{1/2}} \qquad (2.31)$$

This expression is only used when at potentials close to the equilibrium potential where the forward and backward reactions must be considered. At cathodic or anodic potentials much greater than the formal potential E^0, the rates of reaction become markedly different. Hence, depending on which direction the potential is being driven $k_b C_R^{\infty}$ and $k_f C_0^{\infty}$ become insignificant and the Koutecky-Levich equation reduces back to the simple Levich equation presented previously.

2.5.3 Differential Pulse Voltammetry

Differential pulse voltammetry (DVP) is a technique which is rapidly receiving wide-spread interest in the filed of electrochemical detection. This technique is frequently chosen in analytically orientated studies due to the enhanced sensitivity it displays compared to more conventional voltammetric measurements. Also, the selectivity of differential pulse measurements is frequently better than that of d.c. voltammetric measurements [18]. Furthermore, a decrease in the adsorption of substances on electrode surfaces when pulse techniques are used has sometimes been observed [19]. Thus this technique may increase sensitivity and selectivity parameters as well as reducing the possibility of electrode fouling in complex samples. It should be noted however, that the sensitivity enhancement observed during this technique, is due to a minimisation of the capacitive charging current contribution to the observed current, rather than to an enhanced faradaic response. Another possible explanation for the increase in sensitivity of this technique is that it results in a decrease in the diffusion layer thickness arising from pulsed measurements.

The principle of the DVP technique is as follows. A series of potential pulses are applied to a slow rate linear potential ramp. A sweep rate of *ca.* 1mV s^{-1} is commonly used to provide a slowly changing baseline potential. A potential pulse amplitude of *ca.* 5 to 50mV is applied and the pulse is repeated after a time τ_D-τ. The potential waveform is therefore a composite entity comprising of a staircase waveform superimposed on a constant amplitude pulse sequence. The current is then measured over a fixed time interval, just before the pulse application and again towards the end of the pulse. The recorded voltammograms then consists of a plot of the difference of these two current measurements as a function of the baseline potential, i.e., i (τ_D) – I (τ) *versus* E. It has been shown that for semi-infinite diffusion, the differential current, Δi, is related to potential according to the following expression [20,21]

$$\Delta i = \frac{nFAD_{CT}^{1/2}c_{\Sigma}}{\pi^{1/2}(\tau_D - \tau)}\left[\frac{p(1-\delta^2)}{(\delta + p)(1 + P\delta)}\right] \tag{2.32}$$

where P and δ are given by the following expressions

$$P = \exp\left[\frac{nF}{RT}\left(E + \frac{\Delta E}{2} - E_{O/R}^0\right)\right] \tag{2.33}$$

$$\delta = \exp\left(\frac{nF\Delta E}{2RT}\right) \tag{2.34}$$

The difference in current can be seen to depend on the relative position of the potential, E, on the standard redox potential, E^0. When E is much more positive than E^0, it is clear from the above equation that the term P will be great, and therefore Δi will approach zero. On the other hand, when E is far more negative than E^0, it can be seen that P will approach zero and hence so does Δi. Clearly then Δi, approaches a maximum near E = E^0. This explains the peak shaped Δi *versus* E profile, which is normally symmetrical about E^0. Setting $d\Delta i/dP = 0$, it has been shown that Δi is at a maximum when P = 1, which corresponds to Ep = E^0. Setting P = 1 in equation 2.32, the following expression for the peak current, Δi_p, is obtained

$$\Delta i_p = \frac{nFAD_{CT}^{1/2}c_\Sigma}{\pi^{1/2}(\tau_D - \tau)}\left[\frac{(1-\delta)^2}{(1+\delta)^2}\right]$$

$$= \frac{nFAD_{CT}^{1/2}c_\Sigma}{\pi^{1/2}(\tau_D - \tau)}\left[\frac{(1-\delta)(1+\delta)}{(1+\delta)^2}\right] \qquad (2.35)$$

$$= \frac{nFAD_{CT}^{1/2}c_\Sigma}{\pi^{1/2}(\tau_D - \tau)}\left[\frac{(1-\delta)}{(1+\delta)}\right]$$

It must also be noted that the function

$$F(\delta) = \frac{1-\delta}{1+\delta} \qquad (2.36)$$

depends on the pulse magnitude, ΔE. The function decreases with decreasing ΔE, and equals zero when ΔE equals zero. When ΔE is large, $F(\delta) = 1$, and the maximum current possible, Δi is obtained. Typically, ΔE is chosen to be *ca.* 50mV, corresponding to a peak current of 45 to 90% of the maximum current obtainable according to the number of electrons transferred in the redox reaction. Larger amplitudes have been shown to result in a loss of peak resolution as well as an increase in the signal to noise ratio [22]. The pulse amplitude is therefore a critical parameter and must be judiciously selected as a compromise between measuring sensitivity and selectivity.

This technique has some limitations. High signal to noise ratios have been reported for pulse voltammetry at solid electrodes. This could be due to the functional groups on the surface of solid electrodes. These may be subject to electrochemical reaction, resulting in slowly decaying residual currents [23,24].

2.5.4 Electrochemical Quartz Crystal Microbalance

The electrochemical quartz crystal microbalance is a variant of acoustic wave microsensors that are capable of ultrasensitive mass measurements. Under favourable conditions a typical EQCM can measure a mass change of 0.1-1ng/cm^2. The QCM technique was first identified by Sauerbrey [25]. QCM oscillates in a mechanically resonant shear mode under the influence of a high frequency AC electric field applied across the thickness of a quartz crystal. The top and bottom sides of the quartz crystal are coated with a layer of gold that act as the working electrode.

QCM and the combination of QCM and electrochemistry (EQCM) have been widely employed for studies of ion transport processes in polymer films [26], biosensor developments [27] and investigations of the kinetics of the adsorption of adsorbate molecules [28,29]. The mass sensitivity of EQCM originates from the relationship between the oscillation frequency of the total mass of the crystal and the oscillation frequency of the crystal with adlayers of material residing on the metal coated crystal. This relationship is shown in equation 2.37 and is known as the Sauerbrey Equation.

$$\Delta f = -\frac{2f_0^2}{A\sqrt{\mu\rho}}\Delta m \tag{2.37}$$

Here f_0 is the resonant frequency fundamental to the crystal, A is the area of the gold electrode coated onto the crystal, ρ is the density of the crystal and μ is the shear modulus of quartz. In the CH Instruments Model 440 system these values are, f_0 = 8MHz, A = 0.196cm^2, ρ = 2.648g/cm^3, μ = 2.947 x 10^{11} g/cm.s^2. Using these values it is seen that a frequency change of 1Hz corresponds to a mass change of 14ng using the CH Instruments Model 440 EQCM. The minus sign in equation 2.32 determines that a frequency decrease corresponds to a mass increase. The EQCM cell used for this work is shown in figure 2.8.

The EQCM cell consists of three round Teflon pieces. The total height of the cell is 37mm and its diameter is 35mm. The top piece is the cell top that holds the counter and reference electrodes. There are also two 2mm holes for degassing solutions. The centre piece is the cell body used for holding solution. The bottom piece is for mounting the quartz crystals. Four screws are used to seal the bottom and centre pieces together. The quartz crystal is located between the bottom and centre pieces. The top piece may be pressed into the centre piece to complete the cell.

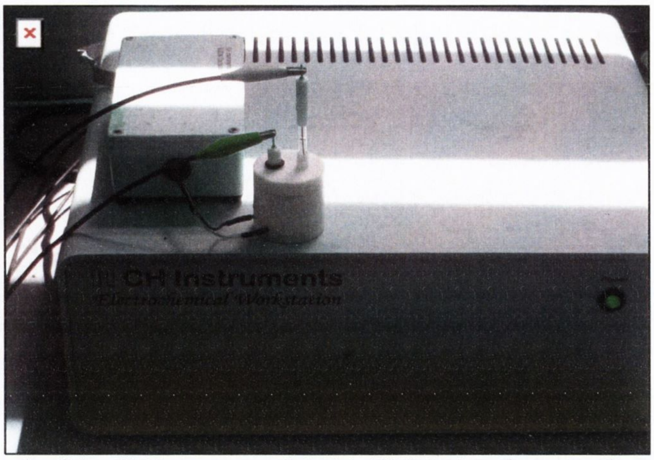

Figure 2.8; Photograph of the CH Instruments Model 440 Workstation as well as the EQCM cell with counter (green) and reference (white) electrode inserted.

2.6 Magnetic Field

The magnetic field was applied using the Magnetic Solutions 'Multi-mag' electromagnet. The magnet consisted of two Halbach Cylinders, one inside the other, which were rotated so that the magnetic field strength could be varied. The magnetic field strengths ranged from 0 – 1 Tesla (T). The cylinder is manufactured from sintered Nd-Fe-B and consists of twelve segments. These segments provide a homogeneous magnetic field in the circular bore (diameter of 54 mm) [30].

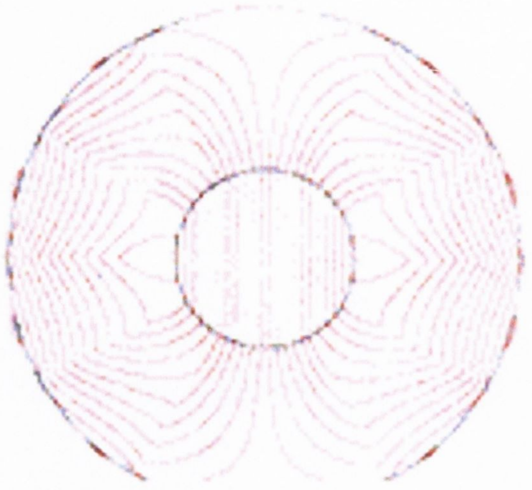

Figure 2.9; Magnetic flux profile in the central plane of the 54 mm bore Halbach Cylinder with a magnetic field strength of 0.5 Tesla.

The electrochemical cell sat in the bore of the multi-mag during the cyclic voltammetry experiments. The housing for the cell was fabricated to sit in the center of the multi-mag. Figure 2.9 shows the magnetic flux profile in the central plane of the magnet.

2.7 Chemicals

All chemicals were of analar grade(Aldrich) and aqueous solutions were made up with triply distilled Millipore^{TM} water. The Millipore water purification contains a carbon, organic and ion exchange cartridge and yields water with a large ohmic resistance of *ca.* 18mΩ. All solutions were completely de-gassed with nitrogen for fifteen mins prior to electrochemical measurement and the atmosphere over the test solutions was purged with nitrogen during experimentation. Standard solutions of electroactive species were prepared freah daily. Ascorbic acid and the catecholamines were kept in the dark or in the refrigerator for short periods when not in immediate use. These solutions were prepared fresh daily and after three hours of use were thrown into the safety waste container.

2.8 References

[1] A. J. Bard, L. R. Faulkner, "*Electrochemical Methods-Fundamentals an Applications*", 2nd ed., J. Wiley & Sons, 2001.

[2] C. M. A. Brett, A. M. O. Brett, "*Electrochemistry- Principles, Methods and Applications*", Oxford Science Publications, 1993.

[3] J. A. Von Fraunhofer, C. H. Banks, "*Potentiostat and its Applications*", Butterworth & Co. Ltd., 1st Edition, 1972.

[4] G. L. Lanz, D. J. G. Ives, "*Reference Electrodes*", Academic Press, New York, 1961.

[5] K. Aoki, K. Tokuda, H. Matsuda, *J. Electroanal. Chem.*, **146**, 417, 1983.

[6] G. A. Mabbott, *J. Chem. Educ.*, **60**, 9, 697, 1983.

[7] R. S. Nicholson, *Anal. Chem.*, **37**(11), 1351, 1965.

[8] P. T. Kissinger, W. R. Heineman, *J. Chem. Educ.*, **60**(9), 702, 1983.

[9] J. Heinze, J. Angew, *Chem. Int. Ed. Engl.*, **23**, 831, 1984.

[10] J. E. B. Randles, *Trans. Faraday Soc.*, **44**, 327, 1948.

[11] A. Sevcik, *Coll. Czech. Chem. Commun.*, **13**, 349, 1958.

[12] R. S. Nicholson, I. Shain, *Anal. Chem.*, **36**, 702, 1964

[13] Southampton Electrochemistry Group; "*Instrumental Methods in Electrochemistry*", ed. T.J. Kemp, Ellis Horwood, Chischester, 1985.

[14] T. Von Karman, Z. Agnew, *Math. Mech.*, **1**, 233, 1921.

[15] W. G. Cochran, *Prog. Camb. Phil. Soc. Math. Phys. Sci.*, **30**, 345, 1934.

[16] V. G. Levich, *"Physiochemical Hydrodynamics"*, Prentice Hall, 1962.

[17] J. Koutecky, V. G. Levich, *Zh. Fiz. Khim.*, **32**, 1565, 1956.

[18] *"Quantitative Analysis of Catecholamines and Related Compounds"*, Ellis Horwood, ed., A. M. Krstulovic, pp163.

[19] K. Stulik, V. Pacakova, *Anal. Chim. Acta*, **158**, 15, 1984.

[20] *"Electroactive Polymer Electrochemistry"*, Part 1, Plenum Press, N.Y. & London, ed., M. E. G. Lyons.

[21] E. P. Parry, R. Oysteryoung, *Anal. Chem.*, **37**, 1634, 1964.

[22] W. A. MacCrehan, *Anal. Chem.*, **52**, 1542, 1981.

[23] V. Majer, J. Vesely, K. Stulik, *J. Electroanal. Chem.*, **45**, 113, 1973.

[24] W. E. Van der Linden, J. W. Dieker, *Anal. Chim. Acta*, **119**, 1, 1980.

[25] E. Sabatani, I. Rubenstien, R. Maoz, J. Sagiv, *J. Electroanal Chem*, **219**, 365, 1987.

[26] E. Sabatini, I. Rubenstien, *J. Phys. Chem*, ***91***, 6663, 1987

[27] E. B. Troughton, C.D. Bain, G. M. Whitesides, R.G. Nuzzo, D. L. Allara, M. D. Porter, *Langmuir*, **4**, 365, 1988.

[28] L. Strong, G. M. Whitesides, *Langmuir*, **4**, 546, 1988.

[29] C. D. Bain, G. M. Whitesides, *J. Am. Chem. Soc*, **110**, 3665, 1988.

[30] J. M. D. Coey, Magnetic Solutions Ltd.

CHAPTER 3

ELECTROCHEMISTRY OF SOLUTION PHASE AND POLYMERIC METHYLENE BLUE

3.1 *Introduction*

Methylene blue is member of the phenothiazines which are a family of very versatile organic dyes. As described previously, MB has been used extensively in the modification of electrodes. The dye adsorbs easily and rapidly onto electrodes and also can be electropolymerised onto electrodes. MB also possesses catalytic properties and so investigation into MB properties is justified. The MB/LMB redox reaction in aqueous solution can be written in the form:

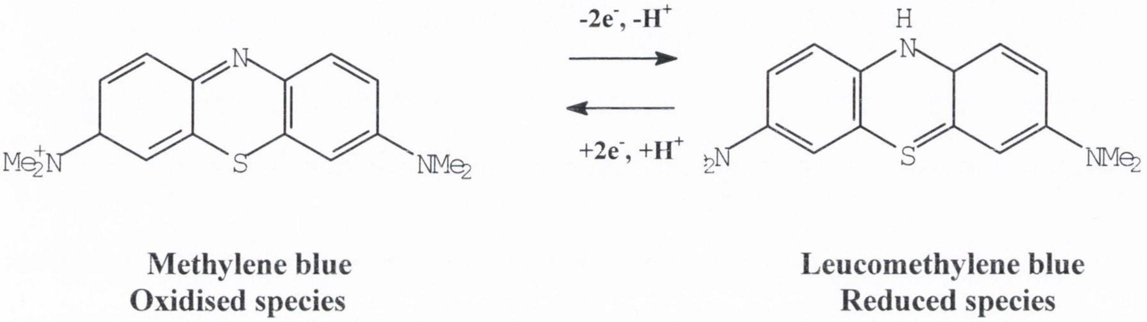

Scheme 3.1; Redox chemistry of the MB/LMB couple.

and involves a 2e$^-$, H$^+$ transfer.

3.2 *Voltammetric Analysis of Solution Phase Methylene Blue*

Cyclic and RDE voltammetry were used to investigate the solution electrochemistry of Methylene Blue (MB). The cyclic voltammetric response of a dilute solution of 1 x 10^{-4}M MB in 0.1M H_2SO_4 (pH~1), 0.1M KCl as supporting electrolyte, is outlined in figure 3.1. Scanning from positive to negative potential at a rate of 20 mV s^{-1}, two well defined peaks are observed, a cathodic peak C_1 (Ep,c = 220mV) which corresponds to the reduction of MB to Leucomethylene blue (LMB) and an anodic counterpart A_1 (Ep,a = 249mV) attributed to the oxidation of LMB to MB. The authors McCreery *at al.* [1] report the C_1/A_1 redox couple centered around +0.2V at a GC electrode in 0.1M H_2SO_4, pH~1. This C_1/A_1 redox couple represents the two electron oxidation/reduction reaction in scheme 3.1. In figure 3.1 we observe a slight shift in the C_1 and A_1 peak potentials indicating some kinetic constraint. At low sweep rates, $\nu < 200 mV\ s^{-1}$, the system exhibits reversible behaviour and can be formally diagnosed as a reversible process if the following is observed

$$\Delta Ep = 30mV\ @T = 293K \tag{3.1}$$

where,

$$\Delta Ep = \frac{2.303RT}{nF} \tag{3.2}$$

and n denotes the number of electrons involved in the redox process. The ΔEp values found experimentally were typically in the region 28-35mV at low scan rates and so the process is considered to be reversible.

Another diagnostic criterion for reversibility is that the C_1/A_1 peak current ratio should be unity. This was not observed as the reduction peak currents were greater than the peak currents for the oxidation process over the range of scan rates employed. This suggests that some process other than that presented in scheme 3.1 is occurring, and is a complicating factor in the reversibility of the system. Sagara and Niki [2] used electroreflectance spectroscopy to investigate MB adsorption processes in solution phase at graphite electrodes with 0.1M H_2SO_4 as the solvent. The authors reported mediation of MB reduction by adsorbed MB species, but the reverse mediation of LMB oxidation by the adsorbed species was thermodynamically unfavourable. This may account for the higher reduction peak currents observed in figure 3.1.

A second distinct couple, assigned C_2/A_2, is observed at *ca.* 110 mV and corresponds to the redox activity of the adsorbed MB/LMB couple at the glassy carbon surface. This couple exhibits reversible electrochemistry over the range of scan rates performed with ΔE_P remaining constant. The C_1/A_1 and C_2/A_2 redox couple potentials are in excellent agreement with those reported by Sagara and Niki [2], in 0.1M H_2SO_4.

In systems that are mass-transport controlled, peak current, I_P, should vary in a linear manner with the square root of the scan rate. This is best described by the Randles-Sevcik equation, presented previously in Chapter 2, and a typical plot of the

$$I_P = 0.446nFA\left(\frac{nF}{RT}\right)^{\frac{1}{2}} C^{\infty} D^{\frac{1}{2}} \nu^{\frac{1}{2}} \tag{3.3}$$

equation is shown in figure 3.2. Data values were taken from voltammograms shown in figure 3.1.

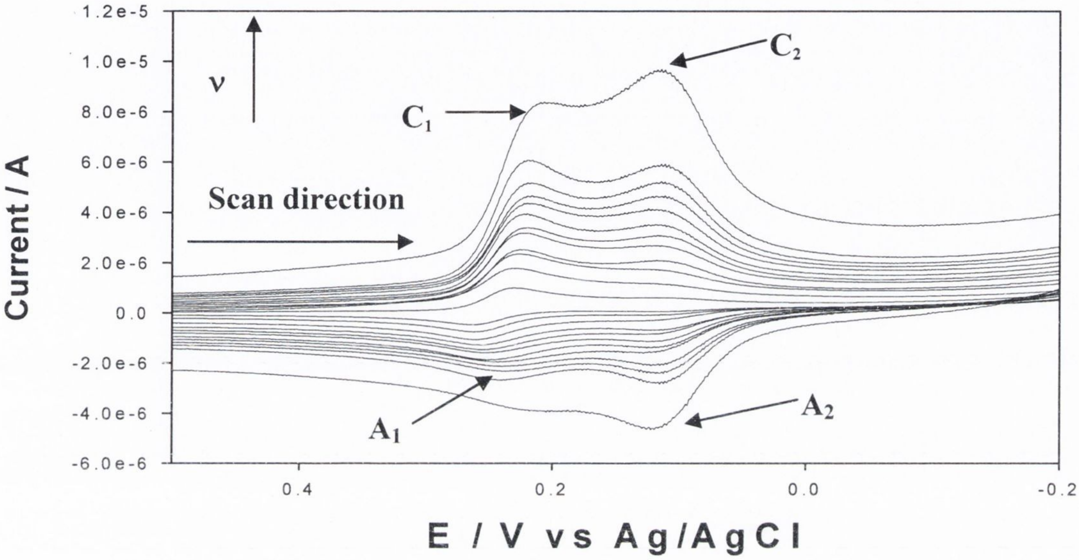

Figure 3.1; Typical Cyclic Voltammograms displaying the redox activity for a 1 x 10^{-4} M MB, 0.1M KCl + 0.1M H_2SO_4, (pH~1), solution at a GC electrode. The voltammetric scan rates ranged from, $\nu = [5 — 200]$ mV s^{-1}.

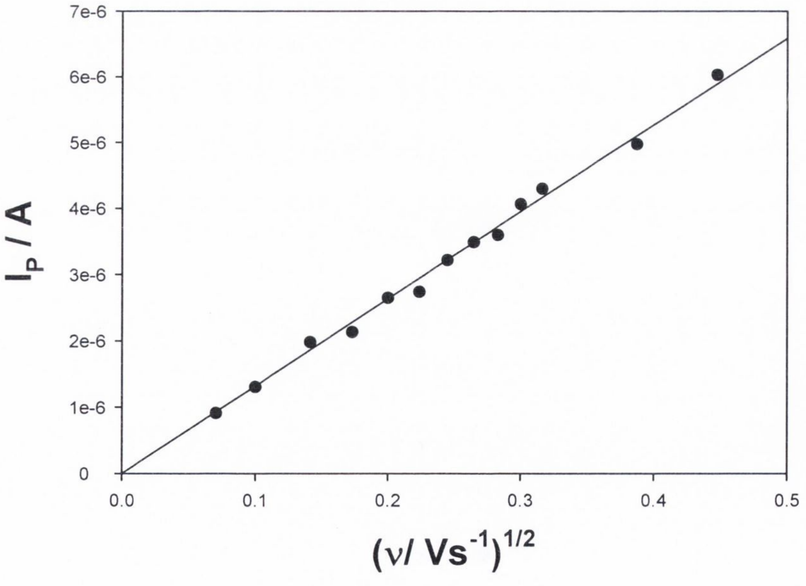

Figure 3.2; Typical Randles-Sevcik plots for the reduction of solution phase MB to LMB (peak C_1) at a GC electrode. [MB] was 1x10^{-4} M in 0.1M H_2SO_4, pH~1. The peak currents for the oxidation process (A_1) were difficult to obtain due to the presence of the preceeding adsorption peak (A_2). Data obtained from CV's shown in fig 3.1.

Good linearity is observed in the R-S plot, indicative of fast charge transfer kinetics, and an average value for the diffusion coefficient of 1.58±0.3 x 10^{-6} cm^2 s^{-1}, was calculated.

A series of RDE experiments were carried out to further investigate the reversibility of the MB system. Figure 3.3 shows a typical RDE voltammetric response for a 1 x 10^{-4} M MB solution, displaying characteristics associated with rapid charge transfer kinetics. The RDE voltammetric response for a mass transport limited process can be described by the Levich equation presented in Chapter 2;

$$I_L = 0.62nFAD^{2/3}\nu^{-1/6}\omega^{1/2}C^{\infty} \tag{3.4}$$

A plot of the limiting current, I_L, versus the square root of the rotation speed, ω, should be linear through the origin. Reversibility in this case requires electron transfer to be rapid relative to the rate of mass transport; hence, the redox process changes from reversible to quasi-reversible as the rotation is increased. This is reflected in a deviation from linearity in the Levich plot (figure 3.4) and may be due to electrode modification by adsorbed species. At rapid rotation speeds, diffusion of MB to the electrode surface approaches a maximum. Thus the effective concentration in the diffusion layer is almost that of the bulk, adsorption of MB to the electrode occurs to the extent that the electrode is modified. This is observed in the RDE voltammogram for 5000rpm shown in figure 3.3 at negative potentials. From the plot gradient, a diffusion coefficient in 0.1M H_2SO_4 was quantified. An average value of 1.8 ± 0.2 x 10^{-6} cm^2 s^{-1} was determined for the concentration 1 x 10^{-4} M, and compares well to the values obtained using C.V. Literature values were reported by the authors Murthy and Reddy [3] for various phenothiazine dyes in 0.1M H_2SO_4, and a calculated diffusion coefficient of 0.81 x 10^{-6} cm^2 s^{-1} for a 5 x 10^{-4} M solution of MB.

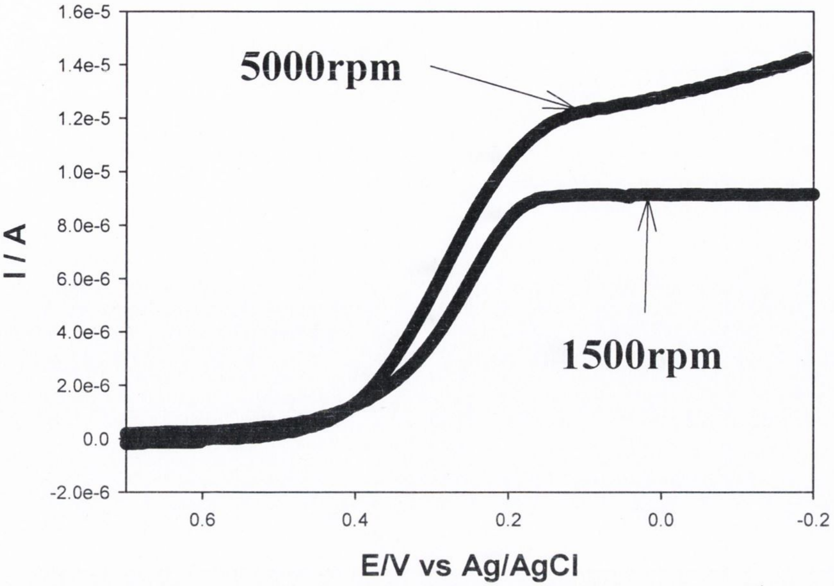

Figure 3.3; Typical Rotating Disk Voltammograms for the reduction of 5 x 10^{-4} M MB in 0.1M H_2SO_4, at a GC electrode. Two rotation speeds are presented. Scanned from 0.7 to -0.2 V.

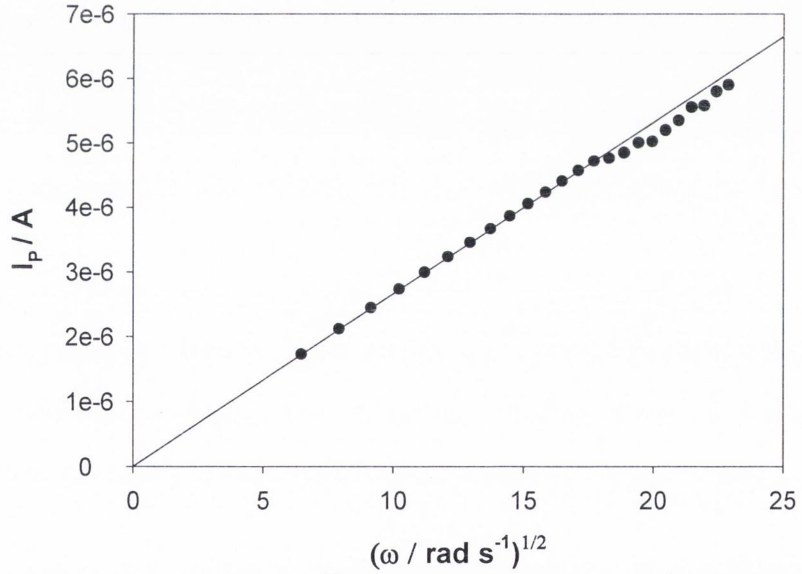

Figure 3.4; Typical Levich plot, I_{LIM} vs. $\omega^{1/2}$, for the reduction of a 1 x 10^{-4} M MB solution at a RDE. Deviation from linearity is observed at rotation speeds > 3000rpm, indicating quasi-reversibility.

It is well established that when a redox system is Nernstian, the current potential response should be described by an equation of the form

$$E = E_{1/2} + \frac{RT}{nF}\ln\{(I_L - I)/I\} \qquad (3.5)$$

Any system that obeys this equation should yield a linear Tafel plot, $\ln\{(I_L-I)/I\}$ versus E, with the slope = nF/RT, and intercept = $E_{1/2}$.

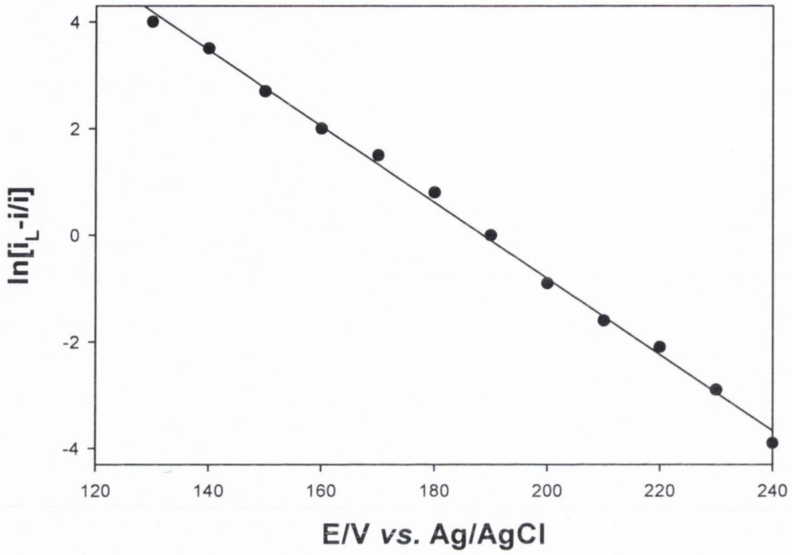

Figure 3.5; Typical Tafel plot, $\ln[i_{LIM}-i/i]$ vs. E/mV, for the reduction of 1×10^{-4} M MB in 0.1M H_2SO_4 at a GC electrode.

One such plot for the MB /LMB system is shown in figure 3.5 and the intercept (185mV) was used to calculate a value for k^0 of 2.66×10^{-3} cm s^{-1}. This value confirms the assumption of facile kinetics.

An important diagnostic criterion for distinguishing the reaction mechanism when using CV is the variation of $I_P/v^{1/2}$ with scan rate. For an ECE process with an irreversible chemical reaction $I_P/v^{1/2}$ should decrease with increasing scan rate. This variation is presented in figure 3.6 for the reduction of MB. The figure indicates that the observed behaviour does not favour the ECE mechanism. Also the ΔEp values suggest that it is a two-electron reversible charge-transfer process involving an EE type mechanism.

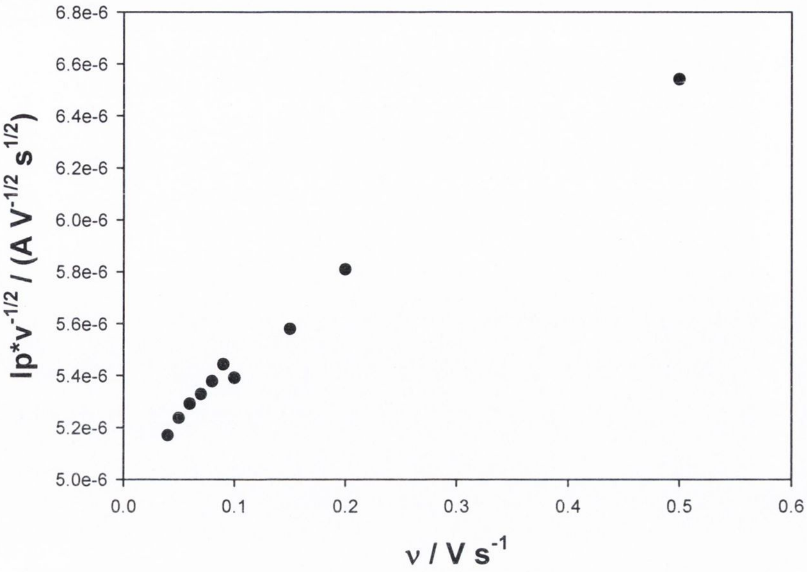

Figure 3.6; Variation of $I_P / \nu^{1/2}$ with scan rate, suggesting that the mechanism is not ECE. Scan rates were varied from 2 – 500 mV s^{-1}. [MB] = 5 x 10^{-4} M.

These results are consistent with those reported by the authors Murthy and Reddy [3] for the MB/LMB system, and Archer *et al.* [4] for the thionine/leucothione system, studied at a platinum electrode. We therefore ascribe these trends to adsorption of MB at the bare glassy carbon electrode, which is dealt with in more detail later in this chapter.

Using CV, kinetic information can also be gleaned from the variation of anodic and cathodic peak separation, ΔEp. For measurements conducted on a $1\text{x}10^{-4}$ mol dm^{-3} concentration of MB, the peak separation varied form *ca.* 32mV at ν = 2mV s^{-1}, to *ca.* 100mV at ν = 500mV s^{-1}. The standard rate constant, k^0, for redox process at the standard potential, E^0, can be quantified from careful analysis of the variation of peak separation of voltammetric peak separation with sweep rate. The reaction is reversible at low scan rates but becomes quasi-reversible with increasing scan rates, and eventually irreversible at high scan rates. Theoretical working curves of $n\Delta Ep^{theor}$ as a function of a kinetic parameter,Ψ, have been numerically elucidated by Nicholson [5], when the voltammetric response under quasi-reversible conditions was examined;

$$\Psi = \frac{(RT)^{1/2} k^0}{\left(nFD_O^{1-\alpha} D_R^{\alpha} \pi \nu\right)^{1/2}} \tag{3.6}$$

where α, ν denote the transfer coefficient and scan rate respectively. If one assumes that $D_O \approx D_R \approx D$ and that $\alpha = 0.5$, equation 3.6 simplifies to

$$\Psi = \frac{(RT)^{1/2} k^0}{(nFD\pi\nu)^{1/2}} \tag{3.7}$$

The aforementioned theoretical working curve can be constructed from values calculated by Nicholson [5]. Values of Ψ that correlate with experimental ΔEp values can be extracted from the curve and values for the standard rate constant can be evaluated. The table 3.1 summarises the parameters found for a range of [MB] using equation 3.7. A significant disadvantage of this approach to quantifying k^0 is that high voltammetric scan rates must be employed if the interfacial electron transfer process is rapid. That is, to measure a heterogeneous rate constant of 1cm s^{-1}, the experimental voltammetric scan rate used must be of the order of 10^3V s^{-1}. Errors relating to uncompensated ohmic solution resistance should be carefully avoided. The magnitude of the present case k^0 values is such that ohmic resistance can reasonably be neglected.

[MB] mol L^{-1}	**$(\Delta Ep)_{exptl}$ V**	**$(n^*\Delta Ep)_{theory}$ V**	**Ψ**	**10^{-3} k^0 cm s^{-1}**
1 x10^{-4}	39	78	1.346	8.269
5 x10^{-4}	38	76	1.503	6.206
1 x10^{-3}	39	78	1.346	5.268
5 x10^{-3}	68	136	0.265	0.971
8 x 10^{-3}	82	164	0.184	0.538
0.010	84	168	0.169	0.493
0.012	76	152	0.210	0.456
0.015	70	140	0.247	0.575
0.018	72	144	0.234	0.487
0.020	73	146	0.225	0.487

* Assuming n = 2

Table 3.1; Typical series of calculations to determine k^0 for a range of [MB] at a scan rate of 100mV s^{-1}, using a theoretical working curve.

3.3 *Dependence of Solution Electrochemistry on bulk MB Concentration*

The solution phase electrochemistry for a range of MB concentrations was investigated in 0.1M H_2SO_4, pH~1 with 0.1M KCl as supporting electrolyte. Typical voltammograms for dilute (1x 10^{-5} - 5 x 10^{-4} M) concentrations of MB are shown in figure 3.7. Interesting concentration effects are observed. At the lowest concentration of 1 x 10^{-5} M, figure 3.7 (d), the adsorbed species redox couple is the dominant process. This can be explained in terms of available monomeric MB. The concentration of available monomer in solution is small and so the C_1/A_1 redox couple contribution to the current response is also small. Adsorption of MB to the GC surface is rapid and the C_2/A_2 couple is observed. As the concentration increases the C_1/A_1 couple becomes the dominant process, figure 3.7 (a)&(b), exhibiting a well defined current response to the applied potential.

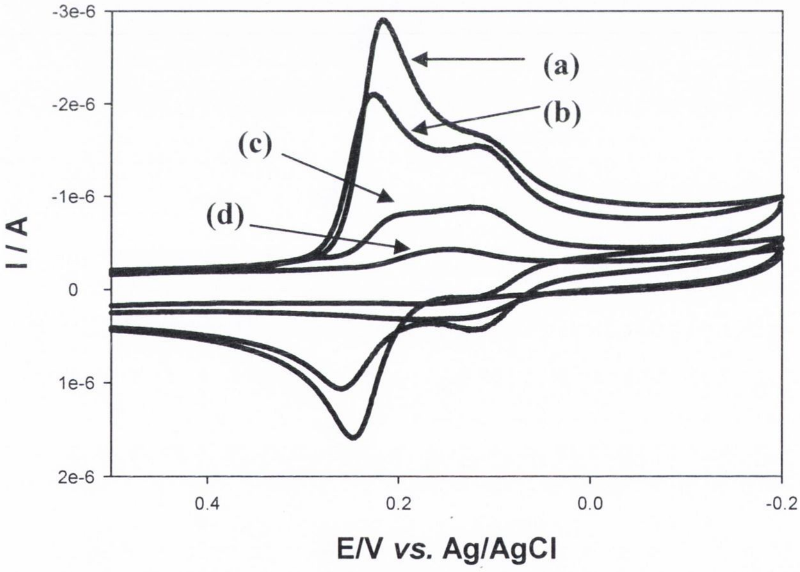

Figure 3.7; Typical cyclic voltammograms of four dilute MB concentrations at a GC electrode; **(a)** = 5 x 10^{-4} M, **(b)** = 1 x 10^{-4} M, **(c)** = 5 x 10^{-5} M, **(d)** = 1 x 10^{-5} M. Supporting electrolyte was 0.1M KCl in a 0.1M H_2SO_4 (pH~1) solution. Scan rate, ν = 20mV s^{-1}, scanned from 0.5 to -0.2 V.

This well defined solution electrochemistry of MB at dilute concentrations is in stark contrast with that at high concentrations. The voltammograms have a totally different appearance in that only one sharp redox couple, a cathodic peak at *ca.* 135 mV s^{-1} and corresponding anodic peak at *ca.* 180 mV s^{-1}, is apparent (Figure 3.8). This shift in

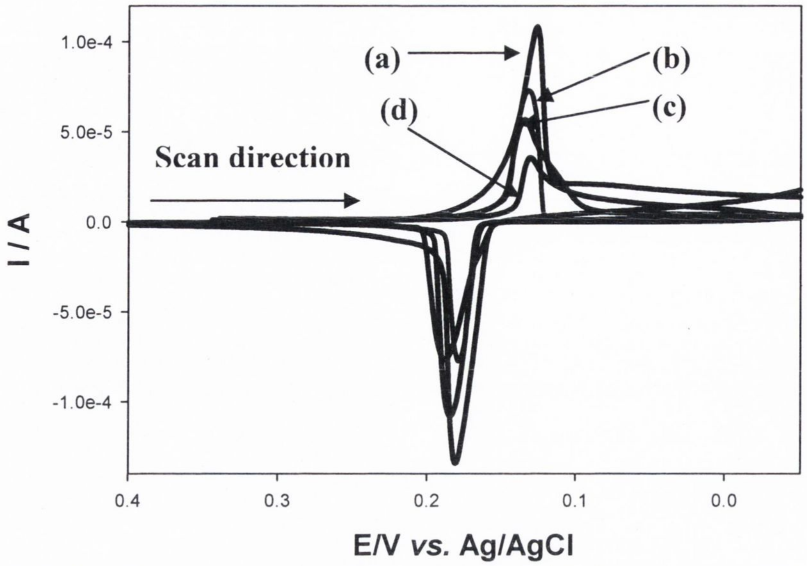

Figure 3.8; Typical cyclic voltammograms of four concentrated MB solutions at a GC electrode; **(a)** = 5 x 10^{-3} M, **(b)** = 1 x 10^{-2} M, **(c)** = 1.5 x 10^{-2} M, **(d)** = 2 x 10^{-2} M. Supporting electrolyte was 0.1M KCl in a 0.1M H_2SO_4 solution (pH~1). Scan rate, ν = 20mV s^{-1}.

peak potential can be justified when dimeric species and larger species are taken into account. Aggregation of dyes in aqueous solutions is known to occur where steric and electrical influences are favourable [6]. This reversible process is achieved *via* hydrogen bonding, van der Waals forces, or interaction of delocalised π–electrons between MB monomers [7]. In spectrophotometry experiments carried out by Bergmann and O'Konski [8], the authors found MB to be present in solution as a dimer in equilibrium with the monomer. The authors concluded that the principle monomer axes lie parallel, so that the monomer units lie face-to-face, with the ionic groups of the molecule situated at opposite ends of the dimer, Scheme 3.2.

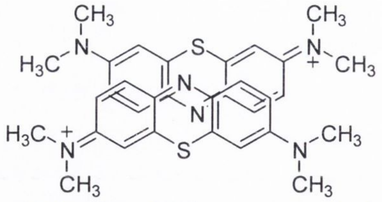

Scheme 3.2: Proposed structure of MB dimer [7] in aqueous solution. One of four resonance forms.

We can now assign the new redox couple at *ca.* +0.135 and +0.180 V to the reduction/oxidation, respectively, of the dimeric species. Previously observed in figure 3.7 was that an increase in MB solution concentration results in an increase of the solution phase redox peaks(C_1/ A_1), masking the redox peaks due to the adsorbed species(C_2/A_2). The new redox couple (+0.135/+0.18V) observed at high MB solution concentrations, therefore, is not due to adsorption of monomeric MB. It may be due to adsorbed dimeric species activity, if not that of solution phase dimers. It must be stated that the peak potentials for a particular concentration varied due to solubility difficulties. Due to the dilute concentration of MB in figure 3.7 voltammograms, dimerisation was minimal and a redox couple for the dimeric species was not observed. To investigate the consequences of dimerisation, monomer fractions for each concentration were elucidated and used to justify the variation in physical parameters quantified for MB solution electrochemistry in 0.1M H_2SO_4, pH~1.

3.3.1 Variation of Monomer Fraction with Concentration

The solution electrochemistry of MB is largely dependent on the bulk concentration of the dye. The higher the bulk concentration of the dye, the greater the tendency towards aggregation, and hence, dimer formation occurs. Consider the monomer-dimer equilibrium

$$2M \xleftrightarrow{K} D \qquad (3.8)$$

The monomer-dimer equilibrium constant K is then given by

$$K = \frac{[D]}{[M]^2} \qquad (3.9)$$

hence

$$[D] = K[M]^2 \qquad (3.10)$$

Let [T] denote the total concentration of monomer and dimer. Now

$$[T] = [M] + 2[D] \qquad (3.11)$$

hence

$$[T] = [M] + 2K[M]^2 \qquad (3.12)$$

or

$$2K[M]^2 + [M] + [T] = 0 \tag{3.13}$$

This expression is a quadratic in [M] and may be solved to yield

$$[M] = \frac{1}{4}K\,[(1 + 8K[T])^{\frac{1}{2}} - 1] \tag{3.14}$$

Let f = monomer fraction, then

$$f = \frac{[M]}{[T]} \tag{3.15}$$

hence

$$f = \frac{1}{4}K[T]\,[(1 + 8K[T])^{\frac{1}{2}} - 1] \tag{3.16}$$

If K is known then [M] can be determined and therefore f may be calculated. For MB solutions, K was taken to be 1.2×10^{-4} $dm^3\ mol^{-1}$ in 0.1M H_2SO_4 solution [7], and the monomer fraction values obtained are summarised in table 3.2.

[T] mol L^{-1}	**log [T]**	**f = [M]/[T]**
1×10^{-5}	-5.000	
5×10^{-5}	-4.301	0.6767
1×10^{-4}	-4.000	0.4700
5×10^{-4}	-3.301	0.2500
1×10^{-3}	-3.000	0.1844
5×10^{-3}	-2.301	0.0872
8×10^{-3}	-2.097	0.0696
0.010	-2.000	0.0625
0.012	-1.921	0.0572
0.015	-1.824	0.0513
0.018	-1.745	0.0470
0.020	-1.699	0.0446

Table 3.2; Monomer fraction values for a range of MB concentrations in 0.1M H_2SO_4, pH~1.

A plot of log [T / mol L^{-1}] versus f is shown in figure 3.9 and yields an interesting relationship.

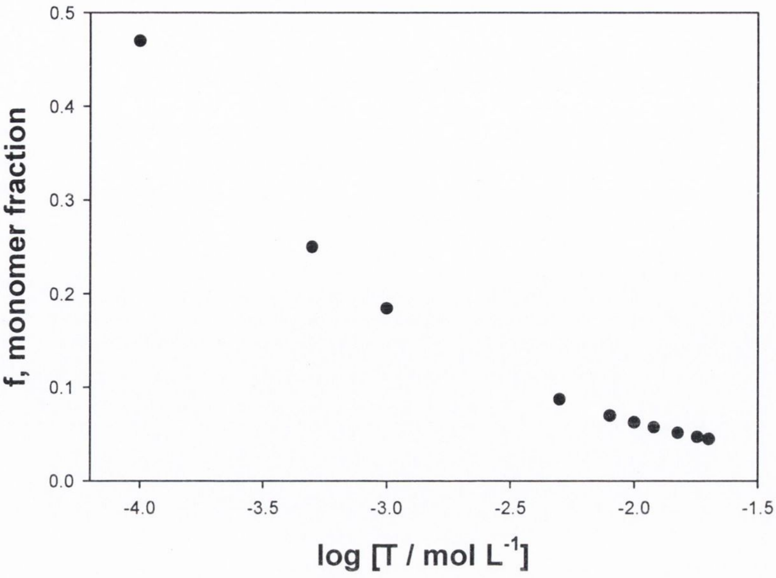

Figure 3.9; A plot of monomer fraction as a function of the log of a range of MB bulk concentrations in 0.1M H_2SO_4 (pH~1) at a glassy carbon electrode.

The monomer fraction rapidly decreases as the MB bulk solution increases due to dimerisation and formation of MB oligomers. The electron-rich nature of the aromatic rings in the MB structure allow for this facile aggregation. A double logarithmic plot was constructed, figure 3.10, and a linear relationship observed.

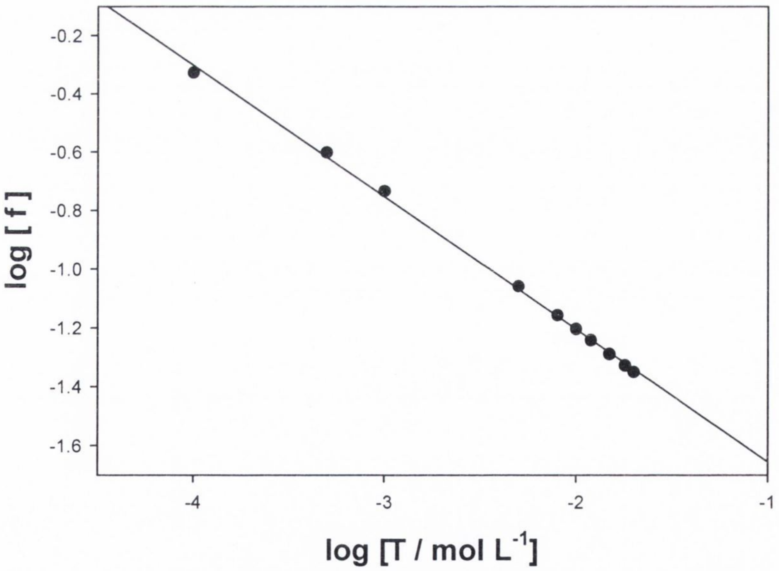

Figure 3.10; A plot of log monomer fraction versus the log [MB] for a range of bulk concentrations in 0.1M H_2SO_4 (pH~1) at a glassy carbon electrode.

From the graph we can predict that monomer fraction is zero at a MB bulk concentration of ca. 2.21×10^{-2} mol L^{-1}, and the slope = -0.45.

3.3.2 Variation of the Diffusion Coefficient with Concentration

The diffusion coefficients for a range of MB concentrations [1x10^{-5} – 2x10^{-2}M] were calculated using CV. Peak currents obtained from the cathodic peaks (e.g. C_1, Fig.3.1) at each scan rate were used to calculate the observed diffusion coefficients and the values plotted as a function of concentration. From figure 3.11 we observe a rapid drop in the magnitude of the diffusion coefficient as the bulk MB concentration increases. At bulk MB concentrations > 5 x 10^{-3} mol L^{-1} monomer fraction approaches zero, and this is reflected by the decreased values of D. The peak current values do not vary linearly with bulk concentration > *ca.* 2 x 10^{-3} mol L^{-1} because the effective bulk concentration decreases rapidly. The degree of aggregation in the dye increases with bulk MB concentration so less monomer is available for reduction, and this is reflected by the rapid drop in diffusion coefficient magnitude. The values found for D at low $[MB]_\infty$ are in good agreement with the literature value of 0.81 x 10^{-6} cm^2 s^{-1}, for a 5 x 10^{-4} M solution in 0.1M H_2SO_4 [3].

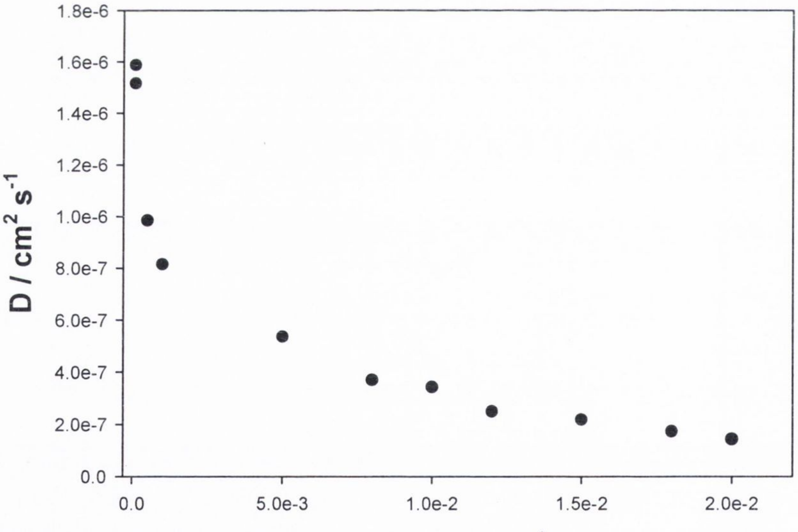

Figure 3.11; A plot of diffusion coefficient values as a function of MB bulk concentrations in 0.1M H_2SO_4 (pH~1) at a glassy carbon electrode.

3.3.3 Kinetic Variation of the Redox Couple MB/LMB with Concentration

The variation of ΔEp with log [MB / mol L^{-1}], when the scan rate was 100mV s^{-1}, is presented graphically in figure 3.12. In the region where [MB] is between 1 x 10^{-5} and 1 x 10^{-3} mol L^{-1}, ΔEp is ca. 45-60mV but increases dramatically as [MB] increases to 2 x 10^{-2} mol L^{-1}. At this concentration, f tends towards zero (Table 3.2), and this is reflected in the relatively large ΔEp (>145mV) values. Therefore, as the monomer fraction decreases, electrode kinetics become sluggish. Although the peak separations are strongly dependent on MB concentration, we observed that for a given concentration, they increased with scan rate in a manner that at first suggests quasi-reversibility. Using the aforementioned Nicholson's analysis, on a large number of performed experiments (At least $n \geq 5$) over the range of concentrations investigated, the average standard rate constants were calculated and found to vary with scan rate. This is not consistent with the finding that the MB/LMB couple is reversible at the bare glassy carbon RDE up to 3000rpm. The solution convection generated in hydrodynamic voltammetry means that a near bulk concentration of MB is present at the electrode surface and adsorption occurs. Adsorption of MB at the bare glassy influences the solution phase electrochemistry and we observe lower redox currents than expected. Archer et al have reported similar results for the thionine/leucothionine couple at a platinum electrode [4].

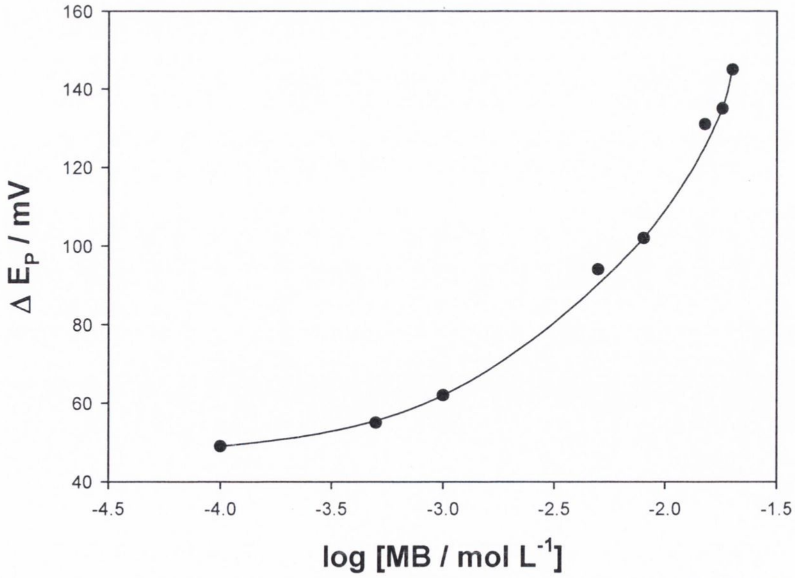

Figure 3.12; Plot of the variation of peak potential separation as a function of [MB]. Data taken from voltammograms with 100mV s^{-1} scan rate in 0.1M H_2SO_4.

Using the same data for a scan rate of 100mV s^{-1}, the standard rate constant was calculated from the ΔE_P values presented in table 3.1. The variation of k^0 with [MB] is graphically presented in figure 3.13.

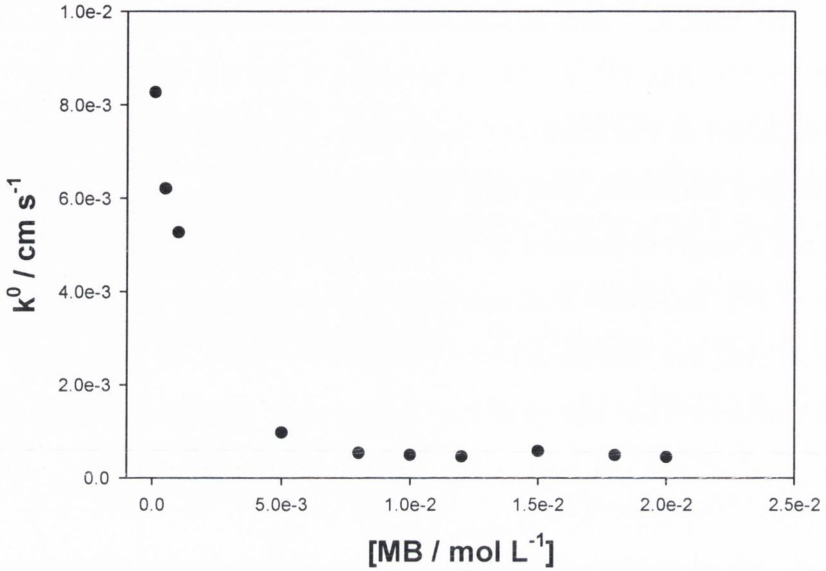

Figure 3.13; Variation of the standard rate constant, k^0, with bulk MB concentration. k^0 values were calculated from ΔE_P values obtained at a scan rate of 100 mV s^{-1}.

AT [MB] concentrations < 5 mM, the rate constants are large but, due to the formation of dimers and oligomers, drop drastically and at [MB] > 5mM remain relatively constant. This suggests that at very high MB solution concentrations, a dimer/oligomer saturation threshold exists, after which no more solution aggregation occurs. This would account for the constant k^0 values at [MB] > 5mM.

3.4 Variation of Surface Adsorption with Concentration

Analysis of the solution electrochemistry of MB over a range of scan rates and concentrations suggest quasi-reversibility, when CV was employed, but reversibility was observed at a glassy carbon RDE. We ascribe this discrepancy to adsorption of MB at the bare stationary electrode and have undertaken a quantitative analysis of this phenomenon using cyclic voltammetry.

Integration of the cathodic peaks (C_2, Fig. 3.1) at each scan rate, corresponding to the reduction of adsorbed MB, for that scan rate, yields the total amount of charge, Q, under the adsorption peak and is given by [9]

$$Q = Q_0 + A[MB]_\infty \nu^{-1/2} \qquad (3.17)$$

where

$$Q_0 = Q_{ads} + Q_{bgr} + Q_{dl} \qquad (3.18)$$

Q_{ads} denotes the charge due to adsorbed MB, Q_{bgr} is the background charge and Q_{dl} corresponds to the double layer charge. A is a constant dependent on the scan limits but not the scan rates. The adsorption peaks only, e.g. C_2 figure 3.1, were analysed in Q_{ads} quantification, while the solution redox peaks, C_1, were ignored. The plot of Q/C versus the inverse square root of the scan rate $[\upsilon/V\ s^{-1}]^{-1/2}$ was plotted (figure 3.14)

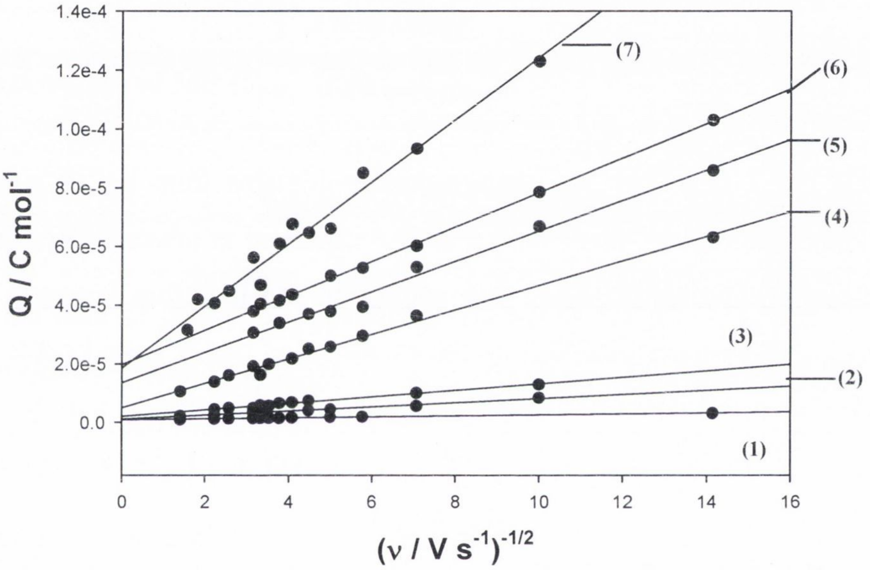

Figure 3.14; Plot of total charge, Q, under the peak for the reduction of MB in 0.1M H_2SO_4 (pH~1) as a function of scan rate, with intercept, Q_0. $10^{-3}[MB]_\infty$ mol L^{-1}: **(1)** 0.1, **(2)** 0.5, **(3)** 1, **(4)** 5, **(5)** 8, **(6)** 12, **(7)** 20.

and linearity was observed for all concentrations analysed. Data was taken from numerous repeated experiments ($5 \leq n \leq 10$ repetition experiments) and averaged. From the intercept of each plot a value for Q_0 was obtained for each concentration of MB examined. From the plot we observe that as each concentration of MB increases so too does the overall charge due to the adsorption species (Q_{ads}). Equation 3.17 predicts a linear relationship between the slopes of each plot in figure 3.14 and $[MB]_\infty$, yielding a value for the constant. From our plot in figure 3.15 the value obtained for the constant, A, was 7.84±0.4 x 10^{-4} C L mol^{-2} $V^{1/2}$ $s^{-1/2}$, where all the symbols have their usual meanings.

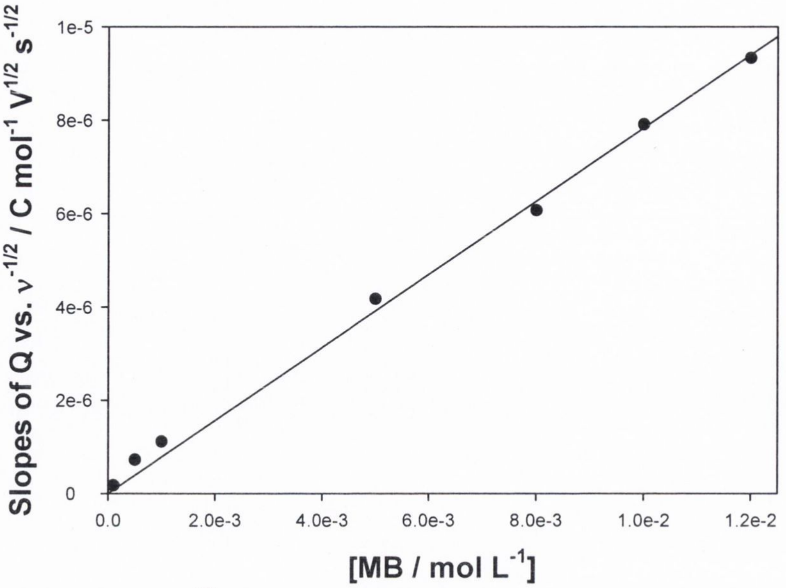

Figure 3.15; Slopes of Q vs. $\nu^{-1/2}$ plots versus bulk concentration for the evaluation of the constant, A, in equation 3.3.1.

At $[MB]_\infty > 1.2 \times 10^{-2}$ M, the proportionality deviates from linearity due to gross solution aggregation, and some scatter is also observed at lower $[MB]_\infty$. It was found that the background charge, Q_{bgr}, was negligible and therefore ignored. The double layer charge, Q_{dl}, was estimated from the examination of CV experiments recorded in 0.1 M H_2SO_4 in the absence of MB at the same glassy carbon electrode. The current variation with sweep rate in the double layer region of the voltammogram was examined, and is presented graphically in figure 3.16.

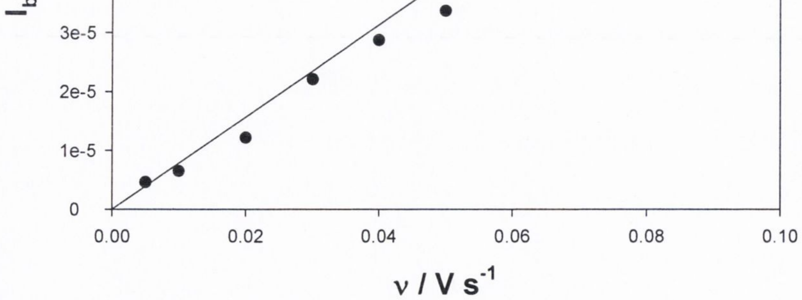

Figure 3.16; Background current recorded in 0.1 M H_2SO_4 in the absence of MB, over a range of scan rates. Peak currents were taken at the potential, $E = 1\times10^{-3}$V.

The slope of this graph corresponds to the double layer capacitance (C_{dl} / farads). Q_{dl} was then calculated from

$$Q_{dl} = C_{dl} \times E \qquad (3.19)$$

where E is the voltage ($1\text{x}10^{-3}$V) at which the peak currents were recorded. The slope obtained was $7.824\text{x}10^{-4}\text{AV}^{-1}\text{s}$, and hence, Q_{dl} was calculated to be $7.825\text{x}10^{-7}$C. Then Q_{ads} is obtained from

$$Q_{ads} = Q_0 - Q_{dl} \qquad (3.20)$$

and surface coverage of MB (Γ_{MB}) from

$$\Gamma_{MB} = Q_{ads} / nFA \qquad (3.21)$$

where n is the number of electrons in MB_{ads} redox behaviour, F is Faradays constant and A is the electrode area (0.0707cm^2).

For an adsorbed monolayer of MB, it is possible to calculate the hypothetical surface coverage, Γ_M, and charge, Q_M, from the area occupied by each molecule [10], assuming various orientations of MB cations in the adsorbed layer [11]. These calculations are outlined in table 3.3. The area occupied value for the flat dimer is per molecule of MB and so, although confusing, it is valid.

Possible MB Cation Orientation	**Area per Molecule / nm^2**	**10^{-10} Γ_M / mol cm^{-2}**	**Layer thickness / Nm**	**Q_M / µC cm^{-2}**
Flat monomer	1.30	1.28	0.325	24.7
Condensed layer	1.08	1.54	0.325	29.7
Flat dimer	0.65	2.56	0.65	49.4
Perpendicular monomer "edge on"	0.55	3.02	0.76	58.2

Table 3.3; Hypothetical charge and surface coverage values calculated when a monolayer of MB adsorbs via four different orientations. Taken from reference [11].

It has been reported that MB adsorbs as a dimer at some interfaces [12,13], a bilayer of MB was reported on mercury [14], and a monolayer made up of dimers has also been optically detected [15]. The scope for possible adsorption orientations and the type of MB species involved, therefore, is quite large. The average surface coverages due to adsorption, Γ_{MB}, calculated for each MB concentration, are summarised in table 3.4.

Concentration MB / mol L^{-1}	**Adsorption Charge (Qads) / C**	**Average Surface Coverage (Γ_{MB}) / mol cm^{-2}**
$1x10^{-4}$	$1.21x10^{-8}$	$8.84\pm0.12x10^{-12}$
$5x10^{-4}$	$6.61x10^{-7}$	$4.85\pm0.75x10^{-11}$
$1x10^{-3}$	$1.42x10^{-6}$	$1.04\pm0.15x10^{-10}$
$5x10^{-3}$	$7.30x10^{-6}$	$5.35\pm0.80x10^{-10}$
$8x10^{-3}$	$1.27x10^{-5}$	$9.34\pm1.4x10^{-10}$
$1.0x10^{-2}$	$1.50x10^{-5}$	$1.10\pm0.17x10^{-9}$
$1.2x10^{-2}$	$1.82x10^{-5}$	$1.33\pm0.20x10^{-9}$
$1.5x10^{-2}$	$2.00x10^{-5}$	$1.47\pm0.23x10^{-9}$
$1.8x10^{-2}$	$2.02x10^{-5}$	$1.48\pm0.22x10^{-9}$
$2.0x10^{-2}$	$2.05x10^{-5}$	$1.51\pm0.23x10^{-9}$

Table 3.4; Average values calculated for adsorption charge, Q_{ads}, and surface coverage, Γ_{MB}, for each $[MB]_\infty$ investigated.

We observe that the value obtained for Γ_{MB} at a 2 x 10^{-2} mol L^{-1} concentration of MB is five times greater than the largest value for a monolayer in table 3.3. From this it can be concluded that a multilayer is formed rather than a monolayer. We can define the fraction of surface coverage as $\theta = \Gamma_{MB}/\Gamma_M$ [16]. Certain assumptions can be made about the orientation of adsorbed MB molecules when monomer fraction, f, is taken into account. For example when f = 0.045, as it is for 2 x 10^{-2} mol L^{-1} MB, then we can assume that there is a good possibility that MB adsorbs as a flat dimer. If this were the case then $\Gamma_M = 2.56x10^{-10}$ mol cm^{-2} and, $\theta = 1.51x10^{-9}/2.56x10^{-10} = 5.9$. On the other hand, if MB was adsorbed as a flat monomer, then Γ_M is $1.28x10^{-10}$ mol cm^{-2} and $\theta = 11.8$. Hence we can assume that θ is in the region $5.9 \leq \theta \leq 11.8$ under the conditions studied.

For the most dilute solution of MB studied, $1x10^{-4}$ M, monomer fraction is 0.47, so possible adsorption species can equally be either monomer or dimer. For flat monomer adsorption, $\theta = 0.07$, for 'edge on' perpendicular adsorption, $\theta = 0.03$, and for flat dimer adsorption, $\theta = 0.035$. θ, then, is in the region $0.03 \leq \theta \leq 0.07$.

In general, adsorption on electrode surfaces is non-uniform in that the surface is not saturated with adsorption molecules. To account for this lack of saturation Langmuir [17] proposed the theory that the species on the surface forms a non-uniform film, that is, certain areas or patches are more densely covered than others. Instead of being covered with a single film, surfaces consist of numerous patches of varying sizes. The problem of quantifying surface adsorbed species was simplified by postulating a surface which is divided up into a large number of squares arranged in a checkerboard fashion. In this theory the black squares are adsorption sites, while the white squares are sites where adsorption does not occur. The likelihood of adsorption is greatest in the centres of the black squares, and conversely, adsorption is least likely at the centres of the white squares. In other words the black squares will have a hill of charge complimentary to adsorption and the white squares will have a valley. This simple theory accounts very well for experimental observation. It is interesting to note that the Langmuir isotherm is analogous to the Michaelis-Menten equation for enzyme kinetics, where the enzyme containing sites behave like black adsorption squares and non-enzyme sites are analogous to the white non-adsorption squares.

The variation of the surface coverage with bulk concentration of adsorbed species in solution is called an adsorption isotherm. One such model is the Langmuir adsorption isotherm, which is valid for low fraction surface coverages, that is, $\theta \leq 1$. The Langmuir adsorption isotherm is given by [16]:

$$\theta = \frac{K[MB]_{\infty}}{(1 + K[MB]_{\infty})} \tag{3.22}$$

where K is the equilibrium constant at low concentrations. The Langmuir adsorption isotherm is derived in the Appendix. The Langmuir isotherm can be linearised to give the following form:

$$\frac{1}{\Gamma_{MB}} = \frac{1}{\Gamma_{M}} + \frac{1}{K\Gamma_{M}[MB]_{\infty}} \tag{3.23}$$

The Langmuir isotherm is valid for values of $\theta \leq 1$ and so is only applicable to $[MB]_\infty \leq 1x10^{-3}$ mol L^{-1} in this body of research. Even so, an adsorption isotherm was constructed for all bulk concentrations of MB studied and is shown in figure 3.17. The curve shape is similar to that of the Langmuir isotherm model and values for the maximum monolayer surface coverage, Γ_M, and equilibrium constant, K, were quantified.

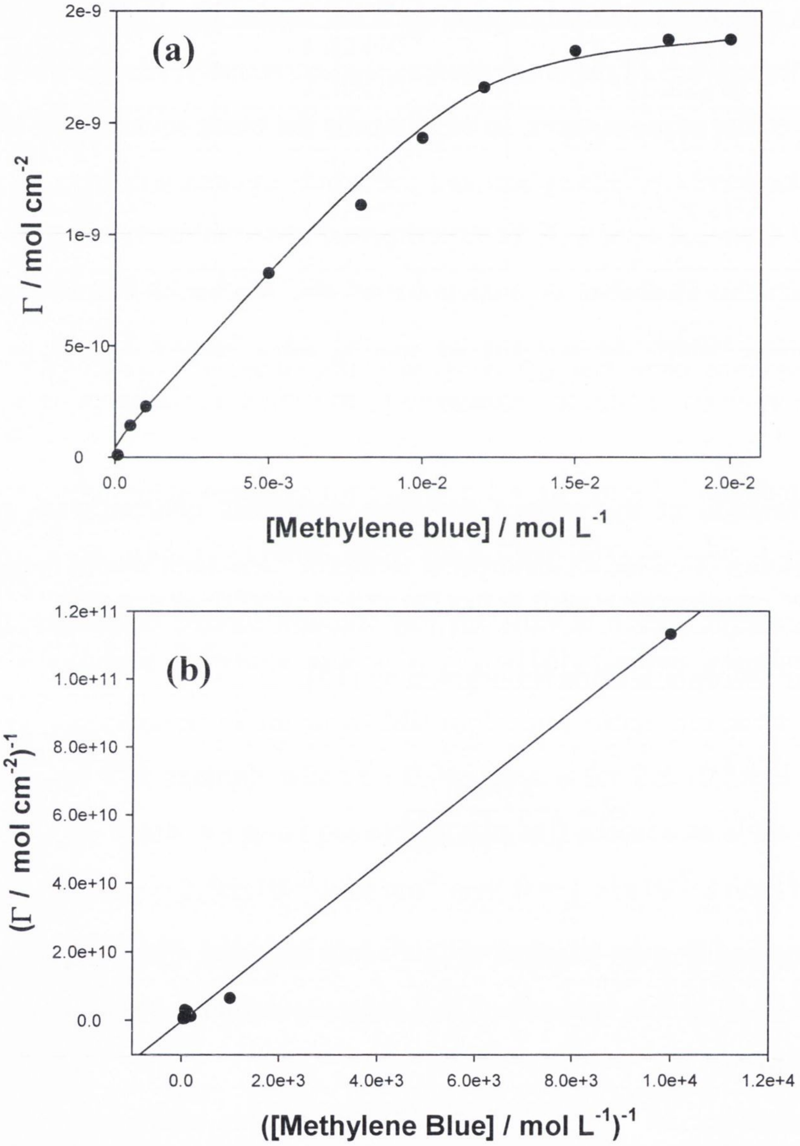

Figure 3.17; (a) Adsorption isotherm constructed for a range of $[MB]_\infty$. **(b)** Plot of equation 3.23 to quantify K and Γ_M.

These average surface coverages do construct a nice curve when plotted against [MB], but it must be stressed that there was scatter and some outliers in the individual data calculations. The maximum surface coverage for a monolayer was found to be 4.64 ± 0.95 x 10^{-10} mol cm^{-2} and K found to be 7.3±1.5 x 10^{-3}. The value obtained for K compares to 5 x 10^{-2} found for Thionine [4]. It must be stated that removal of the lowest [MB] leads to a very different slope in the adsorption isotherm, figure 3.17. For this reason, the values calculated should be taken as estimates rather than absolute values. Svetlicic *et al.* [11] used chronocoulommetry to construct a MB isotherm at the dropping mercury electrode. The authors found that a discontinuous change in surface coverage reflects a condensation of the adsorbed layer that can formally be described as a Frumkin adsorption isotherm with a high lateral interaction of LMB molecules [18-20], and absence of lateral interactions between MB cations.

3.5 Polymethylene Blue

As previously described in Chapter 1, organic molecules can be electropolymerised onto electrode surfaces to form conducting and semi-conducting films [21-23]. Methylene blue is one such organic molecule that can undergo electropolymerisation. The applications of polymethylene blue films are many and include enzyme immobilisation [24,25] at the electrode surface, electron transfer mediation [26], electrocatalysis [27], and biosensors [28,29]. The electropolymerisation is complicated and different polymerisation mechanisms have been proposed [30,31,35,36].

3.5.1 Electropolymerisation Process

In this study MB was electropolymerised at a glassy carbon electrode by repeated potential cycling from -0.4V to 1.2V. The charge carried by each film, and hence the surface coverage, was determined by calculating the area under the polymer redox peaks of the films when cycled in a 0.1M phosphate buffer solution. This was performed for films electropolymerised from three different initial concentrations of MB monomer, for a range of growth cycles.

Figure 3.18 shows the cyclic voltammogram of 10 growth cycles PMB onto a GC electrode from a $[MB]_{\infty}$ of 2.5 x 10^{-3} mol L^{-1} M. An irreversible oxidation was observed when the anodic switching potential reached 0.1 V, Region III, and corresponds to electropolymerisation of MB.

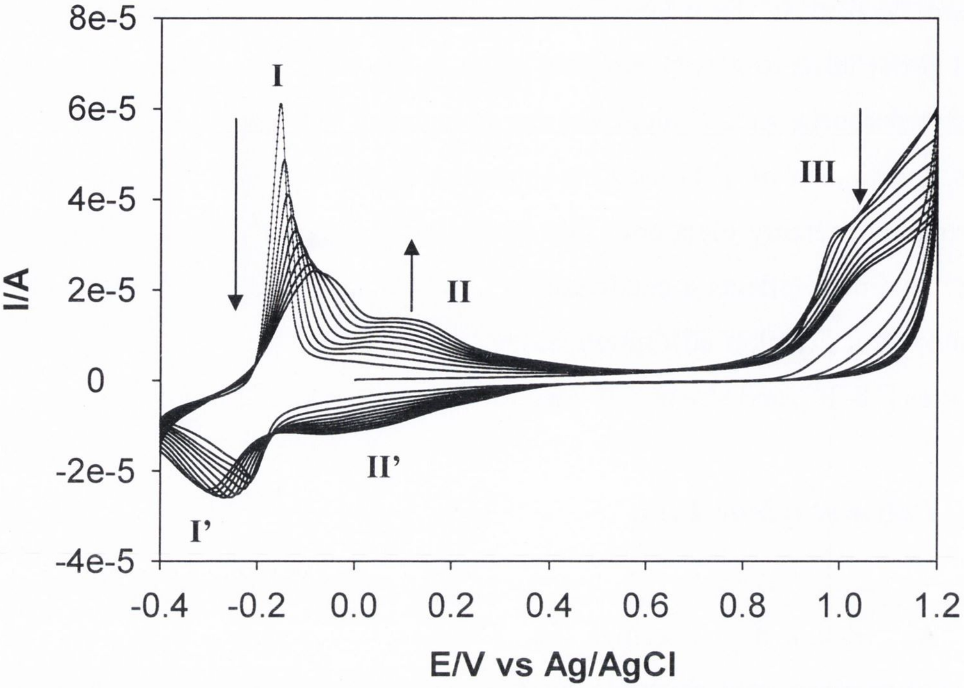

Figure 3.18; Consecutive voltammetric curves are observed during the electrochemical formation of the PMB film at a glassy carbon electrode in the absence of a field. The initial solution was 2.5×10^{-3} mol L^{-1} MB in 0.1 mol L^{-1} phosphate buffer, pH = 7.0. The scan rate was $\nu = 50$ mV/s. Arrows indicate the increasing/decreasing nature of the peaks after each successive scan.

Repetitive cycling from -0.4V to 1.2V forms the polymer film. Peaks (I) and (I') correspond to the oxidation and reduction, respectively, of monomeric MB, while peaks (II) and (II') correspond to the redox activity of the polymer film. The conducting properties of the film can be identified from the upward extension of region II. The electrode surface was covered in a green-blue film layer on inspection. We concur that these parameters, i.e. concentration and scan rate, are optimum conditions for PMB film growth [26].

The electropolymerisation process is complicated with general disagreement in the mechanism of polymerisation [30,31,35,36]. The authors Lyons *et al.* [30] investigated the mechanism of polymethylene blue formation and the general redox properties of the polymer at a glassy carbon working electrode in 0.1M phosphate buffer, pH 6.72. From an examination of the voltammetric response of the modified electrode in solutions of varying pH, a detailed mechanism for film formation and redox behaviour was proposed. The redox process within the polymer film was assumed to be reversible. They then applied the Nernst equation predicting that the modified electrode potential (for a known ratio of species in oxidised and reduced states) should vary linearly with the solution pH. The slope of this plot gave the ratio of electrons to protons for the redox process.

The authors proposed that at pH 6.72, electropolymerisation occurred via the coupling of oxidatively formed radical cations of monomeric MB (scheme 3.3). This results in the carbon-carbon coupling producing the dimeric species. This process can be continued resulting in the eventual formation of an insoluble oligomers coating the GC electrode. This proposed mechanism seems plausible as the electroactive heterocyclic nitrogen atoms are retained, thus the film retains its redox activity when deposited. The redox behaviour of the dimeric species at pH 6.72 was reported to be a 4e$^-$, 2H$^+$ process (Scheme 3.4).

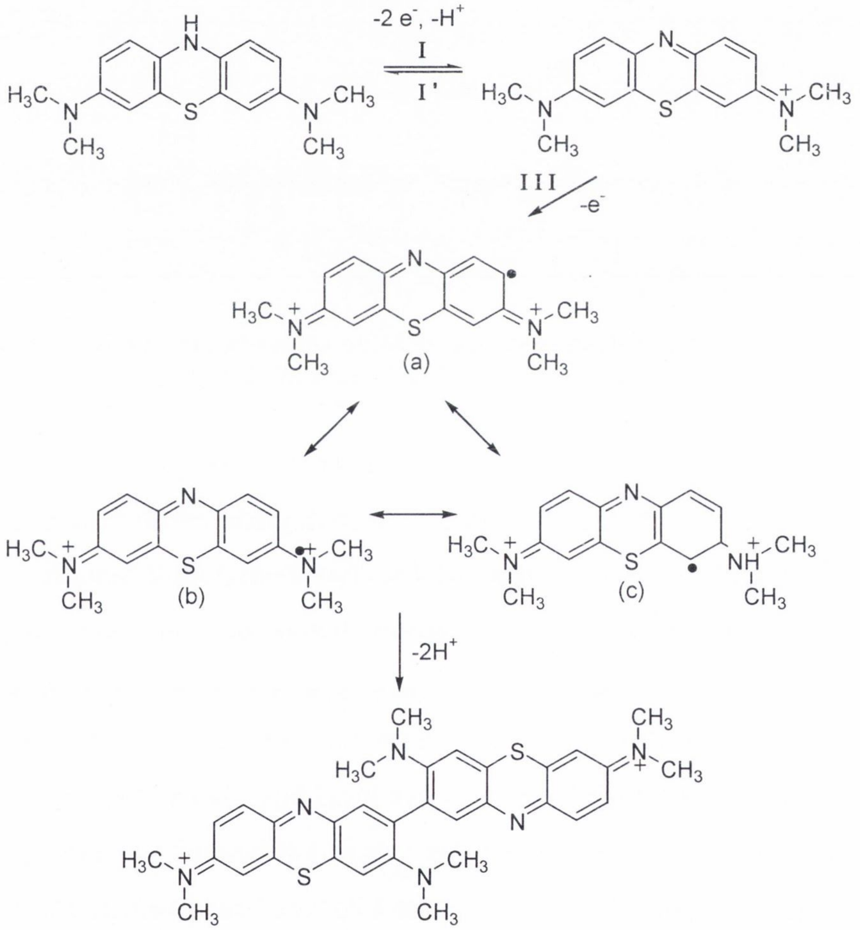

Scheme 3.3; Mechanism of electropolymerisation proposed by Lyons and co-workers [28]. GC electrode, 0.1M phosphate buffer pH 6.72.

This is quite different than the accepted 2e$^-$, H$^+$ redox process but it must be stated that the authors did not observe two distinct redox couples but just a single broad peak, when the modified electrode was cycled in the 0.1M phosphate buffer. It is likely then that the redox behaviour for both couples, in 0.1M phosphate buffer pH 6.72, is described by the $4e^-$, $2H^+$ stoichiometry. Also the assumption that the redox behaviour is reversible is not true, so application of the Nernst equation is not strictly valid.

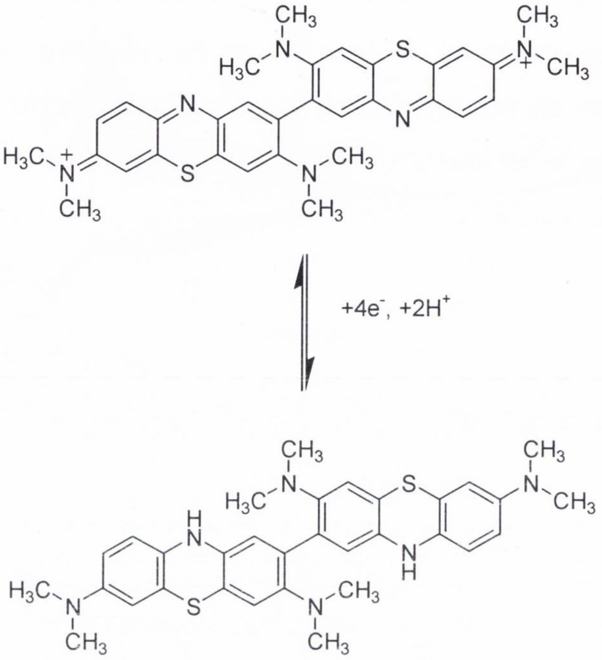

Scheme 3.4; Redox behaviour of the MB modified GC electrode in 0.1M phosphate buffer pH 6.72.

In a paper by the authors Liu *et al.* [31], a different electropolymerisation mechanism (scheme 3.5) was proposed. A methylene blue solution in sodium tetraborate, pH 9.19, was cycled from -0.4 to 1.10V at a GC electrode. The authors compared Raman spectra of solution phase methylene blue and polymethylene blue. Two main peaks at 1628 and 1392 cm^{-1} were present in both spectra. The peak at 1628 cm^{-1} was attributed to phenyl ring stretching vibration. The peak at 1392 cm^{-1} was attributed to the bending vibration of $N-CH_3$ [32], or $N=(CH_3)_2$ in methylene blue [33] because the wavenumber was less than 1400 cm^{-1}. A new peak in the polymethylene blue spectra was observed at 1429 cm^{-1} and attributed to $-N(CH_3)_2$ in polymethylene blue - evidence that the ring was not opened after polymerisation. The authors compared this to the oxidation of phenothiazine which does not have $-N(CH_3)_2$ groups and only forms dimers [34]. Hence, they proposed that electropolymerisation must occur through nitrogen-nitrogen coupling, i.e., via the –

$N(CH_3)_2$ group. In scheme 3.5, the electroactive nitrogen atoms are present so the polymer has the redox sites required for electroactivity.

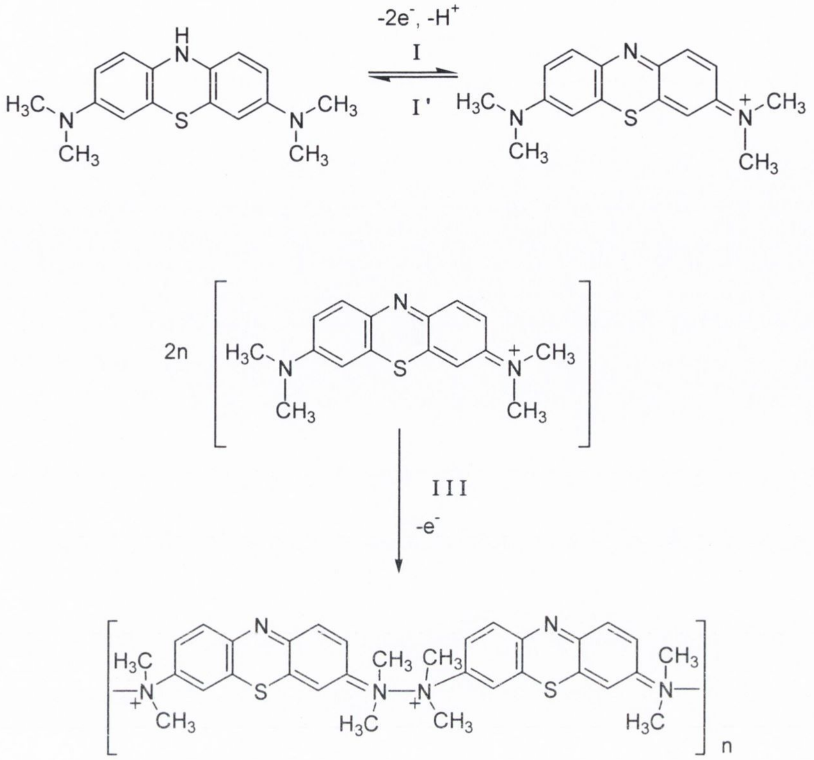

Scheme 3.5; The N-N coupling scheme proposed for electropolymerisation of MB at a GC electrode in 0.5M sodium tetraborate pH 9.19.

Karyakin *et al.* [35] proposed a mixed ring-ring and nitrogen-nitrogen coupling shown in scheme 3.6. The authors, using CV, Visible and IR spectroscopy, investigated the electropolymerisation of different azines, which differ due to the absence/presence of primary, secondary and tertiary amine groups, at GC electrodes in 0.05M phosphate buffers of varying pH. Direct spectroelectrochemical indication of the polymerisation mechanism was not evident, but differences observed for each polyazine allowed a logical hypothesis for the process. Differences in the IR spectra between each monomeric species and corresponding polymer alluded to a changing of the substituents of the aromatic rings in the azine molecules. This, in turn, suggests that the electropolymerisation results in a polymer chain formed by azine molecules.

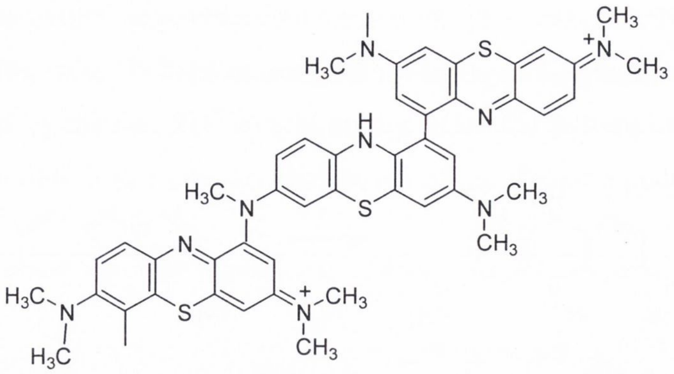

Scheme 3.6; Proposed structure of polymethylene blue at a GC electrode in 0.05M phosphate buffer pH > 6.

When the polymer was oxidised by more than 50%, its redox activity was shifted to more positive values with respect to the monomer. In Visible spectra of the oxidised polymer, the authors observed additional electron acceptor ring substituents. Conversely, the reduced form of the polymer (> 50%) had a redox behaviour at similar negative potentials to the monomer. From this they concluded that at least one of the neighbours of the monomer unit is positively charged in the oxidised state, and behaves as an electron acceptor which causing the observed potential shift.

The authors Kertesz and Van Berkel [36] proposed a third electropolymerisation mechanism. The authors used electrochemistry/electrospray mass spectrometry to elucidate mass-to-charge ratios (m/z) for dimeric and trimeric coupling of MB monomers. The authors report that "nitrogen-to-ring" coupling dominates MB polymerisation. The mass spectra also revealed the presence of demethylated "nitrogen-to-ring" and/or Azure B "ring-to-ring" coupling. The structures of the postulated dimers and trimers are shown in Scheme 3.7. The Azure B monomer results from the demethylation of MB and is denoted **1b** in Scheme 3.7.

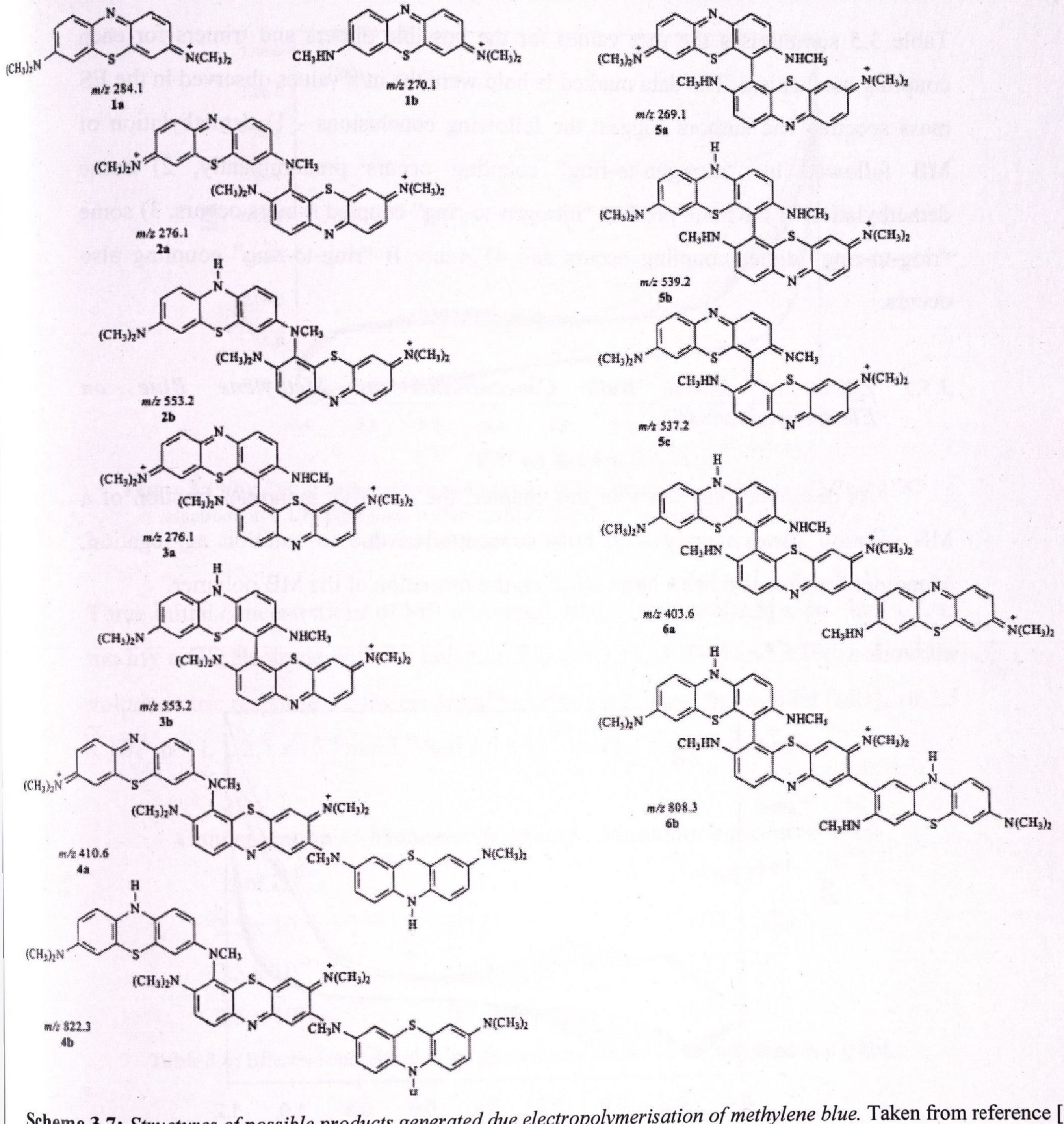

Scheme 3.7; *Structures of possible products generated due electropolymerisation of methylene blue.* Taken from reference [36].

Monomer units [n]	*Charge state*	*MB "ring-to-ring" [m/z]*	*MB "N-to-N" [m/z]*	*MB "N-to-ring" [m/z]*	*MB+Azure B "ring-to-ring" [m/z]*	*Azure B "ring-to-ring" [m/z]*
2	+1	567.2	**539.2**	**553.2**	**553.2**	**537.2/539.2**
2	+2	283.1	**269.1**	**276.1**	**276.1**	**269.1**
3	+1	850.3	794.3	**822.2**	N/A	**808.3**
3	+2	424.6	396.6	**410.6**	N/A	**403.6**

Table 3.5; *Calculated m/z values for the possible dimers and trimers of MB with different charge-state and coupling sites. The m/z values that were observed in the ES spectrum are marked in* ***bold.*** Taken from reference [36].

Table 3.5 summarises the m/z values for the possible dimers and trimers for each coupling mechanism. The data marked in bold were the m/z values observed in the ES mass spectra. The authors suggest the following conclusions - 1) demethylation of MB followed by "nitrogen-to-ring" coupling occurs predominantly, 2) some demethylation of the main product "nitrogen-to-ring" coupled *n*-mers occurs, 3) some "ring-to-ring" dimer coupling occurs and 4) Azure B "ring-to-ring" coupling also occurs.

3.5.2 Effect of Initial Bulk Concentration of Methylene Blue on Electropolymerisation

As described previously in this chapter, the effective monomer fraction of a MB solution varies hugely with bulk concentration due to solution aggregation. Monomer fraction also has a large effect on the formation of the MB polymer.

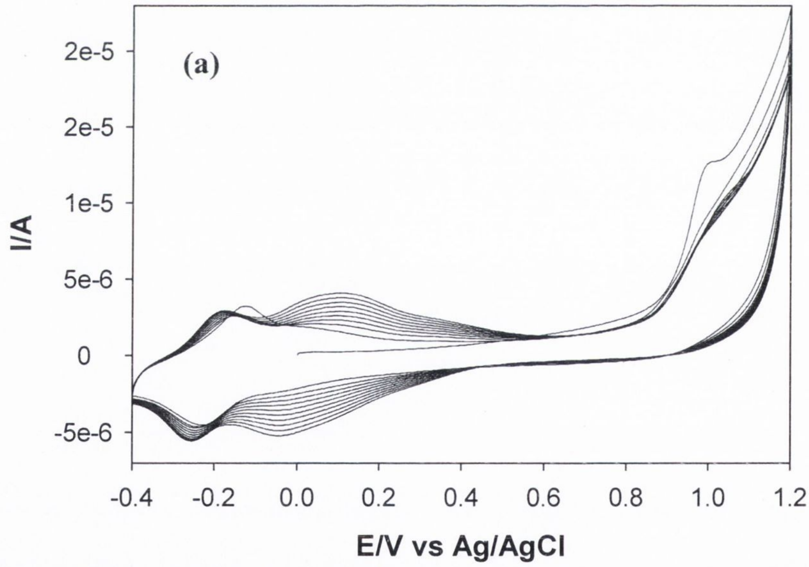

Figure 3.19(a); Ten growth cycle voltammograms of the electropolymerisation of MB at a GC electrode in 0.1 M phosphate buffer, 0.1M KCl, pH = 7. Scan rate was $\nu = 50$ mV s^{-1}. Initial $[MB]_\infty$ was 2.5×10^{-4} mol L^{-1}.

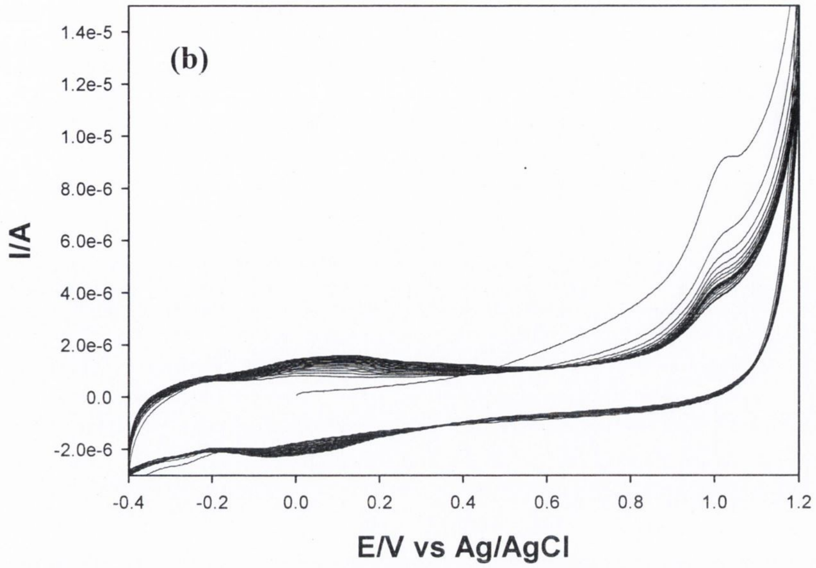

Figure 3.19(b); Ten growth cycle voltammograms of the electropolymerisation of MB at a GC electrode in 0.1 M phosphate buffer, 0.1M KCl, pH = 7. Scan rate was $\nu = 50$ mV s^{-1}. Initial $[MB]_\infty$ was 2.5×10^{-5} mol L^{-1}.

Three initial concentrations of MB were used, [0.025, 0.25 and 2.5] x 10^{-3} mol L^{-1}, to modify a GC electrode with the polymer. Figures 3.18, 3.19(a) and 3.19(b), show the voltammetric response for the electropolymerisation process from initial $[MB]_\infty$ of 2.5 x 10^{-3} mol L^{-1}, 2.5 x 10^{-4} mol L^{-1} and 2.5 x 10^{-5} mol L^{-1} respectively.

Concentration / mol L^{-1}	**Monomer fraction / f**	**Monomer concentration / Mol L^{-1}**
2.5 x 10^{-3}	0.121	3.03 x 10^{-4}
2.5 x 10^{-4}	0.333	8.33 x 10^{-5}
2.5 x 10^{-5}	0.703	1.76 x 10^{-5}

Table 3.6; Effective concentration of MB monomer calculated for different initial $[MB]_\infty$.

Table 3.6 gives a summary of the monomer concentration for each initial $[MB]_\infty$ investigated. The currents generated due to the activity of the monomeric redox couple decreased dramatically with initial $[MB]_\infty$ as expected and generally the profiles were less well defined. Another feature to note is the thinning of Region II. We observe a pronounced 'growth' in Region II in figure 3.18 after each deposition cycle due to greater amounts of polymer being present on the electrode. This increasing charge after each cycle is smaller for more dilute solutions, so in figures

3.19{a}, {b} Region II is not as pronounced. The MB monomer is a cation in pH 7 and so forms ion-pairs with anions in the solution. The anions present are phosphate, HPO_4^-, and chloride Cl^- and may act as spacers for in the developing polymer matrix. As the concentration of MB monomer increased, the amount of ion-pairs should also increase. Consequently the polymer is less compact on formation when polymerized from a higher initial $[MB]_{\infty}$. This allows for more facile diffusion of electrolyte/solvent through the film contributing to the greater charge carrying capacity.

3.5.3 Variation of Peaks I, I' Potentials with Deposition Cycle

Another feature of the voltammogram in figure 3.18 is the variation of the redox peak potentials of the monomeric species with the deposition cycle. The MB reduction peak, I, is shifted more anodically with each deposition cycle. The corresponding oxidation peak potential of LMB, I', is also subject to similar kinetic constraints as illustrated in figure 3.20.

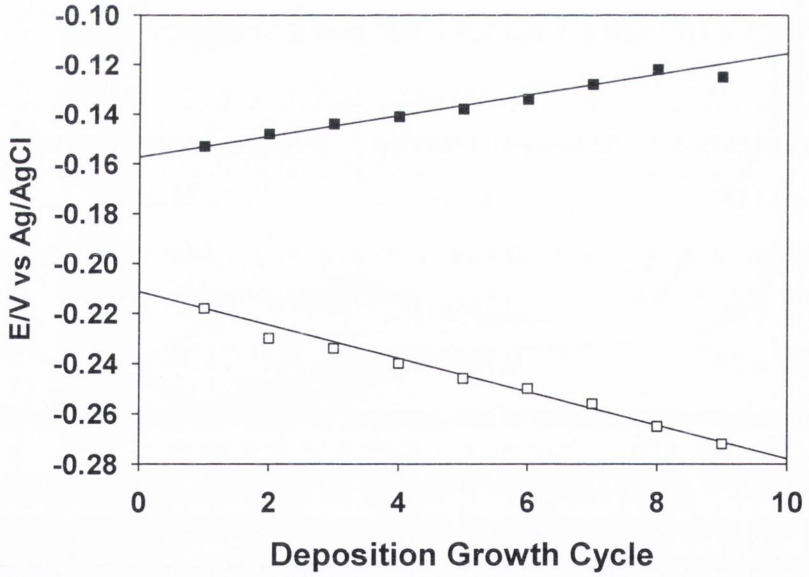

Figure 3.20; Variation of the monomeric peak potentials as a function of polymer deposition cycle in 0.1M phosphate buffer solution, pH~7. Open squares represent peak I, while closed squares correspond to peak I' potentials. Data taken from figure 3.18.

As the polymer film is formed and the electrode is coated, the kinetics for the redox behaviour of the monomer species become more sluggish. Interestingly, after the first ten deposition cycles, the redox peak potentials remain relatively constant. This is observed in the variation of peak separation with the polymer deposition cycle, shown graphically in figure 3.21.

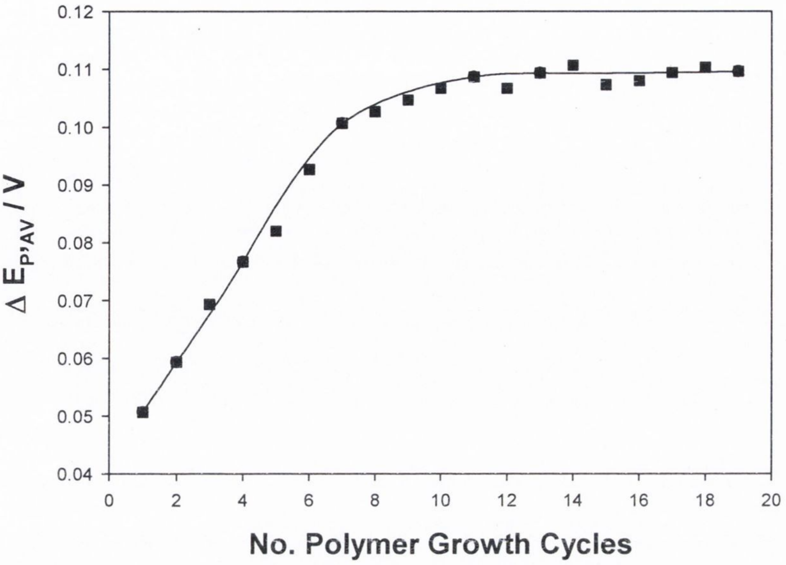

Figure 3.21; Variation of average ΔEp for the redox activity of the monomer species (peaks I&I') as a function of polymer deposition cycle. Data taken from 20 Cycle growth polymer, L = 6.1±0.6 x 10^{-8} cm, in a 0.1M phosphate buffer solution, pH~7.

3.6 Redox behaviour of the PMB/GC Electrodes in 0.1M Phosphate Buffer, pH 7

The electrochemical activity of the films was investigated by cycling the film modified electrodes in 0.1 M phosphate buffer, 0.1M KCL, pH~7. Phosphate buffer was chosen because it is a source of H^+ ions required for the electroneutrality process. Two redox couples were observed for each film as shown in figure 3.22. The couple at the negative potentials (I & I') corresponds to the monomer redox activity while the second redox couple (II & II') is the activity of the PMB film. The charge carried by each film was determined by calculating the area of the polymer redox peaks in the voltammograms of the films in the buffer solution. These present results agree quite well with the more prominent literature findings [28,29,37].

Figure 3.22 shows the voltammograms of a PMB/GC electrode cycled twice in the buffer solution. The two runs map each other closely which is indicative of a stable film with reproducible redox activity.

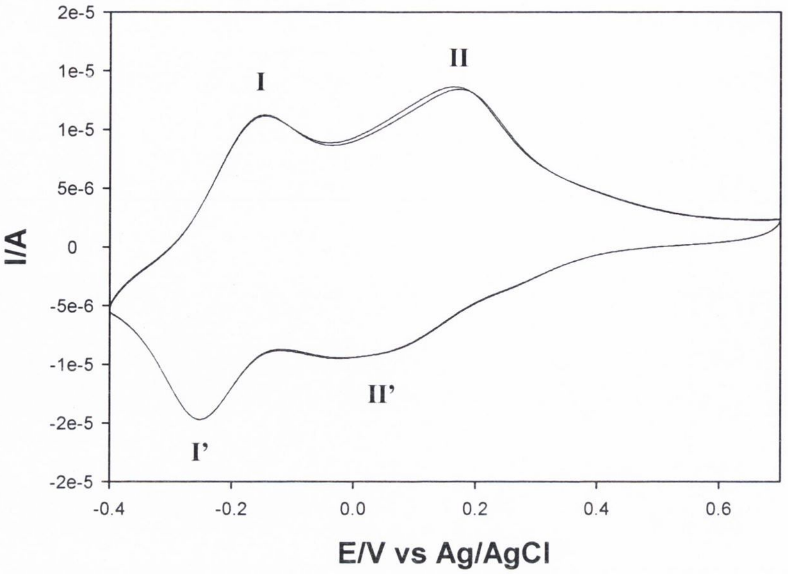

Figure 3.22; Two successive cyclic voltammograms of a glassy carbon electrode modified with a PMB, L = 5.8±2.5 x 10^{-8} cm, in 0.1 mol L^{-1} phosphate buffer, pH = 7.0. The scan rate was ν = 50 mV/s.

Karyakin *et al.* [25] suggest two tentative explanations for the presence of the monomer species, the first being that some MB monomer is absorbed by the polymer during polymerisation. The second, they suggest (and think more plausible), is that there is some monomer-type conjugation present in the MB polymer.

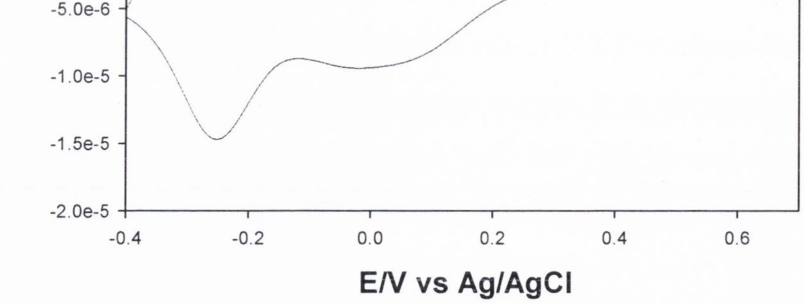

Figure 3.23; Cyclic voltammograms of 10 growth cycle PMB-GC electrodes in 0.1 M phosphate buffer, pH = 7. Initial bulk $[MB]_\infty$ was 2.5x10^{-3}(···), 2.5x10^{-4}(– –), and 2.5x10^{-5} (—) mol L^{-1}. Scan rates were ν = 50mV s^{-1}, L = 4.6±1.2 x 10^{-9} cm.

This feature is more evident when the PMB-GC electrodes are cycled in 0.1M phosphate buffer containing no MB, figure 3.23. The difference in charge passing through each polymer is quite large, highlighting the effect of initial $[MB]_\infty$ on film formation.

3.6.1 Effect of Number of Polymer Growth Cycles on Polymer Charge

The amount of polymer deposited onto the GC surface, i.e. thickness, is governed by the number of potential sweeps or polymer 'growth' cycles. Figure 3.24 shows four polymers of different potential deposition cycles. The charge carried by each polymer visibly increases with the number of deposition cycles. The redox kinetics become increasingly sluggish with increasing polymer thickness and is evident in anodic shifts in oxidation peak potentials, and in cathodic shifts for the reductive processes.

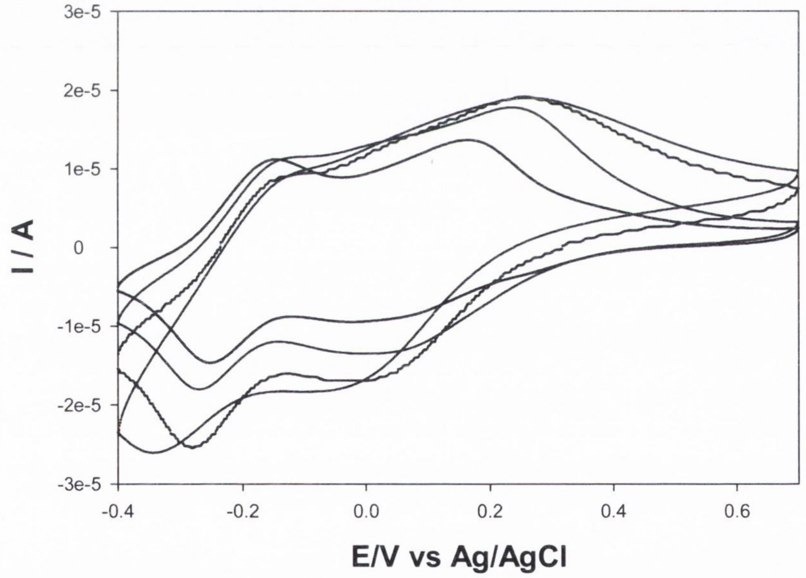

Figure 3.24; Voltammograms of the redox activity of modified GC formed with different polymer deposition cycles from an initial $[MB]_\infty = 2.5\text{x}10^{-3}$ mol L^{-1}. Number of deposition cycles; 10(—), 20(—), 40(—), and 80(—). Data used from scans performed in 0.1M PBS at $\nu = 50\text{mV s}^{-1}$.

The charge carried by the polymers was calculated by integration under the peaks of Region II, the area of interest. Two methods were used to quantify this charge, (1) automatic integration – CH Instrument, and (2), the 'Cut and Weigh' method. The values determined were very consistent with each other for each set of polymers studied. An average value for charge was then plotted against the number of polymer cycles as in figure 3.25.

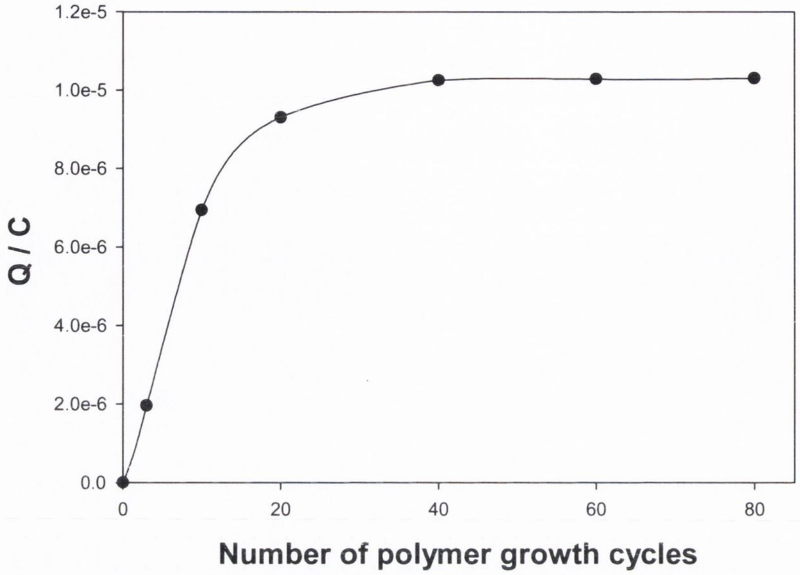

Figure 3.25; The variation of charge carried by the polymers with the number of potential growth cycles. Initial $[MB]_\infty = 2.5\text{x}10^{-3}$ mol L^{-1}. Data used from scans performed at $\nu = 50\text{mV s}^{-1}$.

We observe a dramatic increase of charge carried by the polymer from 3 to 20 growth cycles. The 40 growth cycle polymer carries the maximum charge for this initial $[MB]_\infty$ polymer, thereafter the charge remains constant. The movement of counter-ions through the polymer matrix reaches a threshold value at these particular conditions and becomes the limiting factor in polymer charge transport. If the film does not maintain local electroneutrality, then charge propagation is inhibited. Although the maximum charge is carried by the 40 growth cycle polymer, the 20 growth cycle polymer was used for sensor research due to more facile analyte diffusion through the polymer layer matrix.

3.7 Charge Transfer in Redox Polymers

It has been well established that the oxidation and reduction of spatially distributed redox centres in polymeric films is accompanied by electron and ion transport through the layer [38,39]. Two of the more pertinent charge transport diffusion models have been described by Albery and Saveant [40,41]. Charge transport in a redox polymer film can be described by Ficks law of diffusion as previously described in Chapter 2

$$\partial C/\partial t = D\left(\partial^2 C/\partial x^2\right) \tag{3.24}$$

where C is the concentration of redox sites and D, the charge transfer diffusion coefficient which provides a measure of the facility of electron or ion transport through the layer. If the scan rate is sufficiently low, for a layer of finite thickness, then the redox centres in the layer will be reduced or oxidised by the time the extremity of the perturbation potential scan is reached. The amount of charge required to change the oxidation state of the layer is independent of the scan rate and hence a linear dependence of peak current with scan rate is observed (finite behaviour). As the sweep rate increases, the fraction of the redox centres in the layer reacting in response to the applied potential declines as a result of the altering balance between the facility of the charge transfer kinetics and the length of the experimental timescale. Therefore, as the scan rate increases, at some experimental timescale, the peak current versus the square root of the scan rate will not continue to vary in a linear manner. This is termed semi-infinite behaviour. When the peak current is determined over a wide range of scan rates, a transition should be seen from finite diffusion at low scan rates to semi-infinite diffusion at high scan rates. Three types of behaviour can be found, ranging from (A) semi-infinite linear diffusion, to (B) the mixed case, to (C) the finite case.

Cyclic voltammetry can also be used to obtain qualitative information about the redox process in a PMB film. The efficiency of charge percolation through a polymer film is quantified in terms of the charge transport diffusional coefficient, D_{CT}. The general subscript CT indicates that it is the diffusion coefficient for the overall charge transport process and no particular rate limiting mechanism is implied. The authors Aoki *et al.* [42,43] have presented a diffusion model to describe the process of charge transport through a layer of finite thickness. From this model a value for the charge transport, D_{CT}, within the polymer film can be estimated. There are some inaccuracies and assumptions associated with this model discussed further on.

Consider an oxidation process

$$A \Leftrightarrow B + ne^{-} \tag{3.25}$$

with transposition to a reduction species being immediate. The boundary value problem may be stated as follows:

$$\frac{\partial a}{\partial t} = D\frac{\partial^2 a}{\partial x^2} \tag{3.26}$$

$$\frac{\partial b}{\partial t} = D\frac{\partial^2 b}{\partial x^2} \tag{3.27}$$

assuming $D_a = D_b$. The initial condition in which only A is present in the layer is

$$a(x,o) = C^* = \Gamma / L \tag{3.28}$$

$$b(x,o) = o \tag{3.29}$$

where Γ is surface coverage (mol cm^{-2}), L is layer thickness (cm) and A has volume concentration (mol cm^{-3}) C*. The boundary condition at the polymer-solution interface is

$$\left(\frac{\partial a}{\partial x}\right) = -\left(\frac{\partial b}{\partial x}\right)_{X=L} = 0 \tag{3.30}$$

This implies that the electroactive species cannot pass through the interface between the film and the solution. The boundary conditions at the electrode-polymer interface are

$$\begin{aligned}\left(\frac{b(o,t)}{a(o,t)}\right) &= \exp\left(\frac{nF(E-E^0}{RT}\right) \\ &= \exp(\xi)\end{aligned} \tag{3.31}$$

where

$$\xi = nF / RT(E - E^0) \qquad (3.32)$$

and E^0 is the formal potential.

The other boundary condition relates the flux and the concentration gradient

$$j = i / nFA = D\left(\frac{\partial a}{\partial x}\right)_{X=0} = -D\left(\frac{\partial b}{\partial x}\right)_{X=0} \qquad (3.33)$$

The boundary value problem is solved using the method of the Laplace Transformation and the non-dimentional variables T and X.

Detailed analysis shows that the current potential relationship is

$$i = \left(\frac{n^3 F^3}{RT}\right)^{1/2} A D_{ct}^{1/2} C^* \nu^{1/2} f(\omega, \xi) \qquad (3.34)$$

where

$$f(\omega, \xi) = \omega^{1/2} \int_0^\infty \Theta_2(0/\lambda) \frac{e^{\omega\lambda - \xi(t)}}{1 + e^{\omega\lambda - \xi(t)}} d\lambda \qquad (3.35)$$

Equation 3.35 cannot be evaluated analytically but the integral can be determined using Simpsons Rule. This procedure yields an expression for the peak current variation with scan rate of the form

$$i_p = 0.446 nFA\left(\frac{\Gamma D_{ct}}{L^2}\right) W^{1/2} \tanh Y \qquad (3.36)$$

where

$$W = nFL^2 \nu / D_{ct} RT \qquad (3.37)$$

and

$$Y = 0.56W^{\frac{1}{2}} + 0.05W \tag{3.38}$$

It is also possible to evaluate the scan rate dependence of the peak width at half height $\Delta E_{P/2}$.

$$\Delta E_{P/2} = \frac{RT}{nF}\left\{5.72 + 2.20\tanh(1.38\Psi + 0.4\Psi^3)\right\} \tag{3.39}$$

where

$$P = W^{0.27} - 1.60 \tag{3.40}$$

However, given the broad nature of the peaks obtained for polymethylene blue, the expression for peak current (equation 3.36) was used in preference to equation 3.39 for the diffusion coefficient calculations. It can be shown that the expression outlined in equation 3.36 can yield the correct current-scan rate dependence at low and high values of the latter. For low values of scan rate (small W), tanh Y=Y and equation 3.36 can be written as

$$i_p = 0.446nFA\left(\frac{\Gamma D_{ct}}{L^2}\right)W^{\frac{1}{2}}(0.56W^{\frac{1}{2}} + 0.05W) \tag{3.41}$$

Simplifying and substituting the expression for W into equation 3.41 gives

$$i_p = \frac{n^2F^2A\Gamma}{4RT}\nu + \frac{0.022(nF)^{\frac{5}{3}}A\Gamma L}{(RT)^{\frac{3}{2}}D_{ct}^{\frac{1}{2}}}\nu^{\frac{3}{2}} \tag{3.42}$$

for thin films, the second term on the r.h.s. of equation 3.42 is negligible and consequently one obtains

$$i_P = (n^2 F^2 A\Gamma / 4RT)\nu \qquad (3.43)$$

This is the theoretical expression for a surface Nernstian redox reaction.
On the other hand for large W (i.e. large ν) or thick films

$$\tanh Y \approx 1 \qquad (3.44)$$

and equation 3.36 reduces to

$$i_P = 0.446nFA\left(\frac{\Gamma D_{ct}}{L^2}\right)W^{1/2} \qquad (3.45)$$

or

$$i_P = 0.446\left(\frac{(nF)^{3/2}}{(RT)^{1/2}}\right)AD_{ct}^{1/2}(\Gamma / L)\nu^{1/2} \qquad (3.46)$$

This latter expression is the well known Randles-Sevcik equation characteristic of linear diffusion [44]. The exact regions of validity of the limiting expressions outlined in equations 3.43 and 3.46 are given by

finite diffusion : $\nu < 1.3(RTD_{ct} / nFL^2)$ (3.47)

semi-infinite diffusion : $\nu > 6.9(RTD_{ct} / nFL^2)$ (3.48)

Film thickness can be estimated from the relation L = Γ x V_M [45], where V_M is the molar volume of the methylene blue molecule and is equal to *ca.* 400 cm^3 mol^{-1} [46]. A cautionary note about this estimation of the film thickness is necessary here. Use of the molar volume of an electroactive species to obtain layer thickness is quite widespread in the literature [47]. However, the value of L thus calculated should be considered as no more than rough estimates. This is because the molar volume approximation makes the following assumptions.

1) The redox sites are closely packed.

2) There are no voids in the film due to polymer swelling (swelling ignored).

3) The layer has a uniform thickness.

The degree of swelling in a PMB film with oxidation state has not been reported in the literature to the best of our knowledge.

Another approximation in the Aoki analysis is the quantity c (the concentration of electroactive sites per unit volume) and not a true representation of the actual amount of redox species on the electrode. Such a parameter is the experimentally determined Γ, the surface coverage in moles cm^{-2}. However, in order to insert Γ into the peak current/sweep rate expression, the substitution, $c = \Gamma/L$, must be made. Since L is calculated from essentially the same relationship and not an independent measurement, Γ/L remains a constant value.

The result of this is that no true account of the surface coverage is taken into consideration. The higher the peak current at a particular sweep rate, the larger the value of D_{CT}, irrespective of Γ. Nevertheless, the estimation of D_{CT} by this means can serve a useful purpose. Whatever the inaccuracies of the absolute values of D_{CT}, the orders of magnitude obtained are unlikely to be seriously in error, and so some information about the mechanism of charge transport can be gained. Charge percolation through a redox polymer film involves various processes; charge injection at the polymer/electrode interface, electron hopping, charge-compensating counterion diffusion and possibly limited polymer segmental motion.

The cyclic voltammetric response of the PMB films was examined over a range of scan rates. A plot of equation 3.46 is shown in figure 3.26 and the slope was used to calculate D_{CT}.

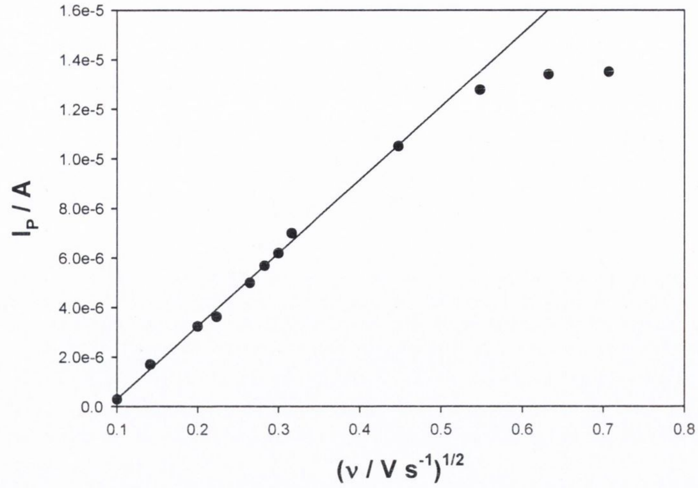

Figure 3.26; Variation of the oxidation peak potential with square root of the scan rate for a PMB/GC electrode, L = $6.92 \pm 1.4 \times 10^{-8}$ cm. The average slope (n=6) was used in eqn. 3.46 to calculate the average charge transfer diffusion coefficient, D_{CT}, for the PMB coated GC electrode. Scan rates 10 – 500mV/s.

For 6 20cycle PMB/GC electrodes, typical shown in figure 3.26, deposited from an initial $[MB]_\infty$ of 2.5×10^{-4} M, the average surface coverage was calculated as $\Gamma = 1.64 \pm 0.4 \times 10^{-10}$ mol cm^{-2}. Therefore the film thickness, L, was $6.56 \pm 1.6 \times 10^{-8}$ cm. In equation 3.46 we can substitute $1/V_M$ for the (Γ/L) term. From this an average diffusion coefficient for charge transport in polymethylene blue was calculated to be 5.38×10^{-14} cm^2 s^{-1}, and any the processes associated with charge percolation through the layer can be rate limiting. This compares to a value of 3.7×10^{-13} cm^2 s^{-1} by Komura and coworkers [48] for a PMB/GC electrode, L = 1.7×10^{-8} cm in a 0.2M NaCl solution, pH 6. A value of 6.5×10^{-13} cm^2 s^{-1} was reported by Albery and co-workers [49] for polythionine modified electrodes in 0.1M HCl, pH 5. Both authors attributed the rate limiting process to counterion motion through the film. The value obtained for the PMB/GC electrodes in 0.1M phosphate buffer may be indicative of a more compact structure of the PMB film in contact with phosphate buffer solutions- the more compact polymer structure hinders motion of the phosphate ions and consequently lowers the charge transport diffusion coefficient. Also, the phosphate counterions are larger than the Cl^- used in [48,49] and so one would expect the diffusion through the polymer matrix to be slower in phosphate buffer. From equations 3.47 and 3.48 we can predict that finite diffusion occurs at scan rates, $\nu < 0.2$ V s^{-1}, while semi-infinite diffusion occurs at scan rates, $\nu > 1.09$ V s^{-1}. From the typical I_p vs $\nu^{1/2}$ plot in figure 3.26 we observe deviation from linearity, at $\nu > 0.2$ V/s$^-$

^{1}. This confirms the limits derived for the finite diffusion but the prediction for semi-infinite diffusion is questionable.

3.7.1 EQCM studies on Film Formation

As described in Chapter 2, EQCM provides a means of monitoring how the formation of the electroactive surface film takes place. For the electropolymerisation process of MB, the film formation on the gold electrode causes the frequency of the oscillating quartz crystal to decrease. This indicates an increase of mass on the gold electrode due to the polymer growth. Figure 3.27 shows the frequency fluctuations during the 10th deposition cycle of film formation. Some of the accompanying frequency changes can also be attributed to the redox behaviour of the film during the polymerisation process.

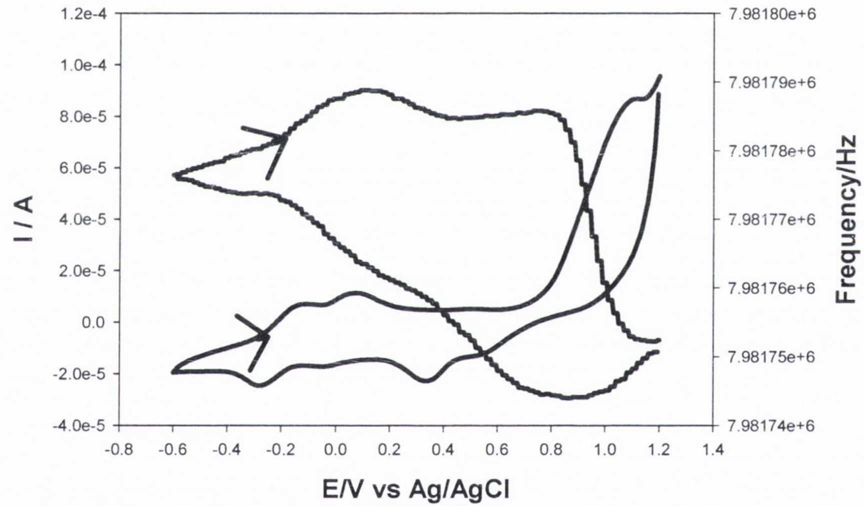

Figure 3.27; EQCM response taken during the 10th electropolymerisation cycle of MB at a gold electrode. Two plots are shown, a cyclic voltammogram and the simultaneous change in oscillation frequency of the crystal. Initial $[MB]_\infty$ was 2.5×10^{-4} M in 0.1M phosphate buffer (pH 7) + 0.1M KCl. Scan rate = 50mV s^{-1}. Initial scan potential is anodic (arrows).

The presence of a new peak on the reduction sweep of the cyclic voltammogram, absent at the GC electrode, is observed at *ca.* +0.35V and corresponds to the reduction of gold surface oxides [28]. This peak shifts cathodically as the polymer is formed which indicates a catalytic effect exerted by the film on surface oxide reduction. The essential feature to note is at the potential of ca. +1.1V, the irreversible oxidation of the MB monomer occurs to initiate film formation. The frequency response corresponding to this irreversible oxidation is prominent; the sharp decrease indicates that a significant gain in mass has accrued on the electrode surface. As film formation progresses, the related frequency of the crystal oscillations decreases as expected. Our results are in good agreement with those reported by the authors Kertesz *et al.* [50]. The authors employed EQCM to investigate polymethylene blue film formation on gold electrodes in 0.01M phosphate buffer, pH 7. The frequency fluctuations that accompany the redox process in 0.1M phosphate buffer, pH 7, are dealt with in detail in section 3.7.2.

3.7.2 EQCM analysis of the PMB Redox Process

When the redox activity of the film modified GC electrode was investigated as a function of solution pH, by the authors Lyons *et al.* [30], it was found to be a $4e^-$, $3H^+$ process at pH > 6. It should be noted that the authors did not observe the monomeric peaks (I & I') in the voltammograms of the modified electrodes in buffer solution. The stoichiometry of the charge transfer process, therefore, required further investigation. In this body of research, mass transport during the redox processes of polymethylene blue in 0.1M phosphate buffer, pH $\approx$ 7, was investigated using EQCM. The movement of anions, cations, solvent molecules and possibly other general species in and out of the film causes the crystal oscillation frequency to fluctuate. A decrease in the crystal oscillation frequency is analogous to a mass increase in the polymer film and conversely an increase in the oscillation frequency of the crystal indicates that ions have been ejected from the polymer film, and hence, the mass decreases. The Sauerbrey equation presented previously in Chapter 2, relates the frequency change to the mass change

$$\Delta f = -\frac{2f_0^2}{A\sqrt{\mu\rho}}\Delta m \qquad (3.49)$$

where f_0 is the resonant frequency fundamental to the crystal, A is the area of the gold electrode coated onto the crystal, ρ is the density of the crystal and μ is the shear modulus of quartz. In the CH Instruments Model 440 system these values are, f_0 = 8MHz, A = 0.196cm^2, ρ = 2.648g/cm^3, μ = 2.947 x 10^{11} g/cm.s^2. Using these values it is seen that a frequency change of 1Hz corresponds to a mass change of 14ng using the CH Instruments Model 440 EQCM. The minus sign in equation 3.49 determines that a frequency decrease corresponds to a mass increase. The Sauerbrey equation is only valid if the film is rigid. Film rigidity can be investigated in terms of admittance. A linear plot of film thickness *vs.* Δmass should pertain if the films are indeed rigid. It should be stated that this was not performed for the EQCM analysis presented here, so a rather large assumption has been made in the analysis.

In this body of research the range of scan rates, 10-50mv s^{-1}, was employed to investigate the redox process [51]. It may have been more pertinent to have used scan rates < 1mV s^{-1} so that kinetic effects were minimised. Figure 3.26 shows the results of an EQCM voltammetric experiment on a polymethylene blue electrode in 0.1M phosphate buffer. The plot shows the simultaneous current – frequency response to the applied potential. As the polymer film is oxidised, the frequency of the crystal oscillations decrease corresponding to an increase in mass. This behaviour is expected as the ingress of an anion is required to maintain electroneutrality, and conversely, the reduction of the polymer film is coupled with the egress of an anion.

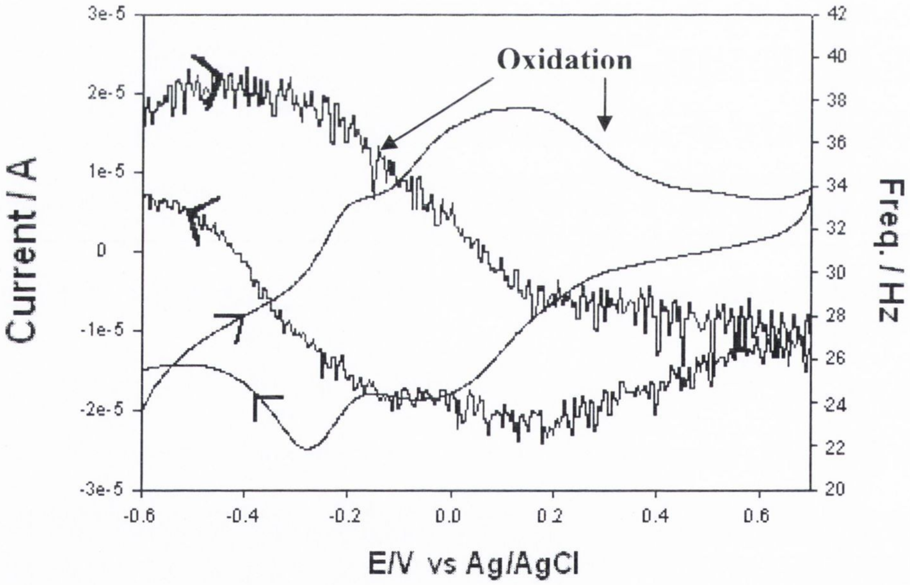

Figure 3.26; Cyclic voltammograms (smooth line) and the simultaneously detected EQCM frequency curve of the Au/polymethylene blue electrode, L = 6.27± 3.2 10^{-8} cm, in 0.1M phosphate buffer (pH=7). Scan rate: 50mV s^{-1}. Initial potential scan direction is anodic.

The corresponding ΔMass and Charge profiles are displayed in figure 3.27. The mass changes can be explained as follows; the polymethylene blue oxidation process stoichiometry is quantified as the loss of $2e^-$, H^+, to generate the reduced state.

Therefore, the ingress of one anion into the film is required to maintain film electroneutrality and this should be evident in the EQCM response as an increase of mass.

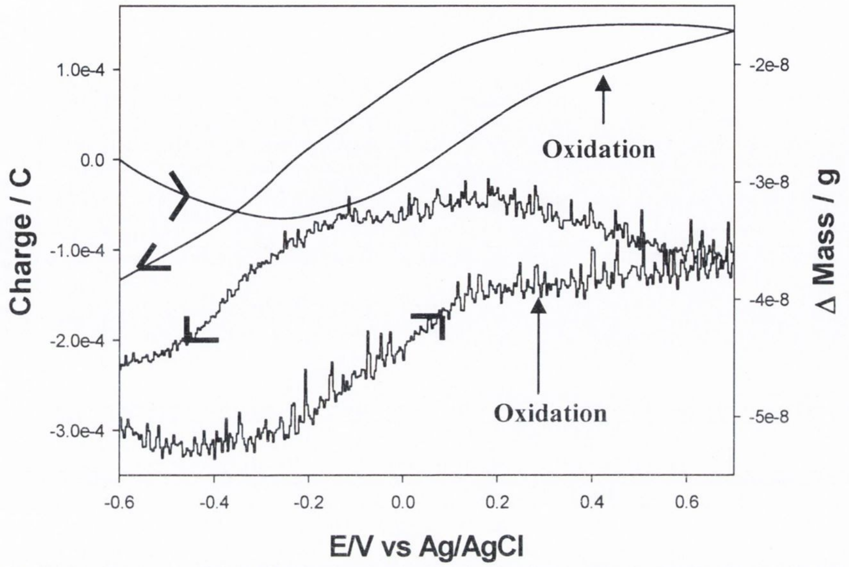

Figure 3.27; Plot of the mass and charge profiles as a function of the applied potential of the same experimental data shown in figure 3.26. When the charge increases on film oxidation, the mass also increases. Initial potential scan direction is anodic. Film thickness, L = 6.27± 3.2 10^{-8} cm.

Indeed we do observe an increase in mass for the oxidation process but the corresponding reduction is more complex and a mass gain occurs up to a potential of ca. +0.1V. We then observe a loss in film mass. An interesting feature of the massogram is the evident hysteresis on completion of the potential scan. The net mass of the film after reduction is slightly higher than the initial mass of the film. However, it was found that the film mass had returned to the initial mass value before further potential scans were performed - an indication that an equilibrating desorption of solvent molecules occurs when no potential is applied. The hysteresis is also observed in the massograms when the scan rate is varied as illustrated in figure 3.28.

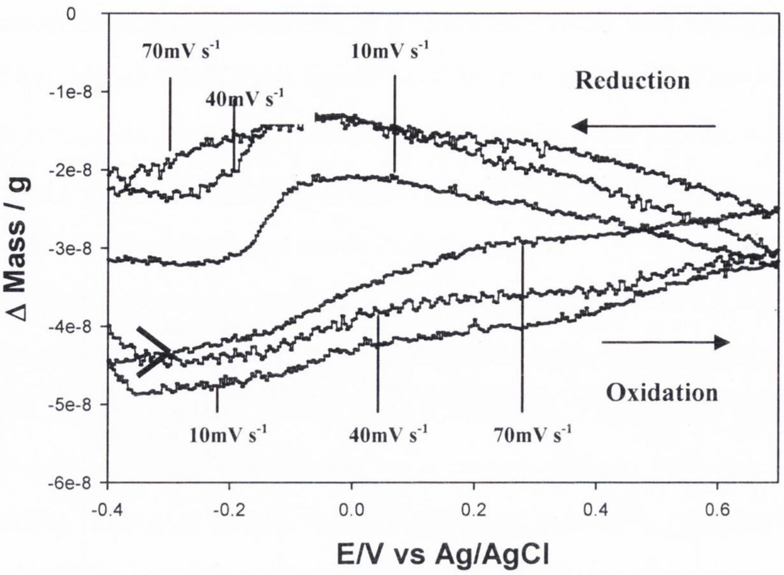

Figure 3.28; Simultaneous massograms for a potential cycle of the PMB/Au electrode in 0.1M phosphate buffer (pH =7) + 0.1M KCl. Hysteresis is observed over the scan rates performed. Initial potential scan direction is anodic. Film thickness, L = 5.29± 2.4 10^{-8} cm.

A simple method of investigating if the mass and charge potentials are analogous is to examine the $E_{1/2,q}$ and $E_{1/2,m}$ values. These are the potentials at which the total charge and mass changes, respectively, are half complete. The variation of the $E_{1/2}$ values with scan rate (figures 3.29 {a}&{b}) measures the ability of the charge and mass quantities to respond to the applied potential [52,53]

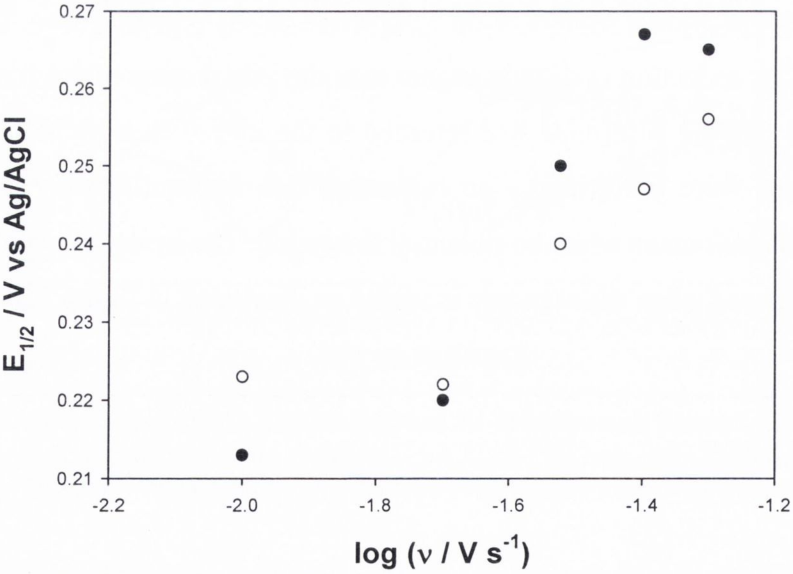

Figure 3.29; {a} Variation of $E_{1/2,q}$ and $E_{1/2,m}$ with log scan rate for a polymethylene blue film, L = 5.91± 1.2 10^{-8} cm, in 0.1M phosphate buffer solution. Oxidation process; open circles = $E_{1/2,q}$ and closed circles = $E_{1/2,m}$.

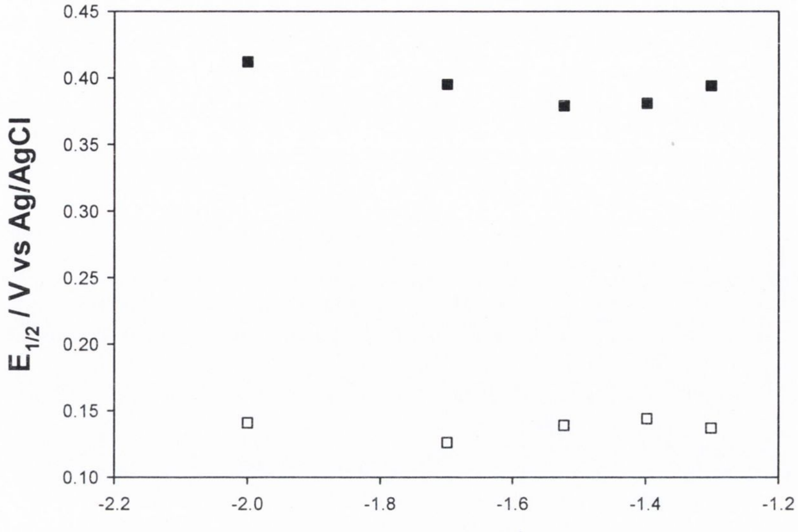

Figure 3.29; {b} Variation of $E_{1/2,q}$ and $E_{1/2,m}$ with log scan rate for a polymethylene blue film, L = 5.91± 1.2 10^{-8} cm, in 0.1M phosphate buffer solution. Reduction process; open squares = $E_{1/2,q}$ and closed squares = $E_{1/2,m}$.

For the oxidation process the figure shows that the mass lags the charge by a small but reasonably constant amount. There is a large discrepancy in the potentials for the reduction process, where the mass change lags the charge. This observation can be explained by the fact that the egress of anions during reduction is more facile than the ingress of anions accompanying oxidation.

Tracking of ΔMass-Q data signifies that mobile species transfer is in equilibrium with the instantaneous oxidation state of the film [64]. When this is the case, the slope of the Δmass (g cm^{-2}) *versus* the normalised charge (mol cm^{-2}) plot yields the molecular weight of the ions accompanying the redox process [65]. The ΔMass-Q plot for the redox activity of the PMB/Au electrode is shown in figure 3.30.

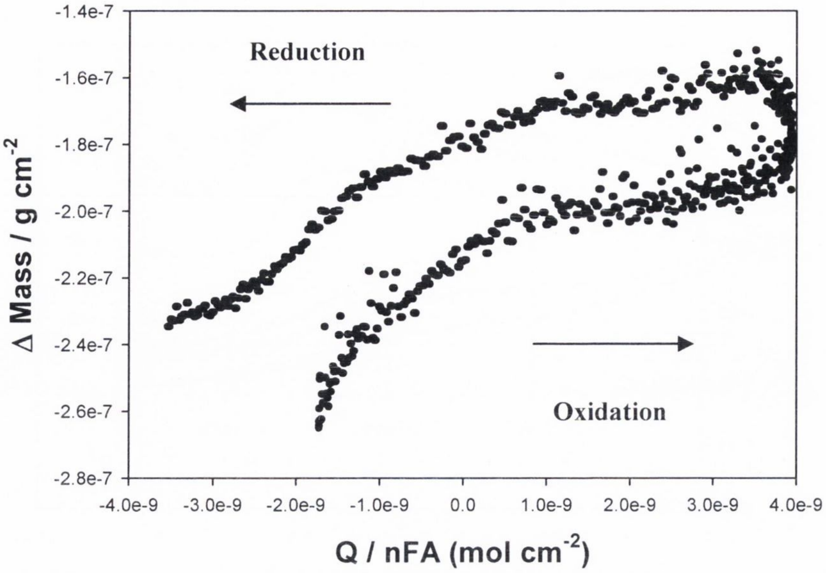

Figure 3.30; Δmass-Q plot to determine if mass changes and charge 'track'. Scan rate = 50mV s^{-1} and the initial scan direction is anodic.

The ΔMass-Q plot verifies that the charge passing through the polymer film is not tracked by the related changes in film mass. This suggests irreversibility and is most likely due to the relatively fast scan rate employed. The slopes corresponding to each redox process do not give values for the molecular weight changes associated with each redox site in the film. Therefore an alternative method must be used to determine these values.

We use the average surface coverage value, $\Gamma = 1.64 \times 10^{-10}$ mol.cm^{-2}, calculated for the polymethylene blue modified gold quartz crystal electrode. We can also determine the average mass increase for the scan rates examined as Δmass = $1.47 \pm 2.3 \times 10^{-8}$g. From our surface coverage value we may then calculate the number of molecules per cm^{2} as:

$$\text{Number Molecules/cm}^2 = \Gamma.N_a$$

$$\Rightarrow \text{Number Molecules/cm}^2 = (1.64 \pm 0.35 \times 10^{-10}\,\text{mol.cm}^{-2})(6.023 \times 10^{23}\text{molecules.mol}^{-1})$$

$$\Rightarrow \text{Number Molecules/cm}^2 = 9.86 \pm 2.1 \times 10^{13}$$

Thus we have determined the number of MB molecules on the surface of our gold electrode. From the average Δmass we can calculate the weight lost per redox site as $1.49 \pm 0.11 \times 10^{-22}$ g molecule^{-1}, which translates (multiply by N_a) to a mass change of molecules lost as 89.83 ± 6.6 g mol^{-1}.

A publication by Bruckenstein *et al.* describes the redox switching stoichiometry for a polythionine film over a range of pH values. Vapour phase absorption studies performed at dry polythionine films show that both H_2O and HA, where HA is the protonated anion, can exist in the polymer phase [56]. The film was also shown, by in situ ellipsometric studies, to contain equal amounts (by volume) of polymer and all other species [57]. At a pH of 7 the reduced form protonation state of polymethylene blue is MBH_2^+ and the film stoichiometry can be described by:

$$\begin{aligned} &MBH^+A^-_{\mathbf{P}}(H_2O)_{m'}(HA)_{y'} + H_3O^+_{\mathrm{S}} + 2e^- = \\ &MBH_2^+A^-_{\mathbf{P}}(H_2O)_{n'}(HA)_{z'} + (m' - n' + 2)H_2O_{\mathrm{S}} + (y' - z')HA_{\mathrm{S}} \qquad (3.50) \end{aligned}$$

where the subscript **p** represents immobile species in the polymer film and **s** signifies mobile species in the bathing electrolyte. Thus a substantial weight change ($\Delta Mass = (y' - z')_{M_{HA}} + (m' - n')_{M_{H_2O}} - {}_{M_{H^+}}$) is expected for the oxidation process. In a pH of 7, the phosphate ion exists as HPO_4^- [58], and so one unsolvated molecule weighs 95.97g mol^{-1}. Therefore if HPO_4^- is the anion entering the film on oxidation, the molecular weight gained per redox site should be at least ca. 96g mol^{-1}, and water (solvent) would have no part in the oxidation process. This seems unlikely as in the previously presented massograms in figure 3.28 continue to equilibrate i.e. lose mass, probably H_2O molecules, after the reduction scan is complete. After an equilibration period, the massograms all had close initial mass values and so subsequent loss of mass after the potential ceased, can be attributed to ejection of solvent molecules. The mobile anion, therefore, must be the chloride ion, Cl^-, with a molecular weight of 35.45g mol^{-1}. This also allows, on calculation, for the ingress of $3H_2O$ molecules along with the chloride ion. This can be verified by repeating the same experiments in deuterated water. Calculated from the expected weight change, $\Delta Mass = +1_{M_{Cl}} + 3_{M_{H_2O}} - 1_{M_{H^+}}$, the total mass gain on oxidation would be 89.45g mol^{-1}. This compares to our experimental value of 89.83 ± 6.6g mol^{-1}. Equation 3.5.27 may now be rewritten as

$$MBH^+A^-_P(H_2O)_4(HA) + H_3O^+_S + 2e^- = MBH_2^+A^-_P(H_2O) + 5H_2O_S + HA_S \qquad (3.51)$$

The fixed ion at each active site of the polymer is probably the HPO_4^- ion which should form an ion-pair with the cationic polymer redox sites. From the equation we observe that one H_2O molecule is also bound to each site. Experimental error and film imperfections would have allowed for quite a larger discrepancy than this and indeed further experimentation may find the need for the cushion of experimental errors.

Finally, the polymer may be classified according to a diagnostic flow chart developed by Hillman *et al.* [54,56]. The Q vs. E (figure 3.27), and ΔMass vs Q (figure 3.30), plots do not track. The non-tracking nature of the Q vs E plot suggests that uncharged mobile solution species play a large part in the mass fluctuations but not on the charge, an observation with which we concur. The ΔMass vs Q plot does not track indicating that the mobile species transfer is not in equilibrium with the instantaneous oxidation state of the film. The redox behaviour of the polymer film, therefore, is under activity control and the transfer of net neutral species is rate determining.

3.8 Conclusions

This chapter detailed the solution phase electrochemistry of methylene blue examined *via* cyclic voltammetry and RDE. The reduction of MB involves the loss of two electrons and a proton to form leucomethylene blue. MB is known to form dimers and bigger aggregates in solution due to the molecular forces such as hydrogen bonding and Van der Waals interactions. The amount of dimerisation that occurs in solution increases with concentration and can be quantified in terms of monomer fraction. The diffusion coefficient and the electron transfer rate constants for MB were found to vary substantially as a function of monomer species present in solution.

MB is also known to adsorb strongly and rapidly to electrode surfaces and at low concentrations conforms to a Langmuir adsorption isotherm. High concentrations were also analysed in terms of adsorption and an adsorption isotherm was constructed. From the isotherm a maximum surface for a MB monolayer was elucidated. When correlated to solution monomer fraction, different orientations of the adsorption species were discussed.

In the latter part of the chapter, methylene blue was electropolymerised onto a GC electrode. The polymerisation was examined as a function of initial MB concentration and number of polymer growth cycles. The properties of the resultant polymer films varied in the amount of charge carried by the polymer-modified GC electrode. Finally, charge transport in the polymer film was quantified in terms of the charge transfer diffusion coefficient, and of counterion motion, using theoretical and experimental (EQCM) techniques. Quantifying the stoichiometry of the counterion and solvent movement through the PMB film has not been reported in the literature to the best of our knowledge.

3.9 Appendix

3.9.1 Derivation of the Langmuir adsorption isotherm [16]:

We know that:

$$\frac{\Gamma_{MB}}{\Gamma_M - \Gamma_{MB}} = K[MB]_\infty$$

introducing $$\theta = \frac{\Gamma_{MB}}{\Gamma_M}$$

we get:

$$\frac{\theta}{1-\theta} = K[MB]_\infty$$

where $$K = \exp\left[\frac{-\Delta G^0{}_{ads}}{RT}\right]$$

Rearranging this equation gives:

$$\begin{aligned}\theta &= K[MB]_\infty(1-\theta)\\ &= K[MB]_\infty(1-\theta)\\ &= K[MB]_\infty - K[MB]_\infty\theta\end{aligned}$$

$$\begin{aligned}\theta + K[MB]_\infty\theta &= K[MB]_\infty\\ \theta(1+K[MB]_\infty) &= K[MB]_\infty\end{aligned}$$

which leads to the Langmuir adsorption isotherm:

$$\theta = \frac{K[MB]_\infty}{1+K[MB]_\infty}$$

re-inserting $\theta = \frac{\Gamma_{MB}}{\Gamma_M}$, we get:

$$\frac{\Gamma_{MB}}{\Gamma_M} = \frac{K[MB]\infty}{1+K[MB]_\infty}$$

or

$$\Gamma_{MB} = \frac{K\Gamma_M[MB]_\infty}{1+K[MB]_\infty}$$

The Langmuir adsorption isotherm is the simplest model of adsorption and is based on the following assumptions:

1. Surface has a fixed number of adsorption sites; at coverage θ, a fraction θ of these are occupied and 1-θ are unoccupied.
2. Each site can hold up to one adsorbate atom or molecule
3. ΔH_{ads} is the same for all sites, and independent of θ.
4. There is no interaction between adsorbed molecules/atoms
5. An incoming atom or molecule striking the surface either encounters an empty site and adsorbs or encounters a filled site and is reflected back to the gas phase.
6. Adsorption stops at one monolayer (defined at θ =1)

3.10 References

[1] H.-H. Yang, R. L. McCreery, *Anal. Chem.*, **71**, 4081, 1999.

[2] T. Sagara, K. Niki, *Langmuir*, **9**, 831, 1993.

[3] A. S. N. Murthy, K. S. Reddy, *J. Chem. Soc., Faraday Trans. I*, **80**, 2745, 1984.

[4] M. D. Archer, I. C. Ferreira, J. Albery, A. R. Hillman, *J. Electroanal. Chem.*, **111**, 295, 1980.

[5] R. S. Nicholson, *Anal. Chem.*, **37**, 1351, 1965.

[6] C. H. Giles, A. P. D'Silva, *Electro-kinetic & Diff. Meas.*, 2516, 1969.

[7] W. Spencer, J. R. Sutter, *J. Phys. Chem.*, **83**, 1573, 1979.

[8] K. Bergmann, C. T. O'Konski, *J. Phys. Chem.*, **67**, 2169, 1963.

[9] Osteryoung, R. A., Lauer, G., Anson, F. C., *J. Electrochem. Soc.*, **110**, 926, 1963.

[10] P. T. Hang, G. W. Brindley, *Clays & Clay miner.*, **18**, 203, 1970.

[11] V. Svetlicic, J. Tomaic, V. Zutic, *J. Electroanal. Chem.*, **146**, 71, 1983.

[12] K. Bergmann, C. T. O'Konski, *J. Am. Chem. Soc.*, **67**, 2169, 1963.

[13] R, B. McKay, P. J. Hillson, *Trans. Faraday Soc.*, **61**, 1800, 1965.

[14] S. Roffia, G. Feroci, *J. Electroanal. Chem.*, **41**, 33, 1973.

[15] J. F.Goelz, A. M. Yacynyck, H. B. Mark, W. R. Heineman, *J. Electroanal. Chem.*, **103**, 277, 1979.

[16] C. M. A. Brett, A. M. O. Brett, *"Electrochemistry; Principles, Methods and Applications"*, Oxford University Press Inc., N.Y., 1993, p.55.

[17] I. Langmuir; *Gen. Elec. Rev.,* **23**, 504, 1920.

[18] E. Laviron, *J. Electroanal. Chem.*, **63**, 245, 1975.

[19] F. Pergola, G. Piccardi, R. Guidelli, *J. Electroanal. Chem.*, **83**, 33, 1977.

[20] G. Piccardi, F. Pergola, M. Foresti, R. Guidelli, *J. Electroanal. Chem.*, **84**, 235, 1977.

[21] A. F. Diaz, K. K. Kanazawa, G. P. Gardini, *J. Chem. Soc. Chem. Comm*, 635, 1979.

[22] K. K Kanazawa, A. F. Diaz, R. H. Geiss, W. D. Gill, J. F. Kwak, J. A. Logan, J. F. Rabolt, J. B. Street, *J. Chem. Soc. Chem. Comm.*, 854, 1979.

[23] G. Tourillon, F. Garnuer, *J. Electroanal. Chem.*, **135**, 173, 1982.

[24] S. L. Mu, H. G. Xue, B. D. Qian, *J. Electroanal. Chem.*, **304**, 7, 1991.

[25] A. A. Karyakin, A. K. Strakhova, E. E. Karyakina, S. D. Varfolomeyev, A. K. Yatsimirsky, *Bioelectrochem. Bioenerg.*, **32**, 35, 1993.

[26] D. Schlereth, W. Schumann, H.-L. Schmidt, *J. Electroanal. Chem.*, **381**, 63, 1995.

[27] L. Tan, Q. Xie, S. Yao, *Electroanalysis,* **16**, 1592, 2004.

[28] A. Silber, N. Hampp, W. Schuhmann, *Biosens. & Bioelect.*, **11**, 215, 1996.

[29] A. A. Karyakin, E. E. Karyakina, W. Schumann, H.-L. Schmidt, S. D. Varfolomeyev, *Electroanalysis*, **6**, 821, 1994.

[30] M. E. G. Lyons, H. J. Fay, C. Mitchel, D. E. McCormack, *Electrochem., Sens. and Anal.*: Proc. Int. Conf. On Electroanalysis, Dublin, June 10-12, (1986), Amsterdam, 285.

[31] J. Liu, S. Mu, *Synthetic Metals,* **107**, 159, 1999.

[32] K. Nakanishi, P. H. Soloman, Infrared Absorption Spectroscopy, 2nd edn., Holden-Day, San Francisco, p.85,1977.

[33] V. Zutic, V. Svetlicic, J. Clavilier, J. Chevalet, *J. Electroanal. Chem.*, **219**, 183, 1987.

[34] D. Thevenot, *J. Electroanal. Chem.*, **46**, 89, 1973.

[35] A. A. Karyakin, E. E. Karyakina, H.-L. Schmidt; *Electroanal.*, **11**, 149, 1999.

[36] V. Kertesz, G. J. Van Berkel, *Electroanalysis*, **13**, 1425, 2001.

[37] A. A. Karyakin, D. D. Schlereth, *J. Electroanal. Chem.*, **395**, 221, 1995.

[38] C. D. Pause, P. G. Pickup, A. G. Ewing, *J. Electroanal. Chem.*, **197**, 265, 1986.

[39] C. E. D. Chidsey, R. W. Murray, *J. Phys. Chem.*, **90**, 1479, 1986.

[40] W. J. Albery, A. R. Hillman, *J. Electroanal. Chem.*, **170**, 27, 1984.

[41] C. P. Andrieux, J.-M. Saveant, *J. Electroanal. Chem.*, **111**, 377, 1980.

[42] K. Aoki, K. Tokuda, H. Matsuda, *J. Electroanal. Chem.*, **146**, 417, 1983.

[43] K. Aoki, K. Tokuda, H. Matsuda, *J. Electroanal. Chem.*, **160**, 33, 1984.

[44] A. J. Bard, L. R. Faulkner, *"Electroanalytical Methods"*, Wiley, N.Y., 2001.

[45] V. Sutlicic, J. Clavilier, V. Zutic, J. Chevalet, K. Elachi, *J. Electroanal. Chem.*, **344**, 145, 1993.

[46] J. Ochmanska, P. G. Pickup, *J. Electroanal. Chem.*, **271**, 83, 1989.

[47] W. J. Albery, M. G. Boutelle, P. J. Colby, A. R. Hillman, *J. Electroanal. Chem.*, **133**, 135, 1982.

[48] T. Komura, G. Y. Niu, T. Yamaguchi, M. Asano, A. Matsuda, *Electroanalysis*, **16**, 1791, 2004.

[49] W. J. Albery, M. G. Boutelle, P. J. Colby, A. R. Hillman, *J. Electroanal. Chem.*, **133**, 135, 1982.

[50] V. Kertesz, J. Bacskai, G. Inzelt, *Electrochim. Acta*, **41**, 2877, 1996.

[51] S. Bruckenstein, C. P. Wilde, M. Shay, A. R. Hillman, D. C. Loveday, *J. Electroanal. Chem.*, **258**, 457, 1989.

[52] A. R. Hillman, D. C. Loveday, M. J. Swan, R. M. Eales, A. Hamnett, S. J. Higgins, *Faraday Discuss. Chem. Soc.*, **88**, 151, 1989.

[53] S. Bruckenstein, C. P. Wilde, M. Shay, A. R. Hillman, D. C. Loveday, *J. Electroanal. Chem.*, **258**, 457, 1989.

[54] A. R. Hillman, M. J. Swann, S. Bruckenstein, *J. Phys. Chem.*, **95**, 3271, 1991.

[55] D. A. Buttry, M. D. Ward, *Chem. Rev.*, **92**, 1355, 1992.

[56] S. Bruckenstein, C. P. Wilde, A. R. Hillman, *J.Phys.Chem*, **94**, 6458, 1990.

[57] A. Hamnett, A. R. Hillman, *J. Electroanal. Chem.*, **233**, 125, 1987.

[58] A. Ookubo, K. Ooi, H. Hayashi, *Langmuir*, **9**, 1418, 1993.

CHAPTER 4

THEORETICAL MODELS

4.1 Introduction

One of the most useful applications of polymer modified electrodes is the electrochemical detection of trace quantities of various substrates in solution. In particular, the ability to efficiently oxidise and reduce small biological molecules allows trace analysis of these substrates. Batch amperometric methods have been investigated as a potential technique for such an analysis. In the past fifteen years significant advances have been made in the development of polymer based materials for use in electrocatalysts and as amperometric chemical and biological sensors. Most biological species do not undergo clean facile electron transfer reactions at metal electrodes, hence the special interest in the use of polymer modified electrodes. Hillman [1], Lyons [2,3], Evans [4], Wring and Hart [5], and Murray [6] provide useful summaries of these advances.

The operation of a chemically modified sensor under amperometric conditions is simple in concept: the substrate reacts with catalytically active sites immobilised in the film rather than at the underlying support electrode. Consequently, the redox chemistry of the substrate/product transformation process is governed by the redox properties of the deposited layer. The immobilised redox sites within the layer mediate electron transfer from the substrate to the underlying electrode surface. This process is termed heterogeneous redox catalysis [7,8]. This is a fully recyclable process since the catalyst/mediator species in the film may be formed as a result of electron transfer at the electrode/layer interface. The exact nature of the interaction between the immobilised sites within the polymer matrix and the substrate has not been explored in any great detail to date. There are however, papers authored by Gorton and co-workers [9-11], and Burke and O'Leary [12], which go some way to begin to address this issue. Work done by this group indicates that the substrate binds to the sites in the polymer matrix to form a complex, which subsequently decomposes to form the product [13-17]. O' Sullivan *et al.* [18] have reported concurrent findings.

A detailed knowledge about the mediation mechanism is paramount to the application and optimisation of electrocatalytic and electroanalytical systems. The processes involved are the injection of charge and substrate at the electrode/polymer and polymer/solution interfaces, respectively, their diffusion within and reaction with the film. A number of theoretical models of the mediation process have been proposed to describe these processes at modified electrodes. The two most notable treatments to date are those of Albery and Hillman [19, 20], Andrieux and Saveant [21-27], and Lyons *et al.* [28, 29]. The model developed by Lyons is based on Michaelis-Menton enzyme kinetics and is described in detail later in this chapter while the Andrieux-Saveant model is briefly summarised.

Although developed separately the Albery-Hillman and Andrieux-Saveant models are essentially equivalent, figure 4.1, and their conclusions are in good agreement. Both treatments consider the general case of a modified electrode and identify a number of possible rate limiting steps. Albery and Hillman's approach makes use of reaction layer thicknesses: X_0 in the case of an electrode reaction (for electrons injected at the electrode/film interface diffusing into a region containing the mediator) and X_L in the case of a surface reaction. The importance of the reaction zone lies in the fact that its thickness conveys what fraction of the film is usefully employed, while its location reflects the relative transport rates of charge and substrate. The analysis produces an effective modified electrode rate constant, k'_{ME}, which can be compared with the bare electrode value, k'_E.

The Andrieux-Saveant model describes the following processes occurring during mediated charge transfer at a modified electrode:

$$P \rightarrow Q + e^- \qquad (4.1.1)$$

$$Q + A \Leftrightarrow P + B \qquad (4.1.2)$$

$$A \rightarrow B + e^- \qquad (4.1.3)$$

where A and B are the mediator redox couple and S and P are the substrate and product, respectively. The cross-exchange reaction, given by eqn. 4.1.2, can be irreversible or reversible with an equilibrium constant, $K = k_f/k_b$. The case of mediated oxidation under steady-state conditions is considered here.

The interpretive scheme used by Andrieux and Saveant is shown in Scheme 4.1. The following assumptions are made:

(1) The film is considered to be uniform, both in thickness and distribution of redox centers.

(2) The propagation of electrons through the film involves a diffusion-like process due to the ionic self-exchange reactions of the A/B couple. This motion is characterised by an electron diffusion coefficient, D_E.

(3) Diffusion of the substrate, S, from the bulk of the solution to the film/solution interface occurs within a stagnant diffusion layer, whose thickness, δ, is given by equation 2.26.

(4) Penetration of the substrate through the film/solution interface is assumed to be facile, with a partition coefficient, κ. The treatment of such partitioning as a possible rate limiting has been developed by Leddy *et al.* [30].

(5) The movement of the substrate in the layer form the film/solution interface to the electrode surface involves only diffusion, characterised by the diffusion coefficient, D_S. If this is sufficiently large, substrate reaction at the electrode surface may occur (eqn. 4.1.3). Migration has not been considered.

(6) Activity coefficients are regarded as negligible.

Four redox situations have been identified which are of practical importance and can be divided into three cases.

Case A: The equilibrium constant for the cross-exchange reaction may take any value and the S/P electrode reaction is kinetically irreversible. Thus the first voltammetric wave corresponds to the mediated reaction only, and no direct oxidation of the substrate occurs at the electrode surface. Any P generated in the cross-exchange reaction cannot be re-reduced at the electrode. This case is often of relevance to electroanalysis.

Case B: The equilibrium constant for the cross-exchange reaction is greater or equal to unity and the S/P electrode reaction is sufficiently kinetically facile to allow immediate re-reduction of any generated P at the electrode.

Case C: The equilibrium constant for the cross-exchange reaction is greater or equal to unity and the S/P electrode reaction occurs at potentials more anodic than does the oxidation of A.

Arising from the above assumptions, the following set of differential equations and boundary conditions are necessary to describe the kinetics of the mediation process. The steady-state diffusion equations for B and S are

$$D_E \partial^2 c_B / \partial x^2 - k_f c_S c_B = 0 \tag{4.1.4}$$

$$D_S \partial^2 c_S / \partial x^2 - k_f c_S c_B = 0 \tag{4.1.5}$$

where c_B and c_S are the corresponding space dependent concentrations of B and S, respectively.

The boundary condition for B at the electrode /film interface, x = 0, is governed by the potential. If this is sufficiently high we get

$$c_B = \Gamma / L \tag{4.1.6}$$

At the film/electrolyte interface, x = L, the partition equilibrium,

$$(c_S)_{L-} = \kappa (c_S)_{L+} \tag{4.1.7}$$

is valid, κ being the partition coefficient. It is the solution of the above differential equations that gives rise to the concentration profiles of B and S within the film.

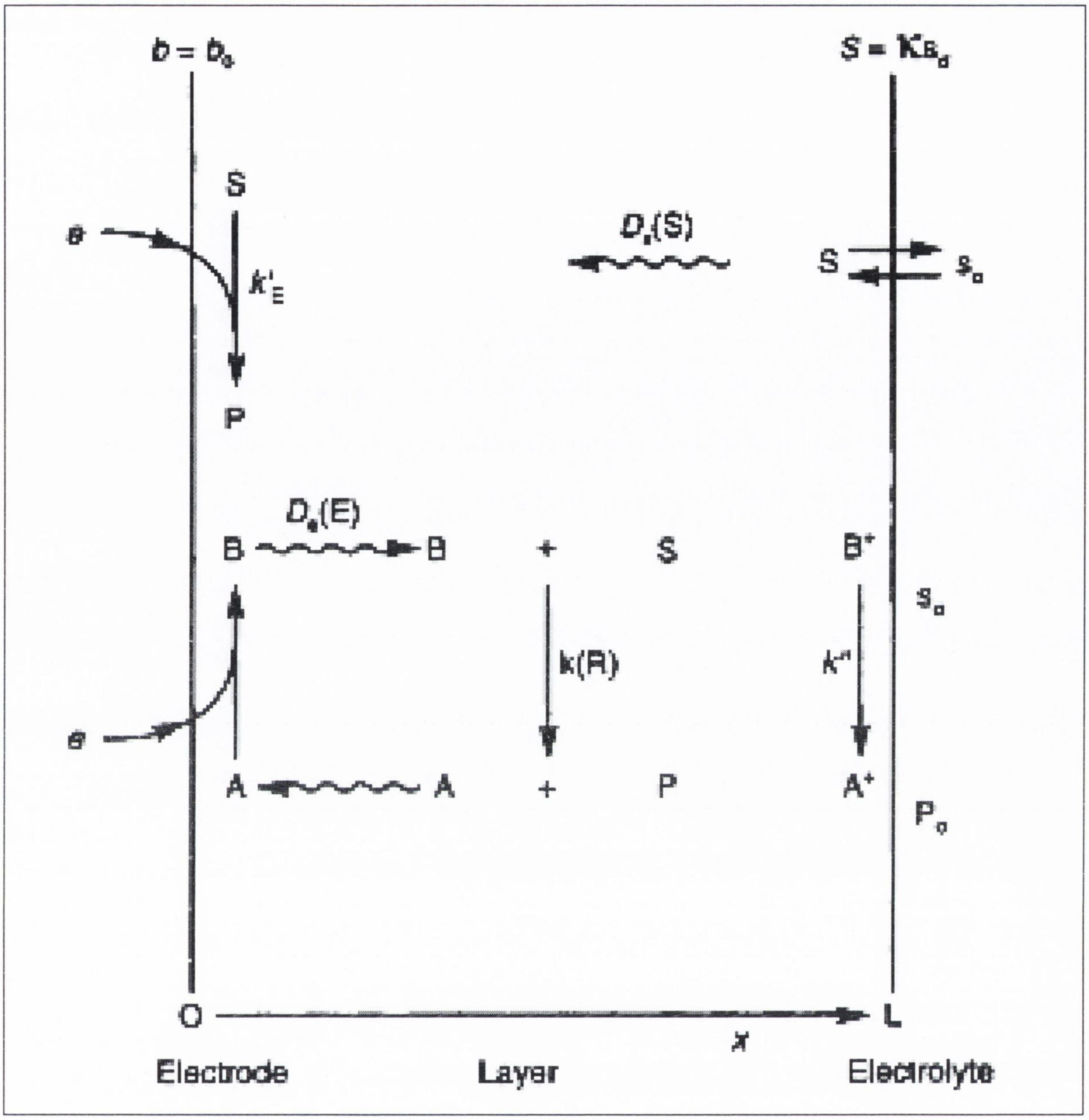

Scheme 4.1; Schematic representation of the Andieux-Saveant and Albery-Hillman models, outlining the transport and kinetic processes occurring within an electroactive polymer film. The process of charge percolation *via* electron hopping is also illustrated. The notation is based on the Albery-Hillman model. Note that k'_E denotes the rate constant for direct, unmediated electron transport at the support electrode, k is the rate constant for mediator/substrate reaction within the layer and k" is a rate constant for substrate/mediator reaction at the layer/solution interface. Substrate partitioning is quantified in terms of a partition coefficient κ, and transport of substrate and charge through the layer is quantified in terms of the diffusion coefficients D_S and D_E, respectively. In the Andrieux-Saveant model, the three primary rate controlling processes are labelled S (equivalent to D_S), E (equivalent to D_E) and R (equivalent to k), corresponding to substrate diffusion in the film, charge percolation through the film and chemical reaction between the mediator and substrate.

Three primary rate controlling processes are labelled S (equivalent to D_S), E (equivalent to D_e) and R (equivalent to k), corresponding to substrate diffusion in the film, charge percolation through the film and chemical reaction between the mediator and substrate.

Andrieux and Saveant also identify four conceptual currents [25], each of which represents the maximum current due to a possible rate limiting process.

$$i_D = nFAD_S c_S^{\infty} / \delta \tag{4.1.8}$$

where c_S^{∞} is the bulk substrate concentration. This is the substrate diffusion in the Nernst diffusion layer and is the plateau current at a bare rotating disk electrode. The remaining currents are given by the following:

$$i_S = nFA\kappa D_S c_S^{\infty} / L \tag{4.1.9}$$

$$i_E = nFA\Gamma D_E / L^2 \tag{4.1.10}$$

$$i_k = nFA\kappa k \Gamma_B c_S^{\infty} \tag{4.1.11}$$

where i_S denotes the substrate film diffusion current, i_E is the film electron diffusion-like current and i_k is the current characteristic of the cross-exchange reaction with forward rate constant, k. Each of these currents may be readily measured experimentally. The smallest characteristic current enables one to determine the rate limiting step. Andrieux and Saveant have constructed concentration profiles describing the various limiting situations [24]. A wide variety of reaction patterns within the polymer film can develop and each depends on the ratios of the characteristic currents.

A comprehensive review by Hillman [31] contains a comparison of the approaches of Albery/Hillman and Andrieux/Saveant. The two treatments are summarised and their notations are matched, thereby emphasising their essential equivalence.

In this body of work it was indicated that the steady state current exhibited bi-phasic behaviour with respect to substrate concentration for the systems under investigation. At low substrate concentrations first order kinetics pertain, whereas for high substrate concentrations, the response is independent of concentration making the kinetics zero order by nature. This type of kinetic cross over is well documented in the study of enzyme kinetic studies and is described in terms of a Michaelis-Menten mechanism [32]. Barlett *et al.* have extended this mechanistic concept to the area of amperometric enzyme electrodes [33-36]. Previous work has been concerned with conductive metal oxide (e.g. RuO_2) particles immobilised in Nafion [37] and carbon paste matrices [38], and with electronically conductive polymers such as polypyrrole doped with counterions such as Cl^- or DBS^- (dodecylbenzene sulphonate ion). The oxidation of substrates such as ascorbate, glucose and catechol all exhibited biphasic current/concentration profiles. The systems examined do not contain redox enzymes, yet the behaviour observed is consistent with a Michaelis-Menten type mechanism.

In order to design the optimum polymer based amperometric sensor for a particular role it is necessary to understand the underlying physical processes that come into play during device operation. Despite the complexity of this undertaking, simple mathematical models have been developed based on the construction of suitable differential equations. These equations describe coupled diffusion and chemical reaction processes in the layer along with associated initial and boundary conditions, which are physically reasonable. If the time dependent boundary value may be solved, the current response may eventually be obtained in an analytical form. In many cases, one is dealing with a time dependent diffusion and reaction process within a finite region. Furthermore, the chemical reaction term may be of a complex form, as pertains for the case of Michaelis-Menten kinetics. Hence a non-linear time dependent differential equation governing the operation of the device is envisaged. With such a complex situation a complete solution may not be possible. The generation of approximate analytical solutions valid under certain specific circumstances may be the best that can be achieved in the current situation. The following analytical derivations and figures were taken with permission form references [28,29].

4.2 The Boundary Value Problem

In trying to define the operation of amperometric sensors in terms of a theoretical model the following assumptions are made. The chemically modified electrode may be thought of as a thin electroactive film deposited onto an electrode surface. This layer is assumed to have a uniform thickness L and a uniform distribution of catalytically active sites within. The entire film may be presumed to be electronically conductive with charge percolation from site to site not a rate-determining step. Initially, the only factors being considered are those arising from substrate diffusion and chemical reaction within the polymer film. Complicating factors like charge polarisation due to concentration effects associated with the substrate are neglected. The chemical reaction of the substrate is assumed to involve the formation of a complex with the immobilised catalyst, which subsequently decomposes to form a product while regenerating the pre-catalyst species. This two step reaction sequence may be outlined as follows:

$$S + C \xrightarrow{K_M} [SC] \xrightarrow{k_c} P + C'$$

$$C' \xrightarrow{k_E'} C$$

where C and C′ represent the catalytically active forms of the immobilised catalyst, and S, P denote substrate and product respectively. This is the Michaelis-Menten tight binding mechanism which is well established. Here, K_M and k_C denote the Michaelis constant and the catalytic rate constant respectively.

The differential equation quantifying the transport and kinetics within the polymer film may be written as:

$$\frac{\partial s(x,t)}{\partial t} = D_s \frac{\partial^2 s(x,t)}{\partial x^2} - \frac{k_c c_\Sigma s(x,t)}{K_M + s(x,t)} \tag{4.12}$$

where s(x,t) denotes the concentration of the substrate at any distance x in the film at any time t, D_s is the diffusion coefficient of the substrate in the layer and c_Σ denotes the total catalyst concentration in the film (units: mol cm^{-3}). This is the time dependent non-linear partial differential equation. The non-linearity arises from the presence of the Michaelis-Menten kinetic term on the right hand side of the equation 4.12.

Through the introduction of the following pseudo first order rate constant; $k = \frac{k_c c_\Sigma}{K_M}$ equation 4.12 becomes;

$$\frac{\partial s}{\partial t} = D_s \frac{\partial^2 s}{\partial x^2} - \frac{ks}{1 + \frac{s}{K_M}} \tag{4.13}$$

this equation must be solved with respect to the initial condition: s = 0 when t = 0. The solution of equation 4.13 must also satisfy all boundary conditions; for t > 0, then when x = 0, $\frac{\partial s}{\partial x} = 0$; and when x = L, $s = \kappa s^\infty$, where κ denotes the partition coefficient and s^∞ represents the bulk concentration of the substrate in solution. The latter boundary condition assumes that substrate diffusion effects in solution may be neglected.

The following parameters may be introduced to transform equation 4.13 into dimensionless form:

$$u = \frac{s}{\kappa s^\infty} \quad \chi = \frac{x}{L} \quad \tau = \frac{D_s t}{L^2} \quad \gamma = \frac{kL^2}{D_s} = \Phi^2 \quad \alpha = \frac{\kappa s^\infty}{K_M} \tag{4.14}$$

where u, χ and τ represent dimensionless concentration, distance and time parameters respectively, α denotes a saturation parameter and γ is related to the Thiele Modulus Φ. The latter quantity is given by $\Phi = \frac{L}{X_K}$, where X_K denotes a characteristic reaction layer thickness. The fraction of the layer that is utilised in the catalytic reaction may be quantified by the Thiele Modulus [37], since the characteristic reaction layer thickness X_K provides an accurate estimate of the distance the substrate travels into the layer prior to interaction with an immobilised catalytic site within the polymer matrix.

Equation 4.13 then reduces to the following dimensionless form:

$$\frac{\partial u}{\partial \tau} = \frac{\partial^2 u}{\partial \chi^2} - \frac{\gamma u}{1+\alpha u} \qquad (4.15)$$

and the initial and boundary conditions reduce to:

$$\tau = 0 \quad 0 \le \chi \le 1 \quad u = 0$$

$$\tau > 0 \quad \chi = 0 \quad \frac{\partial u}{\partial \chi} = 0 \qquad (4.16)$$

$$\tau > 0 \quad \chi = 1 \quad u = 1$$

The problem is defined completely in terms of equations 4.15 and 4.16. In order to obtain an analytical expression for the normalised current response y, the concentration profile u(χ,τ) of substrate within the layer must be solved. From this concentration profile an analytical expression for y may be obtained. The flux j is given by:

$$j = \frac{i}{nFA} = \int_0^L ks(x,t)dx = \frac{D_S \kappa s^{\infty}}{L}\gamma \int_0^1 u(\chi,\tau)d\chi \qquad (4.17)$$

Hence the normalised current response y is given by:

$$y = \frac{iL}{nFAK_M D_S} = \alpha\gamma \int_0^1 u(\chi,\tau)d\chi \qquad (4.18)$$

where i denotes the time dependent amperometric current response. Physically, the boundary value problem described by these equations corresponds to determining the time dependent current response to a step-like increase in substrate concentration. This would be obtained at a polymer modified electrode operating in the batch amperometric mode.

4.3 The Steady State Condition

4.3.1 Neglecting Concentration Polarisation of Substrate in Solution.

Previous work by this group included a preliminary analysis for the steady state current response as $\tau \to \infty$ [15]. Under steady state conditions, it has been shown that $\frac{\partial u}{\partial \tau}=0$ in equation 4.15. The steady state reaction / diffusion term may then be written as:

$$\frac{\partial^2 u}{\partial \chi^2} - \frac{\gamma u}{1+\alpha u} = 0 \qquad (4.19)$$

This is a non-linear differential equation. This expression may be simplified to generate equations which can be integrated to yield the concentration profile $u(\chi)$. This depends on whether the factor $\alpha u << 1$ or $\alpha u >> 1$. The normalised current y is then given by:

$$y = \alpha\left(\frac{du}{d\chi}\right)_{\chi=1} \qquad (4.20)$$

It has been shown [14] that when $\alpha u << 1$, which corresponds to unsaturated kinetics, equation 4.19 may then be integrated to yield:

$$u(\chi) = \cosh\left[\sqrt{\gamma\chi}\right]\operatorname{sec h}\left[\sqrt{y}\right] \qquad (4.21)$$

where $\gamma^{1/2} = \Phi = L / X_K$

Typical concentration profiles are illustrated in figure 4.1 for various values of the Thiele modulus Φ. Typical three-dimensional surface plots (obtained using Sigmaplot) for low and high Φ values are illustrated in figure 4.2.

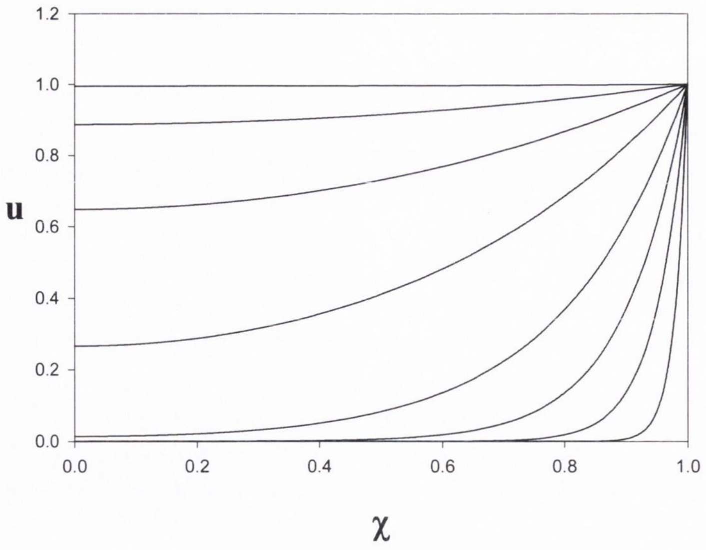

Figure 4.1.; Typical normalised substrate concentration profiles u(χ) corresponding to the situation of unsaturated kinetics (α<< 1) calculated using eq. 4.21 as a function of normalised distance χ = x / L. Each profile corresponds to a specific value of the Thiele modulus: Φ. From top to bottom; Φ = 0.1, 0.5, 1.0, 2.0, 5.0, 10.0, 20.0, 50.0.

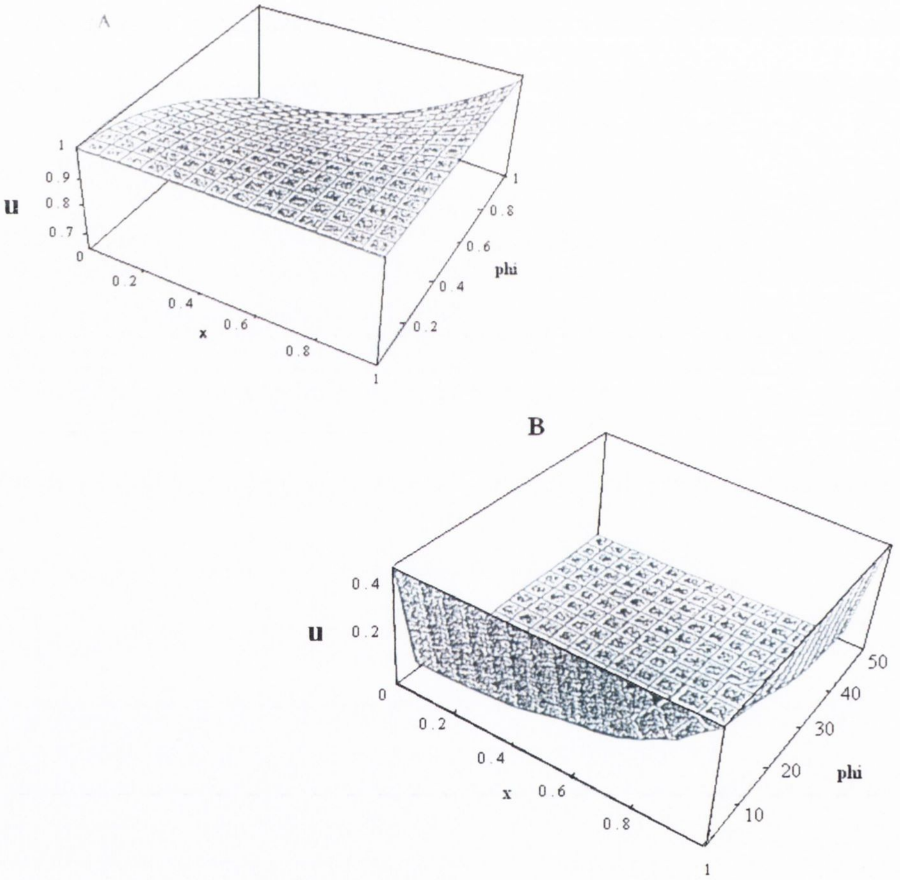

Figure 4.2.; Three-dimensional surface plots corresponding to the concentration profiles u = u(χ,Φ). (a) Corresponding to low Φ values and (b) corresponds to higher Φ values.

When Φ is large, the substrate does not travel very far into the layer before it reacts with immobilised catalyst sites. Substantial concentration polarisation of substrate is then present in the film. The catalytic kinetics are so rapid that the substrate is converted to product in a thin reaction layer near the film/solution interface. This phenomenon can be readily illustrated by examining the form of the concentration profile when $\Phi = \gamma^{1/2}$ is large. Under these conditions, the expression for the concentration profile may be simplified to yield:

$$\cosh\left[\sqrt{\gamma\chi}\right] \approx \frac{1}{2}\exp\left[\sqrt{\gamma\chi}\right]$$

$$\text{and} \quad \sec\text{h}\left[\sqrt{\gamma}\right] \approx 2\exp\left[-\sqrt{\gamma}\right]$$

$$\text{and so} \quad u \approx \exp\left[-\sqrt{\gamma}\,(1-\chi)\right]$$

This expression corresponds to an exponential decay in concentration from an initial value of u = 1 at $\chi = 1$, with a time constant given by $\gamma^{1/2}$ in a direction going into the film. On the other hand, when Φ is small, then, $\sec\text{h}\left[\sqrt{\gamma}\right]\cosh\left[\sqrt{\gamma\chi}\right] \approx \left(1-\frac{\gamma}{2}\right)\left(1+\frac{\gamma\chi^2}{2}\right) \approx 1$. As a result, there is little concentration polarization of substrate within the film, therefore it is only necessary to consider the unsaturated catalytic kinetics and substrate diffusional effects may be neglected due to the fact that the latter are rapid. On the other hand, when $\alpha u << 1$, corresponding to the case where the catalyst is saturated by substrate, equation 4.19 integrates to yield:

$$u(\chi) = 1 + \frac{\gamma}{2\alpha}(\chi^2 - 1) \qquad (4.22)$$

This expression is valid for $\gamma / 2\alpha < 1$. For values greater than this the concentration profile will be negative, which is physically unreasonable. The concentration profiles calculated from equation 4.22, for various Φ values are presented in figure 4.14. Figure 4.15 displays the corresponding three dimensional surface plot.

Using equation 4.20 and equation 4.21, it may be shown that $\alpha u << 1$, the normalised steady state current is given by:

$$y = \alpha\sqrt{\gamma}\tanh[\gamma] \tag{4.23}$$

this expression is the normalised current response for the situation where the catalyst is not saturated by the substrate.

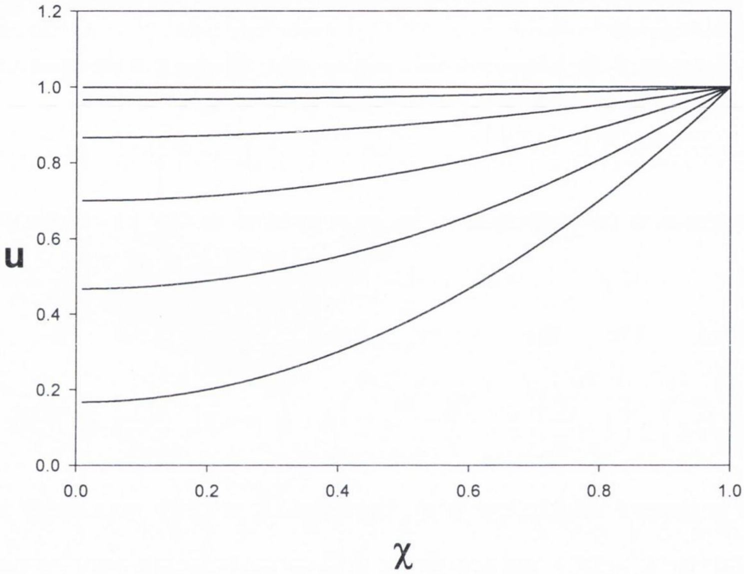

Figure 4.3.; Typical normaised substrate concentration profiles u (χ) corresponding to the case of saturated kinetics, as calculated from equation 4.22 as a function of normalised distance χ for various values of Φ. From top to bottom; Φ = 0.1, 1.0, 2.0, 3.0, 4.0, 5.0.

Figure 4.5 (a) illustrates a plot of equation 4.23 for $\alpha = 0.5$. When this plot is expressed in double logarithmic format, as in figure 4.5 (b), dog leg behaviour is observed. A slope of unity is observed for small γ, changing to a slope of 0.5 at high γ. When γ is small (i.e. $\gamma < 0.33$), then $\tanh\left[\sqrt{\gamma}\right] \approx \sqrt{\gamma}$, and so:

$$y = \alpha\gamma \tag{4.24}$$

This expression describes rate determining unsaturated catalyst kinetics under conditions where diffusion of the substrate through the film is facile. The current response expected for a case I situation is given by equation 4.13. When γ is large (i.e. $\gamma > 3$) then $\tanh\left[\sqrt{\gamma}\right] \approx 1$ and so equation 4.23 reduces to:

$$y = \alpha\sqrt{\gamma} \tag{4.25}$$

Equation 4.25 corresponds to a case II situation and defines the current response expected for thick films and unsaturated catalytic kinetics. The expressions given in equations 4.24 and 4.25 are in good agreement with fig. 4.5 (b). Furthermore, for $\alpha u >> 1$, and using equation 4.20 and equation 4.22 it can be shown that:

$$y = \gamma \tag{4.26}$$

This result means that the rate limiting process is the changeover of the saturated catalyst. Equation 4.26 defines a case III situation. As previously noted, this expression is only valid for $\gamma < 2\alpha$. It will not be valid for large γ values. A different approach must be taken for this situation. This will be termed the case IV situation.

Thick films correspond to larger values for the Thiele modulus Φ. In this situation when $\alpha >> 1$, it can be assumed that the outermost regions of the film are completely saturated, whereas the inner regions of the polymer film will remain unsaturated. This is termed a "mixed case" situation and is illustrated in fig. 4.6, which describes two regions: an inner region R I, and an outer region R II. The differentiation line between R I and R II is set at some value $\chi = \chi^*$. Clearly, when $\chi^* = 0$, the entire layer is saturated, whereas when $\chi^* = 1$ the entire layer is unsaturated. In R I $\alpha u < 1$, whereas in RII: $\alpha u > 1$, at χ^*: $\alpha u = 1$. Furthermore, when $\chi = 0$, $\frac{du}{d\chi} = 0$ and when $\chi = 1$, $u = 1$ as before.

In region R I, $\alpha u < 1$ and so: $\frac{d^2u}{d\chi^2} - \gamma u = 0$ must be solved. This is a standard differential equation which has as solution: $u = A\cosh\left[\sqrt{\gamma}\,\chi\right] + B\sinh\left[\sqrt{\gamma}\,\chi\right]$, where A and B are constants which are determined *via* the boundary conditions. Differentiating this expression yields:

$$\frac{du}{d\chi} = \sqrt{\gamma}\left\{A \sinh\left[\sqrt{\gamma}\,\chi\right] + B\cosh\left[\sqrt{\gamma}\,\chi\right]\right\}$$

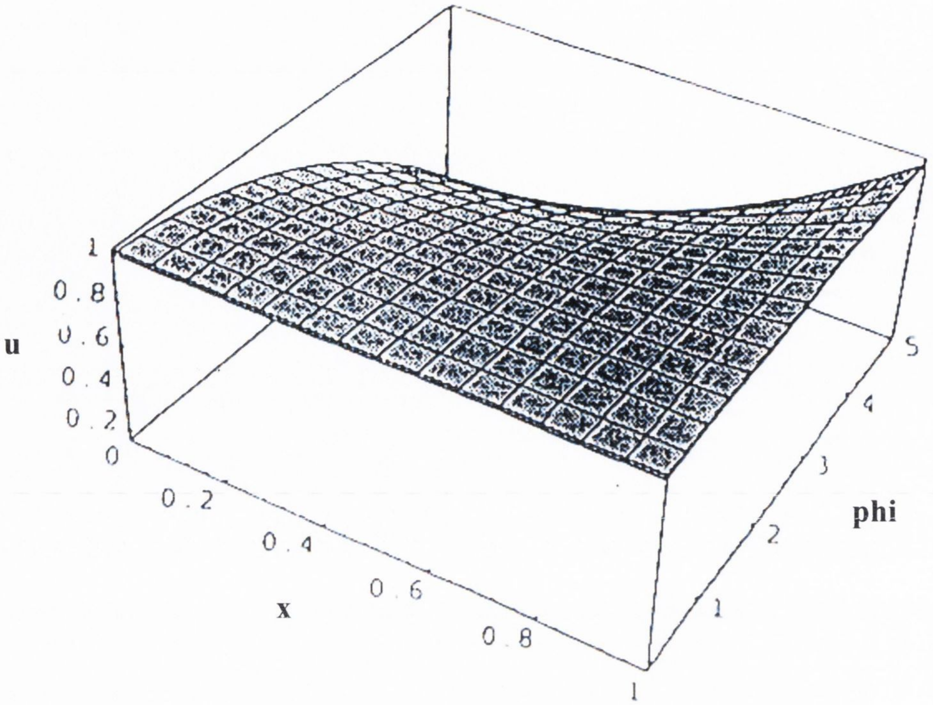

Figure 4.4.; A three-dimensional plot corresponding to u(χ,Φ) in fig. 4.3

In R I it is noted that $\left(\frac{du}{d\chi}\right)_{\chi=0} = 0$, and so B = 0. Also when $\chi = \chi^*$, $\alpha u = 1$ and $u = 1/\alpha$, hence: $A = \frac{1}{\alpha \cosh\left[\sqrt{\gamma}\chi^*\right]}$. From this result the following may be obtained:

$$\left(\frac{du}{d\chi}\right)_{\chi=\chi^*} = \sqrt{\gamma} A \sinh\left[\sqrt{\gamma}\chi^*\right] = \frac{\sqrt{\gamma}}{\alpha}\tanh\left[\sqrt{\gamma}\chi^*\right] \tag{4.27}$$

Next, region R II must be examined. Here $\alpha u > 1$ and so: $\frac{d^2u}{d\chi^2} - \frac{\gamma}{\alpha} = 0$ must be solved. This may be integrated to yield:

$\frac{du}{d\chi} = \frac{\gamma}{\alpha}\chi + C$ and $u = \frac{\gamma}{2\alpha}\chi^2 + C\chi + D$, where C and D denote integration constants. Thus:

$$\left(\frac{du}{d\chi}\right)_{\chi=\chi^*} = \frac{\gamma}{\alpha}\chi^* + C \tag{4.28}$$

The fluxes must balance at $\chi = \chi^*$ and so from equation 4.27 and 4.28 the following expression arises:

$$C = \frac{\sqrt{\gamma}}{\alpha}\tanh\left[\sqrt{\gamma}\chi^*\right] - \frac{\gamma}{\alpha}\chi^* \tag{4.29}$$

Furthermore, the normalised current is given by:

$$y = \alpha\left(\frac{du}{d\chi}\right)_{\chi=1} = \gamma + \alpha C = \gamma + \sqrt{\gamma}\tanh\left[\sqrt{\gamma}\chi^*\right] - \gamma\chi^* \tag{4.30}$$

Hence in order to solve for the normalised current y, χ^* must be evaluated. This is done as follows. When $\chi = 1$, u = 1 in R II and so: $1 = \frac{\gamma}{2\alpha} + C + D$. Also when $\chi = \chi^*$, $u = 1 / \alpha$, and so: $D = \frac{1}{\alpha} - \frac{\gamma}{2\alpha}\chi^{*2} - C\chi^*$. from the latter two expressions on elimination of D, the following expression is obtained; $\frac{\gamma}{2\alpha}\chi^{*2} + C\chi^* + 1 - \frac{1}{\alpha} - \frac{\gamma}{2\alpha} - C = 0$, which is a quadratic in χ^*. Recalling the result for C in equation 4.29 and noting that for large γ, $\tanh\left[\sqrt{\gamma}\chi^*\right] \approx 1$, equation 4.29 reduces to: $C \approx \frac{\sqrt{\gamma}}{\alpha} - \frac{\gamma}{\alpha}\chi^*$.

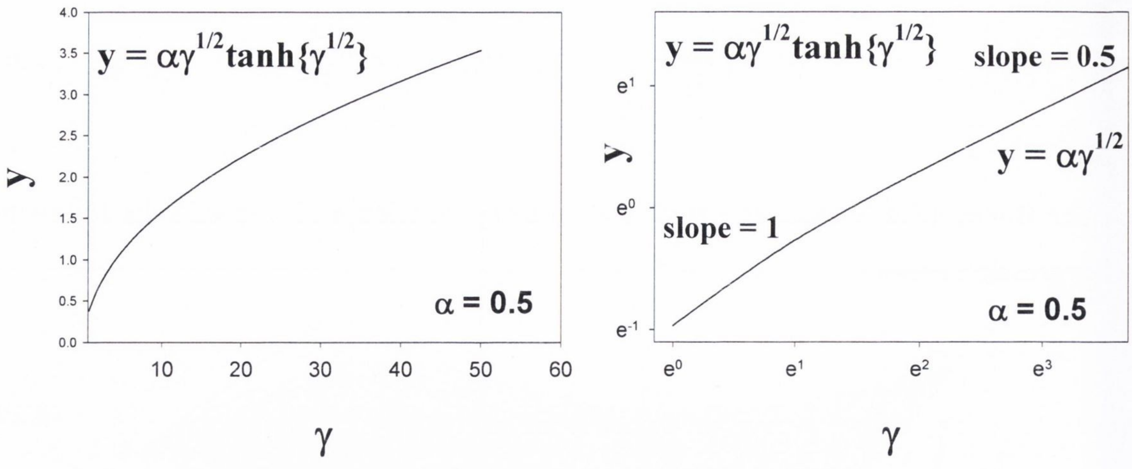

Figure 4.5.; (a) A plot of steady state current response y (where y is defined in equation 4.20) expressed in normalised form as a function of the kinetic parameter γ obtained from equation 4.23. This plot is valid for $\alpha u << 1$. In this plot $\alpha = 0.5$. (b) A plot of equation 4.23 in double logarithmic format. The limiting forms of equation 4.23 for low and high γ values are outlined as inserts.

Substituting this approximate expression for C into the quadratic equation in χ^* and simplifying yields:

$$\chi^{*2} - 2\left\{1+\frac{1}{\sqrt{\gamma}}\right\}\chi^* + 1 - \frac{2\alpha}{\gamma} + \frac{2}{\gamma} + \frac{2}{\sqrt{\gamma}} = 0 \tag{4.31}$$

This expression may be readily solved for χ^* to obtain:

$$\chi^* = \left(1+\frac{1}{\sqrt{\gamma}}\right) - \sqrt{\frac{2\alpha-1}{\gamma}} \approx 1 + \frac{1}{\sqrt{\gamma}} - \sqrt{\frac{2\alpha}{\gamma}} \approx 1 - \sqrt{\frac{2\alpha}{\gamma}} \tag{4.32}$$

where $2\alpha >> 1$ and $\gamma >> 1$. From equation 4.32, the condition for complete saturation within the film, when γ is large, may be defined. Complete saturation occurs when $\chi^* = 0$. Under such conditions: $\gamma = 2\alpha$. Hence for the "mixed kinetics" case, the range of validity is $1 < \alpha < \gamma / 2$.

Substituting the result obtained for χ^* in equation 4.32 into the normalised current expression defined in equation 4.30 and again taking the large γ limit, yields:

$$y \approx \gamma + \sqrt{\gamma} - \gamma\chi^* = \sqrt{\gamma}\left(1+\sqrt{2\alpha}\right) \approx \sqrt{2\alpha\gamma} \tag{4.33}$$

which will be valid when one has thick films (corresponding to $\gamma >> 1$), i.e. when $1 < \alpha < \gamma / 2$ and when part of the layer is saturated and part unsaturated. Equation 4.33 therefore defines the current response expected for a IV situation.

A similar result may be obtained by a direct integration of equation 4.19. If both sides of this equation are multiplied by $\frac{du}{d\chi}$, and noting the following identity :

$\frac{d}{d\chi}\left\{\frac{du}{d\chi}\right\}^2 = 2\frac{du}{d\chi}\left(\frac{d^2u}{d\chi^2}\right)$, then the following is obtained:

$$\frac{d}{d\chi}\left(\frac{du}{d\chi}\right)^2 d\chi = d\left(\frac{du}{d\chi}\right)^2 = \frac{2\gamma u}{1+\alpha u}du \tag{4.34}$$

Integrating then yields:

$$\left(\frac{du}{d\chi}\right)^2 = 2\gamma\int\frac{udu}{1+\alpha u} = 2\gamma\left\{\frac{u}{\alpha} - \frac{1}{\alpha^2}\ln(\alpha u + 1)\right\} + C \tag{4.35}$$

where C is a constant of integration. It may be assumed that $\frac{du}{d\chi} = 0$ when $u = 0$ and so $C = 0$, and therefore equation 4.35 reduces to:

$$\frac{du}{d\chi} = \sqrt{2\gamma\left\{\frac{u}{\alpha} - \frac{1}{\alpha^2}\ln(1+\alpha u)\right\}} = \sqrt{2\frac{\gamma}{\alpha^2}\{\alpha u - \ln(1+\alpha u)\}} \tag{4.36}$$

This expression may not be further simplified to obtain an expression for the concentration profile, due to the fact that the integral may not be expressed in closed form.

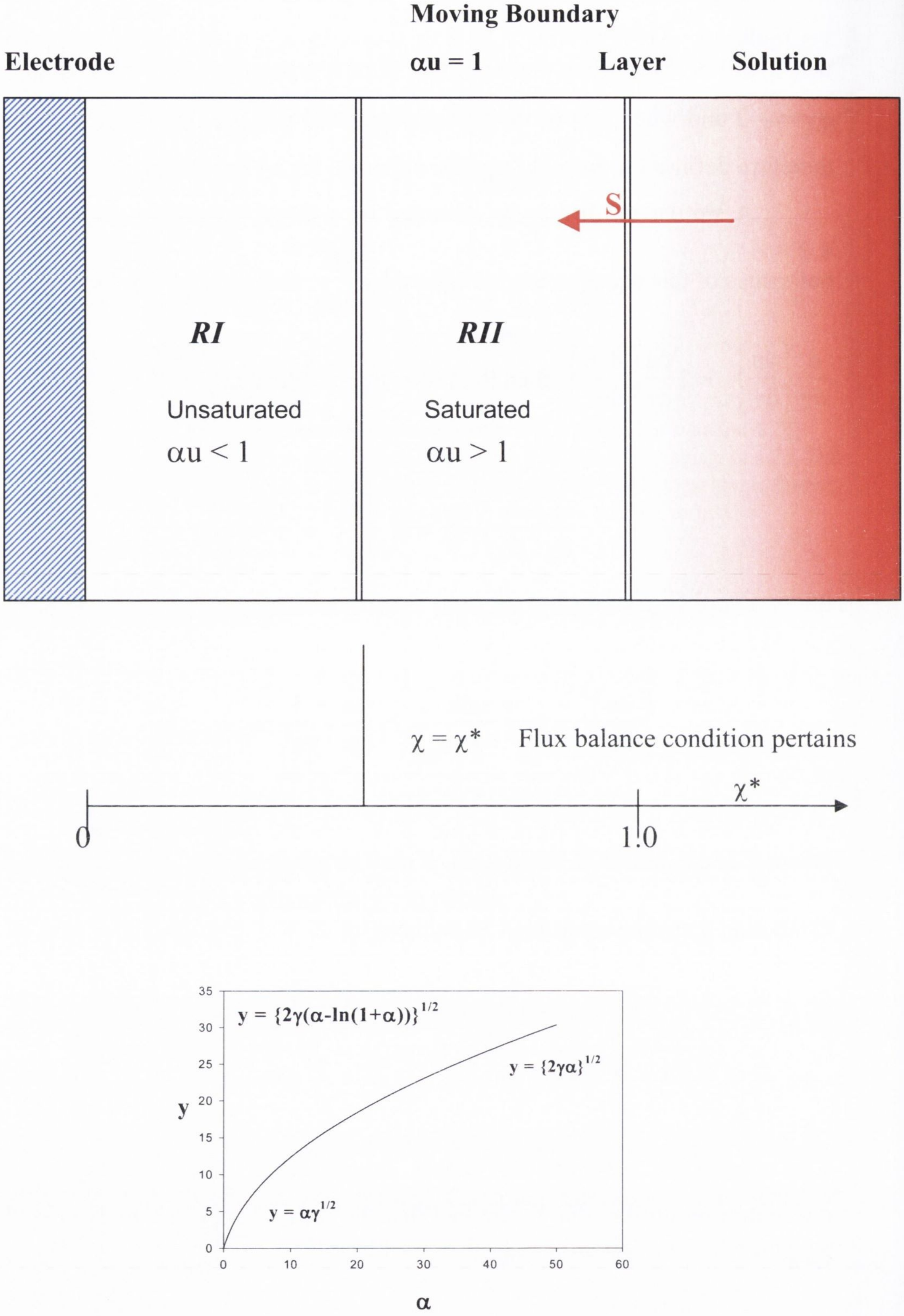

Figure 4.6; (a) The declination of the two region approach used to obtain equation 4.33 which corresponds to the complex situation where $\gamma > 1$ and $\alpha > 1$. R I signifies the unsaturated inner region whereas R II signifies the saturated outer region. The separation lines between these two regions is set at some value $\chi^* > 1-(2\alpha / \gamma)^{1/2}$ as in equation 4.32. When $\chi^* = 0$, complete saturation occurs. (B) A plot of the normalised current response y as a function of the saturation parameter α for $\gamma = 10$. Equation 4.37 was used to obtain this plot. Inserts display the limiting expressions for $\alpha \ll 1$ and $\alpha \gg 1$.

However, equation 4.36 may be used to evaluate the normalised current response y as follows. Noting that when $\chi = 1$, u = 1, then:

$$y = \alpha\left(\frac{du}{d\chi}\right)_{\chi=1} = \sqrt{2\gamma\{\alpha - \ln(1+\alpha)\}} \qquad (4.37)$$

This is the expression for the current response when the saturation parameter $\alpha \approx 1$ and when $\gamma >> 1$. This expression is illustrated in figure 4.6 for the case where $\gamma = 10$.

When $\alpha << 1$ then, $\ln(1 + \alpha) \approx \alpha - \frac{\alpha^2}{2}$ and so equation 4.37 reduces to: $y \approx \alpha\sqrt{\gamma}$ as derived previously in equation 4.25. On the other hand, when $\alpha >> 1$ it may be seen that $\ln(1 + \alpha) \approx \ln \alpha$, and if it is assumed that $\alpha >> \ln \alpha$, then equation 4.37 reduces to: $y \approx \sqrt{2\gamma\alpha}$, as predicted in equation 4.33. Hence it can be seen that equation 4.37 connects the two previous approximate solutions presented in equation 4.25 and equation 4.33. Equation 4.37 can be seen as a connecting equation, which joins kinetic cases II and IV. The two limiting regions are illustrated in figure 4.6.

Next, the situation with very thin films is considered. In such a situation, substrate depletion in the matrix may be neglected and one can assume that u = 1 for all values of χ. In other words, substrate diffusion is very rapid and no reaction layers exist within the film. Under such circumstances, equation 4.19 reduces to:

$$\frac{d^2u}{d\chi^2} = \frac{\gamma}{1+\alpha} \qquad (4.38)$$

Which may be integrated to yield:

$$y = \frac{\alpha\gamma}{1+\alpha} \qquad (4.39)$$

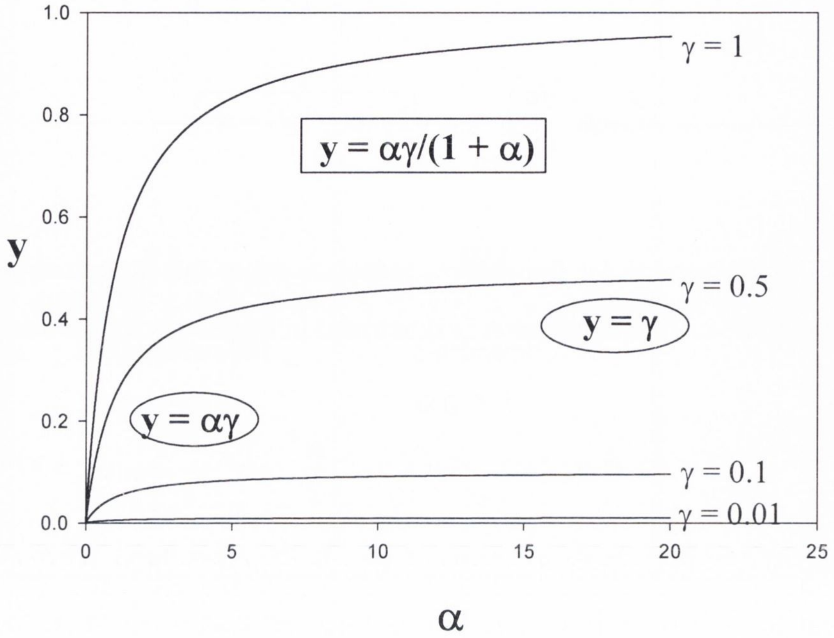

Figure 4.7; A schematic representation of the steady state current response y as a function of the Michaelis-Menten expression presented in equation 4.39.

This is simply a normalised form of the Michaelis-Menten equation, and corresponds to the situation where the chemical kinetics of the substrate reaction at the catalyst surface are rate determining. Equation 4.39 is illustrated in figure 4.7 for various γ values. Furthermore, when $\alpha \ll 1$ then $y \approx \alpha\gamma$, as previously deduced in equation 4.24 (case I). Also when $\alpha \gg 1$ then $y \approx \gamma$ as deduced in equation 4.26 (case III). Hence equation 4.39 connects these two limiting cases. The changeover from first order to zero order kinetics as α increases is readily apparent from figure 4.7. Equation 4.39 will be used in Chapter 5 of this thesis to obtain values of K_M and k_c for the oxidation of different neurotransmitters at polymethylene blue modified electrodes.

Albery, Cass and Shu [37], have examined the kinetics of bound enzyme systems, and have developed an analysis which may be applied to the present system. These workers have constructed an expression which describes the current response when α and γ are close to unity. Using the notation outlined here, the expression derived by Albery and co-workers [37] is given by:

$$y = \sqrt{2\gamma[\alpha - \ln(1+\alpha)]}\ \tanh\left\{\frac{\alpha\sqrt{\gamma}}{(1+\alpha)\sqrt{2[\alpha - \ln(1+\alpha)]}}\right\} \qquad (4.40)$$

this function y (α) is presented figure 4.8 for different γ values (corresponding to different layer thicknesses). It may be seen from these curves that a transition from first order to zero order kinetics is predicted as the normalised saturation parameter α is increased. This biphasic kinetic behaviour is characteristic of Michaelis-Menten kinetics. Also, when γ is large, the transition between the two regions is more extended. Hence, Michaelis-Menten type biphasic behaviour is also to be expected when substrate diffusion effects, as well as the catalytic reaction, are considered.

It is interesting to note from figure 4.8 that the general expression, equation 4.40, which accounts fully for diffusion of substrate in the polymer matrix, is similar in form to the simpler Michaelis-Menten expression for thin films presented in equation 4.39. The expressions presented in equation 4.39 and equation 4.40 are directly compared in figure 4.9. For $\gamma = 0.1$, 1.0 and 10 respectively. The parameter γ can be defined as the ratio of the pseudo first order rate constant k and the diffusional frequency of the substrate within the film, $\left(\frac{D_S}{L^2}\right)$. When γ is small, the reaction kinetics are slower than the diffusion of substrate, making the effect of the reaction kinetics on the overall current response negligible.

Hence, for $\gamma = 0.1$ corresponding to rapid substrate diffusion, the two expressions (i.e. the Michaelis-Menten approximation, equation 4.39 and the Albery expression, equation 4.40) cannot be distinguished. Reasonable agreement is observed for $\gamma = 1$, whereas for large γ values ($\gamma = 10$), the simple Michaelis-Menten equation overestimates the current. Under these conditions substrate diffusion becomes much slower than chemical reaction, and so cannot be neglected. The true current response will be lower than the predicted via use of the Michaelis-Menten expression. The data presented in figure 4.9 are transformed into Lineweaver-Burk form in figure 4.10.

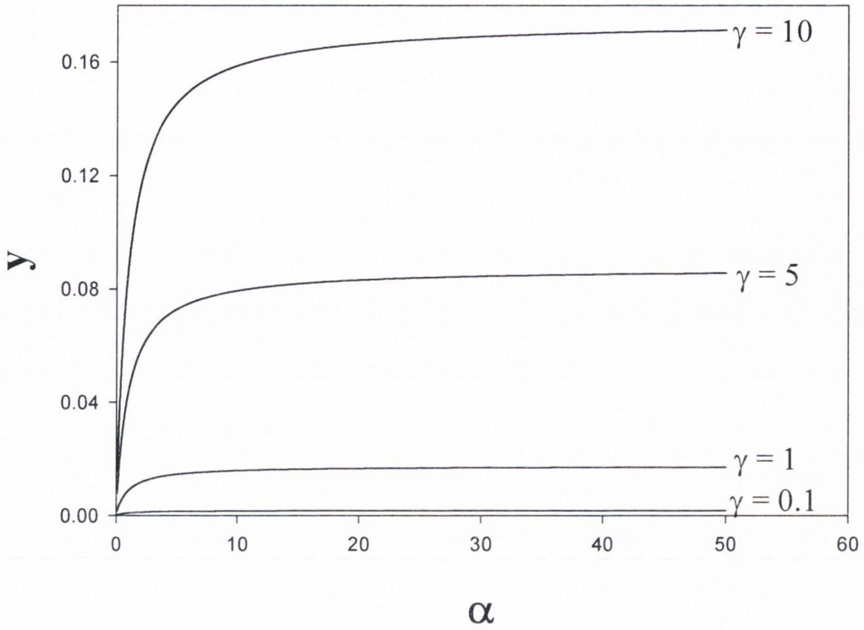

Figure 4.8; A schematic representation of the Albery-Cass-Shu expression (equation 4.40) for the current response for different values of the kinetic parameter γ.

The important point to note from this figure is that Lineweaver-Burk behaviour ($1/y$ proportional to $1/\alpha$) may be expected regardless of whether or not substrate diffusion in the film influences the reaction kinetics. It should be noted that the intercept of the Lineweaver-Burk plot is not sensitive to substrate diffusion effects, but the slope of the plot generally depends on the latter, especially when γ is large.

Figure 4.11 illustrates the variation of the normalised current response y (as predicted from equation 4.40) with the parameter γ for two different α values. In both the unsaturated and saturated situations (low and high α values respectively), the current response increases as γ increases. This is to be expected since the reaction kinetics (quantified *via* the rate constant k) becomes more facile.

Equation 4.40 reproduces the various limiting expressions already derived if suitable limiting values for α and γ are chosen and as such is fundamental to the entire theory. In particular, for $\alpha >> 1$ and for all γ values up to an upper limit of $\gamma = 2\alpha$, one can show using equation 4.40 that:

$$y \approx \sqrt{2\alpha\gamma}\tanh\left[\sqrt{\frac{\gamma}{2\alpha}}\right] \tag{4.41}$$

This expression is not readily derived *via* direct integration of the differential equation, and is illustrated in figure 4.23. Equation 4.41 connects cases III and IV. This can be shown by noting that when γ is small, equation 4.41 reduces to $y = \gamma$ which defines the current response for case III. Also when γ is large equation 4.41 reduces to $y \approx \sqrt{2\gamma\alpha}$ which defines the current response for case I. This prediction is confirmed from figure 4.23.

The simple expressions obtained for the normalised flux for each of the four kinetic cases as follows. Firstly, for $\alpha << 1$ and $\gamma << 1$, then $y = \alpha\gamma$ (case I). In contrast for $\alpha << 1$ and $\gamma >> 1$, $y = \alpha\sqrt{\gamma}$ (case II). Furthermore for $\alpha >> 1$ and $\gamma << 1$ it may be seen that $y = \gamma$ (case III). Finally, for $\alpha >> 1$ and $\gamma >> 1$ then $y \approx \sqrt{2\gamma\alpha}$ (case IV). When the specific expressions for γ, y and α are introduced into these limiting forms of the flux, a clear relationship between the current response and the fundamental experimental variables c_Σ, L and s^∞ are obtained.

An unusual half order dependence with respect to bulk substrate concentrations s^∞ is predicted for the case IV situation where one has a situation of thick films and high substrate concentrations. Furthermore each case corresponds to a particular set of dependencies with respect to the experimentally viable parameters c_Σ, L and s^∞. It is important to note from this is that an approximate mathematical analysis enables one to make unambiguous predictions as to the expected current response, which may subsequently checked experimentally. These results may be presented in terms of a kinetic case diagram shown in figure 4.13.

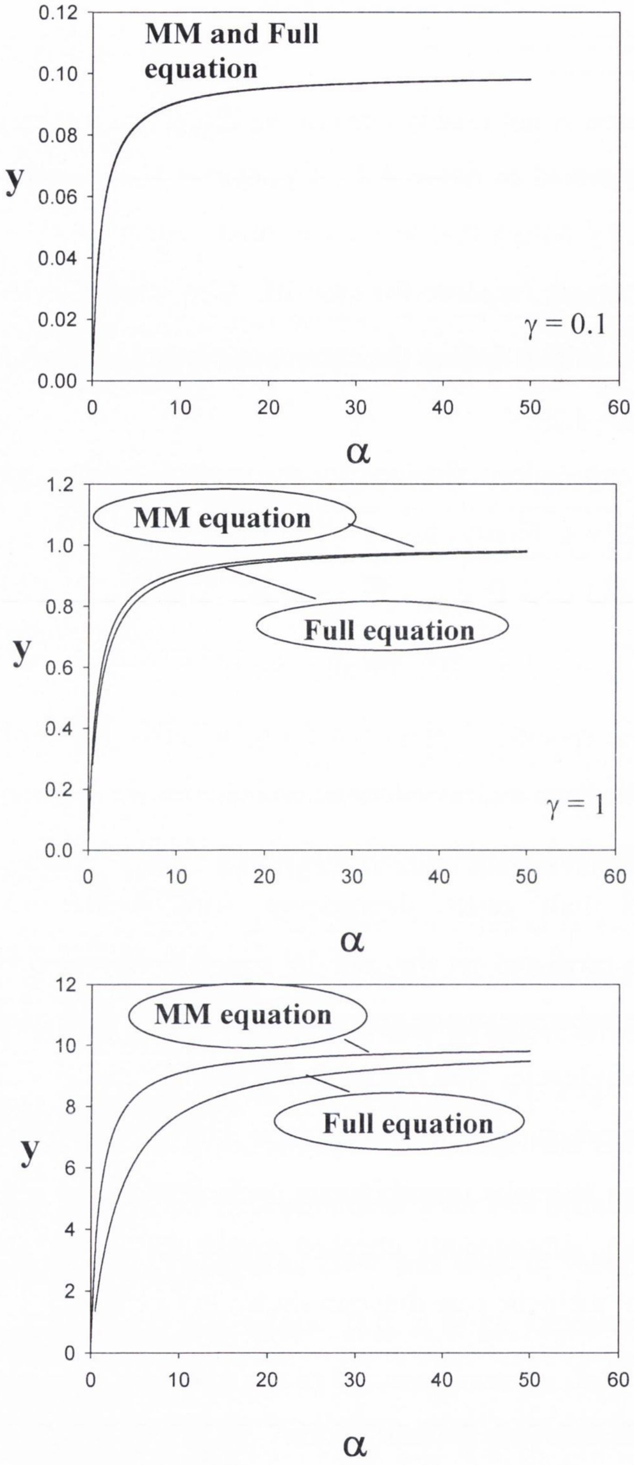

Figure 4.9; The generalised Albery-Cass-Shu expression for the normalised current response presented in equation 4.40 as a function of the saturation parameter α, compared with a simpler Michaelis-Menten expression. (A) and (B) When γ is small good agreement is obtained. (C) When γ is large marked deviations occur.

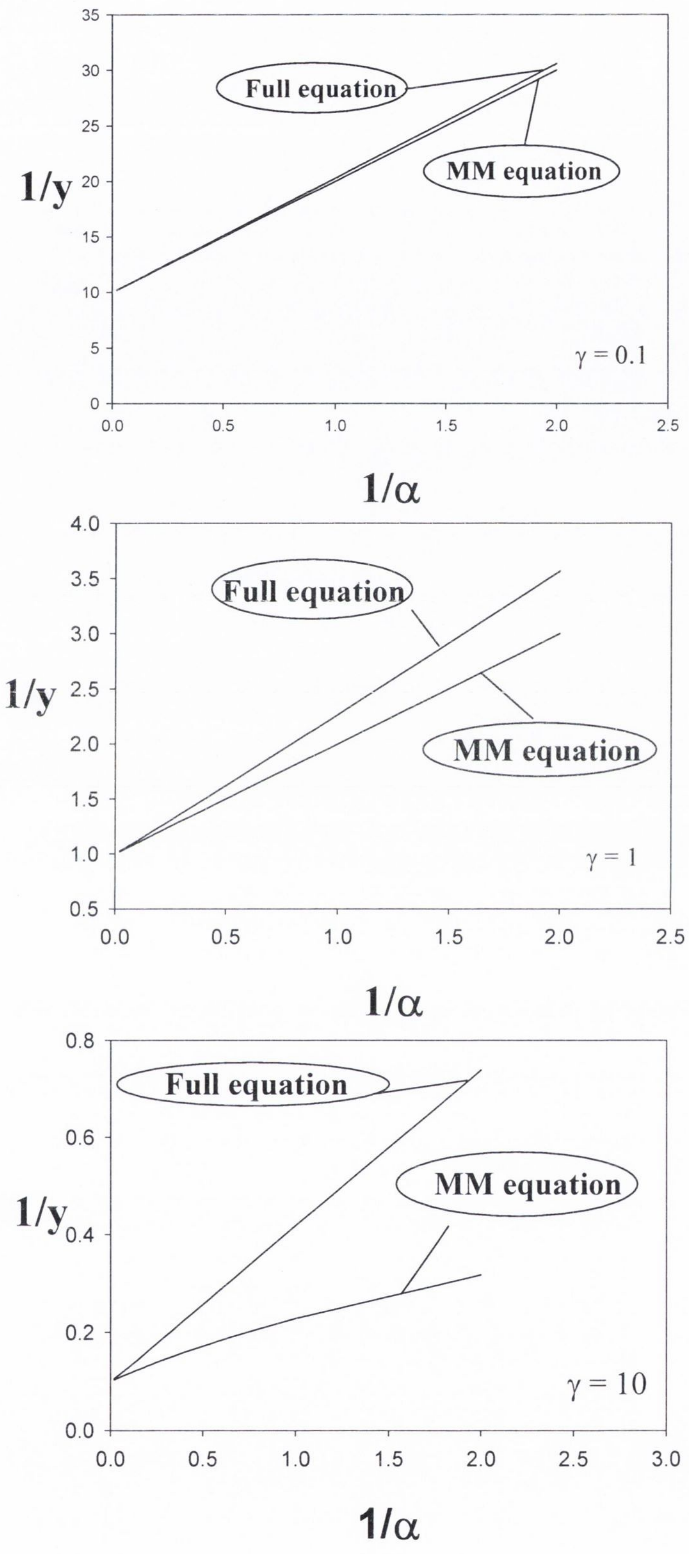

Figure 4.10; Transformation of the curves presented in figure 4.9 to linear Lineweaver-Burk format.

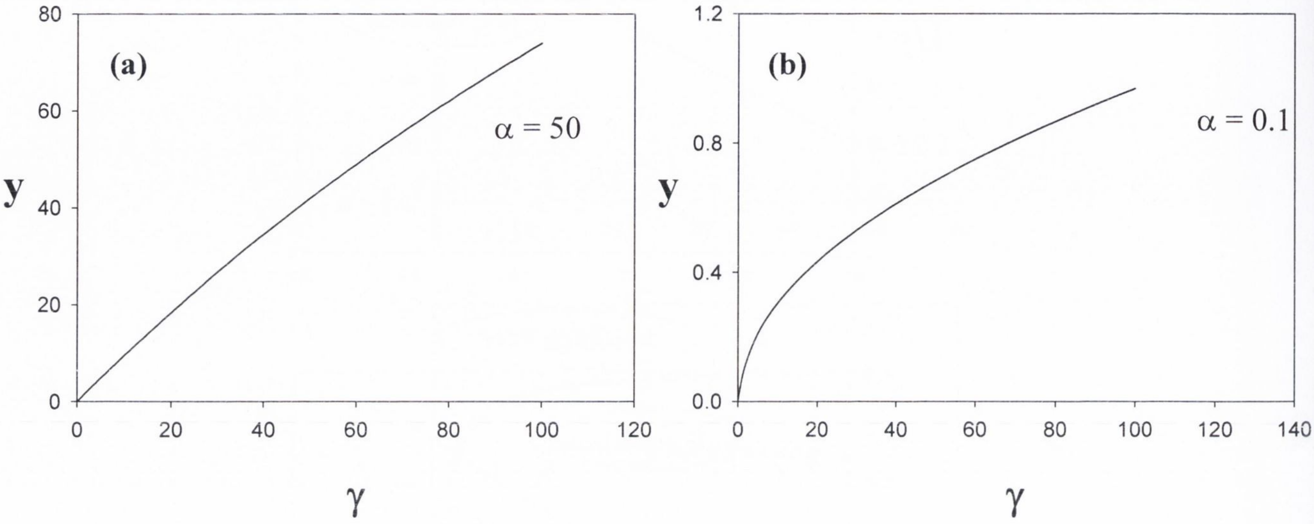

Figure 4.11; Variation of the normalised current response y calculated from eqn. 4.40 with the parameter γ for (a) = 50 and (b) α = 0.1.

Equation 4.19 may alternatively be solved using the following approximation:

$$\frac{u}{1+\alpha u} \approx \frac{\alpha + u}{(1+\alpha)^2} \tag{4.42}$$

where $0 \leq u \geq 1$.

This approximation will only be valid for certain values of α and γ. In appendix I it is shown that the approximation presented in equation 4.42 will be valid for all values of u when the Michaelis - Menten kinetics are unsaturated (i.e. when $\alpha < 1$). For saturated Michaelis-Menten kinetics, the approximation becomes inaccurate if significant substrate depletion occurs, i.e. if u falls to less than 0.8 at any point in the film. This will of course depend to the γ value. The approximation will be poor for large γ values.

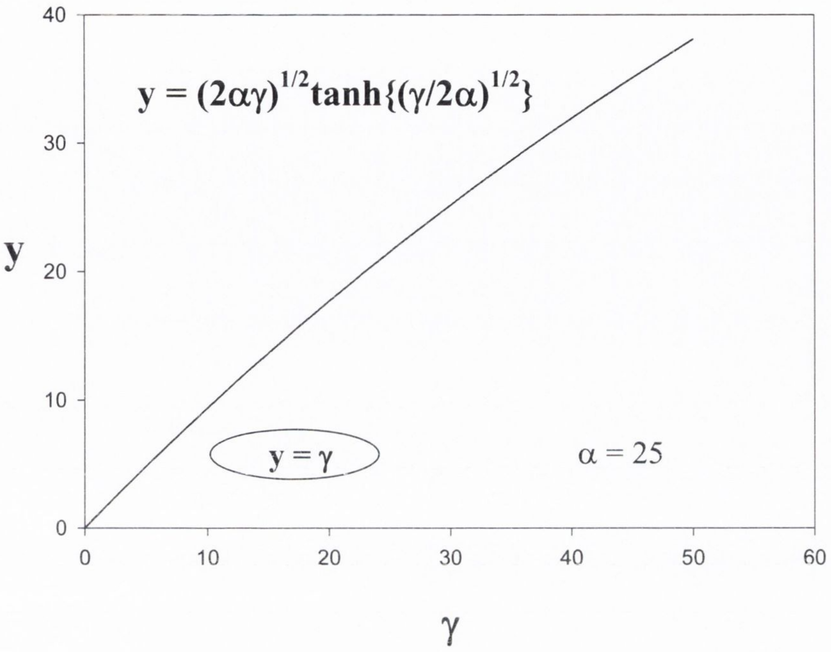

Figure 4.12; Plot of equation 4.42 obtained as a substrate of the general expression for the current response presented in equation 4.41. The expression is valid for $\alpha >> 1$ and for all γ up to a limit of $\gamma = 2\alpha$.

Using equation 4.42 it is noted that the steady state reaction diffusion equation presented in equation 4.19 reduces to:

$$\frac{d^2u}{d\chi^2} - \frac{\gamma(\alpha + u)}{(1+\alpha)^2} = 0 \tag{4.43}$$

Hence the resultant reaction diffusion is transformed into linear form which may be readily solved (see appendix II) to yield:

$$u(\chi) = (1+\alpha)\cosh\left[\frac{\sqrt{\gamma}\chi}{(1+\alpha)}\right]\operatorname{sech}\left[\frac{\sqrt{\gamma}}{(1+\alpha)}\right] - \alpha \tag{4.44}$$

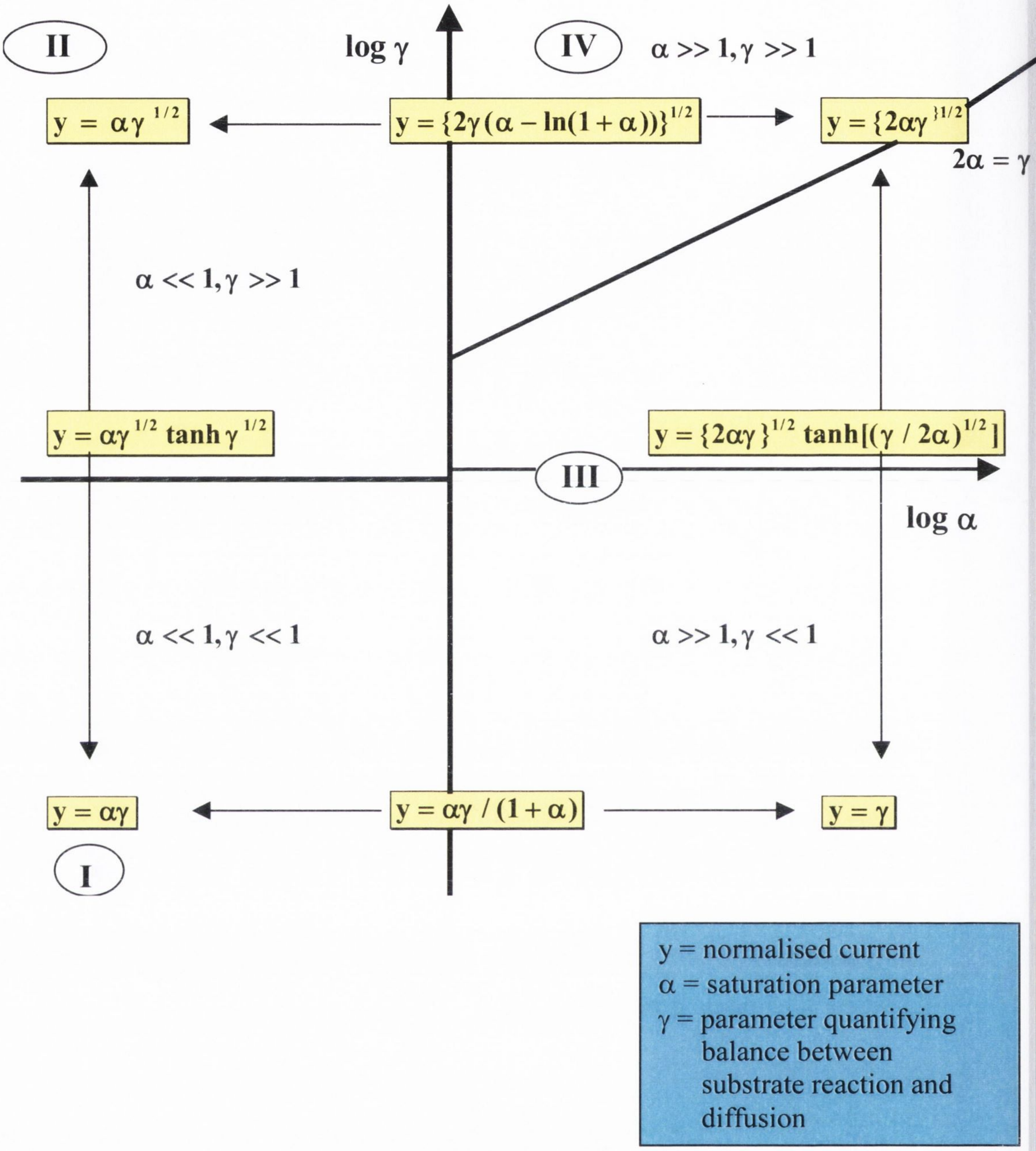

Figure 4.13; The kinetic case for the steady state reaction diffusion problem. The diagram consists of a plot of log γ vs log α. The approximate analytical expressions for the normalised current for various limiting values of α and γ are also included as insets.

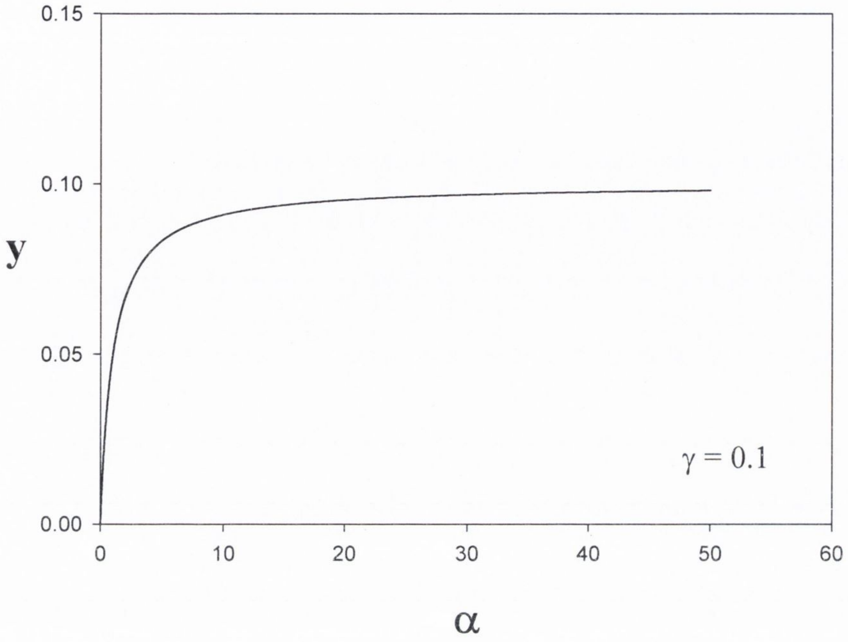

Figure 4.14; The correspondence between the current response as outlined in equation 4.45 and the simpler Michaelis-Menten expression (equation 4.39) for the current response.

It may readily be shown that the normalised current response is given by:

$$y = \alpha\left(\frac{du}{d\chi}\right)_{\chi=1} = \alpha\sqrt{\gamma}\tanh\left[\frac{\sqrt{\gamma}}{(1+\alpha)}\right] \tag{4.45}$$

When α << 1, then equation 4.45 reduces to:

$$y \approx \alpha\sqrt{\gamma}\tanh\left[\sqrt{\gamma}\right] \tag{4.46}$$

which is identical in form to equation 4.23 (see figure 4.5(a)). Hence this expression connects cases I and II. Furthermore when γ is small and for all values of α, it can be shown that $\tanh\left[\frac{\sqrt{\gamma}}{(1+\alpha)}\right] \approx \frac{\sqrt{\gamma}}{(1+\alpha)}$, and so equation 4.45 reduces to:

$$y \approx \frac{\alpha\gamma}{(1+\alpha)} \tag{4.47}$$

This is the simple Michaelis-Menten equation (connecting cases I and III) previously outlined in equation 4.39. The correspondence between equation 4.45 and equation 4.39 is presented in figure 4.14.

Alternatively when $\alpha >> 1$, equation 4.45 reduces to:

$$y \approx \alpha\sqrt{\gamma}\tanh\left[\frac{\sqrt{\gamma}}{\alpha}\right] \tag{4.48}$$

This expression differs from equation 4.41 (which connects cases III and IV), but for small γ it can be seen that equation 4.48 reduces to $y = \gamma$ which is case III. Equation 4.41 also reduces to the same result under the same conditions. Finally, it is useful to compare equation 4.45 with the expression presented in equation 4.37 which connects cases II and IV. This is done in figure 4.15 for $\gamma = 50$. It is clear that the agreement between the two expressions is very poor. This is to be expected since the approximation given in equation 4.42 breaks down when substrate depletion within the film becomes appreciable, which will happen when γ is large.

4.3.2 Inclusion of Concentration Polarisation of Substrate in Solution.

To consider the effect of substrate diffusion in solution as well as inside the polymer film it is necessary to extend the analysis of the steady state current response. In this case the boundary conditions are given by:

$$x = 0 \quad \frac{ds}{dx} = 0$$

$$x = L \quad s = \kappa s_L \tag{4.49}$$

$$x = L \quad D_F\left(\frac{ds}{dx}\right)_{x=L} = \frac{D_s}{X_D}(s^\infty - s_L)$$

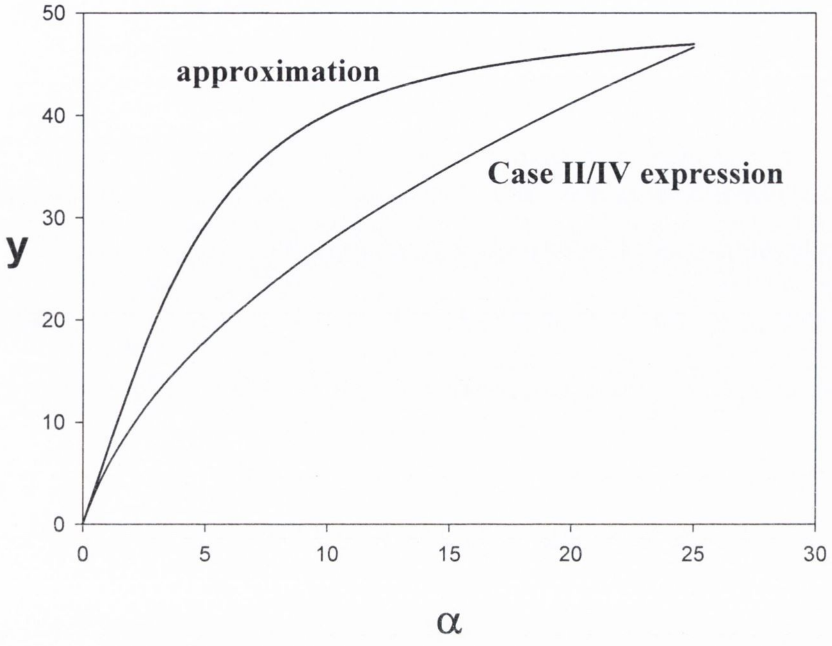

Figure 4.15; Illustration of the breakdown of the approximation given in equation 4.42 compared to the response predicted using equation 4.37, for larger values of γ.

The first boundary condition is the same as previously outlined. The second differs from that given in the previous discussion since s^{∞}, the bulk concentration of substrate has been replaced with s_L the concentration of substrate at the film / solution interface. It is also necessary to introduce a third boundary condition of flux balance at film / solution interface. In the last boundary condition expressed in equation 4.49, D_S and D_F denote the diffusion coefficients of the substrate S in the solution and film respectively, and X_D represents the diffusion layer thickness. The normalised steady state current response y and the parameter γ may be redefined *via* differentiation between D_F and D_S, as: $y = \frac{iL}{nFAK_M D_F}$ $\gamma = \frac{kL^2}{D_F}$. A diffusional rate constant k_D may be introduced as follows: $k_D = \frac{D_S}{X_D}$. This parameter quantifies the rate of substrate transport in the solution.

Now to introduce the Biot number ν as follows:

$$\upsilon = \frac{k_D L}{\kappa D_F} \tag{4.50}$$

This dimensionless parameter compares the rate of substrate diffusion in the solution to the rate of diffusion of substrate within the film. The boundary conditions can now be expressed in dimensionless terms as follows:

$$\chi = 0 \quad \frac{du}{d\chi} = 0$$

$$\chi = 1 \quad \left(\frac{du}{d\chi}\right)_1 = \upsilon\,(1 - u_1) \tag{4.51}$$

$$\chi = 1 \quad u = u_1$$

The steady state reaction diffusion problem defined by equation 4.19 and equation 4.51 may now be solved. To do this the approximation introduced in equation 4.42 is used.

As outlined in appendix III the approximate solution for the concentration profile is given by:

$$u(\chi) = u_1 \cosh\left[\frac{\sqrt{\gamma}\chi}{(1+\alpha)}\right] \mathrm{sec\,h}\left[\frac{\sqrt{\gamma}}{(1+\alpha)}\right] + \alpha\left\{\cosh\left[\frac{\sqrt{\gamma}\chi}{(1+\alpha)}\right] \mathrm{sec\,h}\left[\frac{\sqrt{\gamma}}{(1+\alpha)}\right] - 1\right\} \tag{4.52}$$

where u_i is given by:

$$u_1 = \frac{\upsilon - \dfrac{\sqrt{\gamma}\alpha}{(1+\alpha)} \tanh\left[\dfrac{\sqrt{\gamma}}{(1+\alpha)}\right]}{\upsilon + \dfrac{\sqrt{\gamma}}{(1+\alpha)} \tanh\left[\dfrac{\sqrt{\gamma}}{(1+\alpha)}\right]} \tag{4.53}$$

Hence it is clear that the u_1 factor contains the effect of external mass transfer.

The steady state current response y is given by:

$$y = \alpha\upsilon(1-u_1) = \alpha\upsilon\left\{1-\frac{\upsilon-\frac{\sqrt{\gamma}\alpha}{(1+\alpha)}\tanh\left[\frac{\sqrt{\gamma}}{(1+\alpha)}\right]}{\upsilon+\frac{\sqrt{\gamma}}{(1+\alpha)}\tanh\left[\frac{\sqrt{\gamma}}{(1+\alpha)}\right]}\right\} \tag{4.54}$$

which simplifies to:

$$y = \frac{\alpha\sqrt{\gamma}\tanh\left[\frac{\sqrt{\gamma}}{(1+\alpha)}\right]}{1+\frac{\sqrt{\gamma}}{\upsilon(1+\alpha)}\tanh\left[\frac{\sqrt{\gamma}}{(1+\alpha)}\right]} \tag{4.55}$$

This function is illustrated in figure 4.16 where y is plotted as a function of α for a given value of γ (γ=0.1) and for various values of the Biot number [37,38]. When υ is small, the effect of external diffusion is most pertinent, but when υ is large (i.e. >50) the observed normalised current response is indistinguishable from the Michaelis-Menten expression (equation 4.39) or from the Albery equation (equation 4.40). Hence when ν is large concentration polarisation in the solution may be neglected. This may also be noted from examination of equation 4.55. When υ is large then $\upsilon^{-1} \to 0$ and equation 4.55 reduces to equation 4.45.

Equation 4.55 may then be inverted to obtain the following expression:

$$\frac{1}{y} = \frac{1}{\alpha\sqrt{\gamma}}\coth\left[\frac{\sqrt{\gamma}}{(1+\alpha)}\right]+\frac{1}{\alpha(1+\alpha)\upsilon} \tag{4.56}$$

This allows a clear separation between substrate diffusion / reaction in the polymer film and substrate diffusion in the Nernst diffusion layer adjacent to the polymer film. It must be noted that equation 4.55 will be valid for all α values provided that γ is not too large. An upper limit of γ is ca. 2.

When γ is small and $\gamma^{1/2} << \alpha$ and $\alpha << 1$ then equation 4.56 reduces to a case I situation:

$$\frac{1}{y} = \frac{1}{\alpha\gamma} + \frac{1}{\alpha\upsilon} \tag{4.57}$$

Transforming into dimensioned quantities results in the following expression:

$$\frac{nFA}{i} = \frac{K_M}{k_c c_\Sigma L\kappa s^\infty} + \frac{1}{k_D s^\infty} = \frac{K_M}{k_c c_\Sigma L\kappa s^\infty} + \frac{1}{F_L s^\infty \omega^{1/2}} \tag{4.58}$$

In this expression it is assumed that mass transport in solution is controlled *via* use of a rotating disc electrode, and the mass transport rate constant k_D is defined in terms of this electrode configuration. It is recalled that for a RDE configuration $k_D = 1.55 D_s^{2/3} \nu^{-1/6} \omega^{1/2}$. The rotation speed ω is expressed in Hertz (Hz). Equation 4.58 is a simple Koutecky - Levich type expression, where the Levich factor, F_L [$F_L = 1.55 D_s^{2/3} \nu^{-1/6}$, (where ν denotes the kinematic viscosity of the solution)] has been introduced. On the other hand when γ is large then equation 4.56 reduces to:

$$\frac{1}{y} = \frac{1}{\alpha\sqrt{\gamma}} + \frac{1}{\alpha\upsilon} \tag{4.59}$$

This corresponds to a case II situation. Translating to dimensioned parameters this becomes:

$$\frac{nFA}{i} = \sqrt{\frac{K_m}{k_c c_\Sigma D_F}}\,\frac{1}{\kappa s^\infty} + \frac{1}{k_D s^\infty} = \sqrt{\frac{K_m}{k_c c_\Sigma D_F}}\,\frac{1}{\kappa s^\infty} + \frac{1}{F_L s^\infty \omega^{1/2}} \tag{4.60}$$

This predicts linear Koutecky - Levich behaviour (i^{-1} linear with $\omega^{-1/2}$). It is interesting to note that as γ becomes very large (assuming that $\alpha << 1$) then $\gamma^{-1/2} \rightarrow 0$ in equation 4.59 and the observed current response becomes totally dominated by external diffusion. This will become clear in a Koutecky - Levich plot which exhibits a zero intercept. When $\alpha >> 1$, and for small γ (case III) it is noted that equation 4.56

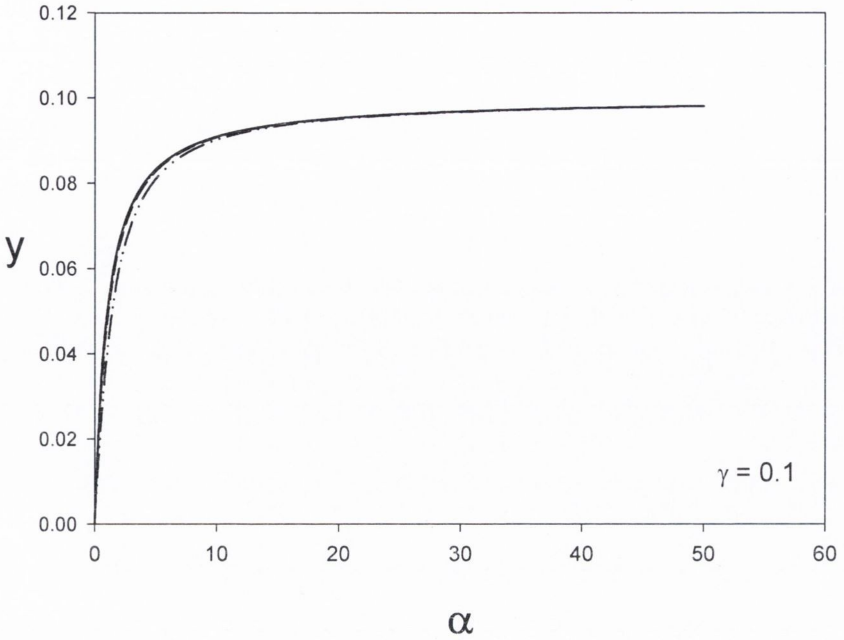

Figure 4.16; Plot of the normalised current response y as a function of the saturation parameter α form various values of the Biot number υ which quantifies substrate diffusion in the Nernst diffusion layer adjacent to the polymer film. Equation 4.55 was used to compute the curves illustrated.

reduces to:

$$\frac{1}{y} = \frac{1}{\gamma} + \frac{1}{\alpha^2 \upsilon} \qquad (4.61)$$

In terms of dimensioned parameters this becomes:

$$\frac{nFA}{i} = \frac{1}{k_c c_\Sigma L} + \frac{K_M}{\kappa s^{\infty 2} F_L \omega^{1/2}} \qquad (4.62)$$

In this case the variation of i^{-1} with $\omega^{-1/2}$ is linear, but the slope of the latter plot varies as α^{-2} rather than α^{-1} as would be predicted from a simple Koutecky - Levich expression.

As previously outlined, the approximation given in equation 4.42 does not work for the range of α and γ values. This analysis has therefore not considered the case IV situation corresponding to the case of large γ and $\alpha > 1$.

For the steady state situation it is assumed that the diffusion coefficients of reactant and product within the film are equal for simplicity

$$\begin{aligned} &\frac{\delta^2 \upsilon}{\delta \chi^2} - \frac{\gamma \upsilon}{1+\alpha \upsilon} = 0 \\ &\alpha \nu \delta \frac{\delta^2 \omega}{\delta \chi^2} - \frac{\gamma \upsilon}{1+\alpha \upsilon} = 0 \end{aligned} \tag{4.63}$$

where ω denotes the normalised product concentration given by $\omega = \frac{p}{\kappa s^{\infty}}$ and p represents the concentration of product in the film. The boundary conditions for a potentiometric sensor are given by:

$$\begin{aligned} &\chi = 0, \quad \frac{du}{d\chi} = 0 \quad \text{and} \quad \frac{d\omega}{d\chi} = 0 \\ &\chi = 1, \quad u = 1 \quad \text{and} \quad \omega = 1 \end{aligned} \tag{4.64}$$

Adding the two expressions in equation 4.63 the following is obtained

$$\frac{d^2 u}{d\chi^2} + \frac{d^2 \omega}{d\chi^2} = 0 \tag{4.65}$$

This expression may be readily integrated twice, using the boundary conditions presented in equation 4.64, to obtain the following relationship between u and ω:

$$\omega(\chi) = 1 - u(\chi) \tag{4.66}$$

Hence the concentration profile of product through the film may be readily evaluated. It can be shown that:

$$\omega(\chi)=\left[(1-\alpha)\cosh\left(\frac{\sqrt{\gamma}\chi}{1+\alpha}\right)\operatorname{sec h}\left(\frac{\sqrt{\gamma}}{1+\alpha}\right)-\alpha\right]=$$
$$(1+\alpha)\left[1-\operatorname{sec h}\left(\frac{\sqrt{\gamma}\chi}{1+\alpha}\right)\operatorname{sec h}\left(\frac{\sqrt{\gamma}}{1+\alpha}\right)\right] \qquad (4.67)$$

In particular, the sensor device measures the product concentration ω_0 at $\chi=0$ and so it is noted that:

$$\omega_0=(1+\alpha)\left[1-\operatorname{sec h}\left(\frac{\sqrt{\gamma}}{1+\alpha}\right)\right] \qquad (4.68)$$

When $\alpha<<1$, equation 4.68 reduces to:

$$\omega_0\approx 1-\operatorname{sec h}(\gamma) \qquad (4.69)$$

whereas when a>>1, the following is obtained

$$\omega_0=\alpha\left[1-\operatorname{sec h}\left(\frac{\sqrt{\gamma}}{\alpha}\right)\right] \qquad (4.70)$$

When examining amperometric responses at high substrate concentrations, to maintain experimental/theoretical correlation the following general equation is used

$$y=a\sqrt{2}\sqrt{b\left[\frac{s^{\infty}}{c}-\ln\left(1+\frac{s^{\infty}}{c}\right)\right]}\tanh\left(\frac{\frac{s^{\infty}b}{c}}{\frac{s^{\infty}}{c}\left\{2\left[\frac{s^{\infty}}{c}-\ln\left(1+\frac{s^{\infty}}{c}\right)\right]\right\}}\right) \qquad (4.71)$$

where a, b and c are given by: $a=\frac{nFAK_M D_S}{L}$, $b=\frac{k_c c_\Sigma L^2}{K_M D_S}$, $c=K_M$. L is the polymer layer thickness and c_Σ is the bulk substrate concentration.

4.4 Conclusions

The steady state amperometric response for a polymer modified electrode system which exhibits Michaelis-Menten kinetics has been discussed in some detail. Approximate analytical solutions to the non-linear reaction diffusion equation have been presented and the limits of validity of each solution evaluated. Finally the concentration polarisation of substrate in solution was considered.

Chapter 5 exhibits the experimental verification of some of the above analysis, using the electro-oxidation of different neurotransmitters at a PMB modified glassy carbon electrode as a model electrode process. The theoretical model presented for the steady state amperometric response is used to quantify the steady state current response profiles, recorded under batch amperometric conditions. Experimental batch amperometry data was compared to theoretical current responses given by equation 4.40. Non-linear least squares fitting of equation 4.40 to the experimental data yielded numerical values for the fundamental kinetic parameters defining the Michaelis-Menten mechanism.

4.5 References

[1] A. R. Hillman, *"Electrochemical Science and Technology of Polymers"*, ed. R. G. Linford, Elesevier Applied Science, Amsterdam, 1987.

[2] M. E. G. Lyons, *Ann. Rep. C. R. Soc. Chem.*, **87**, 119, 1990.

[3] M. E. G. Lyons *"Electroactive Polymer Chemistry: Fundamentals and Applications"*, Plenum Press, NY, 237, 1994.

[4] G.P. Evans, in Advances in Electrochemical Science and Engineering, eds, H. Gerisher, C. W. Tobias, *VCH Weinheim*, **1**, 1990.

[5] S. A. Wring, J. P. Hart, *Analyst*, **119**, 805, 1994.

[6] R. W. Murray, (Ed.), *"Molecular Design of Electrode Surfaces Techniques of Chemistry Series"*, Wiley Interscience, NY, Vol. XXII. 1992.

[7] F. Beck, H. Schultz, *Electrochim. Acta*, **29**, 1569, 1984.

[8] C. P. Andrieux, J. M. Savaent, R. W. Murray, (Ed), *"Molecular Design of Electrode Surfaces"*, Techniques of Chemistry Series, Wiley Interscience,

NY, Vol. XXII, 1992.

[9] L. Gorton, A. Torstenssen, H. Jaegfeldt, G. Johansson, *J. Electroanal. Chem.*, **161**, 103, 1984.

[10] L. Gorton, A. Torstenssen, H. Jaegfeldt, G. Johansson, *J. Electroanal. Chem.*, **196**, 81, 1985.

[11] L. Gorton, *J. Chem. Soc.*, 86, 1245, 1986.

[12] L. D. Burke, W. A. O'Leary, *J. Chem. Soc.*, **135**, 1965, 1988.

[13] M. E. G. Lyons, C. H. Lyons, D. E. Mc Cormack, T. Mc Cabe, W. Breen, J. F. Cassidy, *Anal. Proc.*, **28**, 104, 1991.

[14] M. E. G. Lyons, C. H. Lyons, A. Michas, P. N. Bartlett, *J. Electroanal. Chem.*, **351**, 245, 1993.

[15] M. E. G. Lyons, C. H. Lyons, A. Michas, P. N. Bartlett, *Analyst*, **117**, 1271, 1992.

[16] M. E. G. Lyons, D. E. Mc Cormack, A. Michas, C. H. Lyons, P. N. Bartlett, *Key Eng. Mater.*, **72 / 74**, 477, 1992.

[17] M. E. G. Lyons, C. A. Fitzgerald, M. R. Smyth, *Analyst*, **119**, 855, 1994.

[18] E. J. M. O' Sullivan, J. R. White, *J. Electrochem. Soc.*, **136**, 2576, 1989.

[19] W. J. Albery, A. R. Hillman; *Ann. Rep. Prog. Chem. C,* 377, 1981.

[20] W. J. Albery, A. R. Hillman; *J. Electroanal. Chem.,* **170**, 27, 1984.

[21] C. P. Andrieux, J.-M. Saveant; *J. Electroanal. Chem.,* **93**, 163, 1978.

[22] C. P. Andrieux, J.-M. Saveant; *J. Electroanal. Chem.,* **111**, 377, 1980.

[23] C. P. Andrieux, J. M. Dumas-Bouchiat, J.-M. Saveant; *J. Electroanal. Chem.,* **114**, 159, 1980.

[24] C. P. Andrieux, J. M. Dumas-Bouchiat, J.-M. Saveant; *J. Electroanal. Chem.,* **131**, 1, 1982.

[25] C. P. Andrieux, J.-M. Saveant; *J. Electroanal. Chem.,* **134**, 163, 1982.

[26] C. P. Andrieux, J.-M. Saveant; *J. Electroanal. Chem.,* **142**, 1, 1982.

[27] C. P. Andrieux, J. M. Dumas-Bouchiat, J.-M. Saveant; *J. Electroanal. Chem.,* **169**, 9, 1984.

[28] J. C. Greer, C. A. Fitzgerald, T. Bannon, P. N. Bartlett, M. E. G. Lyons; *Analyst,* **121,** 715 ,1996.

[29] T. Bannon, G. Hinds, S. Rebouillat, M. E. G. Lyons; *Analyst*, **123**, 1947, 1998.

[30] J. A. Leddy, A. J. Bard, J. T. Maloy, J.-M. Saveant; *J. Electroanal. Chem.,* **187**, 205, 1985.

[31] A. R. Hillman; *"Electrochemical Science and Technology of Polymers"*, [Linford, R. G., ed.], Vol. 1, Ch. 4, Elsevier, 1987.

[32] K. J. Laidler, *"Chemical Kinetics"*, 3rd edition, Harper and Row, NY, 1987.

[33] P. N. Bartlett, R. G. Whitaker, *J. Electroanal. Chem.*, **224**, 37, 1987.

[34] P. N. Bartlett, P. Tebbutt, C. H. Tyrrell, *Anal. Chem.*, **64**, 138, 1992.

[35] P. N. Bartlett, P. Tebbutt, R. G. Whitaker, *Prog. React. Kinet.*, **16**, 55, 1991.

[36] W. J. Albery, P. N. Bartlett, B. J. Driscoll, R. B. Lennox, *J. Electroanal. Chem.*, **323**, 77, 1992.

[37] W. J. Albery, A. E. G. Cass, Z. X. Shu, *Biosens. & Bioelectron.*, **5**, 367, 1990.

[38] R. Aris, in *"The Mathematical Theory of Reaction and Diffusion in Permeable Catalysis"*, Clarendon press, Oxford, 2 vols., 1975.

CHAPTER 5

REDOX CATALYSIS
AT THE
PMB/GC ELECTRODE

5.1 Introduction

In mammalian tissue ascorbic acid (AA) is vital to immune response and wound healing but cannot be synthesised by some mammals including humans. It has been shown that AA is an antioxidant, aids in detoxification and improves iron absorption [1]. Ascorbic acid was also found to play an important role in the body as a free-radical scavenger, which may help to prevent free-radical induced diseases such as cancer and Parkinson's disease. The content of ascorbic acid in biological fluids can be used to asses the oxidative stress in human metabolism [2].

Dopamine (DA), norepinephrine (NE), and epinephrine (EP) are very important catecholamine neurotransmitters in the mammalian central nervous system (CNS). Abnormal catecholamine levels in the CNS have been linked to many brain disorders, such as Parkinson's disease [2] and schizophrenia [3]. Information regarding the action of antipsychotic drugs can be gleaned from its concentration flux analysis. Therefore, the accurate quantitative determination of catecholamine levels in biological fluids provides important information on its physiological functions and the diagnosis of some diseases in clinical medicine. *Yuan et al.* [4] have reported on the use of a poly(2-picolinic acid) modified glassy carbon electrode for the detection of dopamine. The electrochemical behaviour of epinephrine at a modified electrode [5,6] and the electrocatalytic oxidation of norepinephrine by a Nafion® chemically modified electrode has been reported [7,8].

In reality though, AA coexists in excess with catecholamines in the extracellular fluid of the CNS. It can be oxidised at a potential close to that of catecholamines at most solid bare electrodes, resulting in overlapping voltammetric responses. Therefore it is a challenging task to detect and quantify catecholamine concentrations in the presence of AA. Many authors have reported the successful quantitative determination of AA using polymer modified electrodes [9-11]. Polymer modified electrodes have been widely used in the development of electrochemical biosensors, as techniques used for film fabrication are advantageous for their applications [12,13]. Electropolymerisation of conducting polymers generally results in polymer films which are uniform and adhere strongly to the electrode surface. In addition, polymer films can be deposited onto a small area with a high degree of conformity, this aspect being particularly important in manufacturing microsensors.

Advantages of conducting polymers include their wide potential window for interfacial electron transfer, controllable thickness, and controllable level of doping.

The permselective properties of many polymers towards negatively charged compounds, have allowed their use as a barrier in the detection of different catecholamines, in the presence of AA. The efficiency of some polymeric films to effectively reject the negatively charged ascorbic acid (AA) and 3,4-dihydroxyphenylacetic acid (dopac) has been widely demonstrated [14-19]. *Wu et al.* [15] have shown the selective determination of DA at glassy carbon electrodes modified with an over-oxidized poly (N-acetylaniline). The authors Ogorevc and Mo [16] have recently proposed the use of carbon fiber microelectrodes coated with overoxidized poly-(1,2-phenylenediamine) to obtain a highly sensitive and selective DA quantification. *Rubianes et al.* reported on the use of a glassy carbon electrode modified with a melanin-type polymer electrogenerated from L-dopa for the highly selective DA quantification [17]. The authors Chen and Link have shown the electrocatalytic activity of polymerized luminal film-modified electrodes that allows the selective measurement of DA and AA [18]. *Ohsaka et al.* have reported on the use of a glassy carbon electrode modified with an electropolymerized film of N,N-dimethylaniline for the sensitive and selective quantification of DA [19].

Films can also be deactivated deliberately [20-24], and can greatly improve selectivity and sensitivity of voltammetric analyses of ionic analytes. In polypyrrole films, negative charges and porosity are introduced into the film during deactivation which enables the permeation of cationic analytes [21-24]. In essence, deactivation of conducting polymer films converts them into selective ion-exchange polymer films. Redox polymers can form charged films when polymerised from the ionic monomeric form, and hence can also act as selective barriers to particular analytes. Many authors have published their findings on redox polymer modified electrodes [25-30]. The phenothiazine derivatives azur A and methylene blue, polymerised on platinum and gold electrodes, have been used to achieve a quasi-reversible electrochemistry of haemoglobin [26,29]. *Karyakin et al.* reported on a dehydrogenase electrode based on the electropolymerisation of methylene blue (PMB) on a glassy carbon electrode [30].

There are certain criteria that should be met when considering the value of a good biosensor:

1) Do enough people want or need to have a sensor for the analyte of interest?

2) Does the sensor present clearly defined advantages over the older technology, or is it simply a small variation on a well established theme? Unless this new sensor is so innovative that it is interesting for its conception alone, the following five issues should be addressed.

3) The chemical stability of each component used to prepare the sensor must be considered.

4) The stability of the sensor itself needs to be thoroughly tested both in use and in storage at a range of temperatures. The prepared sensor should be stabile for at least six months for any practical commercial application.

5) If the sensor is intended for biological samples, it should be tested in biological samples and not just aqueous buffers.

6) If a sensor is intended to be used in tissue it must be biocompatible. The tissue reaction to the foreign implant must be considered both for its effect on the sensor and on the organism.

7) The dynamic range of the sensor must be tested appropriate to the anticipated analyte concentration in real samples. The concentration of catecholamines in brain tissue is of the order of nanomoles.

Polymethylene blue is a redox polymer, easily electropolymerised to electrode surfaces. This alone is not a sufficient criterion for developing a sensor for ascorbic acid and catecholamines. In order for catalytic oxidation of said analytes by the PMB/GC electrode to occur, the E_0 value of the modified electrode must be less anodic than those of the analytes of interest. The E^0 values of the analytes, therefore, have to be elucidated and compared to that of the PMB/GC electrode. Table 5.1 shows the E^0 values for the PMB/GC electrode, AA, DA, EP and NE in 0.1M

	PMB/GC	**AA($E_{P,OX}$)**	**DA**	**EP**	**NE**
E^0 / V	**0.115**	**0.321**	**0.292**	**0.312**	**0.391**

Table 5.1;E^0 values determined using cyclic voltammetry (Data shown in Section 5.3) for PMB/GC (film thicknesses, L = 6.77±0.36 x 10^{-8} cm) electrode and for the redox behaviour of Dopamine(DA), Epinephrine(EP), Norepinephrine(NE) and the oxidation potential for Ascorbic Acid(AA) at a GC electrode in 0.1 phosphate buffer, pH 7.

phosphate buffer obtained at a bare GC electrode using cyclic voltammetry. Data for AA and catecholamine redox behaviour at the bare GC electrode is presented in Section 5.3. We observe that the E^0 value for the PMB/GC electrode is less anodic than those of the analytes. Catalysis of analyte oxidation by the modified electrode is possible and so developing the PMB/GC sensor for ascorbic acid and catecholamine detection is worth pursuing.

Having decided to investigate the PMB/GC electrode as a sensor for catecholamines, the parameters for the best modified electrode were determined. Polymer coatings can tune the selectivity of the electrodes as sensors but conversely, the response time of the sensors can decrease. Diffusion coefficients of molecules in the polymers tend to be much slower than those in the solution, and the resultant delay in response time can result in distortions in the cyclic voltammograms. Therefore polymer layer thickness can play a vital part in sensor performance. As previously determined, the optimum layer thickness for the sensing qualities of a PMB modified GC electrode, was 20 potential deposition cycles

In this body of research we report on the sensing properties of electrogenerated poly(methylene blue) modified glassy carbon (PMB/GC) electrodes to the catecholamines, DA, E and NE, in addition to AA. Figure 5.1 shows the typical voltammetric response of the PMB/GC electrode to each of the analytes. AA has a different oxidation potential than the catecholamines at the PMB/GC electrode and so selective determination may be possible. The analytical applications of these polymeric layers were evaluated in connection with the selective detection of DA over AA.

5.2 Cyclic Voltammetric analysis of Ascorbic Acid at a PMB/GC electrode

The electrochemical oxidation of AA, at pH 7, involves the net loss of two electrons and two protons [31]. At a bare glassy carbon electrode the potentially driven oxidation is irreversible (Scheme 5.1)

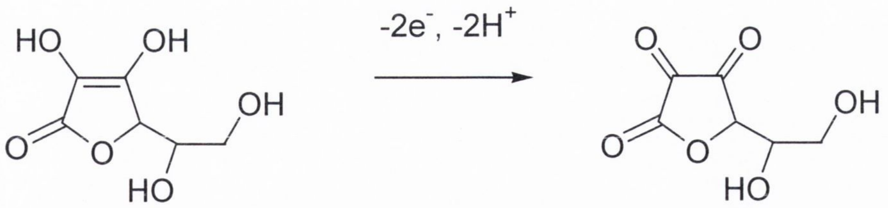

Scheme 5.1; The irreversible 2e$^-$ oxidation of ascorbic acid at a bare glassy carbon electrode.

Typical cyclic voltammograms for a range of scan rates, of 1mM AA in 0.1M phosphate buffer solution (PBS), pH 7, at a GC electrode are shown in figure 5.2. The AA irreversible oxidation peak potential (Ep,ox) at the bare GC electrode is ca. +0.26 V at ν = 20 mV, a potential that correlates well with literature values [32]. The oxidation potential remains relatively constant with increasing scan rate up to ν = 200 mV s^{-1}. This observation is indicative of a system with kinetics that is under mass transport control, and not limited by electron transfer at the electrode surface.

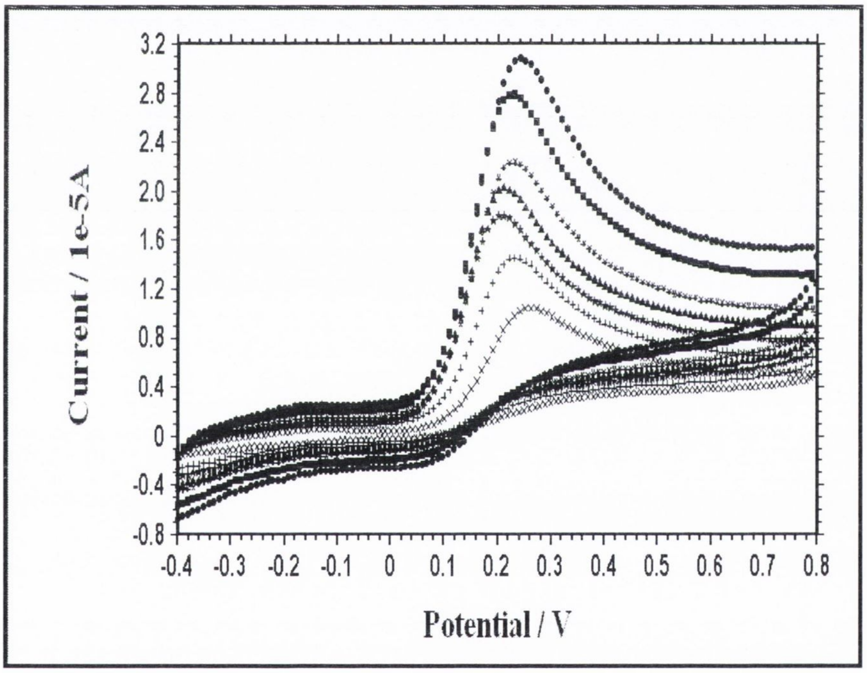

Figure 5.2; Cyclic voltammograms of 1 x 10^{-3} M Ascorbic Acid in 0.1 M PBS (pH 7) at a bare GC electrode. Scan rates, ν = (✕) 20, (+) 40, (★) 60, (▲) 80, (✱) 100, (■) 150 and (●) 200 mV s^{-1}.

When the PMB/GC is cycled in 0.1M PBS the oxidation peak potentials for the monomeric LMB/MB and polymeric LMB/MB redox couples are evident at, -0.1 and +0.1 V, respectively (Figure 5.3).

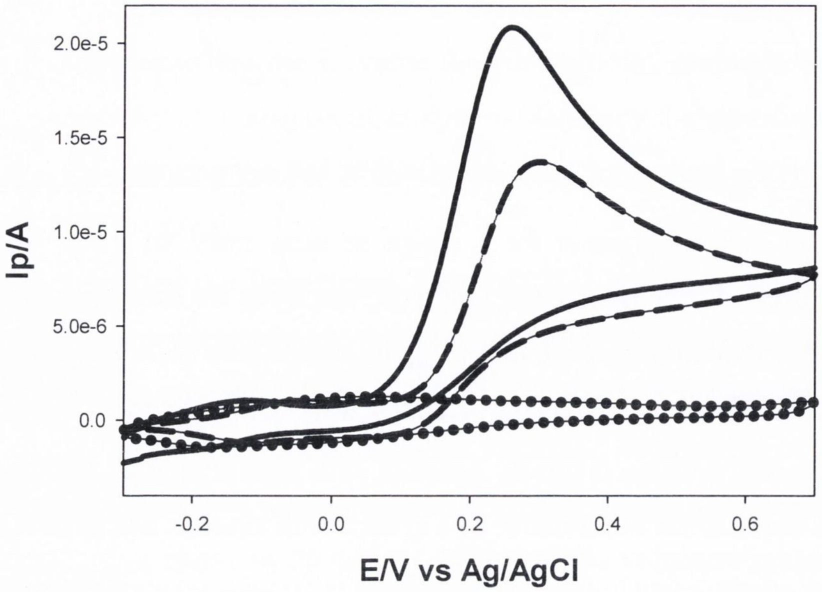

Figure 5.3; Cyclic voltammograms of, (—) 2mM Ascorbic Acid + 0.1 M PBS at the bare GC, (- -) 2mM Ascorbic Acid + 0.1 M PBS at the PMB/GC electrode, and (●) 0.1 M PBS, at the PMB/GC electrode. Scan rate, ν = 20 mV s^{-1}, and pH = 7. PMB film thicknesses, L = 6.35±0.27 x 10^{-8} cm.

Similar peak potentials for the MB/LMB and PMB redox couples are observed in a 2mM AA solution, with the oxidation of AA occurring at a potential of ca. +0.3 V. The solid line CV in Figure 5.3 is the oxidative response of 2mM AA at a bare GC electrode, with an oxidation potential ca. 0.08V less anodic than at the PMB/GC. The AA oxidation currents are greatly diminished at the modified GC and the more anodic oxidation potential suggests a kinetic inhibition. However a small catalytic effect is evident at the PMB/GC electrode, with the AA oxidation starting at the same potential as the polymer film oxidation.

The cyclic voltammograms for a range of scan rates, of 2mM AA in 0.1M phosphate buffer solution (pH 7) at the PMB modified GC electrode, are shown in Figure 5.4. The $E_{P,OX}$ of AA at the PMB/GC electrode increased with increasing scan rate from, ca. +0.3 V (at ν = 20 mV s^{-1}), to ca. +0.44 V (at ν = 200 mV s^{-1}).

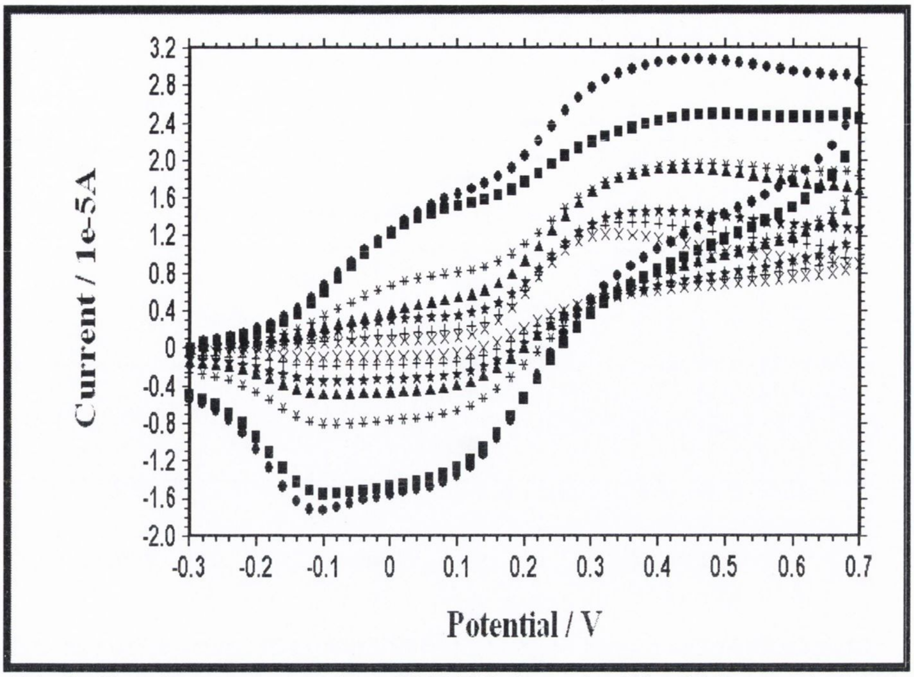

Figure 5.4; Cyclic voltammograms using a PMB/GC electrodes (film thicknesses in the range, L = 6.12±0.6 x 10^{-8} cm) in 2 x 10^{-3} M Ascorbic Acid and 0.1 M PBS (pH 7). Scan rates, ν = (✕) 20, (+) 40, (★) 60, (▲) 80, (✱) 100, (■) 150 and (●) 200 mV s^{-1}.

Positive shifts in $E_{P,OX}$ with increasing scan rate indicate a kinetic limitation in the reaction between AA and the PMB modified GC electrode. The observed shift for Ep,ox at the PMB/GC electrode was ca. +0.13 V, over the range of scan rates performed. The electron transfer kinetics of the AA oxidation can thus be classified as a mass transport governed process, occurring *via* the permeation of AA through the PMB film to the electrode surface. It is likely then that the electron exchange occurs either at the electrode/polymer interface or throughout the PMB film, and not at the polymer/solution interface. The cation MB, when polymerised, is thought to form a film exhibiting a slightly positive environment. One might expect a catalytic effect through the ionic attraction between the AA anion and the film to occur. This may indeed be the case to a certain extent, reflected in the anodic oxidation potentials exhibited at the PMB/GC electrode. But overall an inhibiting effect on the current response is observed. This inhibition comes about from the slight ionic attraction between the AA anions and the cationic film redox centers, retarding diffusion of analyte to the electrode surface.

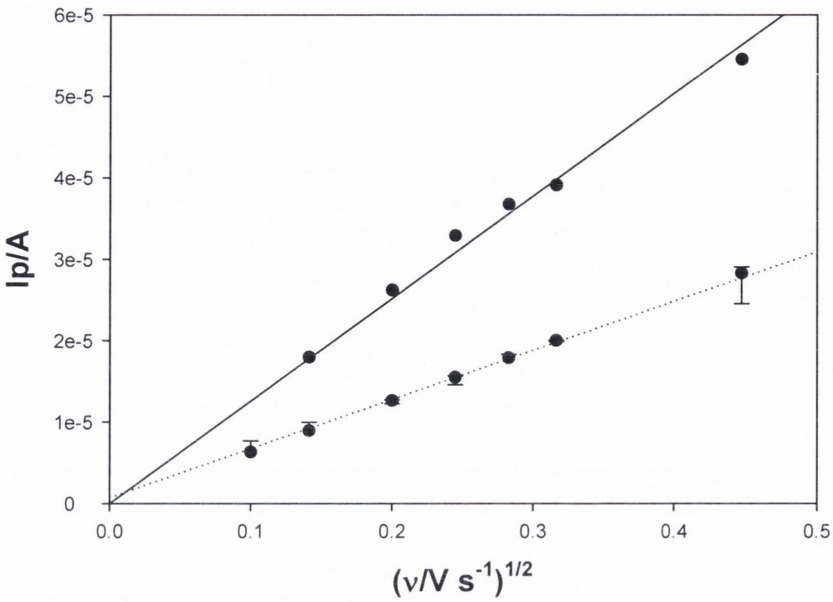

Figure 5.5; Randles-Sevcik plots for 2mM Ascorbic Acid + 0.1M PBS at the (—) bare GC and the error corrected at the (- -) PMB/GC electrode. Linearity is observed form the range 10-200 mV s^{-1}, for the bare GC but some deviation occurs at 200 mV s^{-1}, for the PMB/GC electrode. Data taken from averaged (n = 5) oxidation currents with typical CVs shown in figures 5.2 and 5.4.

The Randles-Sevcik plot for the oxidation of 2mM AA at the bare GC electrode (Figure 5.5), linear and passing through the origin, yields a diffusion coefficient of 1.67 x 10^{-6} cm^2 s^{-1} which is comparable with the literature values of 5.3 x 10^{-6} cm^2 s^{-1} [33] and 6.5 x 10^{-6} cm^2 s^{-1} [34]. The error corrected (n = 5) Randles-Sevcik plot for the oxidation of 2mM AA at the PMB/GC electrode is also displayed in figure 5.5. The peak currents vary linearly with square root of the scan rate in the range 10-100 mV s^{-1}, indicating the electrode reaction is indeed diffusion controlled [35(a)]. A kinetic limitation is evident in the small non-zero intercept. At 200mV/s, the current output due to AA oxidation, on average, is diminished, as the experimental timescale is too rapid for diffusion of fresh AA to the polymer/electrode interface or for oxidation to occur in the film reaction layer.

Ignoring the outliers at 200 mV s^{-1}, the R-S slope for AA at the PMB/GC electrode is smaller than that for the bare GC electrode. By dividing the R-S slope of the PMB oxidised AA by the R-S slope at the bare GC electrode, we can determine an average (n = 5 experiments) partition coefficient of 0.467±0.13. Experimental evidence therefore suggests that the PMB/GC electrode does exhibit a slight catalytic oxidation of AA. The PMB film either behaves as a permeable membrane, allowing AA oxidation to occur at the polymer/electrode interface, or AA oxidation occurs in a reaction layer throughout the polymer film. Preconcentration of the AA in the film is also a possibility, and is taken into account when calculating the kinetic parameters later in this chapter.

Another point to note is the effect of pH on AA oxidation in a phosphate buffer solution. At pH > 6.5, the low proton availability for MB redox process has a retardation effect on AA oxidation [36]. Conversely, above AA's pKa value (*ca.* 4.5), the oxidation process only involves the loss of one proton as AA exists as AH^- not AH_2 [37].

5.3 Cyclic Voltammetric behaviour of Catecholamines

Adams and co-workers [38] characterised the electrochemical oxidation of catecholamines in aqueous solution at carbon paste electrodes. The overall reaction is assigned an ECE mechanism [39] shown in scheme 5.2. Direct electrochemical oxidation of the catecholamine (CA) to the o-quinone (OQ) form at an electrode occurs *via* the loss of two electrons and two protons (reaction 1). This anodic oxidation peak was assigned A_1 in the cyclic voltammograms. The corresponding peak C_1, in the voltammograms, describes the reduction of o-quinone back to the catecholamine. The o-quinone has an electron deficient ring and an electron donating amine group. If the amine group is deprotonated, a 1,4 Michael addition resulting in a cyclization reaction (reaction 2) can occur, forming the leucoaminochrome (LAC) species. The leucoaminochrome is easily oxidised to the aminochrome (AC) form (reaction 3). This oxidation is a homogeneous electron transfer reaction with the o-quinone in solution [39]. The aminochrome can then be reduced at the electrode back to leucoaminochrome and is identified as a second, more cathodic voltammetric peak, assigned C_2 [38].

The rate for the cyclization reaction for each catecholamine varies and follows the order dopamine < norepinephrine < epinephrine. The apparent rate constants calculated for the intracyclisation reaction are; dopamine, $0.13\pm05\ s^{-1}$, norepinephrine, $0.98\pm0.52\ s^{-1}$, and epinephrine, $87\pm10\ s^{-1}$ [40]. These differences in rate can be observed through cyclic voltammetry measurements of catecholamines at scan rates under 300 V/s [39], and the results obtained are outlined in this section.

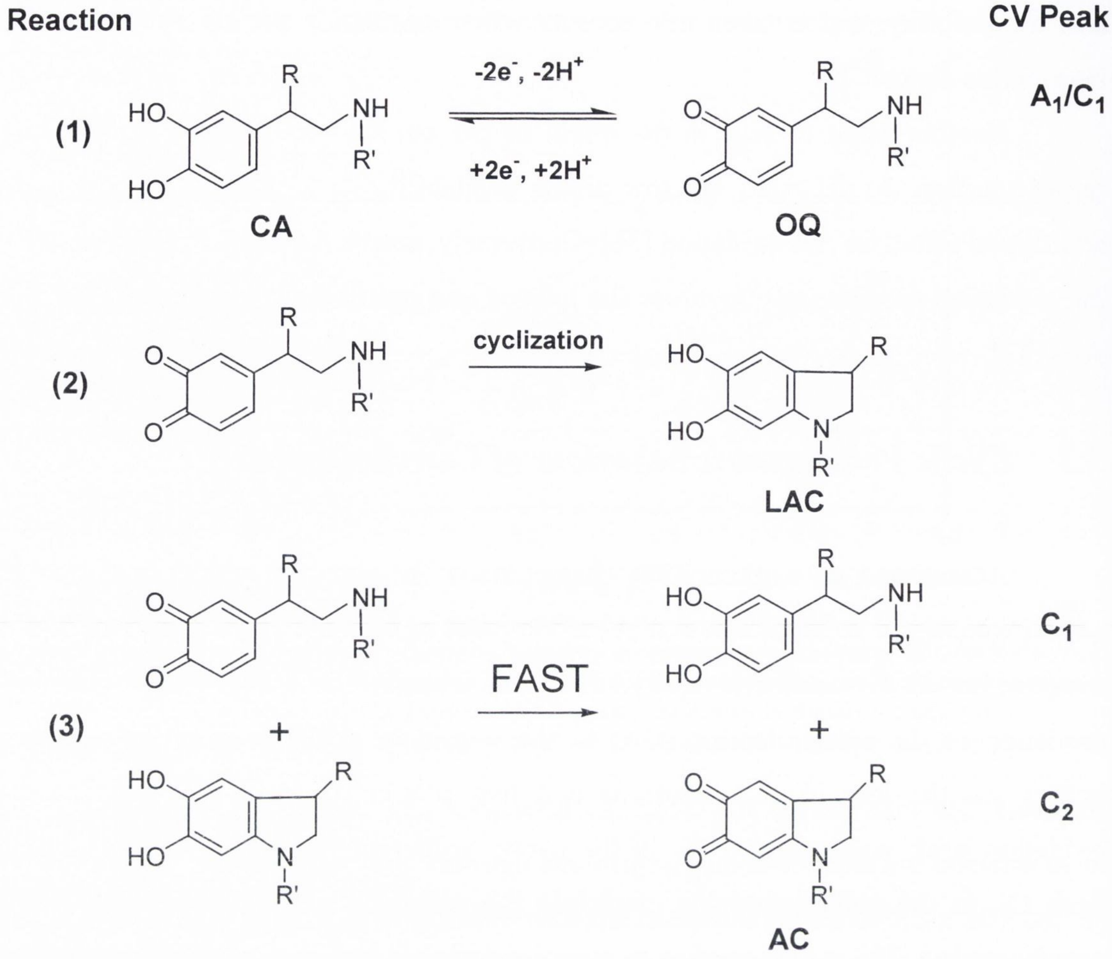

Scheme 5.2; Mechanism of catecholamine disproportionation. For each of the catecholamines, R and R' are, respectively, as follows: Dopamine, H, H, Norepinephrine, OH, H, Epinephrine, OH, CH_3. CA = catecholamine, OQ = o-quinone, LAC = leucoaminochrome, AC = aminochrome.

5.3.1 Cyclic Voltammetric analysis of Dopamine at a PMB/GC electrode

The anodic oxidation of dopamine to dopamine-quinone corresponds to a two-electron, two proton process (reaction 1, Scheme 5.2), and the oxidation peak is assigned A_1 in figure 5.6. The cyclic voltammogram of dopamine (DA) shows a quasi-reversible character. The anodic peak potential is +0.34V at ν = 10mV/s, and shifts slightly positively to ca. +0.36V at ν = 200mV/s, indicating only a subtle kinetic constraint. The corresponding reduction of DA-quinone, peak C_1, back to dopamine occurs at *ca.* +0.28 V. A second reduction peak is observed at ca. -0.1 V. This peak is due to the reduction of dopachrome to leuco-dopachrome and is assigned C_2. This peak is more pronounced at lower scan rates and becomes less prominent as the scan rate reaches 200mV s^{-1}. The redox potentials compare to those found in the literature for a bare glassy carbon electrode [39].

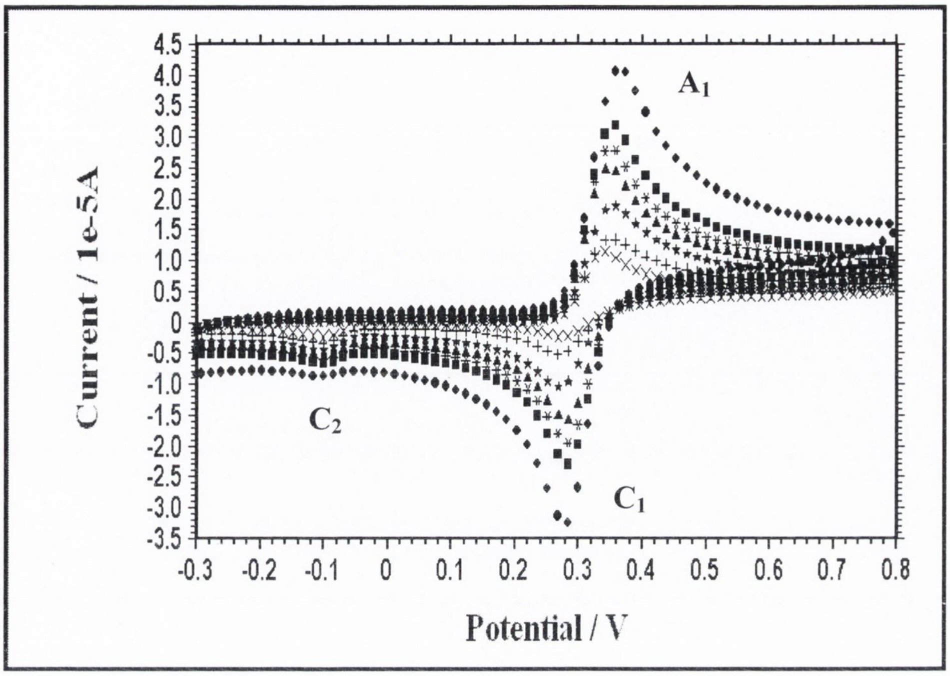

Figure 5.6; Cyclic voltammograms using a bare GC electrode in 2 x 10^{-3} M Dopamine and 0.1 M PBS (pH 7). Scan rates, ν = (✕) 20, (+) 40, (★) 60, (▲) 80, (✱) 100, (■) 150 and (●) 200 mV s^{-1}.

This can be rationalised in terms of experimental timescale. At slow scan rates the intracyclisation reaction has time to occur unhindered, but at faster scan rates, experimental time constraints govern the amount of dopachrome produced. The ΔE_P values for the redox process remain constant at *ca.* 70-80 mV for the range of scan rates, but the I_P,a/I_P,c ratio, A_1/C_1, approaches unity at higher scan rates. The summation of both reductive peaks yields a I_P,a/I_P,c ratio, A_1/C_1+C_2, just short of unity, for all scan rates. Randles-Sevcik analysis of the dopamine oxidation data yields a linear plot through the origin. A typical plot for a 2mM solution of DA in 0.1M PBS is displayed in figure 5.9.

The electrochemical behaviour of DA oxidation at the PMB/GC electrode was investigated in 0.1 M PBS and a comparison cyclic voltammogram (ν = 20 mV s^{-1}), is presented in Figure 5.7. At the PMB/GC electrode, a DA oxidation peak is observed at, $E_{P,OX}$ = +0.43 V, and like AA, a slight catalytic effect by the film is observed. A well defined DA-quinone reduction peak occurs at +0.16 V. The second reduction, if present, may go at the same potential as the monomeric MB/LMB reduction peak.

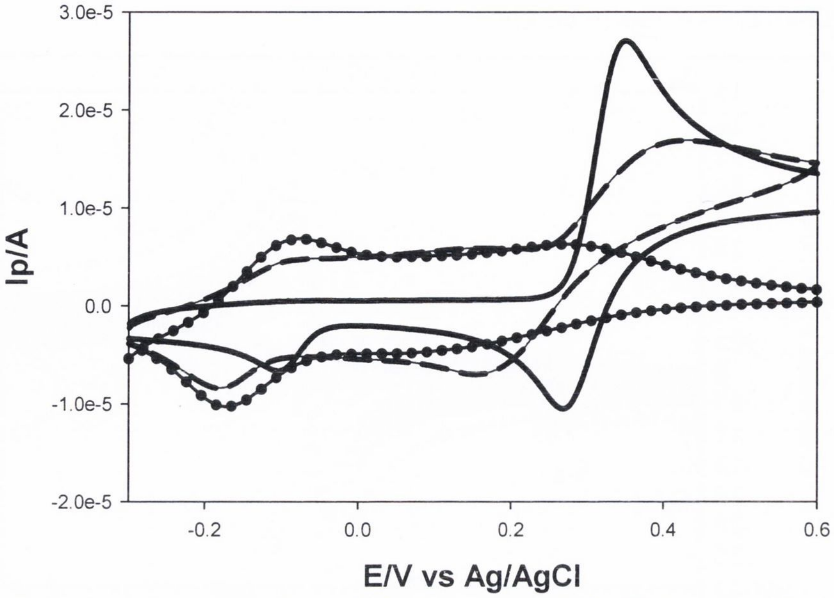

Figure 5.7; Cyclic voltammograms of, (—) 2mM Dopamine + 0.1 M PBS at a bare GC electrode, (- -) 2mM Dopamine + 0.1 M PBS and (•) 0.1 M PBS, at the PMB/GC electrode (L = 6.55±0.15 x 10^{-8} cm. Scan rate, $\nu = 20$ mV s^{-1}, and pH = 7.

The DA oxidation peak current output is diminished at the PMB/GC electrode by *ca.* 40%. $E_{P,OX}$ is shifted anodically while $E_{P,RED}$ is more cathodic, suggesting more facile kinetics at the bare electrode.

The presence of 2mM DA does not impede the mobility of electrolyte through the film, and hence charge passed through the polymer is relatively unaffected. This can be rationalised in that DA exists as a cation in pH 7, so is not ionically bound to the sites throughout the polymer film. While some coulombic repulsion may exist between the polymer charged sites and the DA cations, it is offset by the greater ionic attraction of the DA cations to the electrode surface. The effect of scan rate can be seen in Figure 5.8. The $E_{P,OX}$ becomes slightly more anodic as the scan rate increases. Again this suggests some, but not major, kinetic limitations of the PMB/GC electrode. Permeation of the DA through the film to the electrode surface is governed by a slight steric hindrance between the DA ions and the polymer matrix, and some coloumbic repulsion between DA cations and the charged sites in the film.

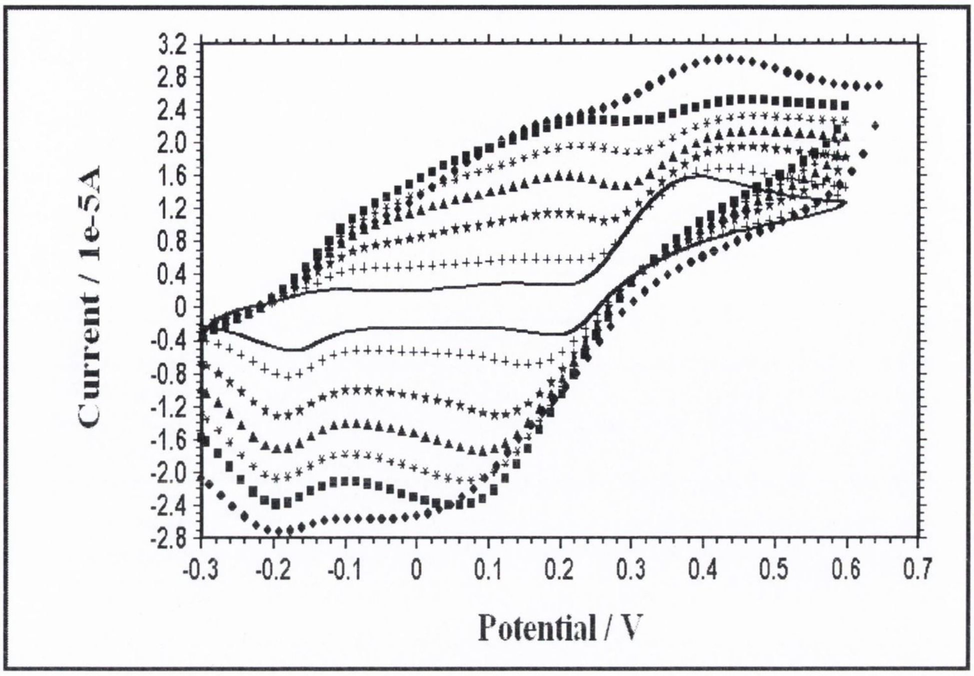

Figure 5.8; Cyclic voltammograms of the PMB/GC electrode (L in the range 5.88±0.92 x 10^{-8} cm) in 2 x 10^{-3} M Dopamine in 0.1 M PBS (pH=7). Scan rates, ν = (—) 10, (+) 20, (★) 40, (▲) 60, (✱) 80, (■) 100 and (●) 200 mV s^{-1}.

Therefore, one would expect the electron transfer kinetics to be diffusion controlled. Figure 5.9 displays plots of oxidation peak current versus square root of the scan rate for 2mM DA at the bare and modified [error corrected (n = 5)] GC electrodes. The diffusion coefficient for DA at the bare electrode at 20 ^{0}C was calculated to be 3.17±1.13 x 10^{-6} cm^2 s^{-1}. This is in good agreement with values found in the literature [32,41-43], which range from, 2.7–6.9 x 10^{-6} cm^2 s^{-1}, in various aqueous media and temperatures.

The Randles-Sevcik plot for the PMB/GC electrode exhibits excellent linearity, thus confirming the observation that the electron transfer kinetics is diffusion controlled. The small non-zero intercept, however, does indicate some kinetic constraint. The R-S slope {$S_{R\text{-}S}$ = 6.99±2.37 x 10^{-5} A / ($V^{1/2}$ $s^{-1/2}$)}, for the modified electrode was over two times smaller than that for the bare GC electrode. Therefore the catalytic effect on the DA oxidation exhibited by the film is of negligible magnitude. This yields a partition coefficient of 0.362±0.67, which is indicates that only one third of the bulk [DA] is present in the film. A partition coefficient less than unity would suggest the polymer film extends into the solution, so some degree of DA catalysis does occur.

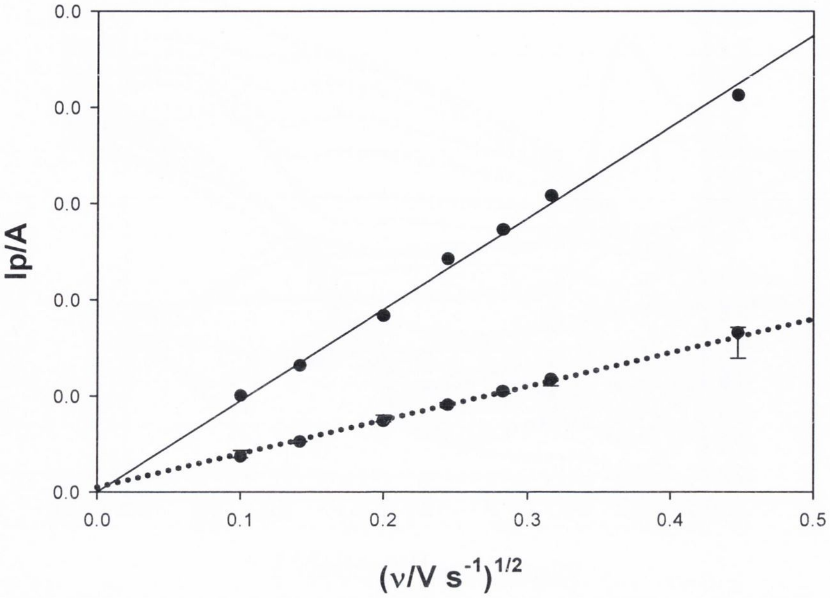

Figure 5.9. Randles-Sevcik error plot for 2mM Dopamine in 0.1M PBS at the PMB/GC electrode. Oxidation peak current varies linearly with scan rates, $\nu = 10 - 100$ mV s^{-1}, but deviation occurs at the PMB/GC electrode at 200 mV s^{-1}. Data taken from averaged (n = 5) oxidation currents with typical CVs shown in figures 5.6 and 5.8.

A linear plot passing through the origin proves the electron transfer kinetics is under mass transport control. Like AA, at $\nu = 200$mV/s, deviation from linearity is observed with the PMB/GC electrode for the same reason, that is, the experimental timescale is too rapid to allow for either diffusion of fresh analyte to the electrode surface, or oxidation to occur at the redox sites within the film. The resultant current response of the modified electrode is, therefore, smaller than the mass transport dictated ideal.

5.3.2 Cyclic Voltammetric analysis of Norepinephrine at the PMB/GC electrode

Like Dopamine, the neurotransmitter Norepinephrine (NE) (also known as Noradrenaline), is thought to oxidise to NE-quinone with the loss of two electrons and two protons. At a bare GC electrode NE shows quasi-reversible behaviour (Figure 5.10).

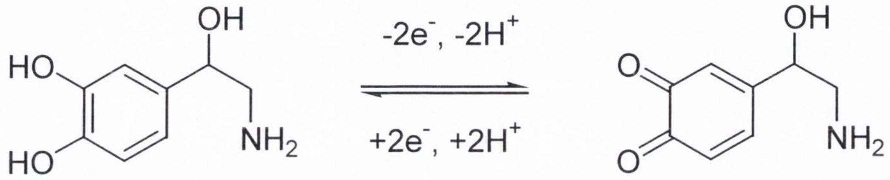

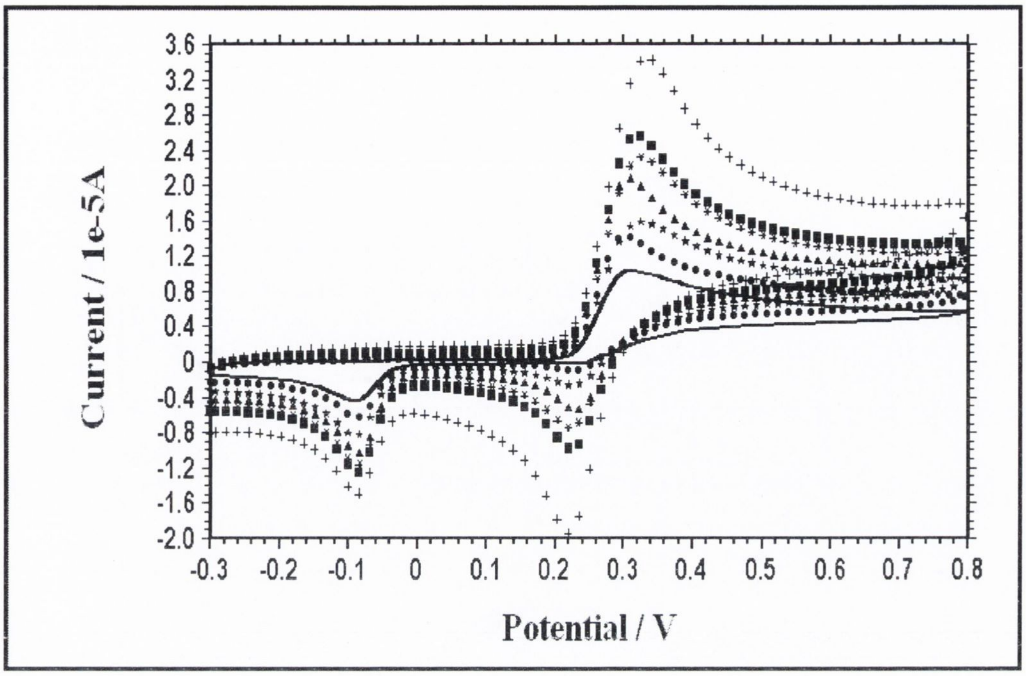

Figure 5.10; Typical cyclic voltammograms using a bare GC electrode of $1x10^{-3}$ M Norepinephrine + 0.1 M PBS (pH=7). Scan rates, ν = (—) 10, (●) 20, (★) 40, (▲) 60, (✱) 80, (■) 100 and (+) 200 mV s^{-1}.

The NE oxidation peak, A_1, lies in the narrow potential window of +0.31 to +0.34 V over the range of scan rates performed, which suggests facile electron transfer kinetics. The first reduction peak, C_1, can be seen at *ca.* +0.22 V, and is assigned to the reduction of NE-quinone to NE. The ΔEp values for the NE/NE-quinone redox couple, range from 70mV at ν = 20mV/s, to *ca.* 115mV at ν = 200mV/s. The second reduction peak, C_2, is found at *ca.* -0.09 V, and can be attributed to the reduction of the aminochrome species, generating leucoaminochrome. This redox behaviour is very similar to that of DA. The authors Chen *et al.* [44] found the NE redox potentials at a bare glassy carbon electrode to be $E_{P,OX}$ = +0.48 V and $E_{P,RED}$ = -0.15 V *vs* a Ag/AgCl reference electrode.

The cyclic voltammetric response of NE at the PMB/GC was studied and a comparison of the modified electrode in 0.1 M PBS and in 2mM NE at, ν = 20mV/s, is presented in Figure 5.11. The monomeric and polymeric LMB/MB redox couples are maintained at the same potentials in the NE solution. The NE oxidation peak begins after the LMB/MB polymer oxidation potential indicating no catalysis occurs due to the film. The $E_{P,OX}$ lies at *ca.* +0.48 V and the corresponding reduction of NE-quinone occurs at a potentials of *ca.* +0.1. The reduction of the aminochrome form occurs at *ca.* -0.2 V. The effect of scan rate on the current output is shown in Figure 5.12.

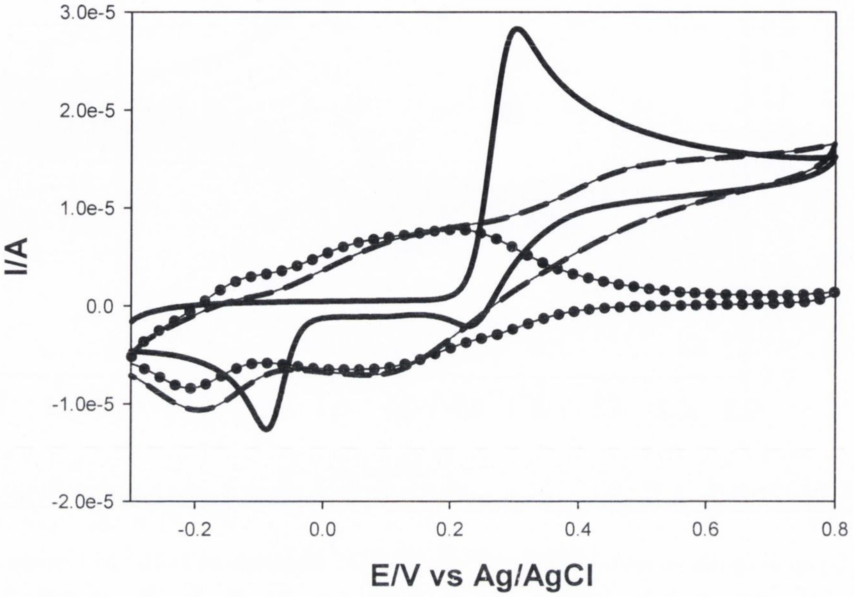

Figure 5.11; Cyclic voltammograms of, (—) 2mM Norepinephrine + 0.1 M PBS at a bare GC electrode, (- -) 2mM Norepinephrine + 0.1 M PBS and (•) 0.1 M PBS, at the PMB/GC electrode, L = 5.8±0.66 x 10^{-8} cm. Scan rate, ν = 20 mV s^{-1}, and pH = 7.

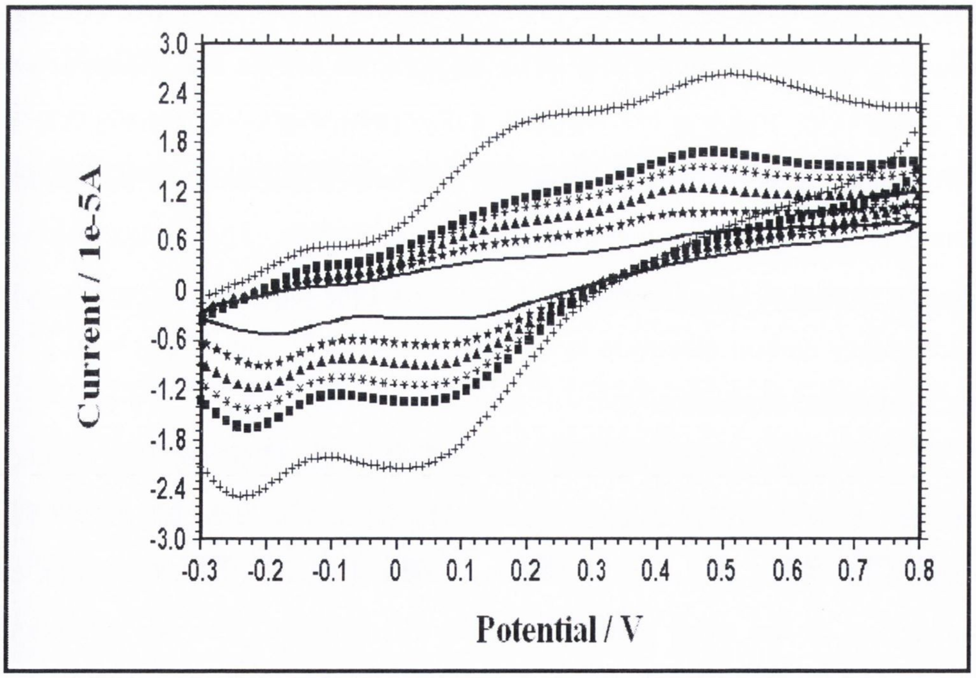

Figure 5.12; Typical cyclic voltammograms using a PMB/GC electrode (L in the range 6.08±0.78 x 10^{-8} cm) of $2x10^{-3}$ M Norepinephrine in 0.1 M PBS (pH 7). Scan rates, ν = (—) 20, (★) 40, (▲) 60, (✱) 80, (■) 100 and (+) 200 mV s^{-1}.

Like DA, NE is of similar structure and is also cationic at pH 7, so it should therefore, experience a similar degree of coloumbic repulsion within the PMB film. This is observed in the $E_{P,OX}$ values shifting anodically, from +0.31 at the bare GC to electrode +0.48V at the PMB/GC electrode. With increasing scan rate, the oxidation potential shifts from +0.48V at 20mV/s to +0.51V at 200mV/s, as expected with this type of mass transport limitation. A notable feature is that the ΔE_P increases from *ca.* 400mV at ν = 10mV/s, to 500mV at ν = 200mV/s.

The associated Randles-Sevcik plots, for the voltammetric behaviour of NE at the bare and modified electrodes, are shown in figure 5.13. This is typical data obtained for NE oxidation at the bare GC electrode and the diffusion coefficient was calculated as, $D = 1.97\times10^{-6}$ cm^2 s^{-1}, which is in good agreement with the literature values of $\sim10^{-6}$ cm^2 s^{-1} for catecholamines [42,45]. The oxidation peak current response of the PMB/GC electrode also vary in a linear manner with square root of scan rate and a partition coefficient of 0.356±1.9 calculated from the ratio of Randles-Sevcik slopes. The magnitude of this partition coefficient again can be attributed to the process of NE permeation through the polymer film and is roughly one third of the bulk [NE].

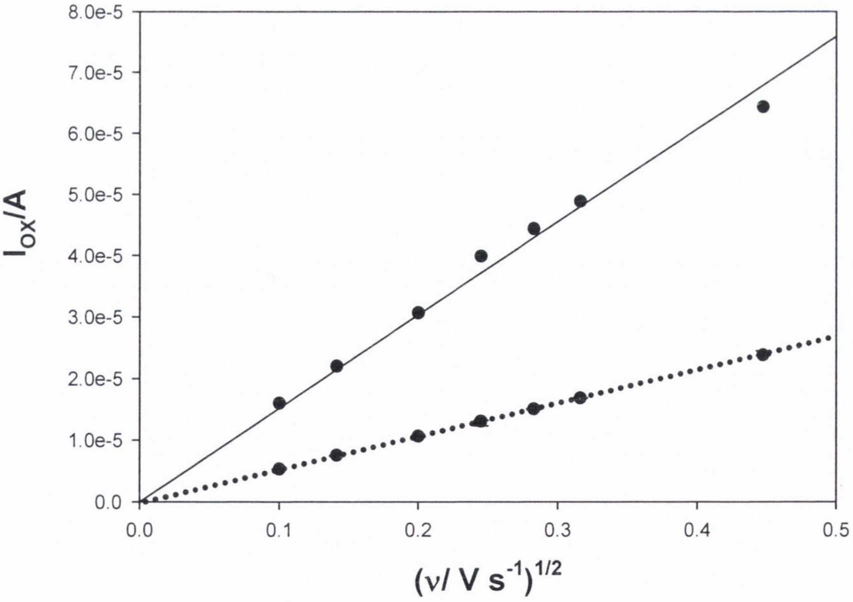

Figure 5.13; Randles-Sevcik error plot for 2mM Norepinephrine in 0.1M PBS at the PMB/GC electrode. Scan rates vary in the range, ν = 10 – 200 mV s^{-1}. Data taken from averaged (n = 5) oxidation currents with typical CVs shown in figures 5.10 and 5.12.

A notable difference between NE and DA is that the current response *versus* square root of scan rate relationship remains linear for NE at rapid scan rates. Diffusion of NE through the polymer matrix to the electrode surface, therefore, is rapid and relatively unhindered even at high scan rates.

5.3.3 Cyclic Voltammetric analysis of Epinephrine at the PMB/GC electrode

The redox behaviour of Epinephrine (EP) contrasts to that of NE at the bare GC electrode in that only one well defined reduction peak is observed at -0.085 V over the range of scan rates performed (Figure 5.14). This corresponds to the reduction of the aminochrome form to leucoaminochrome. The $E_{P,OX}$ varies from +0.34 to +0.42 V over the same range of scan rates, and describes the oxidation of epinephrine to epinephrine-quinone. These redox potentials compare to $E_{P,RED}$ = -0.15 V and $E_{P,OX}$ = +0.35 V found by the authors Chen *et al.*[44], at a bare glassy carbon electrode, pH 7. The reduction peak, C_2, is not evident in the voltammograms. This is due to the rapid rate of the intracyclisation reaction followed by the oxidation of the leucoaminochrome form to aminochrome. This oxidation proceeds *via* an homogeneous electron transfer with epinephrine in solution.

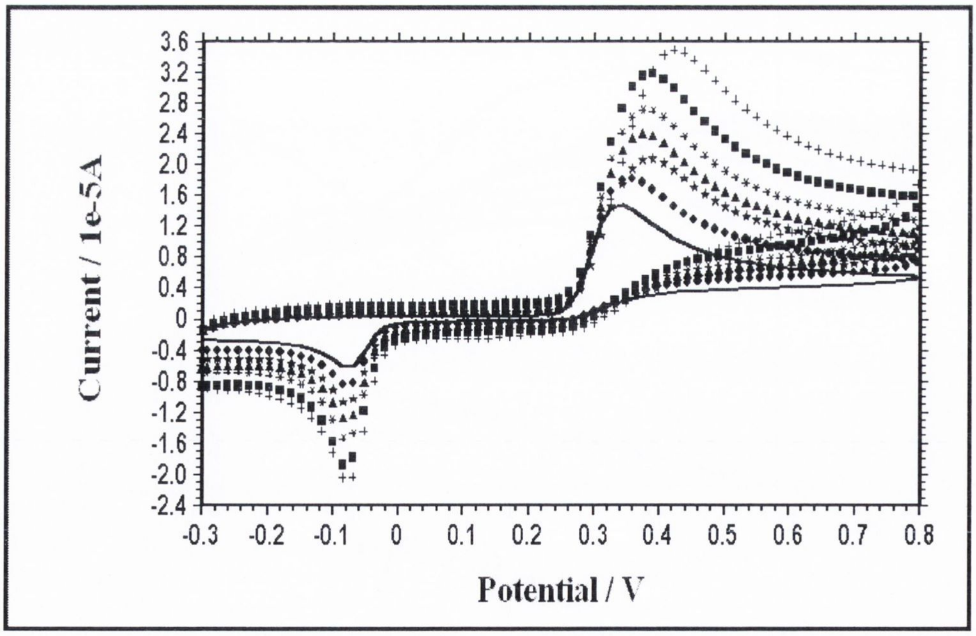

Figure 5.14; Typical cyclic voltammograms of 1x10^{-3} M Epinephrine + 0.1 M PBS (pH 7) at a bare GC electrode. Scan rates, ν = (—) 10, (●) 20, (★) 40, (▲) 60, (✱) 80, (■) 100 and (+) 200 mV s^{-1}.

A typical voltammogram for the EP oxidation at the PMB/GC electrode is presented in figure 5.15, while the effect of scan rate is outlined in figure 5.16.

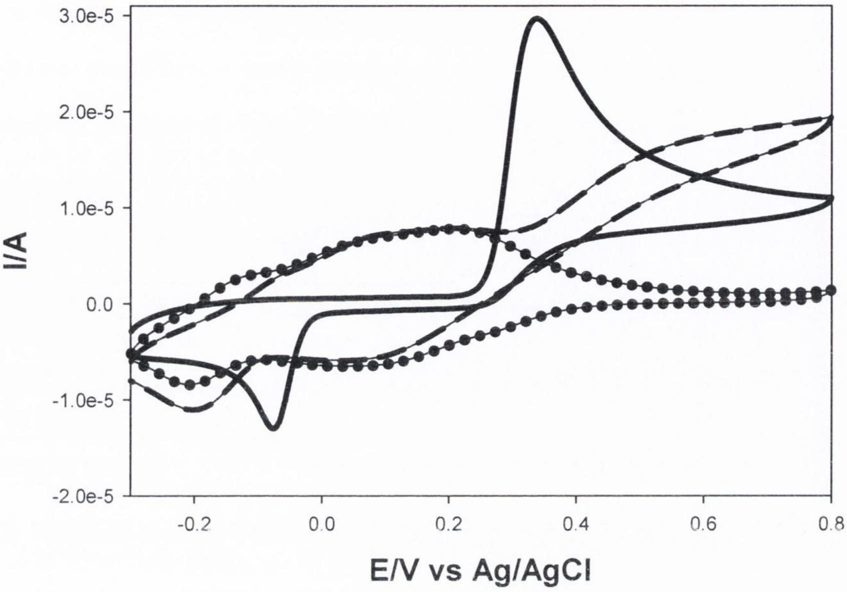

Figure 5.15; Cyclic voltammograms of, (—) 2mM Epinephrine + 0.1 M PBS at a bare GC electrode, (- -) 2mM Epinephrine + 0.1 M PBS and (•) 0.1 M PBS, at the PMB/GC electrode (L = 6.22±0.77 x 10^{-8} cm). Scan rate, ν = 20 mV s^{-1}, and pH = 7.

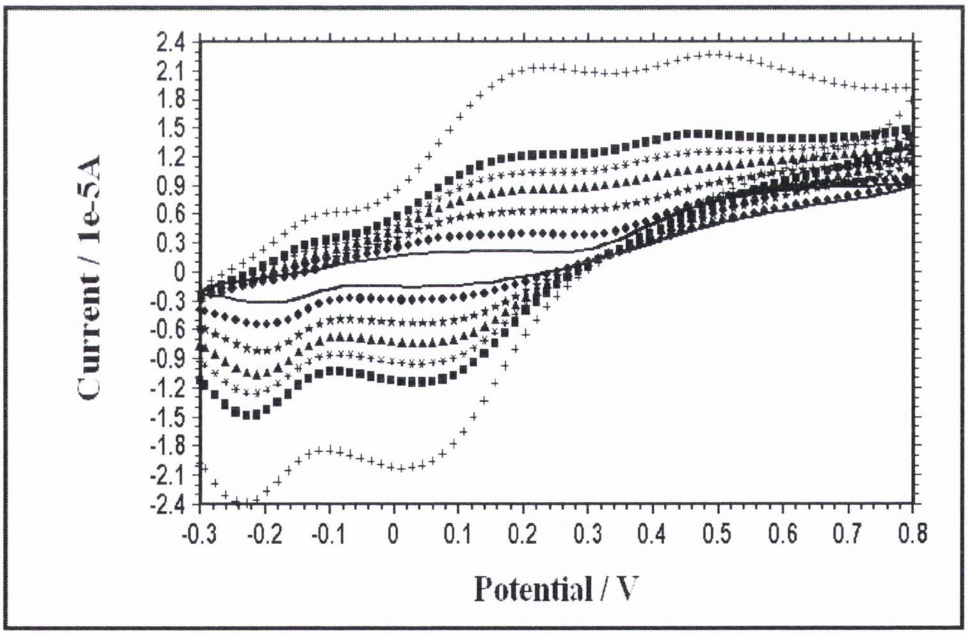

Figure 5.16; Cyclic voltammograms, using a PMB/GC electrode, L = 6.05±0.29 x 10^{-8} cm, of $2x10^{-3}$ M Epinephrine in 0.1 M PBS (pH 7). Scan rates, ν = (—) 10, (●) 20, (★) 40, (▲) 60, (✱) 80, (■) 100 and (+) 200 mV s^{-1}.

The resultant voltammograms (figures 5.15 and 5.16) are very similar to NE oxidation at the PMB/GC electrode, with the EP oxidation process also starting at potentials more anodic than the film redox potentials. The corresponding peak currents for EP oxidation at both the bare and modified electrodes were used to construct a Randles-Sevcik plot (figure 5.17). Analysis of the R-S slope yield a diffusion coefficient, for EP at the bare GC electrode, of $D = 2.11 \times 10^{-6}$ cm^2 s^{-1}, which concurs reasonably well with the literature values [42,46].

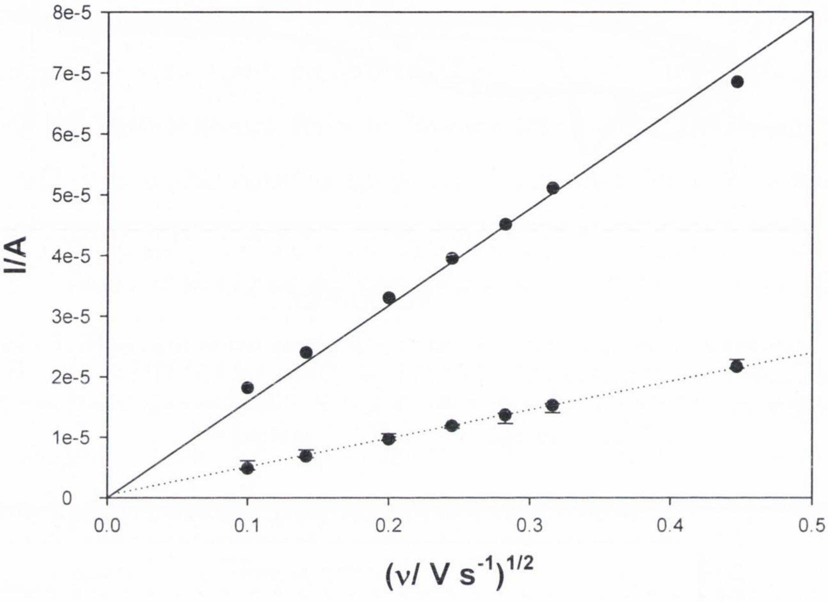

Figure 5.17; Randles-Sevcik error plot for 2mM Epinephrine in 0.1M PBS at the PMB/GC electrode. PMB film thickness was, $L = 6.73 \pm 0.62 \times 10^{-8}$ cm. Scan rates vary in the range, $\nu = 10 - 200$ mV s^{-1}. Data taken from averaged (n = 5) oxidation currents with typical CVs shown in figures 5.14 and 5.16.

The R-S plot for the PMB/GC electrode also yields a straight line. From the ratios of the bare and modified R-S slopes, a partition coefficient of 0.307±0.88 was calculated. Again this provides supporting evidence that electron transfer occurs throughout the polymer film or at the polymer/electrode interface.

The diffusion coefficients and partition coefficients calculated for each analyte studied *via* cyclic voltammetry at the bare and PMB modified GC electrodes respectively, are summarised in Table 5.2. All values elucidated for the bare GC electrode are in reasonable agreement with those found in the literature (recorded at T > 30 °C), but are slightly smaller due to our experimental temperature of 20±1 °C. All values are quoted with associated errors calculated using the standard deviation (minimum, n = 5) of the Randles-Sevcik regression lines. Literature values for diffusion coefficients of the analytes at modified electrodes are quoted between 10^{-6} and 10^{-8} cm^2 s^{-1} [46] and depend on the experimental temperature, diffusion layer thickness, and the catalytic properties of the modifying films.

Analyte	**Diffusion Coefficient / cm^2 s^{-1}**	**Diffusion Coefficient at PMB/GC / cm^2 s^{-1}**	**Partition Coefficient**
Ascorbic Acid	1.67±0.33 x 10^{-6}	3.41±0.53 x 10^{-7}	0.467±0.13
Dopamine	3.17±0.42 x 10^{-6}	4.68±0.47 x 10^{-7}	0.362±0.67
Norepinephrine	1.97±0.21 x 10^{-6}	2.41±0.43 x 10^{-7}	0.356±1.9
Epinephrine	2.11±0.35 x 10^{-6}	1.99±0.23 x 10^{-7}	0.307±0.88

Table. 5.2; Diffusion coefficients with associated errors calculated for AA, DA, NE and EP, at the bare GC and PMB/GC electrodes, using cyclic voltammetry. Film thicknesses were in the range, L = 6.56±0.6 x 10^{-8} cm. Solution temperature was 20±1°C.

5.4 Determination of Diffusion Coefficients for AA, DA, NE and EP Solutions, in 0.1M Phosphate Buffer pH 7, at a bare GC electrode using Rotating Disk Electrode Voltammetry

RDE voltammetry, to eliminate mass-transfer effects, was employed to determine the diffusion coefficients of AA, DA, NE and EP at the bare GC electrode. Typical RDE voltammograms for the oxidation of AA, DA, NE and EP are outlined in figures 5.18(a)-5.21(a). Each displays well defined oxidation current plateaus for the rotation speeds performed. The oxidation currents obtained from the plateaus were used to draw Levich plots. The relationship between the oxidation current and rotation speed, if mass-transfer controlled, should obey the Levich equation [35(b)].

$$I_{OX} = I_{Lev} = 0.62nFAD^{2/3}\nu^{-1/6}\omega^{1/2}C_0 \tag{5.1}$$

where D, ν, ω, and C_0 are the diffusion coefficient (cm^2 s^{-1}), kinematic viscosity (1.1 x 10^{-2} cm^2 s^{-1} [45]), rotation speed(s) and the bulk concentration (Mol cm^{-3}) of the reactant in solution, respectively. Plotting I_{OX} vs $\omega^{1/2}$ in equation (5.1) should yield a straight line that passes through the origin {Figures 5.18(b)-5.21(b)}. All Levich plots display excellent linearity and intersect the origin, which is indicative of mass transport governed kinetics.

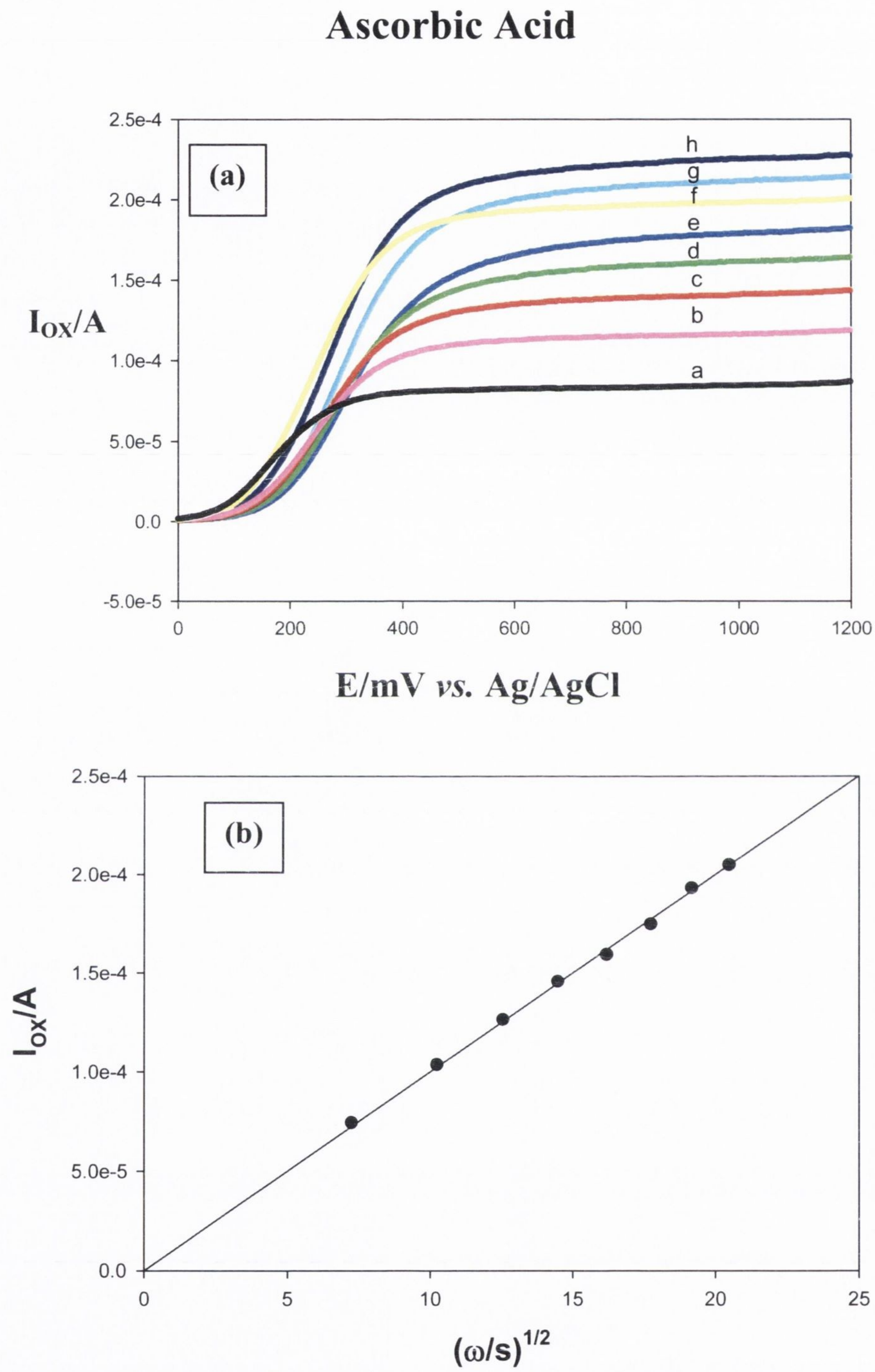

Figure 5.18; (a) Typical RDE voltammograms for the oxidation of 2mM Ascorbic Acid in 0.1M PBS at the bare GC electrode (pH 7.0). The rotation speeds are (a, —)500, (b, —)1000, (c, —)1500, (d, —)2000, (e, —)2500, (f, —)3000, (g, —)3500, and (h, —)4000 rpm at a scan rate of, $\nu = 20$ mV s^{-1}. **(b)** The corresponding Levich plot for the oxidation of 2mM Ascorbic Acid at the bare GC electrode.

Dopamine

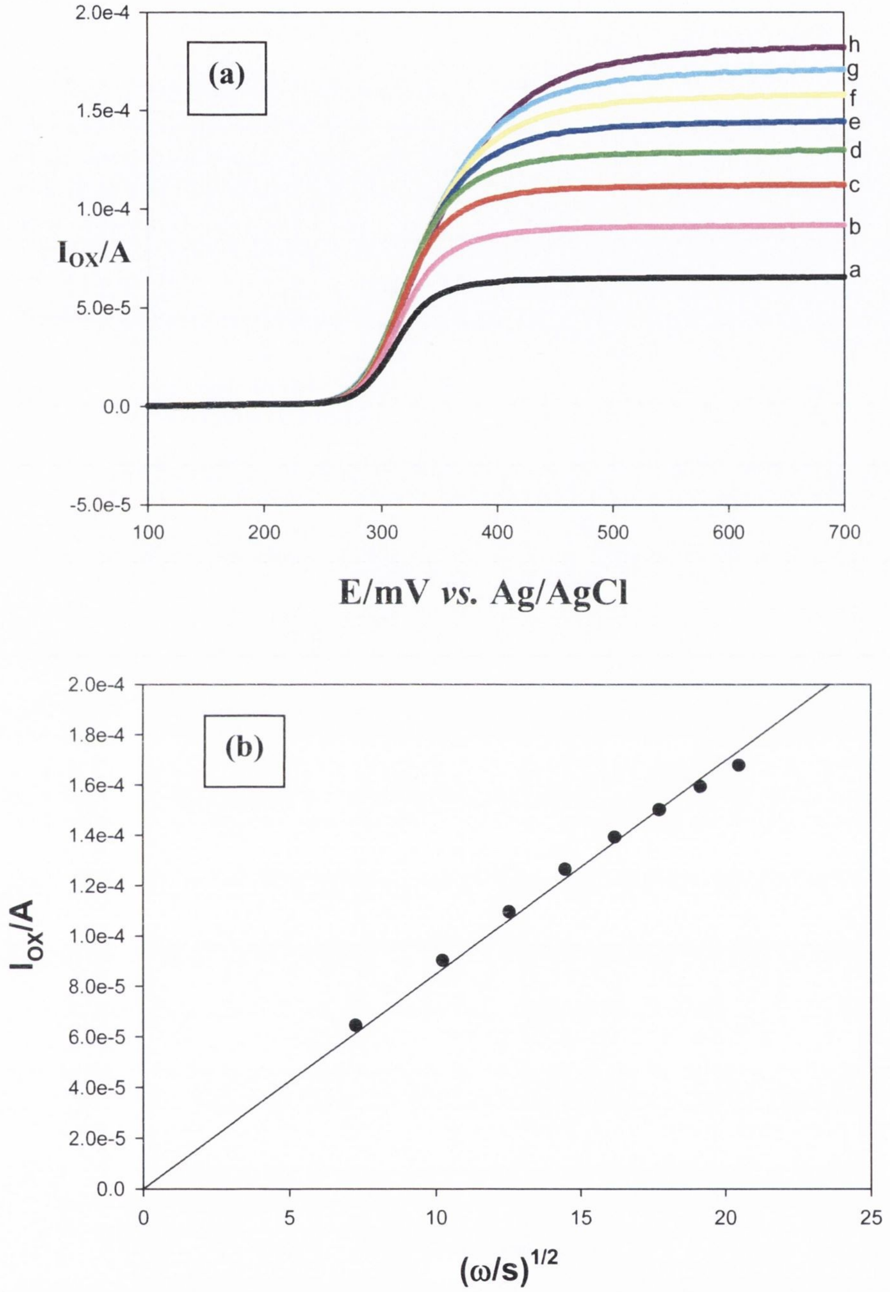

Figure 5.19; (a) Typical RDE voltammograms for the oxidation of 2mM Dopamine in 0.1M PBS at the bare GC electrode (pH 7.0). The rotation speeds are (a, —)500, (b, —)1000, (c, —)1500, (d, —)2000, (e, —)2500, (f, —)3000, (g, —)3500 and (h, —)4000 rpm at a scan rate of, $\nu = 20$ mV s^{-1}. **(b)** The corresponding Levich plot for the oxidation of 2mM Dopamine at the bare GC electrode.

Norepinephrine

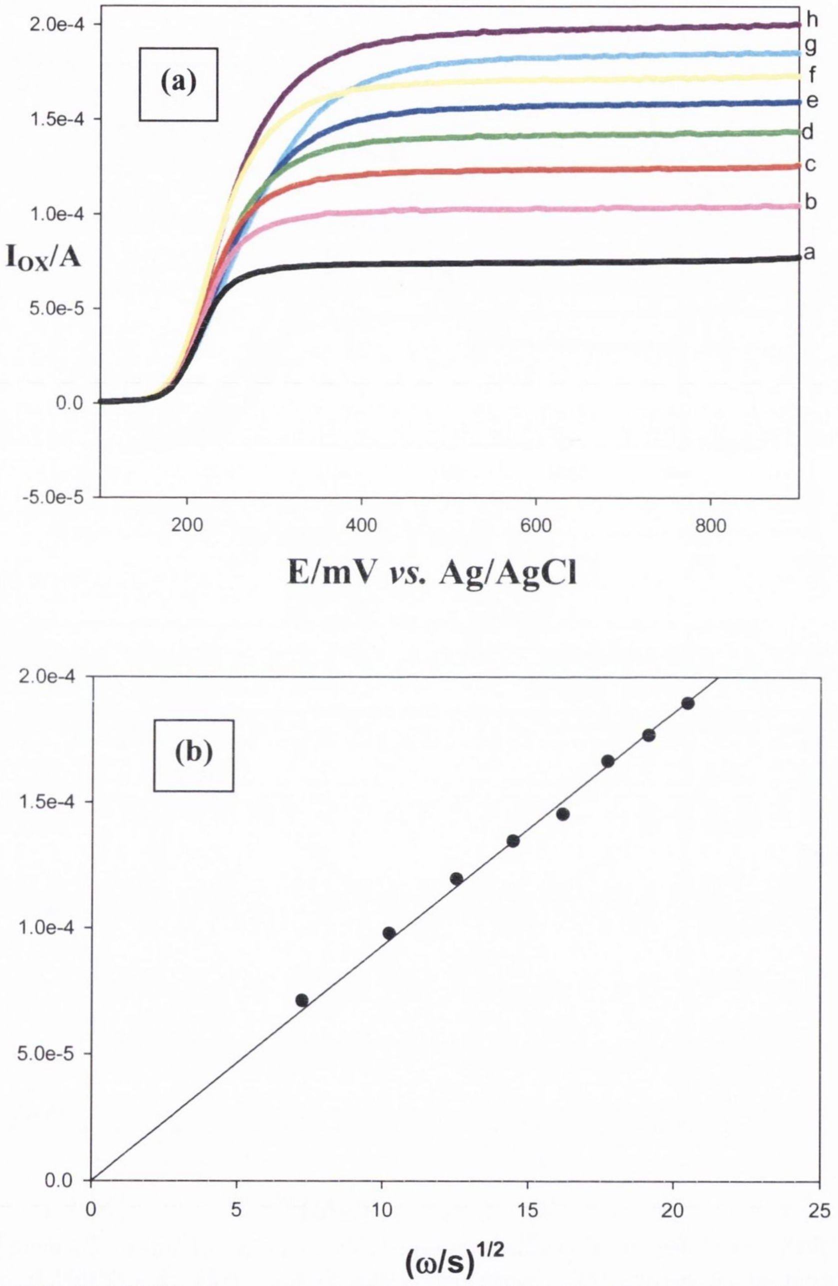

Figure 5.20; (a) Typical RDE voltammograms for the oxidation of 2mM Norepinephrine in 0.1M PBS at the bare GC electrode (pH 7.0). The rotation speeds are (a, —)500, (b, —)1000, (c, —)1500, (d, —)2000, (e, —)2500, (f, —)3000, (g, —)3500 and (h, —)4000 rpm at a scan rate of, $\nu = 20$ mV s^{-1}. **(b)** The corresponding Levich plot for the oxidation of 2mM Norepinephrine at the bare GC electrode.

Epinephrine

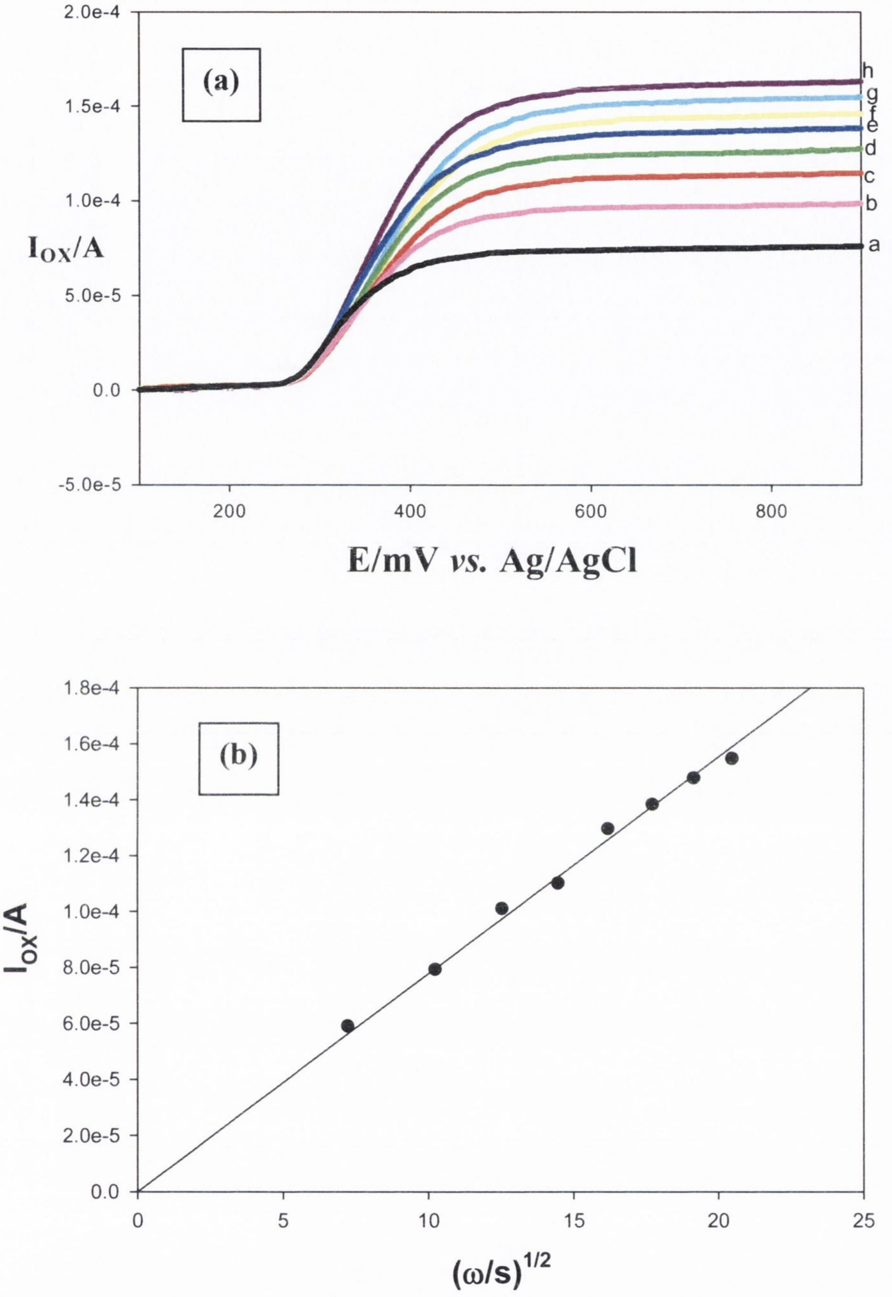

Figure 5.21; (a) RDE voltammograms for the oxidation of 2mM Epinephrine in 0.1M PBS at the bare GC electrode (pH 7.0). The rotation speeds are (a, —)500, (b, —)1000, (c, —)1500, (d, —)2000, (e, —)2500, (f, —)3000, (g, —)3500 and (h, —)4000 rpm at a scan rate of, $\nu = 20$ mV s^{-1}. **(a)** The corresponding Levich plot for the oxidation of 2mM Epinephrine at the bare GC electrode.

From the Levich slope the diffusion coefficients of all analytes were calculated, and are summarised in Table 5.2. The values are quoted with their associated errors, calculated as standard deviations (n = 5) of the Levich plot regression lines. They compare very well with the literature values and are of similar magnitude with one another. This is to be expected as the structures are closely related.

5.5 Determination of AA, DA, NE and EP Substrate Diffusion Coefficients through the PMB Modified GC Electrode, in 0.1M Phosphate Buffer pH 7, using Rotating Disk Electrode Voltammetry

The electrochemical response of the PMB/GC electrode towards AA, DA, NE, EP oxidation was investigated using rotating disk electrode (RDE) voltammetry. Figures 5.22(a)-5.25(a) shows the typical RDE responses of the analytes at the PMB/GC electrode, scanned from 0 to +1.2 V at 500-4000 rpm with a scan rate of 20 mV s^{-1}. The limiting currents obtained from the plateau (at +0.7 V) were used to construct Levich plots {Figures 5.22(b)- 5.25(b)}, and the Levich slopes used to calculate the substrate diffusion coefficients through the polymer film. All Levich plots were background corrected and are linear passing through the origin, indicating the electrode kinetics are mass-transport controlled. A comparison of diffusion coefficients found at the bare and PMB/GC electrodes are summarised in Table.5.3.

Diffusion Coefficients	$E_{P,OX}$ Bare GC	Bare GC $cm^2\ s^{-1}$	$E_{P,OX}$ PMB/GC	PMB/GC $cm^2\ s^{-1}$
Ascorbic Acid	**0.42V**	**$3.61 \pm 0.36 \times 10^{-6}$**	**0.5V**	**$5.55 \pm 0.86 \times 10^{-7}$**
Dopamine	**0.42V**	**$3.82 \pm 0.58 \times 10^{-6}$**	**0.6V**	**$5.02 \pm 0.58 \times 10^{-7}$**
Norepinephrine	**0.40V**	**$3.01 \pm 0.38 \times 10^{-6}$**	**0.65V**	**$4.15 \pm 0.28 \times 10^{-7}$**
Epinephrine	**0.46V**	**$3.06 \pm 0.21 \times 10^{-6}$**	**0.65V**	**$6.23 \pm 0.43 \times 10^{-7}$**

Table 5.3; Diffusion coefficients with associated errors calculated for AA, DA, NE and EP, at the bare GC and PMB/GC electrodes, using RDE voltammetry. Film thicknesses were in the range, L = $6.31 \pm 0.73 \times 10^{-8}$ cm. Solution temperature was 20±1°C.

The fact that the values are quite similar in magnitude is reasonable as the substrates are of similar size. The diffusion coefficients calculated at the PMB/GC electrodes are about an order of magnitude smaller than those found at the bare GC electrodes. This is indicative of a permeation process of analyte through the polymer film. The location of the reaction layer for each of the analytes is diagnosed in Section 5.8.

Ascorbic Acid at a PMB/GC electrode

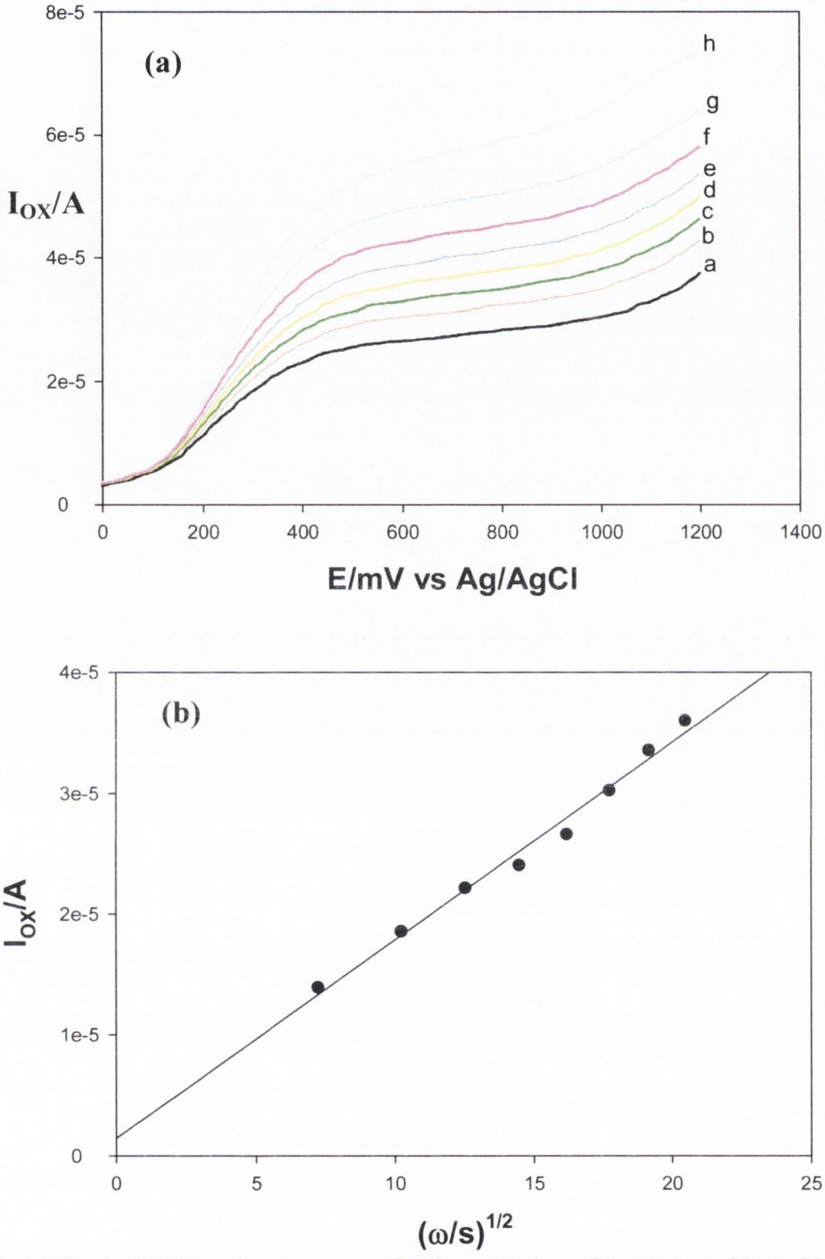

Figure 5.22; (a) Typical RDE voltammograms for the oxidation of 2mM Ascorbic Acid in 0.1M PBS at the PMB/GC electrode (pH 7.0). The rotation speeds are (a, —) 500, (b, —) 1000, (c, —)1500, (d, —) 2000, (e, —) 2500, (f, —) 3000, (g, —) 3500 and (h, —) 4000 rpm with a scan rate of, $\nu = 20$ mV s^{-1}. **(b)** The Levich plot for the oxidation of 2mM Ascorbic Acid at the PMB/GC electrode. For each AA oxidation experiment a new PMB/GC electrode was prepared with film thickness in the range, $L = 6.21 \pm 0.66 \times 10^{-8}$ cm.

Dopamine at a PMB/GC electrode

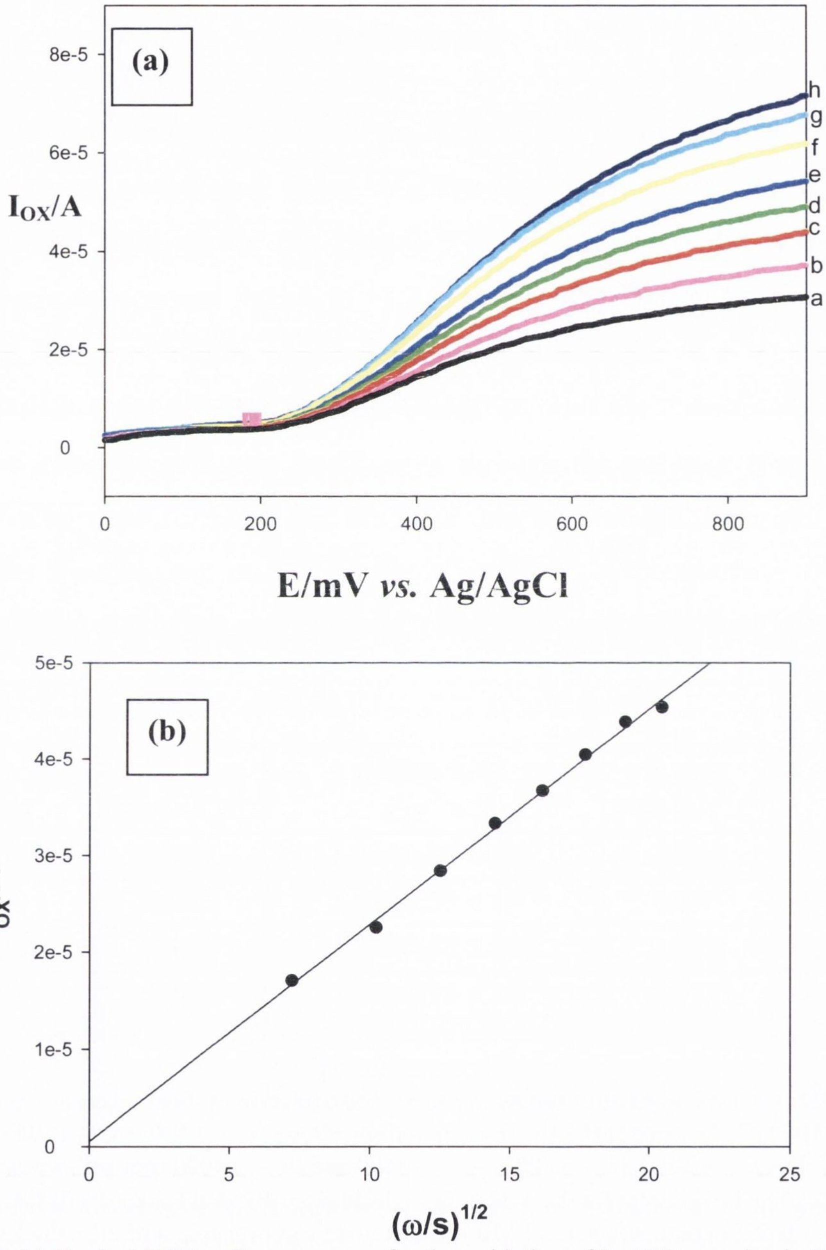

Figure 5.23; (a) Typical RDE voltammograms for the oxidation of 2mM Dopamine in 0.1M PBS at the PMB/GC electrode (pH=7). The rotation speeds are (a, —)500, (b, —)1000, (c, —)1500, (d, —)2000, (e, —)2500, (f, —)3000, (g, —)3500 and (h, —)4000 rpm with a scan rate of, ν = 20mV s^{-1}. **(b)** The corresponding Levich plot for the oxidation of 2mM Dopamine at the PMB/GC electrode. For each DA oxidation experiment a new PMB/GC electrode was prepared with film thickness in the range, L = 6.57±0.82 x 10^{-8} cm.

Norepinephrine at a PMB/GC electrode

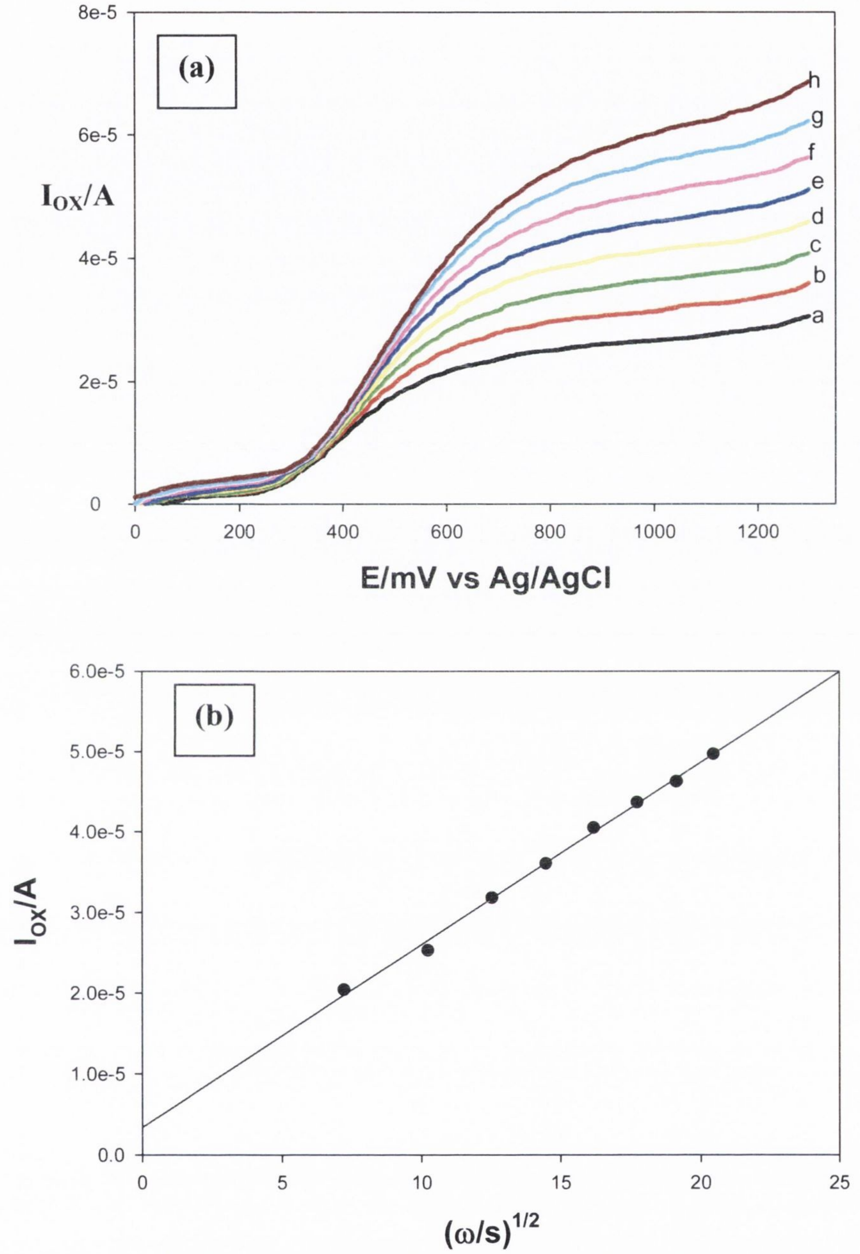

Figure 5.24; (a) Typical RDE voltammograms for the oxidation of 2mM Norepinephrine in 0.1M PBS at the PMB/GC electrode (pH 7.0). The rotation speeds are (a, —)500, (b, —)1000, (c, —)1500, (d, —)2000, (e, —)2500, (f, —)3000, (g, —)3500 and (h, —)4000 rpm with a scan rate of, ν = 20 mV s^{-1}. **(b)** The corresponding Levich plot for the oxidation of 2mM Norepinephrine at the PMB/GC electrode. For each NE oxidation experiment a new PMB/GC electrode was prepared with film thickness in the range, L = 5.98±0.49 x 10^{-8} cm.

Epinephrine at a PMB/GC electrode

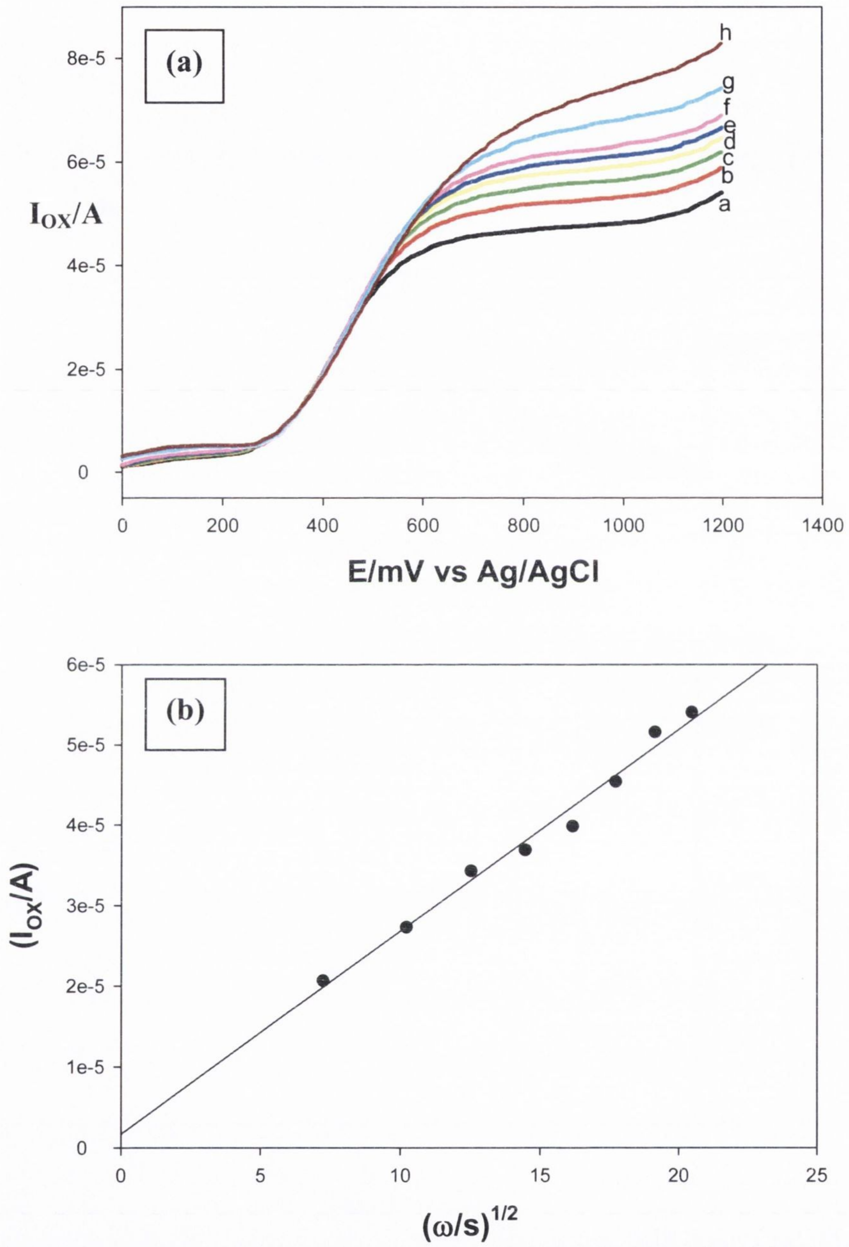

Figure 5.25; (a) Typical RDE voltammograms for the oxidation of 2mM Epinephrine in 0.1M PBS at the PMB/GC electrode (pH 7.0). The rotation speeds are (a, —)500, (b, —)1000, (c, —)1500, (d, —)2000, (e, —)2500, (f, —)3000, (g, —)3500 and (h, —)4000 rpm with a scan rate of, ν=20mV s^{-1}. **(b)** The corresponding Levich plot for the oxidation of 2mM Epinephrine at the PMB/GC electrode. For each AA oxidation experiment a new PMB/GC electrode was prepared with film thickness in the range, L = 6.44±0.63 x 10^{-8} cm.

5.6 *Tafel analysis of AA, DA, NE, and EP at the PMB/GC electrode*

In RDE voltammetry, the observed current is not limited by the transport of reactants to the electrode surface. Therefore, theory is required to describe interfacial kinetics, where the observed current is dependant on applied potential. Tafel found that current can be related exponentially to the overpotential, η. A Tafel plot is the plot of log $(i_L - i_0/i_0)$ vs. η in Equation 5.2, and from it kinetic parameters of interfacial redox processes can be determined. For the irreversible/quasi-reversible oxidation processes studied in this report, the anodic branch with slope $(1-\alpha)F/2.3RT$ was used to calculate the reaction transfer coefficient, α. The transfer coefficient is a measure of the symmetry of the energy barrier, that is, the geometry of the intersection region. If $\alpha = ½$, then the intersection is symmetrical [35(d)].

$$\log\left(\frac{i_L - i_0}{i_0}\right) = -\left(\frac{\alpha nF}{2.3RT}\right)\eta \qquad (5.2)$$

where overpotential, $\eta = (E-E^0)$. Typical Tafel plots for AA, DA, NE and EP obtained at the PMB/GC electrode are illustrated in Figure 5.26. The Tafel slopes yielded transfer coefficients of $\alpha = 1$ for all analytes examined. This implies that the solvent distribution function, ΔG_S, is equal to ΔG, the overall free energy change for the reaction. Therefore almost all the applied overvoltage is being used in generation of the transition state. This occurs so close to the electrode surface that the transition state has a structure much closer to the product than to the reactant [35(d)].

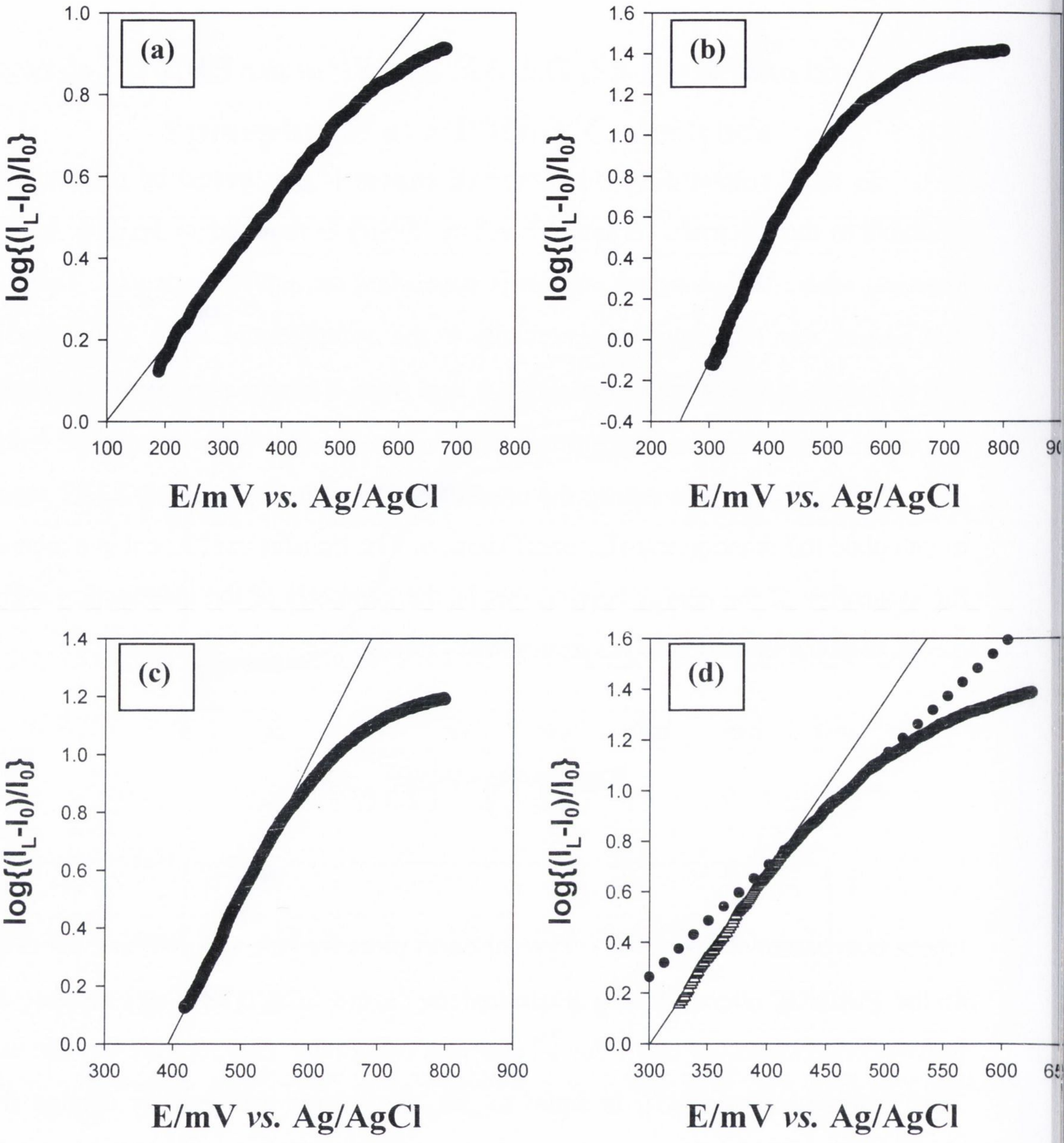

Figure 5.26; Tafel plots for the electro-oxidation of 2mM **(a)** Ascorbic Acid, **(b)** Dopamine, **(c)** Norepinephrine and **(d)** Epinephrine in 0.1M PBS at the PMB/GC (film thicknesses, L = 6.02±.98 x 10^{-8} cm) rotating disk electrode with rotation speed of 1000rpm.

5.7 *Koutecky-Levich analysis at a PMB/GC electrode*

Kinetic parameters for the analyte oxidation at the PMB/GC modified electrodes were determined *via* Koutecky-Levich analysis. A method for the determination of values for the limiting currents for AA and the catecholamines DA, NE and EP at rotation speeds 0-4,000 rpm was outlined in the pervious section. Confirmation of this data was obtained by monitoring the current response to stepped increments in the rotation speed of the electrode while an oxidative potential was being applied. Figures 5.27 – 5.30 illustrate typical responses obtained at the PMB/GC electrodes for oxidative applied potentials for AA, DA, NE and EP, respectively. All experiments were conducted in a 2 mM solution of analyte. The latter concentration value was chosen since it is well established that a Koutecky-Levich analysis requires that the substrate reaction kinetics be first order. Good steady state responses were recorded at all rotation speeds and analyte concentrations with excellent reproducibility being achieved.

Kinetic information can be gleaned form the RDE data in the absence of any mass-transfer effects, by applying the Koutecky-Levich equation [35(c)], equation (5.3)

$$\frac{1}{i_{LIM}} = \frac{1}{nFAD^{2/3}k_{ME}C_0} + \frac{1.61}{nFAv^{-1/6}D^{2/3}C_0\omega^{1/2}} \qquad (5.3)$$

where k_{ME} is the heterogeneous rate constant (cm s^{-1}) for analyte oxidation at the PMB/GC electrode. Koutecky-Levich analysis was employed to analyse the raw experimental data. This analysis, as was discussed in Chapter 2, involves plotting $1/i_L$ versus $1/\omega^{1/2}$ according to the expression. The intercept, $I_{K\text{-}L}$, and slope, $S_{K\text{-}L}$, were used to calculate k_{ME} and diffusion coefficient respectively. These plots should be linear where the slope is independent of potential.

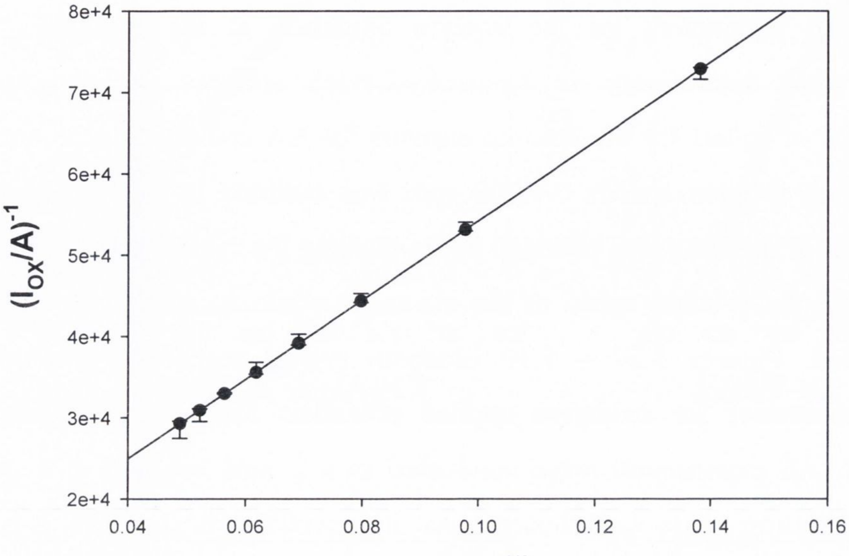

Figure 5.27. The Koutecky-Levich plot for the oxidation of 2mM Ascorbic Acid in 0.1M PBS, pH 7, at the PMB/GC electrode. L = 6.11±0.78 x 10^{-8} cm.

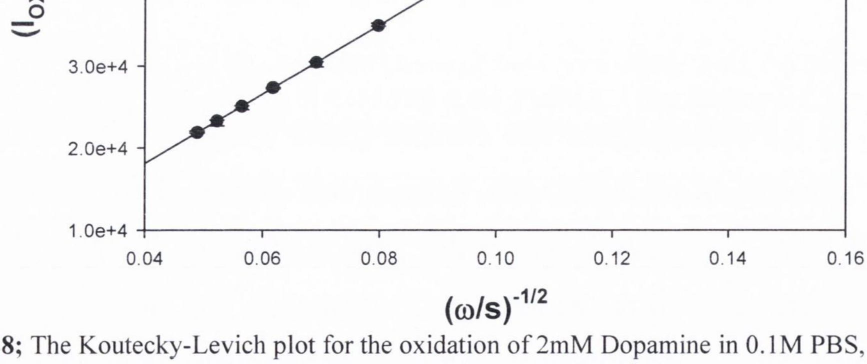

Figure 5.28; The Koutecky-Levich plot for the oxidation of 2mM Dopamine in 0.1M PBS, pH 7, at the PMB/GC electrode. L = 6.68±0.53 x 10^{-8} cm.

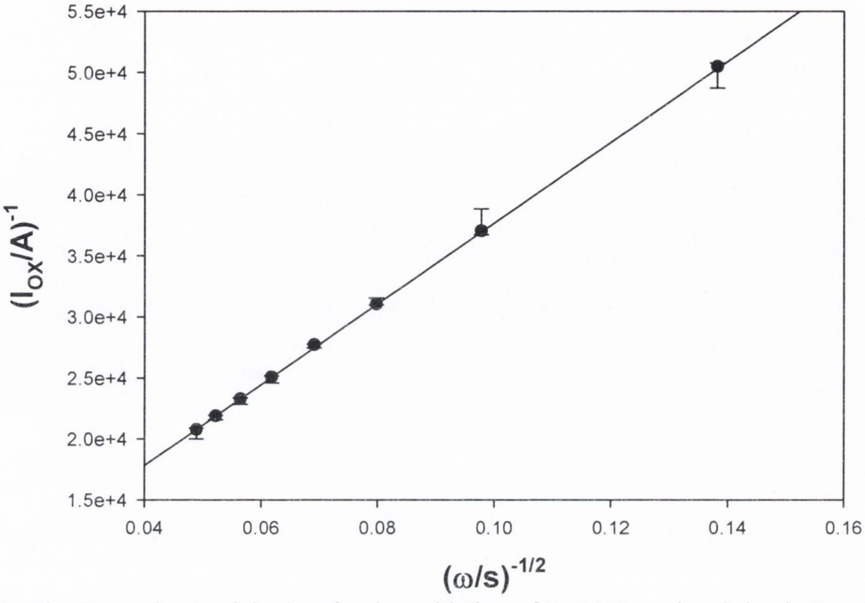

Figure 5.29; The Koutecky-Levich plots for the oxidation of 2mM Norepinephrine in 0.1M PBS, pH 7, at the PMB/GC electrode, at +0.6 V. L = 5.97±0.86 x 10^{-8} cm.

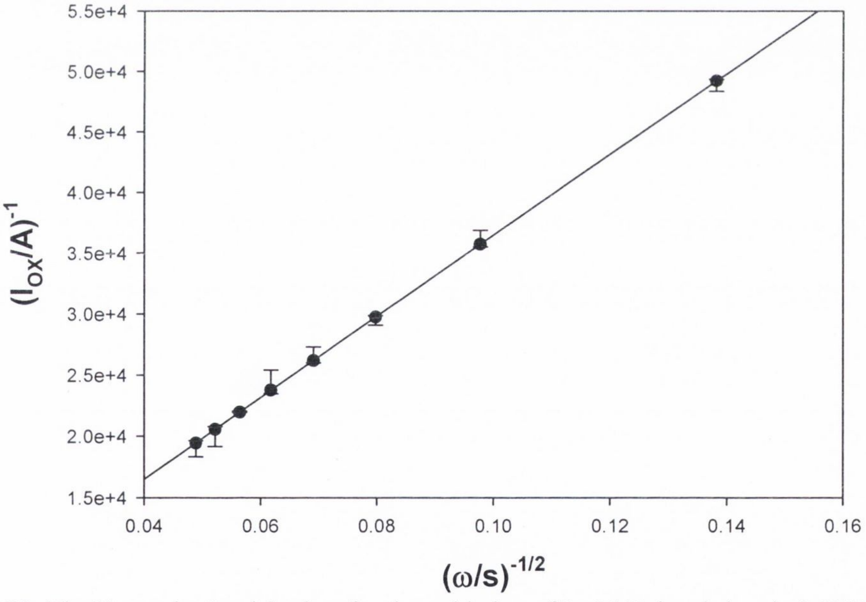

Figure 5.30; The Koutecky-Levich plots for the oxidation of 2mM Epinephrine, in 0.1M PBS, pH 7, at the PMB/GC electrode, at +0.6 V. L = 6.43±0.46 x 10^{-8} cm.

Table 5.4 summarises the values obtained for the diffusion coefficient, heterogeneous electrochemical rate constant (obtained from the Koutecky-Levich plot) and diffusional rate constant (obtained via the relationship $k_d = 0.62D^{2/3}\upsilon^{-1/6}\omega^{1/2}$) at the PMB modified electrodes for the four analytes, when oxidative potentials were applied. The substrate diffusion coefficients compare well to those presented in Table 5.3, which also are of the order ~10^{-7} cm^2 s^{-1}.

Analyte	k_{ME} / cm s^{-1}	D / cm^2 s^{-1}	k_d / cm s^{-1}
Ascorbic Acid	119	**4.28±0.86 x 10^{-7}**	**5.4 x 10^{-4}**
Dopamine	140	**5.31±0.58 x 10^{-7}**	**6.2 x 10^{-4}**
Norepinephrine	97	**7.60±0.28 x 10^{-7}**	**7.9 x 10^{-4}**
Epinephrine	102	**7.27±0.43 x 10^{-7}**	**7.7 x 10^{-4}**

Table 5.4; Parameters from Koutecky-Levich analysis of analyte oxidation at the PMB/GC electrode. The substrate diffusion coefficients compare quite well with those quoted in Table 5.3

5.8 Diagnosis of the PMB reaction layer in the oxidation of AA, DA, NE and EP

5.8.1 Andrieux-Saveant Analysis

As outlined in Chapter 4, the Andrieux-Saveant model uses four characteristic currents to determine the rate limiting steps:

$$i_D = nFAD_S c_S{}^{\infty} / \delta \tag{5.4}$$

$$i_S = nFA\kappa D_S c_S{}^{\infty} / L \tag{5.5}$$

$$i_E = nFA\Gamma D_E / L^2 \tag{5.6}$$

$$i_k = nFA\kappa k\Gamma_B c_S{}^{\infty} \tag{5.7}$$

The current due to substrate reaction at the bare electrode, i_D, has been quantified. Determination of i_S, however, is problematic. When two distinct waves (i_1 and i_2) are observed at a modified electrode, the first wave corresponds to a direct electrode substrate reaction, while the second wave is due to the mediated substrate reaction.

Location of reaction zone:

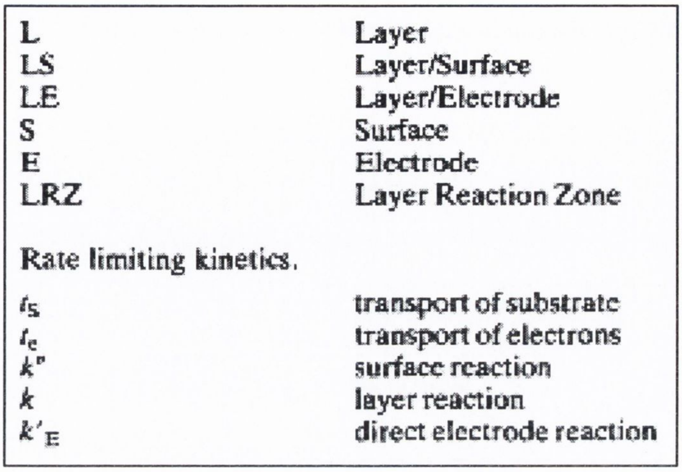

L	Layer
LS	Layer/Surface
LE	Layer/Electrode
S	Surface
E	Electrode
LRZ	Layer Reaction Zone
Rate limiting kinetics.	
t_S	transport of substrate
t_e	transport of electrons
k''	surface reaction
k	layer reaction
k'_E	direct electrode reaction

Limiting expressions for k'$_{ME}$

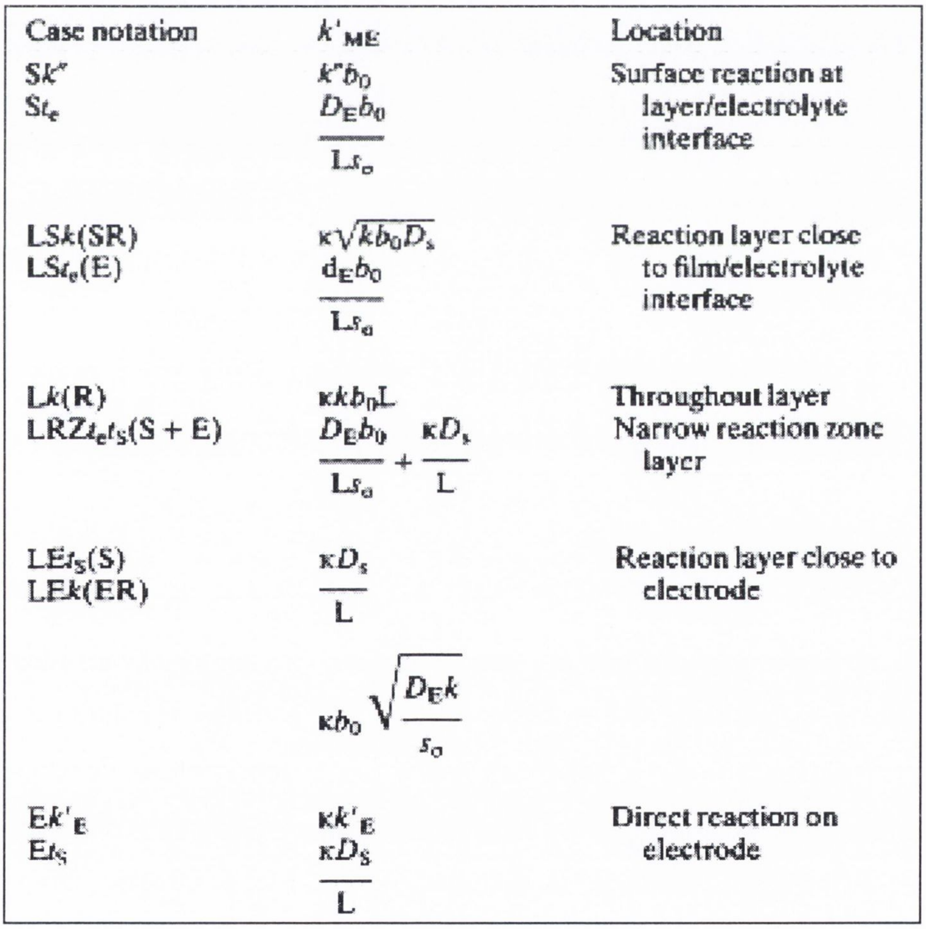

Case notation	k'_{ME}	Location
Sk''	$k''b_0$	Surface reaction at layer/electrolyte interface
St_e	$\frac{D_E b_0}{L s_o}$	
$LSk(SR)$	$\kappa\sqrt{k b_0 D_s}$	Reaction layer close to film/electrolyte interface
$LSt_e(E)$	$\frac{d_E b_0}{L s_o}$	
$Lk(R)$	$\kappa k b_0 L$	Throughout layer
$LRZt_e t_S(S + E)$	$\frac{D_E b_0}{L s_o} + \frac{\kappa D_s}{L}$	Narrow reaction zone layer
$LEt_S(S)$	$\frac{\kappa D_s}{L}$	Reaction layer close to electrode
$LEk(ER)$	$\kappa b_0 \sqrt{\frac{D_E k}{s_o}}$	
Ek'_E	$\kappa k'_E$	Direct reaction on electrode
Et_S	$\frac{\kappa D_S}{L}$	

Table 5.5; Albery-Hillman case notation (with Andrieux-Saveant case notation in brackets) for electroactive polymers.

These waves can be used to determine i_S using the relation $1/i_l = 1/i_D + 1/i_S$. In the RDE voltammograms, obtained at the PMB/GC electrodes, only one wave was observed. In this case an electroinactive film should have been used to determine i_S. In the present system the film itself, not a dopant species, is the mediator. A summary of the rate limiting cases (in brackets) are shown in Table 5.5. According to Andrieux-Saveant diagnostic criteria [47], the absence of a second wave in the RDE voltammograms eliminates the (R) and (ER) cases. The polymer charge transfer diffusion coefficient, D_{CT}, calculated in Chapter 3 most likely represents the limiting rate due to counter ion motion through the film and not the electron diffusion coefficient required to determine i_E. A value of 10^{-14} cm^2 s^{-1} is very slow when compared to the ~10^{-9} cm^2 s^{-1} value usually obtained for D_E. D_E should have been experimentally determined using rotating ring-disk electrode voltammetry.

However, we can eliminate the (S+E), and (E) cases as the K-L slopes vary inversely with substrate concentration. We can narrow it down to two possible limiting cases, (S) and (SR) [47], as the intercept of the K-L plots vary also inversely with analyte concentration.

The (SR) limiting case is typical of a substrate reaction layer close to the film/electrolyte interface and the (S) case denotes a reaction layer close to the electrode surface. The calculated substrate diffusion coefficients through the PMB film ~10^{-7} cm^2 s^{-1} is relatively fast which suggests that the (S) case pertains.

5.8.2 Albery-Hillman Diagnosis

The Albery-Hillman approach is based on the relative rates of charge and substrate transport through the layer, expressed in terms of the reaction layers, X_0 and X_L, i.e., the fraction of the film usefully employed in catalysis. The transport and kinetic processes are quantified in terms of the modified rate constant k'_{ME}, obtained *via* Koutecky-Levich analysis. The two general expressions for k'_{ME} developed in the Albery-Hillman model are complex but simpler more convenient expressions may be obtained for a number of physically reasonable specific situations. These limiting expressions are presented in Table 5.5, from which the rate limiting process and reaction zone location can be determined. The corresponding Andrieux-Saveant notation is also shown (in brackets).

The dependence of the limiting current on the rotation rate as well as the dependence of k'_{ME} on the layer thickness can diagnose the location of the reaction. Figures 5.27 – 5.30 clearly show that the limiting current does depend on the rotation speed. This behaviour is not consistent with the surface case, St_e. The case where the reaction occurs at the electrode/film interface, LEk, can be eliminated because the K-L plots are linear. Also, the K-L gradients are less than the inverse Levich constant, B^{-1}, found from direct oxidation of the substrate at the bare electrode. This indicates, using the Albery-Hillman diagnostic scheme [48] that the $LRZt_et_s$ limiting case pertains. The LRZ case describes a catalysic reaction that occurs in the layer reaction zone in the centre of the polymer film, with the transport of electrons/substrate rate limiting. The corresponding case in the Andrieux-Saveant model is the (S+E) case, which we have previously eliminated! The Albery-Hillman diagnosis is consistent with the redox site-substrate complex theory in the Michaelis-Menten analysis, in which, the reaction layer is throughout the polymer film. We therefore decided to use the Michaelis-Menten analysis to quantify the kinetic parameters for the catalytic oxidation of ascorbic acid and the catecholamines at the PMB/GC electrode.

5.9 Amperometric analysis of AA, DA, NE, and EP detection at the PMB/GC Rotating Disk Electrode

When the anodic peak current response for the couple is measured under constant reaction conditions, it is found that amperometric current response varies with the concentration of supplied substrate [S]. The constant conditions referred to are the applied potential, typically held at approximately 0.7 V (elucidated *via* voltammetry) to ensure maximal oxidation of substrate at the electrode interface and the substrate flow patterns are governed by the rotating disc (typical speed. 3,000 rpm).

It is found that the steady state current (I_{max}) varies with the concentration of supplied substrate [S], this substrate being the injections of a series of aliquots of a analyte solution to the phosphate buffered cell solution. Typical amperometric responses obtained at a PMB/GC electrode clearly depicted the I_{max} values obtained after each injection of analyte. When these values of I_{max} are plotted against the corresponding values of [S], a characteristic rectangular hyperbolic plot is usually obtained. This effect is illustrated in figure 4.11.

A number of features are noteworthy. Low concentrations of the analyte may be detected amperometrically because a very small background current (<3 μA) is exhibited for the electrolyte in the absence of substrate. The response of the modified electrode is rapid and steady state current responses easily obtained. At low values of concentration, the observed current peaks rise in a manner directly proportional to the substrate concentration (linear profile), but at larger values of [S] the current responses become independent of the actual substrate concentrations. That is, at very low concentrations of substrate the reaction is first order with respect to substrate. At higher concentrations the current reaches a maximum value, I_{max}, where the current is independent of substrate concentration and the reaction is zero order with respect to the substrate. This change in reaction order suggests the operation of a Michaelis-Menten type mechanism, involving the formation of an intermediate substrate complex, which subsequently decomposes to yield a product.

All experiments were carried out in phosphate buffer at a constant pH of 7 with the disc electrode rotating at a constant 3,000 rpm. The electro-oxidation of ascorbic acid and the three catecholamines were examined at the PMB/GC electrode. Calibration curves for each analyte and the associated kinetic parameters were elucidated (Figures 5.31 - 5.34). From the calibration curves for AA and DA at the PMB/GC electrode, we observe electrode fouling. After addition of *ca.* 6.5mM AA and 0.3mM DA, the respective PMB/GC electrode current response reached a plateau. The distinctive zero to first order dependency of current response on analyte concentration was not evident. Therefore, a true limiting current was not observed.

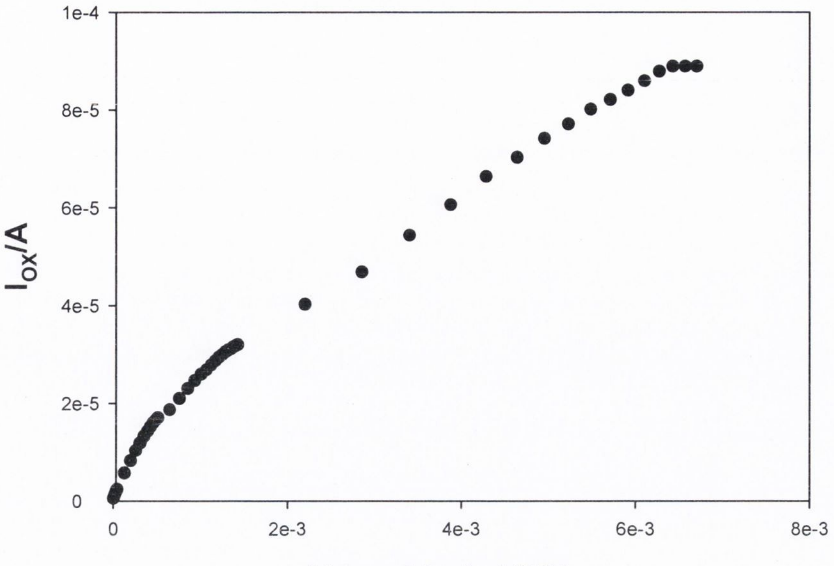

Figure 5.31; Calibration curve for Ascorbic Acid in 0.1M PBS at the PMB/GC electrode at a rotation speed of 3000rpm and holding potential of +0.6 V. Layer thickness, L = 6.06±0.8 x 10^{-8} cm.

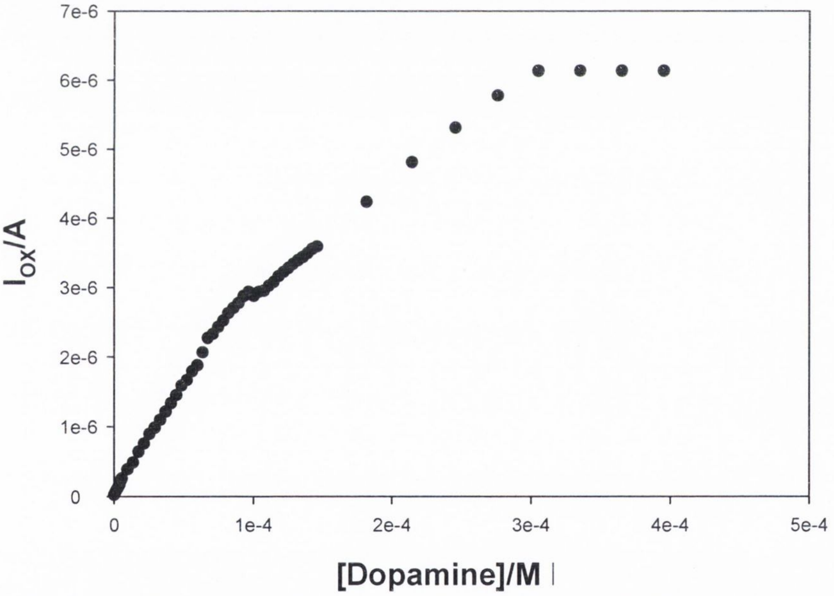

Figure 5.33; (a) Calibration curve for Dopamine in 0.1M PBS at the PMB/GC electrode at a rotation speed of 3000rpm and holding potential of +0.7 V. Layer thickness, L = 6.57±0.31 x 10^{-8} cm.

The amperometric voltammetry studies carried out on NE and E at the PMB/GC electrode returned some excellent data (Figures 5.34, 5.35) without electrode fouling.

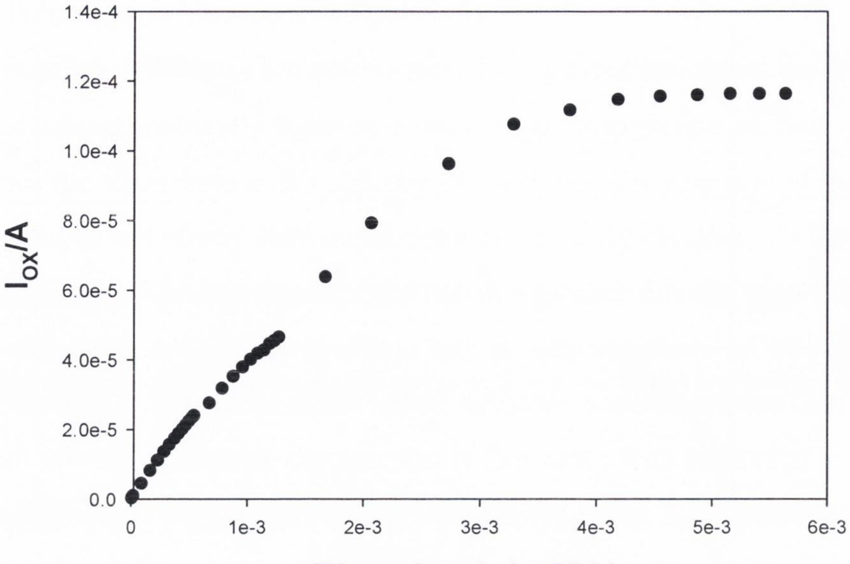

Figure 5.34; Calibration curve for Norepinephrine in 0.1M PBS at the PMB/GC electrode at a rotation speed of 3000rpm and holding potential of +0.7 V. Layer thickness, L = 6.96±0.74 x 10^{-8} cm.

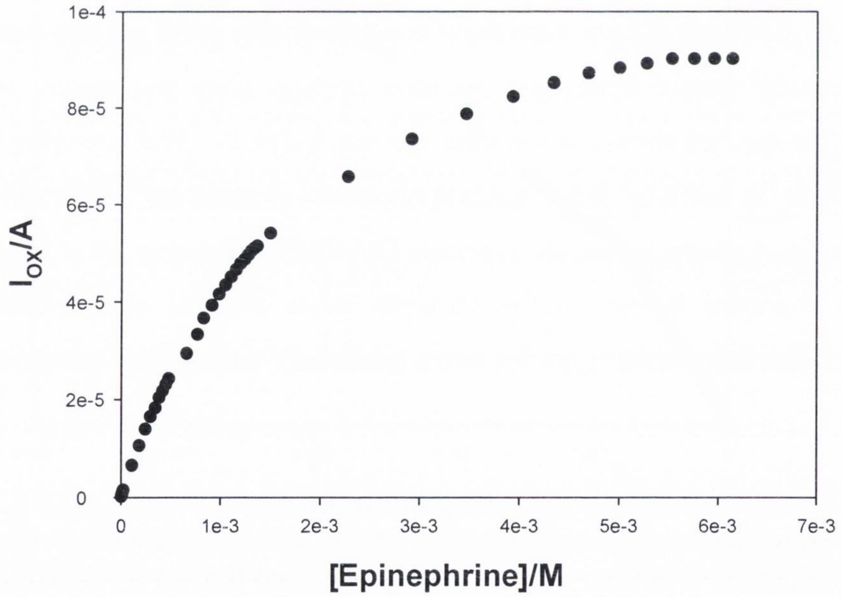

Figure 5.35; Calibration curve for Epinephrine in 0.1M PBS at the PMB/GC electrode at a rotation speed of 3000rpm and holding potential of +0.7 V. Layer thickness, L = 6.0±0.22 x 10^{-8} cm.

5.9.1 Michaelis-Menten Analysis

The change in order of the amperometric responses with respect to substrate concentration from first order at low substrate concentrations to zero order at higher values of concentration suggests the operation of Michaelis-Menten kinetics. Michaelis-Menten kinetics offers an analysis of the mediation process within the polymer layer or at the polymer/electrode interface. A fundamental characteristic of the amperometric response is that a transition from first order to zero order kinetics is observed near a critical substrate concentration termed the Michaelis-Menten constant, K_m.

The kinetics of AA, DA, NE, and EP oxidation can be described in terms of a Michaelis-Menten or 'saturation kinetics' reaction scheme. This involves the formation of a complex between the catalytic surface species and the analyte. This complex decomposes to generate the pre-catalyst and the product. This may be described by:

$$\mathrm{S+Pol^+} \overset{K_m}{\rightleftharpoons} [\mathrm{S\ Pol^+}] \xrightarrow{k_c} \mathrm{P+Pol}$$

$$\mathrm{Pol} \longrightarrow \mathrm{Pol^+}$$

where S and P denote the substrate and product and $\mathrm{Pol^+}$ and Pol the oxidised(catalytically active) and reduced forms of the immobilised polymer. The term k_c represents the first order catalytic rate constant for the decomposition of the substrate-catalyst intermediate $[\mathrm{SPol^+}]$. If it is assumed that substrate diffusion through the polymer layer is fast, then one only considers the chemical reaction between substrate and site. It can be shown that the kinetic parameters k_c and K_m can be evaluated using the following equation which relates the rate of the chemical reaction (expressed as a current) to the bulk concentration of the substrate, s^∞.

$$i = \frac{nFAk_c\Gamma s^\infty}{K_m + s^\infty} = \frac{i_m s^\infty}{K_m + s^\infty} \tag{5.8}$$

where Γ denotes the surface coverage of the polymer active sites, i_m represents the maximum current observed at high substrate concentrations. This expression is an electrochemical form of the Michaelis-Menten equation and can be transformed into a linear form termed the Lineweaver-Burk (LB) [35] equation, given by

$$\frac{1}{i} = \frac{K_m}{nFAk_c\Gamma s^\infty} + \frac{1}{nFAk_c\Gamma} = \frac{S_{LB}}{s^\infty} + I_{LB} \tag{5.9}$$

where S_{LB} and I_{LB} denote the slope and intercept of the LB plot(plot of 1/i versus 1/[S]) and are given by

$$S_{LB} = \frac{K_m}{nFAk_c\Gamma} \qquad I_{LB} = \frac{1}{nFAk_c\Gamma} \tag{5.10}$$

The Lineweaver-Burk plot is a useful diagnostic tool to confirm the operation of Michaelis-Menten kinetics. Simple manipulation of the equations for the slope and intercept allow quick evaluation of the Michaelis constant K_m. A low K_m value signifies higher substrate affinity for the active sites. The value for the catalytic rate constant k_c is also easily elucidated provided the value for the surface coverage of active sites for the polymer layer can be determined. A small value for k_c indicates that the polymer substrate complex dissociates rapidly into product, resulting in a quick turnover. The surface coverage is evaluated *via* integration of the cyclic voltammetric peak obtained from cyclic voltammetry recorded under conditions of low sweep rate and in the absence of substrate.

Typical LB plots for the four analyte oxidation calibration curves at the polymer modified electrodes are illustrated in figures 5.36 – 5.39. Accurate values for I_{LB} and S_{LB} were determined *via* least squares curve fitting software (Sigmaplot). From these values, K_m and k_c were determined for each analyte and are illustrated in Table 5.6.

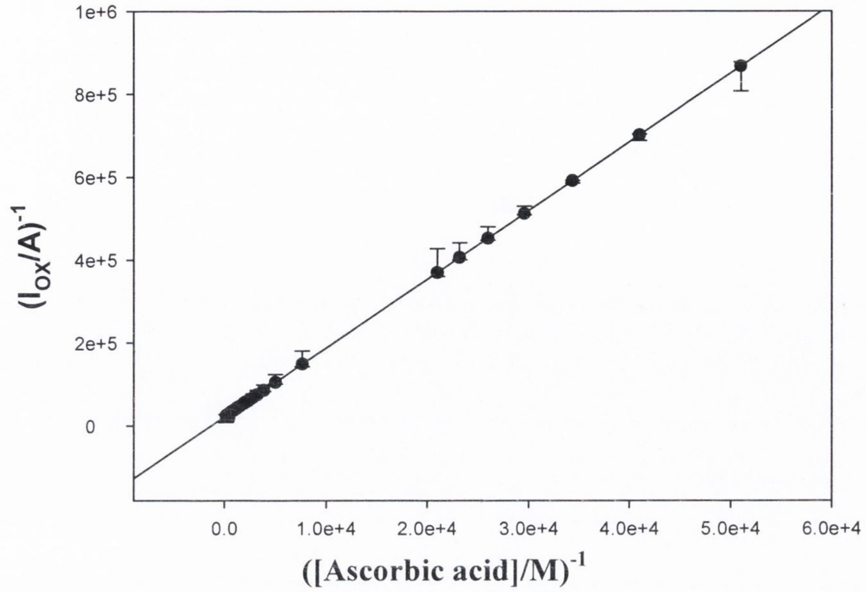

Figure 5.36; Lineweaver-Burk of AA calibration curves with associated error bars (n = 3). Layer thickness, L = $6.06\pm0.8 \times 10^{-8}$ cm

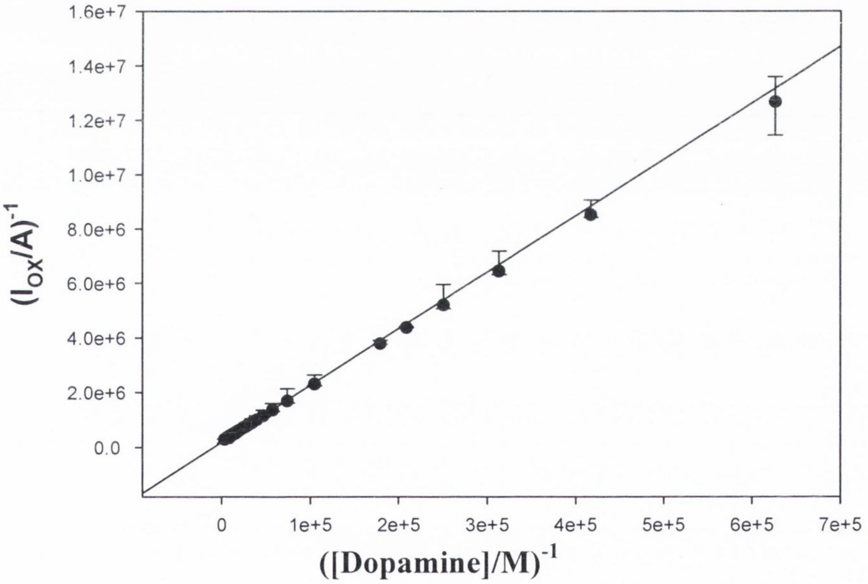

Fig. 5.37; Lineweaver-Burk analysis of the data gleaned from the calibration plots (n = 3) of Dopamine in 0.1M PBS at the PMB/GC electrode at a rotation speed of 3000rpm and holding potential of +0.7 V. Layer thickness, L = $6.57\pm0.31 \times 10^{-8}$ cm.

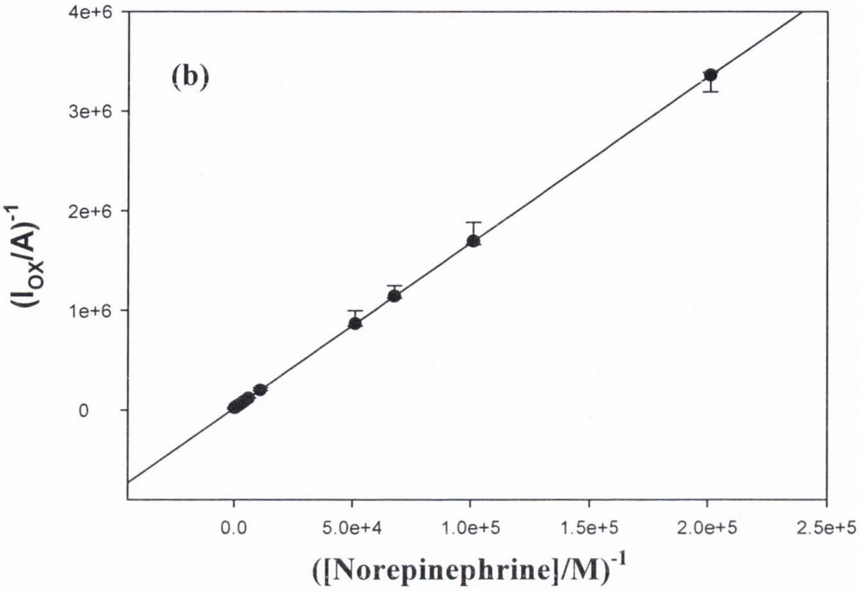

Figure 5.38; Lineweaver-Burk analysis of the data gleaned from the calibration plots (n = 3) of Norepinephrine in 0.1M PBS at the PMB/GC electrode at a rotation speed of 3000rpm and holding potential of +0.7 V. Layer thickness, L = 6.96±0.74 x 10^{-8} cm.

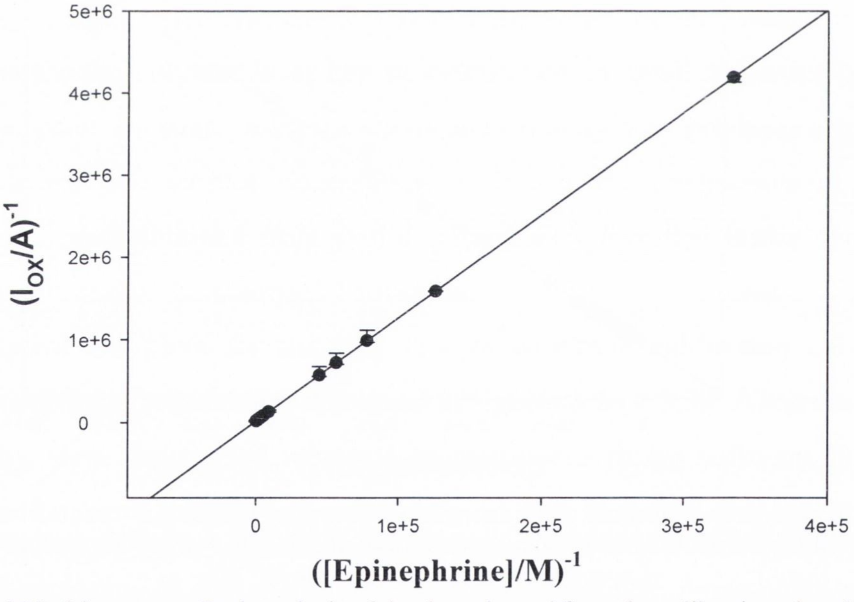

Figure 5.39; Lineweaver-Burk analysis of the data gleaned from the calibration plots (n = 3) of Epinephrine in 0.1M PBS at the PMB/GC electrode at a rotation speed of 3000rpm and holding potential of +0.7 V. Layer thickness, L = 6.0±0.22 x 10^{-8} cm.

The data may also be examined using the Eadie-Hofstee (EH) plot which arises from the following equation

$$\frac{i}{s^{\infty}} = \frac{nFAk_c\Gamma}{K_m} - \frac{i}{K_m} = I_{EH} - S_{EH}i \tag{5.11}$$

A plot of the inverse of the substrate equation should be linear with slope, S_{HE}, and intercept, I_{EH}, given by,

$$S_{EH} = -\frac{1}{K_M} \qquad\qquad I_{EH} = \frac{nFAk_c\Gamma}{K_m} \tag{5.12}$$

Figures 5.40 – 5.43 show the resultant plots from the batch amperometry experiments using the Eadie-Hofstee analysis and the parameter values are summarised in Table 5.6.

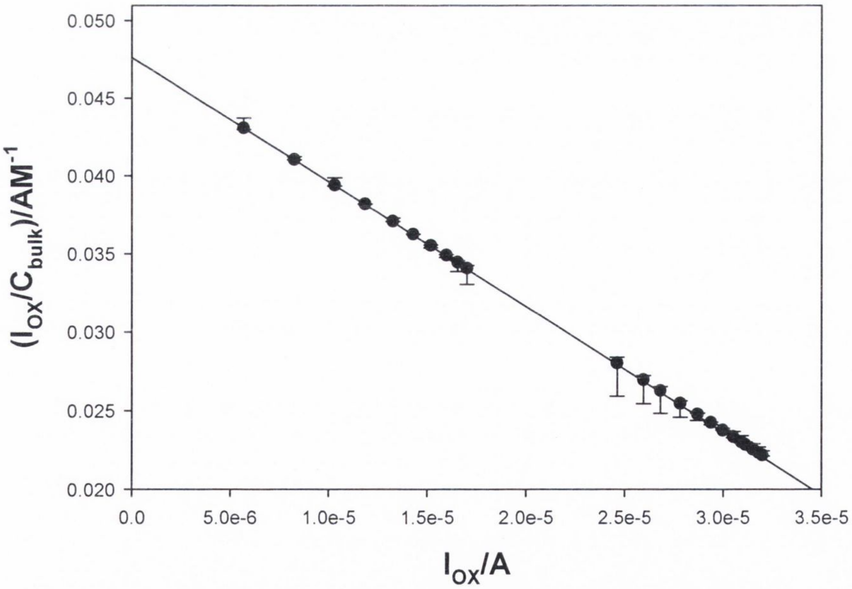

Figure 5.40; Eadie-Hofstee plot for Ascorbic Acid oxidation at the PMB/GC electrode. Layer thickness, L = 6.08±0.08 x 10^{-8} cm.

All Eadie-Hofstee plots were constructed with associated errors for each data point.

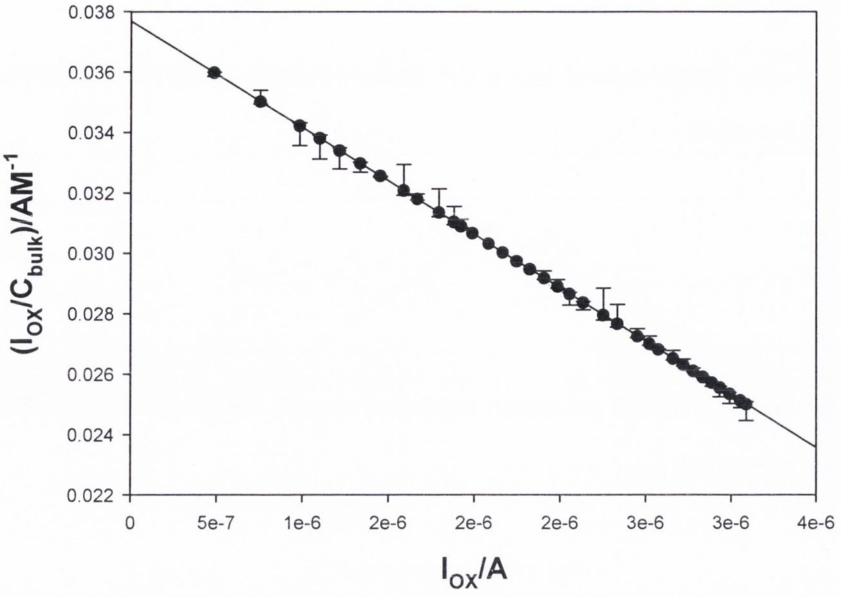

Figure 5.41; Eadie-Hofstee plot for Dopamine oxidation in 0.1M PBS at the PMB/GC electrode. Layer thickness, L = 6.57±0.31 x 10^{-8} cm.

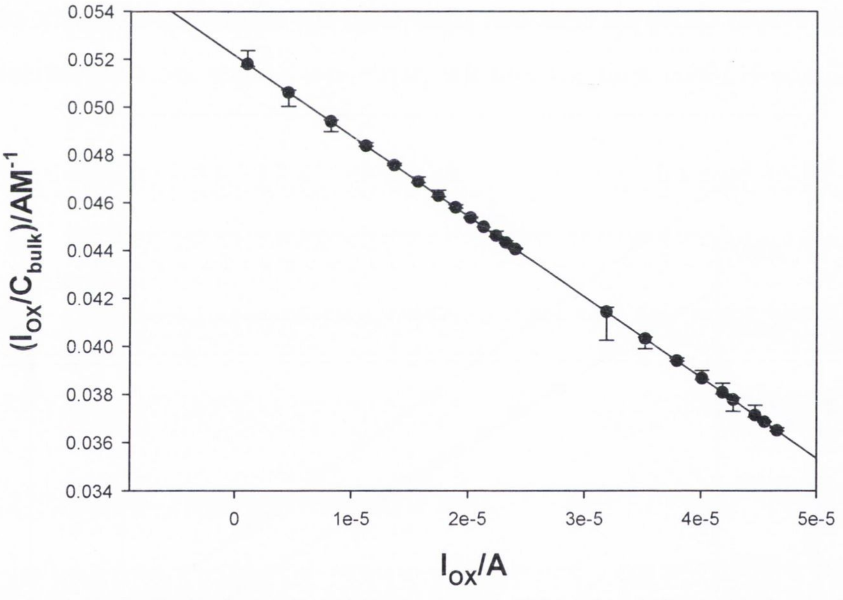

Figure 5.42; Eadie-Hofstee plot with error bars for Norepinephrine oxidation in 0.1M PBS at the PMB/GC electrode. Layer thickness, L = 6.96±0.74 x 10^{-8} cm.

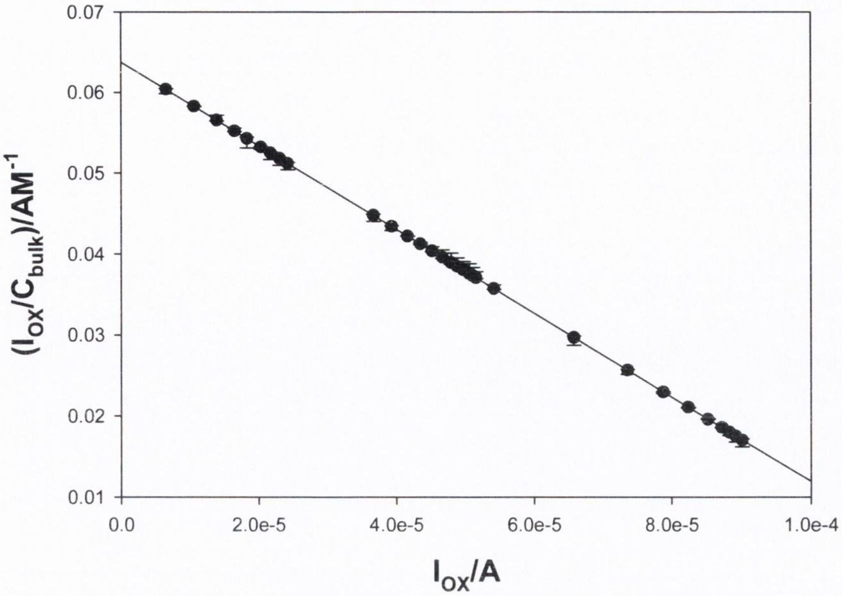

Figure 5.43; Eadie-Hofstee plot with error bars for Epinephrine oxidation in 0.1M PBS at the PMB/GC electrode. Layer thickness, L = 6.0±0.22 x 10^{-8} cm.

For many years these methods of analysis was the only ones available for determination of values for K_m and k_c. However there are limitations to this method of analysis. Firstly no kinetic values other than K_m and k_c can be gleaned from LB or EH data. Also both analysis techniques attempt to express an intrinsically non-linear expression in a linear form. This results in compression of experimental data and therefore the inevitable generation of inaccuracies in the estimation of the kinetic parameters K_m and k_c. Finally LB and EH analysis does not account for substrate diffusion within the layer but assumes infinitely fast diffusion kinetics. It was therefore concluded that a non-linear analysis of batch amperometry was needed and that data elucidated from LB and EH analysis only be used to provide estimates of the kinetic parameters.

Non-linear reaction/diffusion equations describing the substrate transport and reaction kinetics within the film were formulated and developed in chapter 4. Four distinct limiting cases were derived and are schematically illustrated in figure 4.13. This allows the use of specific non-linear equations to examine and characterise amperometric profiles for thin and thick films while saturated or during saturation. Therefore the first issue to be assessed was what specific reaction/diffusion equations i.e. Case I, II, III or IV, were the correct ones to apply to measured responses or in simple terms are the layers classed as 'thin, 'thick', 'saturated' or 'unsaturated'.

A reaction occurring at a polymer electrode interface can in theory occur at three separate areas: the film/solution interface, the electrode/film interface or alternatively throughout the entire film. Typical results of the NLLS fitting to equation 4.47 are outlined in figures 5.44 - 5.47 and all elucidated kinetic data is given in Table 5.6.

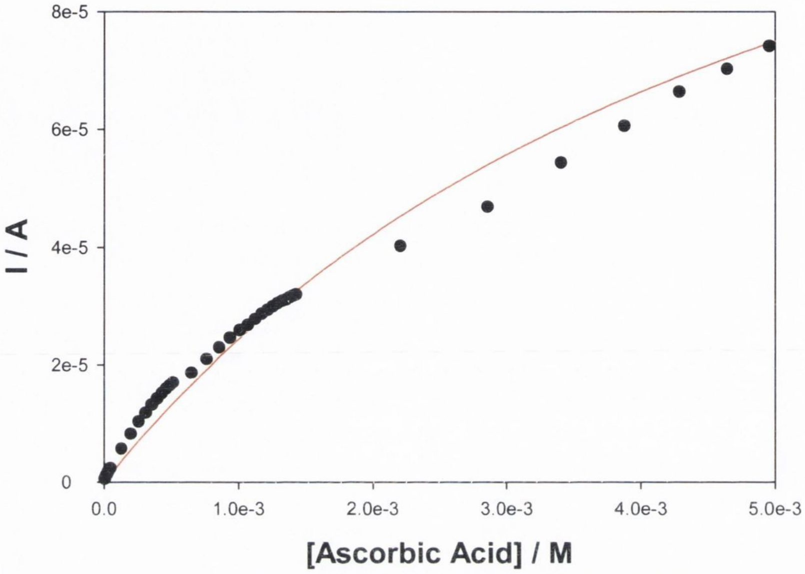

Figure 5.44; Typical batch amperometric responses obtained and the NLLS fit curve obtained from Simple Michaelis-Menten equation for Ascorbic Acid oxidation in 0.1M PBS at the PMB/GC electrode. Layer thickness, $L = 6.06 \pm 0.8 \times 10^{-8}$ cm.

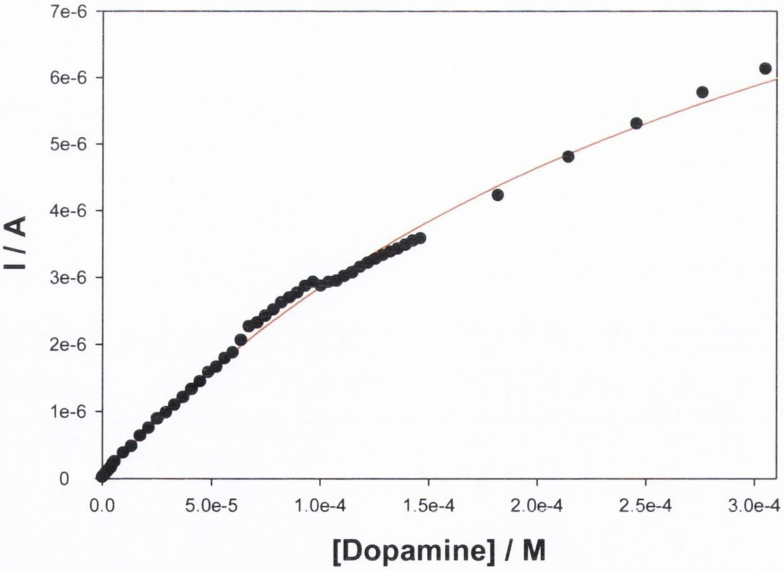

Figure 5.45; Typical batch amperometric responses and the NLLS fit curve obtained from Simple Michaelis-Menten equation obtained for Dopamine oxidation in 0.1M PBS at the PMB/GC electrode. Layer thickness, $L = 6.57 \pm 0.31 \times 10^{-8}$ cm.

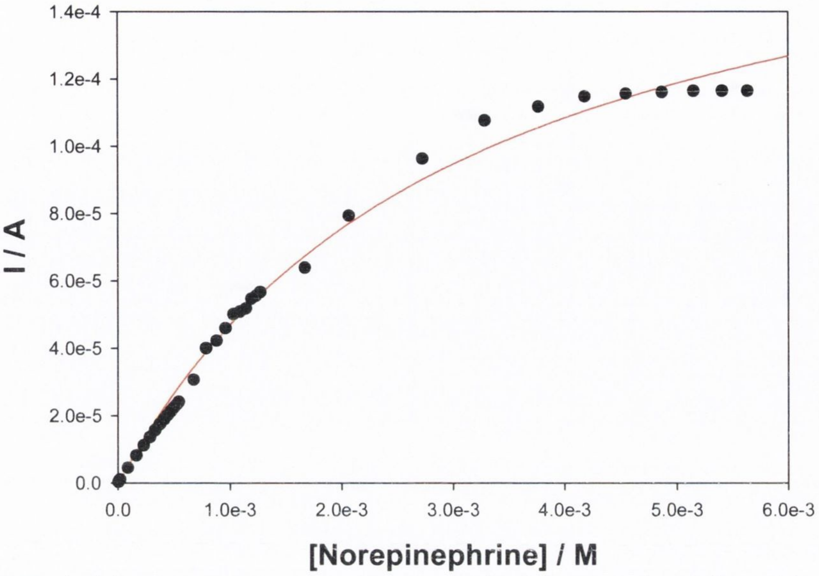

Figure 5.46; Typical batch amperometric responses obtained for Norepinephrine oxidation in 0.1M PBS at the PMB/GC electrode. The discrete data points represent the batch amperometric results and the line represents the NLLS fit curve obtained from Simple Michaelis-Menten equation. Layer thickness, L = 6.96±0.74 x 10^{-8} cm.

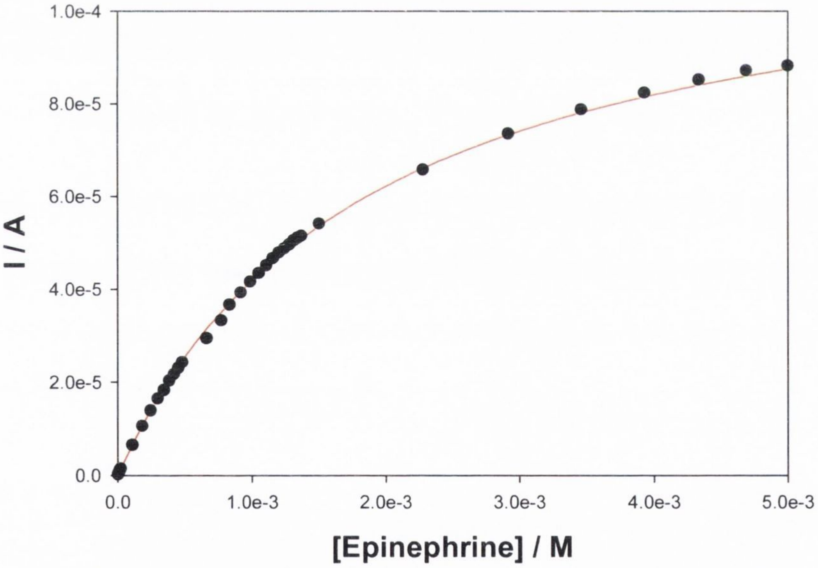

Figure 5.47; Typical batch amperometric responses obtained for Epinephrine oxidation in 0.1M PBS at the PMB/GC electrode. The discrete data points represent the batch amperometric results and the line represents the NLLS fit curve obtained from Simple Michaelis-Menten equation. Layer thickness, L = 6.0±0.22 x 10^{-8} cm.

The criteria for fitting the theoretical simple Michaelis-Menten model to the experimental data involved inputting two values, one for K_M and the other for k_C.

Analyte	Km $_{LB}$ (mM)	$k_{C\ LB}$ (s^{-1})	Km $_{EH}$ (mM)	$k_{C\ EH}$ (s^{-1})	Km $_{M\text{-}M}$ (mM)	$k_{C\ M\text{-}M}$ (s^{-1})
Ascorbic Acid	0.93	1.93	1.25	2.16	5.32	5.65
Dopamine	0.133	0.225	0.284	0.39	0.52	0.45
Norepinephrine	2.39	4.76	2.98	5.7	3.07	6.99
Epinephrine	1.33	3.42	1.93	4.49	1.86	4.39

Table 5.6; Summary of the kinetic data gleaned from the Lineweaver-Burk, Eadie-Hofstee and Simple Michaelis-Menton methods of analysis.

It should be noted that the determined value for K_m is given with the partition coefficient κ remaining unknown ($K'_m = K_m/\kappa$). Initial comparisons between the kinetic parameters determined *via* LB, EH analysis and *via* simple Michaelis-Menten analysis reveal similar values. The electrode fouling that occurred during AA oxidation meant that true Michaelis-Menton behaviour was not observed. The values calculated *via* the Michaelis-Menton fit are very poor. The Michaelis-Menton fit for NE and EP oxidation is reasonably accurate and this is reflected in the similar kinetic parameters elucidated from the data. In general the K_m values are quite large which is indicative of low analyte affinity for the active sites in the PMB/GC electrode. The differences in the values obtained for K_m can be explained in the fact that non-linear data was linearised to facilitate LB and EH analysis. The high values for k_C imply that a slow dissociation of the polymer substrate complex occurs. The polymer film, therefore, only acts as a permeable membrane through which the analyte can diffuse to undergo oxidation at the polymer/electrode interface. This means that the electrode itself is the catalyst for the analyte oxidation. Although the values obtained for the kinetic parameters using the simple Michaelis-Menten equation for DA, NE and EP are reasonable, the fitted lines do not describe the experimental data perfectly. This may be explained by the fact that the complicating effect of substrate diffusion within the film is ignored.

The more complicated full Michaelis-Menten fit for three parameters (a, b and c in equation 4.71) proved to be extremely difficult when applying the full Michaelis-Menten fit, due to the difficulties to obtain consistently reasonable results when using three as opposed to two fitting parameters. Unfortunately a successful reasonable fit was not obtained. This is probably due to the polymer nature in that no obvious catalysis is observed in the oxidation of each analyte. Substrate polarisation of the polymer film, therefore, probably has little bearing on the kinetic parameters evaluated.

5.10 Detection Limits

A concentration detection limit (C_{DL}) was determined for each of the analytes at the PMB/GC electrode using the data collected from successive determinations of individual samples. The formula used for this calculation is, $C_{DL} = ts/m$, and the values are presented in Table 5.7.

t is the level of confidence determined from the signal to noise ratio = 3.
s is the signal deviation of individual subsamples = 7×10^{-9} A.
m is the mean value for the slope of the calibration curve.

Analyte	**C_{DL} / M**
Ascorbic Acid	**1.2×10^{-9}**
Dopamine	**1×10^{-9}**
Norepinephrine	**1.1×10^{-9}**
Epinephrine	**1.5×10^{-9}**

Table 5.7; Concentration detection limits at the PMB/GC electrode.

5.11 Selectivity of the PMB/GC electrode

Figure 5.48 compares the differential pulse voltammograms of the PMB/GC electrode in 1mM AA and in 0.1M PBS. The oxidation peak for the AA is not present or maybe masked by the PMB/GC redox activity. Certainly no catalysis is evident, and so the PMB acts a permeable membrane for AA to diffuse through, allowing oxidation to occur at the electrode surface.

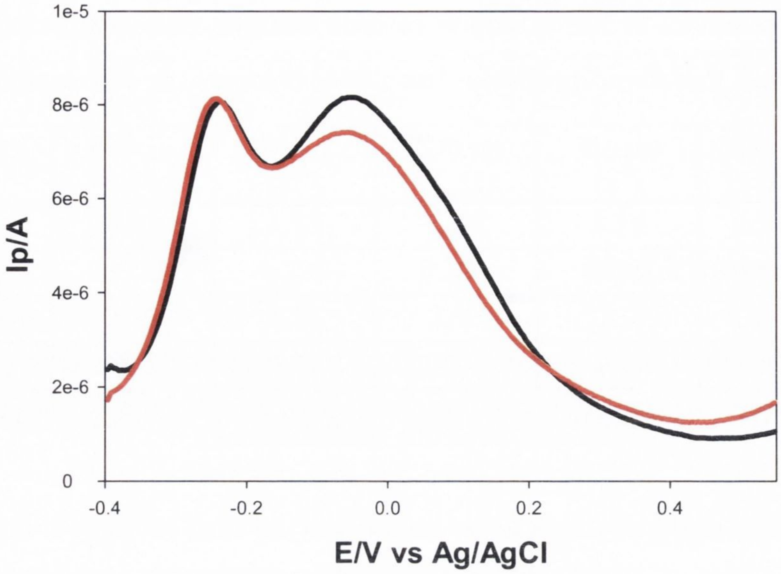

Figure 5.48; Differential pulse voltammograms comparing the PMB/GC in (—) 1mM Ascorbic Acid + 0.1M PBS, and in (—) 0.1M PBS. Pulse amplitude and width were, 0.05 V and 0.08 s, respectively. Layer thickness, L = 6.72±0.37 x 10^{-8} cm.

For analysis, differential pulse voltammetry (DPV) can be superior to CV, as AA and DA oxidation peaks can be more defined and have been shown to be distinctly separate at an unmodified graphite electrode [49]. At the PMB/GC electrode a well defined peak is observed for DA oxidation, in the absence and presence of AA (Figure 5.49).

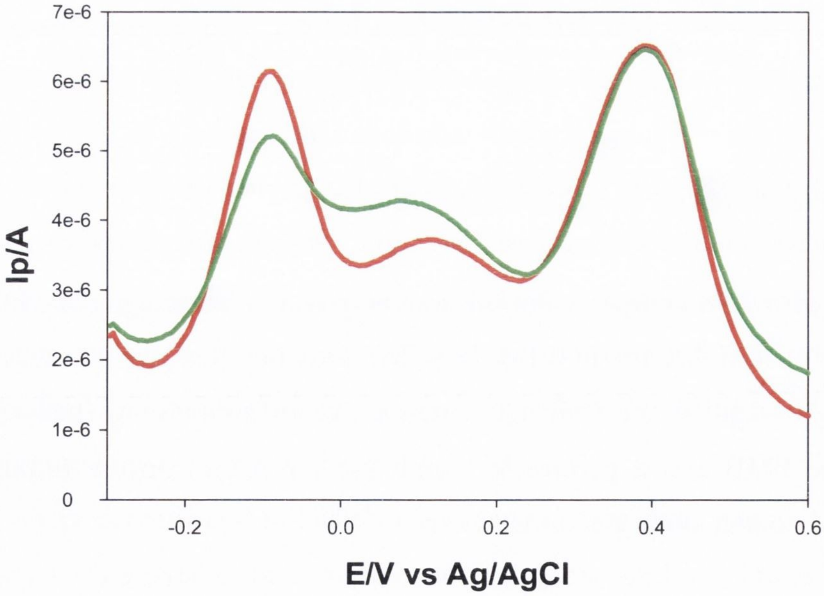

Figure 5.49; Differential pulse voltammograms comparing the PMB/GC in (—) 1mM Dopamine + 0.1M PBS and (—) 1mM Ascorbic Acid + 1mM Dopamine in 0.1M PBS. Pulse amplitude and width were, 0.05 V and 0.08 s respectively. Layer thickness, L = 6.04±0.96 x 10^{-8} cm.

The DA oxidation peak current does not decrease and peak potential is not affected by the presence of AA. This result also held true for smaller DA concentrations tested and a mathematical subtraction of the AA in PBS yielded well defined DA oxidation voltammograms (Figure 5.50).

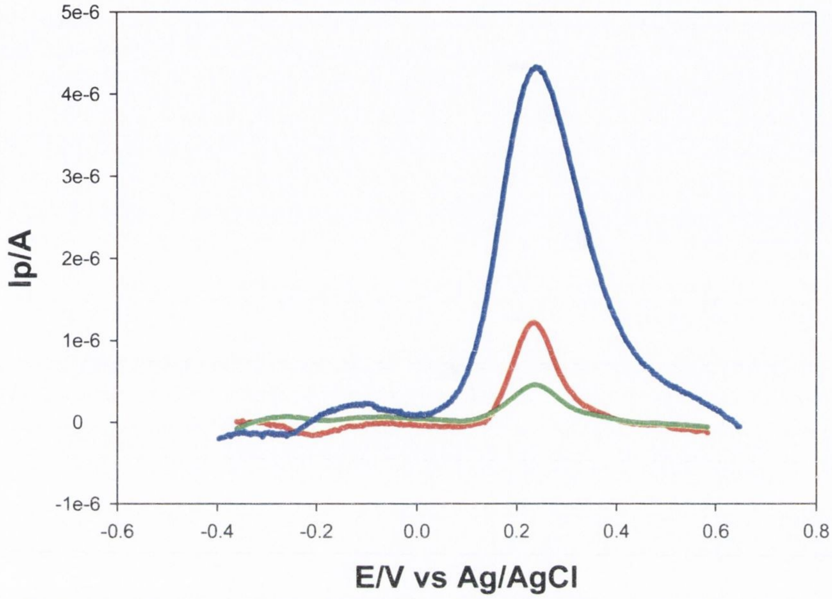

Figure 5.50; Background subtracted (1mM AA in 0.1M PBS) differential pulse voltammograms of the PMB/GC in (—) 1mM, (—) $5x10^{-4}$M and (—) $5x10^{-5}$M Dopamine. Pulse amplitude and width were, 0.05 V and 0.08 s respectively. Layer thickness, L = 6.97±0.61 x 10^{-8} cm.

The PMB/GC exhibited the same selectivity for NE in the presence of AA and the combined DPV results for a 1mM concentration are outlined in figure 5.51. A notable feature is that the monomeric LMB oxidation peak diminishes on the addition of AA and the catecholamines.

The epinephrine oxidation peak was also separated from the AA oxidation peak and was shifted to a slightly more positive anodic potential than DA and NE. The background corrected voltammograms for 1mM DA, NE and E are shown in figure 5.52 to highlight their different oxidation potentials at the PMB/GC electrode.

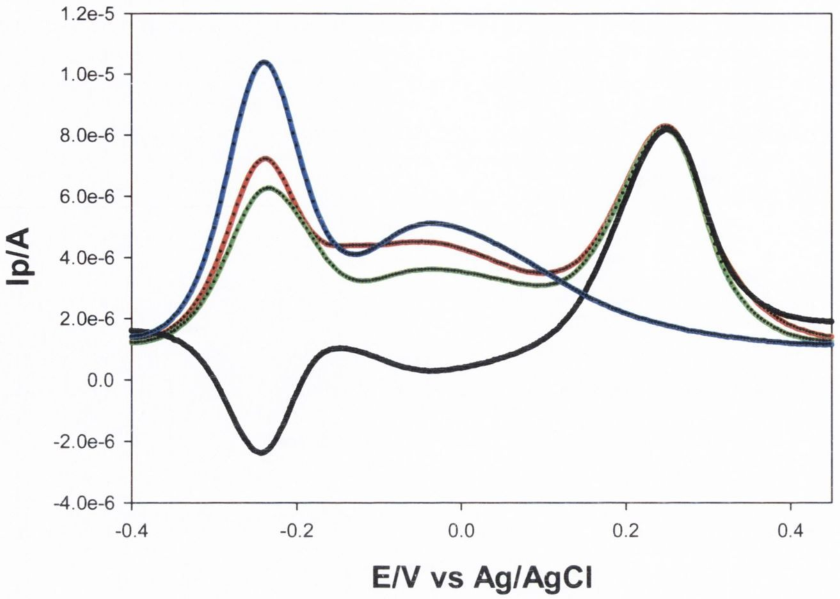

Figure 5.51. Differential pulse voltammograms of the PMB/GC in (—) 0.1M PBS, (—) 1mM AA+NE in 0.1M PBS, (—) 1mM NE in 0.1M PBS, (—) 1mM NE background subtracted (1mM AA in 0.1M PBS). Pulse amplitude and width were, 0.05 V and 0.08 s respectively. Layer thickness, L = 6.88±0.95 x 10^{-8} cm.

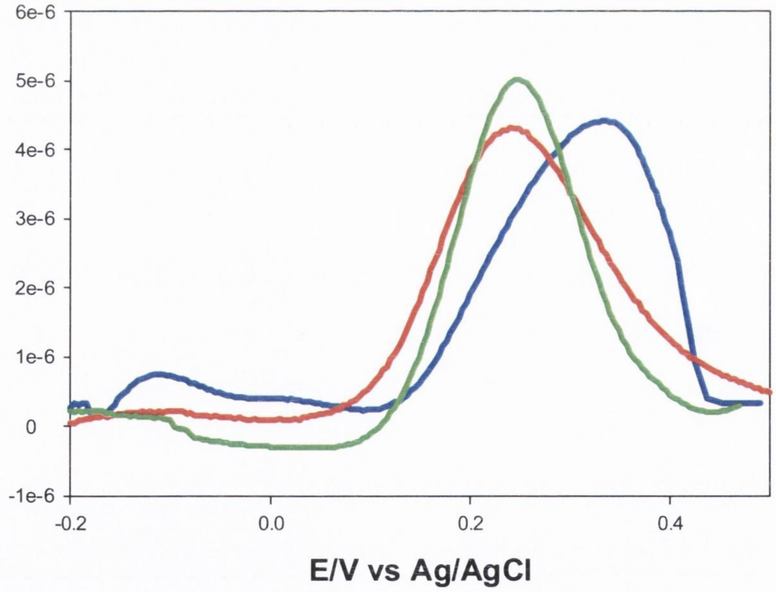

Figure 5.52; Background subtracted (1mM Ascorbic Acid in 0.1M PBS) differential pulse voltammograms for 1mM (—) Dopamine, (—) Norepinephrine and (—) Epinephrine at the PMB/GC electrode. Pulse amplitude and width were, 0.05 V and 0.08 s, respectively. Layer thickness, L = 6.27±0.54 x 10^{-8} cm.

In the case of the PMB/GC electrode, separate peaks for DA, NE and E are observed in the presence of AA using DPV. The selectivity of the PMB/GC electrode is due in part to the experimental timescale employed by DPV and also to the affinity that the anionic AA has for the cationic redox sites throughout the polymer. This AA-redox site complex is rendered electro-inactive during the course of the DPV experiment. This effect may be tentatively rationalised in that a threshold level of voltage must be applied to the PMB/GC electrode for dissociation of AA from the redox sites to be thermodynamically favourable. By the time this threshold has been applied, diffusion of the AA to the polymer/electrode interface is too slow for oxidation to occur before the pulse has ran its sweep. In any event the AA and catecholamine signals do not overlap allowing for determination of the catecholamine concentration.

5.12 Conclusions

The electrochemical oxidation of Ascorbic Acid, Dopamine, Norepinephrine, and Epinephrine was analysed at unmodified glassy carbon electrodes and at polymethylene blue polymer modified electrodes using cyclic voltammetry. The redox diffusion coefficient for AA and the catecholamines at both the bare and PMB/GC electrodes was subsequently elucidated.

Rotating disc voltammetric studies were also performed to quantify diffusion coefficients for the analytes at the bare and PMB modified electrodes. The amperometric data was analysed using the mass transport corrected Tafel equation and it was noted that much of the applied potential is required, thermodynamically, to oxidise the analytes. The oxidation kinetics of each of the analytes was investigated at the rotating disc electrode *via* linear sweep voltammograms and subsequently *via* Koutecky-Levich analysis. An attempt to locate the reaction zones using the Albery-Hillman and Andrieux-Saveant models proved difficult. The models predicted different reaction zones even though both models are essentially equivalent.

Calibration curves of ascorbic acid and the catecholamines (at constant pH) at modified electrodes were constructed from batch amperometric data. Kinetic parameters, K_m and k_C, were quantified using the linear Lineweaver-Burk and Eadie-Hofstee equations. The theoretical analysis of steady-state amperometric responses for a polymer modified electrode that exhibits Michaelis-Menten kinetics was applied. Non-linear least square analysis of the amperometric data in tandem with the LB and

EH expressions produced reasonable values for the Michaelis-Menten constant K_m, the catalytic rate constant k_C. Analyte detection limits were also calculated.

Finally, the selectivity of the PMB/GC was investigated using DPV. The ionic association between the cationic polymer redox sites and the anionic AA, coupled with the short experimental timescale, made the selective detection of the catecholamines possible in the presence of AA.

As a redox catalytic sensor for AA and the catecholamines, the PMB/GC electrode exhibits many shortcomings. Electrode fouling occurs in high concentrations of AA and DA, and the actual catalytic oxidation of the analytes is minimal at best. However, the permselective properties of the PMB/GC using DPV are excellent and could be exploited as part of an improved sensor system.

5.13 References

[1] G. F. Combs, *"The Vitamins: Fundamental Aspects in Nutrition and Health"*, 2nd edition, Acedemic press, San Diego, CA, Chapter 9, 1992.

[2] C. Martin, *Chem. Br.*, **34**, 40, 1998.

[3] M. Pufulete, *Chem. Br.*, **33**, 31, 1997.

[4] H. Zhao, Y. Zhang, Z. Yuan, *Analyst*, **126**, 358, 2001.

[5] S.-M. Chen, K.-C. Lin, *J. Electroanal. Chem.*, **523**, 93, 2002.

[6] S.-F. Wang, D. Du, Q.-C. Zou, *Talanta*, **57**, 687, 2002.

[7] M. Wei, M. Li, N. Lei, Z. Gu, X. Duan, *Electrochim. Acta*, **47**, 2673, 2002.

[8] H. Zhao, Y. Zhang, Z. Yuan, *Anal. Chim. Acta*, 454, 75, 2002.

[9] M. E. G. Lyons, W. Breen, J. Cassidy, *J. Chem. Soc., Faraday Trans.*, **87**, 115, 1991.

[10] H Mao, P. G. Pickup, *J. Electroanal. Chem.*, **265**, 127, 1989.

[11] C. Ueda, D. Chi-Sing Tse, T. Kuwana, *Anal. Chem.*, **54**, 850, 1982.

[12] P. N. Bartlett, J. M. Cooper, *J. Electroanal. Chem.*, **362**, 1, 1993.

[13] S. Cosnier, *Biosen. & Bioelectron.*, **14**, 443, 1999.

[14] H. Zhao, Y. Zhang, Z. Yuan, *Analyst*, **126**, 358, 2001.

[15] L. Zheng, S. Wu, X. Lin, L. Rui, *Analyst*, **126**, 736, 2001.

[16] J.-W. Mo, B. Ogorevc, *Anal. Chem.*, **73**, 1996, 2001.

[17] M. D. Rubianes, G. A. Rivas, *Anal. Chim. Acta*, **440**, 99, 2001.

[18] S.-M. Chen, K.-C. Link, *J. Electroanal. Chem.*, **523**, 93, 2002.

[19] P. R. Roy, T. Okajima, T. Ohsaka, *Bioelectrochemistry*, **59**, 11, 2003.

[20] Z. Gao, A. Ivaska, *Anal. Chim. Acta*, **284**, 393, 1993.

[21] Z. Gao, B. Chen, and M. Zi, *Analyst [London]*, **119**, 459, 1994.

[22] Z. Gao, B. Chen, and M. Zi, *J. Chem. Soc., Chem. Commun.*, **675**, 1993.

[23] Z. Gao, M. Zi, and B. Chen, *J. Electroanal. Chem.*, **373**, 141, 1994.

[24] Z. Gao, M. Zi, and B. Chen, *Anal. Chim. Acta*, **286**, 213, 1994.

[25] A. A. Karyakin, A. K. Strakhova, E. E. Karyakina, S. D. Varfolomeyev, A. K. Yatsmirsky, *Bioelectrochem. Bioenerg.*, **32**, 35, 1993.

[26] S. Dong, Q. Chu, *Electroanalysis*, **5**, 135, 1993.

[27] J. M. Bauldreay, M. D. Archer, *Electrochim Acta*, **28**, 1515, 1983.

[28] A. Torstensson, L. Gorton, *J. Electroanal. Chem.*, **130**, 199, 1981.

[29] D. D. Schlereth, W. Mantele, *Biochemistry*, **31**, 7494, 1992.

[30] A. A. Karyakin, E. E. Karyakina, W. Schuhmann, H.-L. Schmidt, S. D. Varfolomeyev, *Electroanalysis*, **11,** 553, 1999.

[31] X. Han, J. Tang, J. Wang, E. Wang, *Electroanalysis*, **13**, 1093, 2001.

[32] J. Wang, M. Li, Z. Shi, N. Li, Z. Gu, *Electroanalysis*, **14**, 225, 2002.

[33] G. Gerhardt, R. N. Adams, *Anal. Chem.*, **54**, 2618, 1982.

[34] P. Karabinas, D. Jannakoudakis, *J. Electroanal. Chem.*, **160**, 159, 1984.

[35] A. J. Bard, L. Faulkner, *"Electrochemical Methods, Fundamentals and Applications"*, Wiley, NY, 2nd ed., 2001, (a) p. 231, (b) p.339, (c) p.341 and (d) p.104.

[36] S. B. Khoo, F. Chen, *Anal. Chem.*, **74**, 5734, 2002.

[37] M. E. G. Lyons, W. Breen, J. Cassidy, *J. Chem. Soc. Faraday Trans.*, **87**, 115, 1991.

[38] M. D. Hawley, S. V. Tatawawadi, S. Piekarski, R. N. Adams, *J. Am. Chem. Soc.,* **89**, 447, 1967.

[39] E. L. Ciolkowski, K. M. Maness, P. S. Cahill, R. M. Wightman, D. H. Evans, B. Fosset, C. Amatore, *Anal. Chem.*, **66**, 3611, 1994.

[40] E. L. Ciolkowski, B. R. Cooper, J. A. Jankowski, J. W. Jorgenson, R. M. Wightman, *J. Am. Chem. Soc.*, **114,** 2815, 1992.

[41] R. E. Sabzi, S. Zare, K. Farhadi, G. Tabrizivand, *J. Chin. Chem. Soc.*, **52**, 1079, 2005

[42] E. V. Mosharov, L.-W. Gong, B. Khana, D. Sulzer, M. Lindan, *J. Neuroscience*, **23,** 5835, 2003.

[43] S. H. Duvall, R. L. McCreery, *J. Am. Chem. Soc.*, **122**, 6759, 2000.

[44] S.-M. Chen, K.-T. Peng, *J. Electroanal. Chem.*, **547**, 179, 2003.

[45] J. Wang, M. Li, Z. Shi, N. Li, Z. Gu, *Electroanalysis*, **14**, 225, 2002.

[46] C. Amatore, Y. Bouret, L. Midrier, *Chem. Eur. J.*, **5**, 2151, 1999.

[47] Andrieux, C. P., Dumas-Bouchiat, J. M., Saveant, J.-M.; *J. Electroanal. Chem.,* **131**, 1, 1982.

[48] W. J. Albery, A. R. Hillman, *J. Electroanal. Chem.*, **170**, 27, 1984.

[49] B. Doung, R. Arechabaleta, N. J. Tao, *J. Electroanal. Chem.*, **447**, 63, 1998.

CHAPTER 6

THE MAGNETOHYDRODYNAMIC EFFECT

6.1 The Magnetohydrodynamic Effect

When a magnetic field is coupled to an electric field in a perpendicular direction, a force is generated at right angles to both. As outlined in Chapter 1, this force is called the Lorentz force and causes convection in solution. Thus for electrochemical systems limited by mass transfer, an enhanced current due to the magnetic field, I_B, is observed. Much research has pushed the development of equations relating the mass transport limited current, I_B, with the parameters that control the magnetohydrodynamic (MHD) convection [1-6]. Analyses of experimental results however, vary to large extent. This is due in part to the nonlinear character of the hydrodynamic equations, coupled with the fact that neither the velocity nor concentration profile near the electrode is known a priori. In the most comprehensive relationship to date, proposed by the authors Legeai *et al.* [6] investigating the oxidation of ferrocycanide, I_B can be expressed as the function:

$$I_B = \mathrm{K} C^{4/3} D d^{5/3} \nu^{-2/3} \varepsilon^{-7/4} B^{1/3} \tag{6.1}$$

C represents the electroactive species concentration (mol m^{-3}), D the diffusion coefficient of the electroactive species ($m^2\ s^{-1}$), d the working electrode diameter, ν the kinematic viscosity of the electrolyte (cS), ε the dielectric constant of the solution, B the magnetic field strength (T), n the number of electrons involved in the redox process and K is a proportionality constant [$K = (1.2 \pm 0.1) \times 10^9\ \mathrm{Amol}^{-4/3}\ \mathrm{m}^{1/3}\mathrm{s}\ \mathrm{cS}^{2/3}\ \mathrm{T}^{-1/3}$]. The two most important variables for each system researched are field strength and concentration of the redox species of interest. Much of the research performed has predicted conflicting exponential dependencies of I_B on each parameter varied.

The bulk of most recent findings though, predict that the following relationship holds true, for systems involving both macro- and microelectrodes [7].

$$I_B C^{\infty} \propto (B * C^{\infty})^{1/3} \tag{6.2}$$

where C^{∞} is bulk concentration.

Using cyclic voltammetry to explore these equations, the effect of an applied magnetic field on the reduction of ferricyanide, was investigated at macro- and microelectrodes for a range of ferricyanide concentrations. The main aim was to quantify the exponential dependency of I_B on, (a) the applied magnetic field strength and, (b) the bulk concentration of the redox species. Gold, Glassy Carbon and Platinum macroelectrodes (diameter = 3mm) and a platinum microelectrode (diameter = 10μm) were used. The anodic current was assigned a positive polarity so that the experiments yielded positive reduction currents.

Visual evidence for the magnetic field induced solution convection is presented in the voltammogram for a 0.1M ferri/ ferrocyanide solution, scan rate 5mV/s, in figure 6.1. A marked increase of redox currents is observed in the voltammograms performed in a 1 Tesla magnetic field. The solution convection induced by the magnetic field serves to replenish fresh analyte at the electrode surface, effectively causing a narrowing of the depletion layer. The resultant voltammograms exhibit well defined, sharp redox peaks approaching limiting current behaviour in the 1 Tesla magnetic field. Indeed the S-shaped redox waves in a 1 Tesla magnetic field voltammogram are similar to what one might expect from RDE voltammetry.

6.2 Dependence of I_B on Magnetic Field Strength

It has been shown that over a narrow range of B, a wide variety of exponential dependencies of I_B on B^y (e.g., y = 1, 1/3, and 1/2), can all be statistically justifiable with the same set of experimental data of I_B [8]. For this reason, the double logarithmic plot is an appropriate method for the elucidation of the dependence of I_B on B [9].

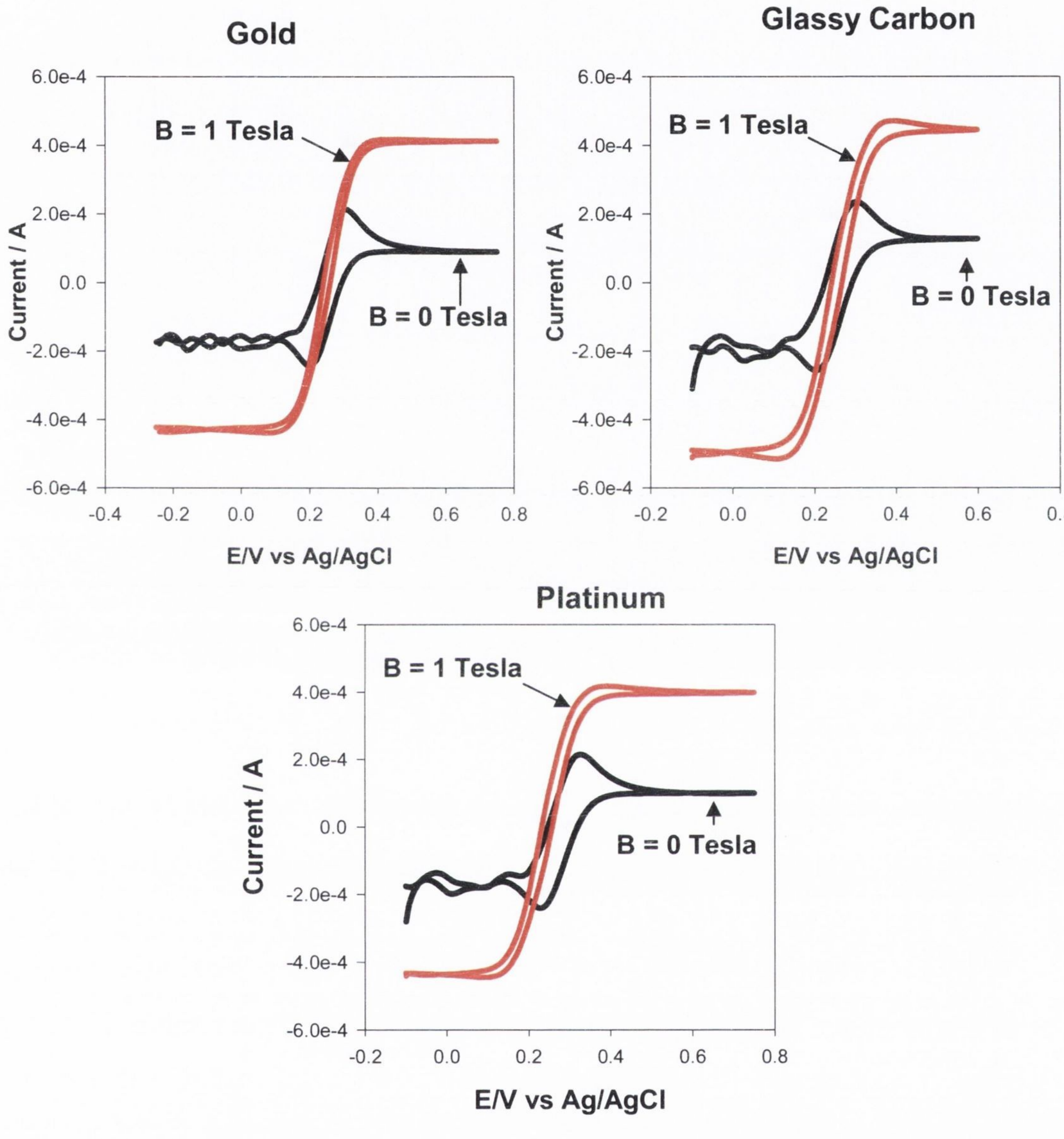

Figure 6.1; Typical voltammograms for a 0.1 M ferri/ferrocyanide solution in the presence (– 1 Tesla) and absence (– 0 Tesla) of a magnetic field. Working electrodes were Gold, Glassy Carbon and Platinum. Scan rate = 5mV/s.

The reduction of ferricyanide was investigated over a range of concentrations in the presence of varying magnetic field strengths. A log (I_B / A) *vs*. log (B / Tesla) plot was then constructed for each concentration. Figure 6.2 shows two such double logarithmic plots for 0.1M and 1M ferricyanide reduction at Gold, Glassy Carbon and Platinum macroelectrodes.

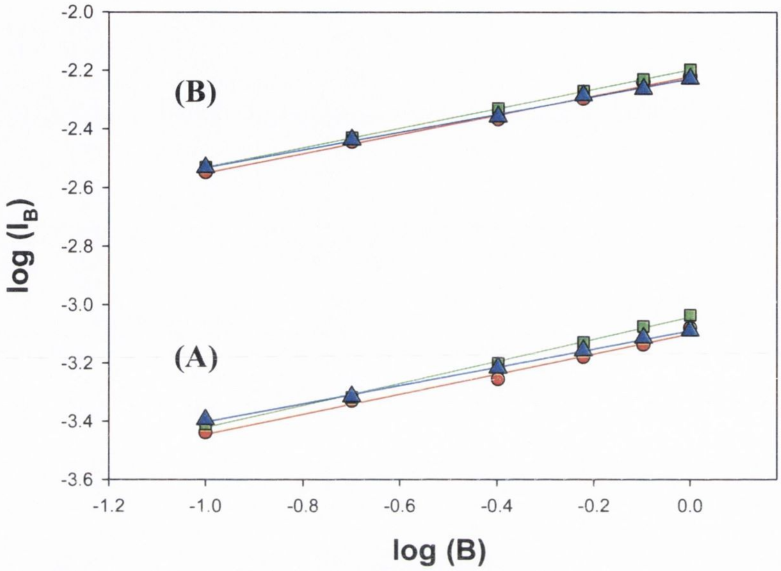

Figure 6.2; Dependence of log I_B on log B for the reduction of (A) 0.1M and (B) 1M Ferricyanide at Gold (●), GC (■) and Platinum (▲) macroelectrodes. The magnetic field was varied form 0.1 – 1 Tesla and the CV's swept at 5mV/s.

The plots are linear indicating a simple power-law dependence of I_B on B, in agreement with equation (6.1). The ferricyanide concentration was varied from 1mM to 1M and all double logarithmic plots exhibit good linearity (correlation > 0.99). For all electrodes the slopes were very close to 1/3 for both concentrations and are parallel for each electrode type. This result is in agreement with literature values [1,4,5] and confirms the I_B dependence on B in equation 6.1. One notable feature is that at low B values, the limiting current generated by ferricyanide reduction, is larger at the platinum electrode than at the gold and glassy carbon electrodes. At the highest value of B (i.e. B = 1T), the limiting current is lower at platinum than at the gold and glassy carbon electrodes. This is reflected in the slopes - the gold and glassy carbon electrodes have parallel slopes, whereas the platinum electrode is somewhere in between. A difference in the surface morphology of the electrodes could be the reason for this observation as the I_B has been shown to depend on $A^{3/4}$[4], where A = electrode area.

The I_B dependence on $B^{1/3}$ was also true for the platinum microelectrode ($r^2 > 0.99$). A plot of I_B *vs.* $B^{1/3}$ for the reduction of 0.1M ferricyanide at a platinum microelectrode is presented in figure 6.3. Three different scan rates are shown and concur with results published by the authors Lee et al at a 50μm platinum microelectrode [10].

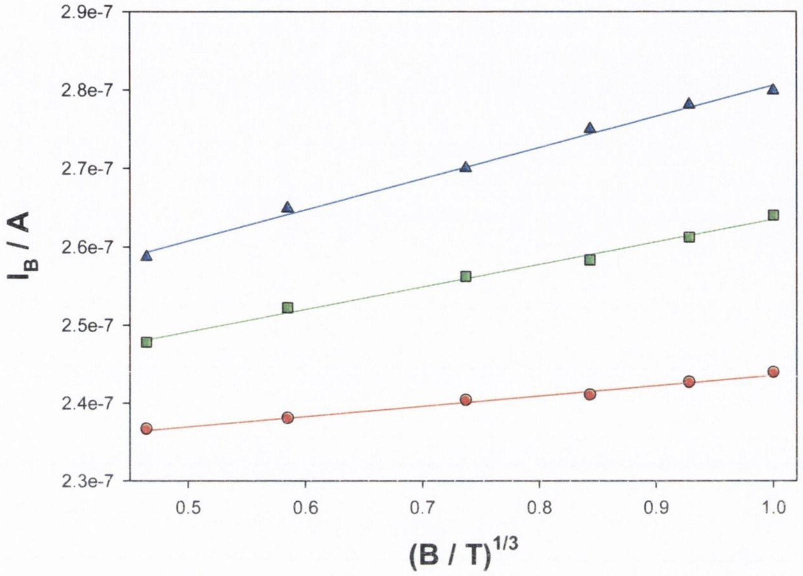

Figure 6.3; Evolution vs. $B^{1/3}$ of limiting current for the reduction of 0.1M ferricyanide at a 10μm Platinum microelectrode. Scan rates were 5mV/s (●), 70mV/s (■), and 300mV/s (▲).

Another important relationship examined was the percentage current enhancement due to the magnetic field, $I_B - I_0/I_0$. White and co-workers claim the following relationship between B and the steady state limiting currents at microelectrodes to be true [5,10,11],

$$I_B - I_0 \propto I_0 * B \tag{6.3}$$

This is disputed by the authors Aaoubi and Chopart [3,12,13] at both common size and microelectrodes. A plot of the enhancement of the voltammetric reduction current, $|I_B - I_0|$, *vs.* $I_0 * B$ is presented in figure 6.4 for a 0.1M ferricyanide solution. The enhancement is not linear over the range of B, but the limiting current enhancement approaches a plateau as the solution convection increases. This can be rationalised in that the limiting current maximum value is governed by the bulk ferricyanide concentration, irrespective of the magnitude of solution convection. Thus current enhancement cannot be infinitely linear. Deviation from linearity occurs at B > 0.5 Tesla for the 0.1M ferricyanide solution for each of the electrode types.

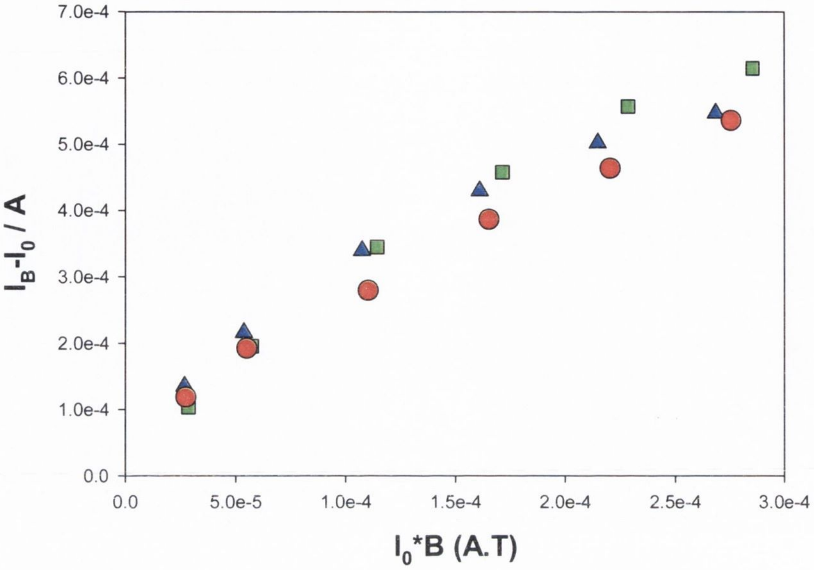

Figure 6.4; Plot of enhancement of voltammetric current $|I_B-I_0|$ for the reduction of 0.1M ferricyanide as a function of I_0*B at a scan rate of 5mV/s. The electrodes used were Gold (●), Glassy Carbon (🟩), and Platinum (▲).

6.3 Dependence of I_B on Analyte Concentration

The dependence of I_B on the concentration of ferricyanide was investigated by cyclic voltammetry over six concentrations. The double logarithmic plot of log I_B *vs.* log C* was again utilised to quantify this dependency and is shown in figure 6.5. The three macroelectrodes used exhibit very similar slopes, the average being 1.296 ± 0.015, ($r^2 > 0.995$). This value is in good agreement with the average slope of 1.34 ± 0.01 found by Leventis and co-workers [4], and confirms the $C^{4/3}$ term in equation 6.1.

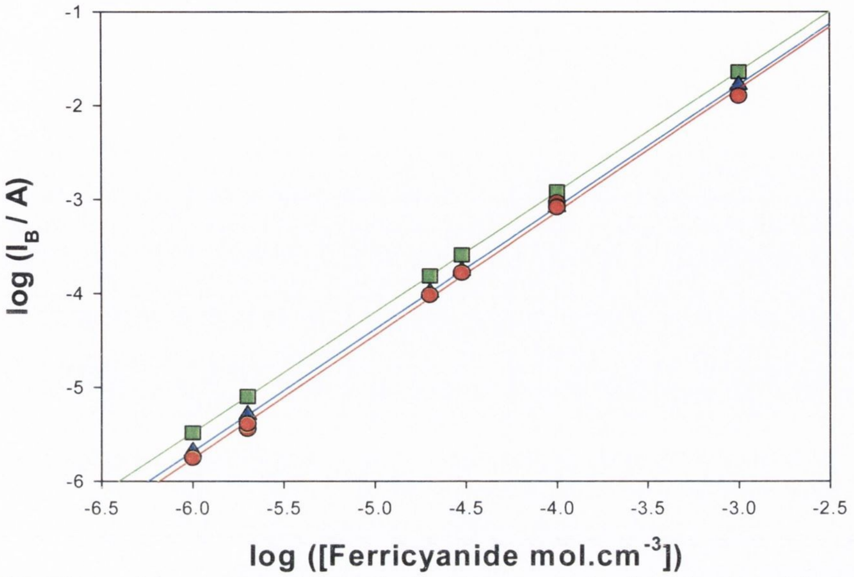

Figure 6.5; Effect of the concentration on the limiting current for the reduction of ferricyanide. The electrodes used were Gold (●), Glassy Carbon (■), and Platinum (▲).

Equation 6.2 considers the dependence of I_B on both variables, analyte concentration and magnetic field strength. With the exponential dependencies of I_B on B and C^∞ quantified, verification of this relationship was tested. The I_B/C^∞ *vs.* $(B^*C^\infty)^{1/3}$ plots for the reduction of 0.1M ferricyanide are shown in figure 6.6 at gold, glassy carbon and platinum macroelectrodes and a platinum microelectrode. The proportionality is valid for the three macroelectrodes and the platinum microelectrode used. This is in good agreement with literature results obtained at both macro- and microelectrodes [3,7]. The results obtained in this body of research show, that when the electroactive species concentration is high enough, the magnetic field B effects are of similar magnitude at both macro- and microelectrodes.

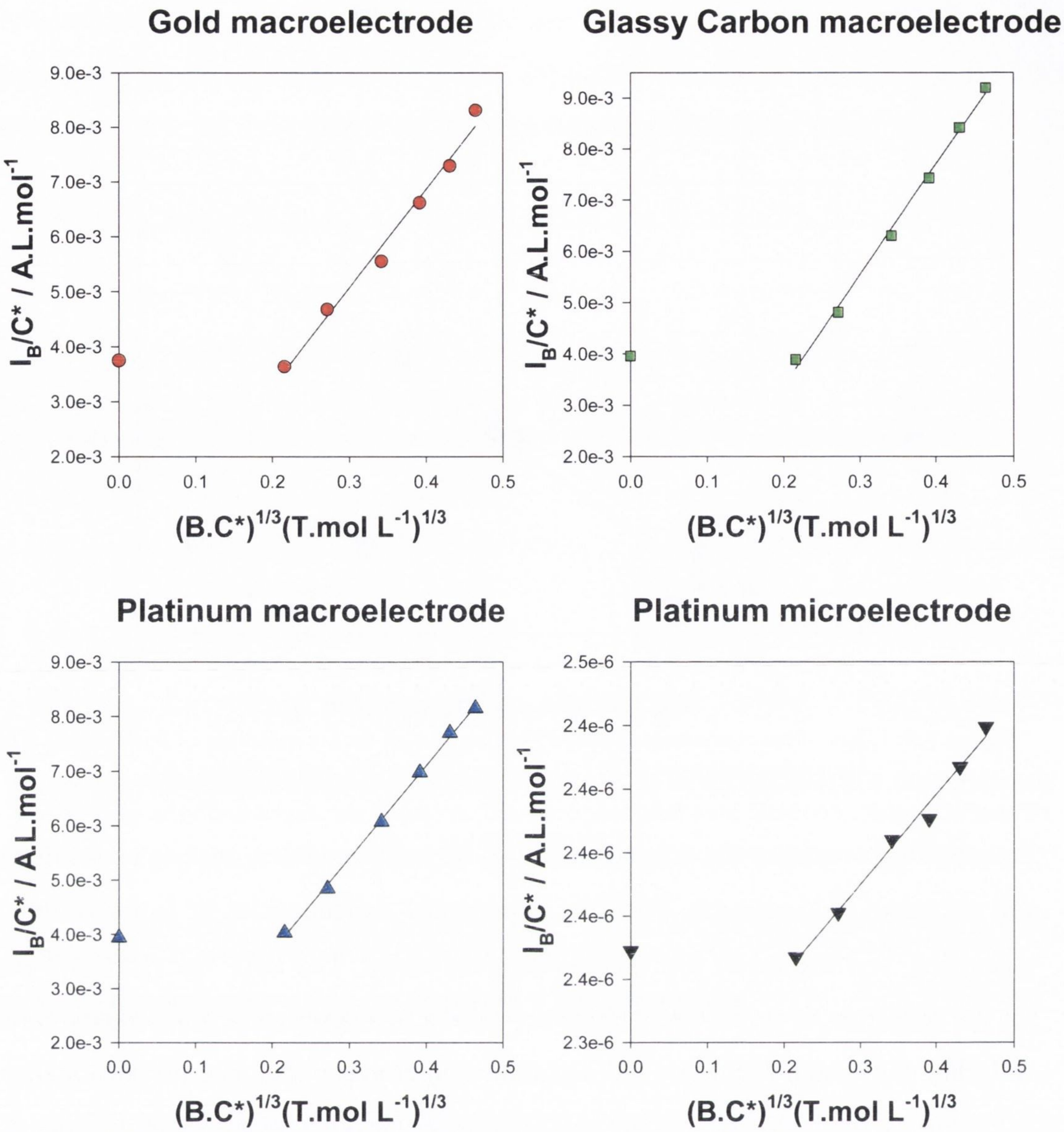

Figure 6.6; The limiting current for the reduction of ferricyanide as a function of analyte concentration and field strength. The electrodes used were Gold (●), Glassy Carbon (■), and Platinum (▲) macroelectrodes; Platinum microelectrode (▼). Scan rate, 5mV/s.

In some cases, at low B value actually results in smaller I_B than the non-field I_0 equivalent. The authors Aaboubi *et al.* [7] showed that these deviations can be attributed to the bidimentional flow of electrolyte at the electrode surface. The initial Lorentz force at low B values actually repels ions form the electrode surface. It is not powerful enough to cause a solution convection that narrows the depletion layer, but instead, a slight inhibition of the limiting current occurs. According to MHD theory, kinetic parameters corresponding to the influence of this perpendicular component of the electrolyte flux, should be included in the steady-state equation. Deviations attributed to this behaviour at low redox species concentration at the macroelectrodes are particularly evident in figure 6.7.

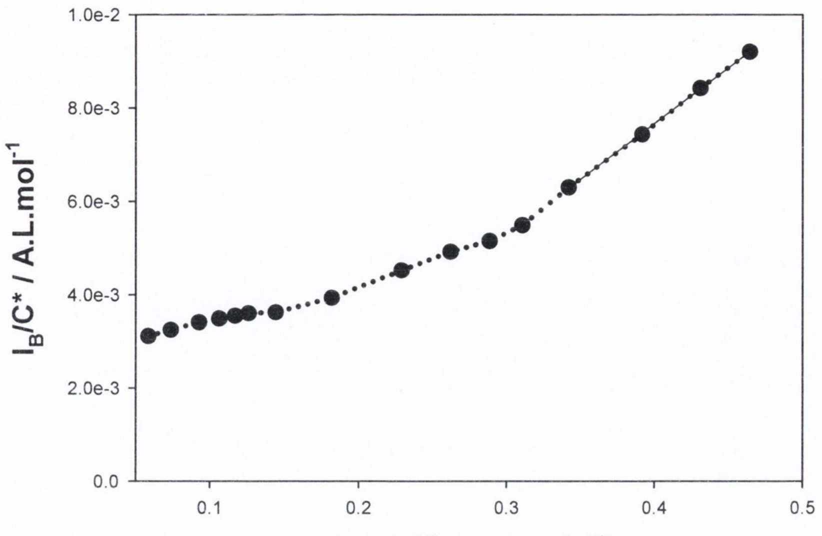

Figure 6.7; Reduced experimental limiting current I_B/C^* *vs.* $(B.C^*)^{1/3}$ obtained at a Glassy Carbon macroelectrode for a range of concentrations of $Fe(CN)_6^{3-}$ ions.

For low concentrations of redox active species at macroelectrodes, the relationship of equation 6.2 breaks down, the resultant plot for a 2 mM concentration of ferricyanide displayed in figure 6.8.

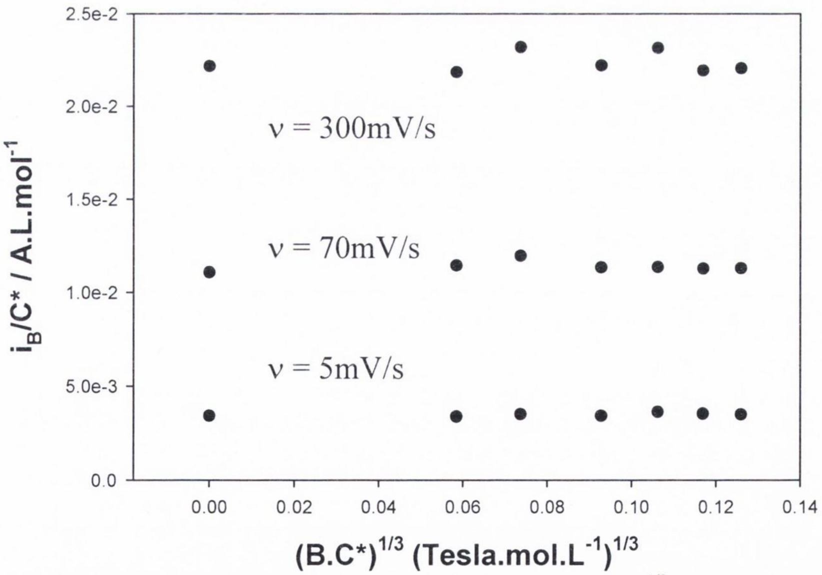

Figure 6.8; Reduced experimental limiting current I_B/C^* *vs.* $(B.C^*)^{1/3}$ obtained at a Platinum macroelectrode for a 2 mM concentration of $Fe(CN)_6^{3-}$ ions at three different scan rates.

From figure 6.8, it can be seen that the slopes of the three plots approach zero at 2 mM analyte concentration. The reason for this can be assigned to the aforementioned bidimentional flow of the electrolyte at the electrode surface. So this effect occurs at low values of B and C^{∞} at macroelectrodes. The same plot was constructed for the platinum microelectrode (Figure 6.9). The microelectrode has a radial distribution and so, relatively, a 2mM concentration of ferricyanide, is not a low concentration. Hence, the relationship remains valid.

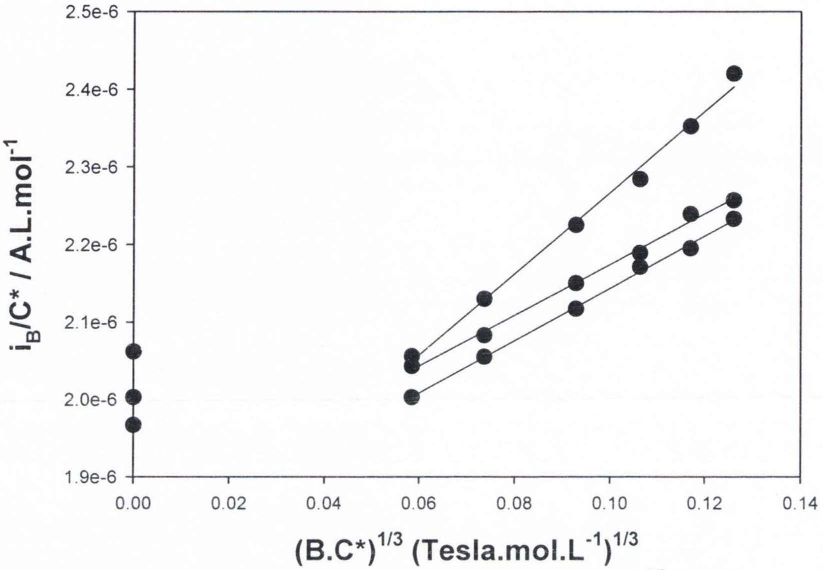

Figure 6.9; Reduced experimental limiting current I_B/C^* *vs.* $(B.C^*)^{1/3}$ obtained at a Platinum microelectrode for a 2 mM concentration of $Fe(CN)_6^{3-}$ ions at three different scan rates.

The unusual aspect of this plot is that the largest current enhancement occurs at a scan rate of 300mV/s. The largest enhancement is expected to occur at the lowest scan rate as this increases the experimental timescale, thus, allowing time for the manifestation of field induced convection.

6.4 Effect of Experimental Timescale on I_B

The effect of experimental timescale on I_B has not been given much attention with respect to published research. All MHD effects reported in the literature have been investigated using a low scan rate because the action of solution convection requires some time to take effect. Some aspects of increasing the voltammetry scan rate need to be highlighted as there is a change in the exponential dependency of I_B on C^{∞} and B.

Firstly, the percentage current enhancement decreases as the scan rate increases, and indeed, as the non-field limiting current, I_0, increases. This scan rate/I_0 duality is presented in figure 6.10. In the absence of the magnetic field an increase in the scan rate results in an increase of I_0. Conversely in the presence of a magnetic field, I_B decreases as scan rate increases, due to a decrease in the experimental timescale. This results in a decrease in percentage current enhancement.

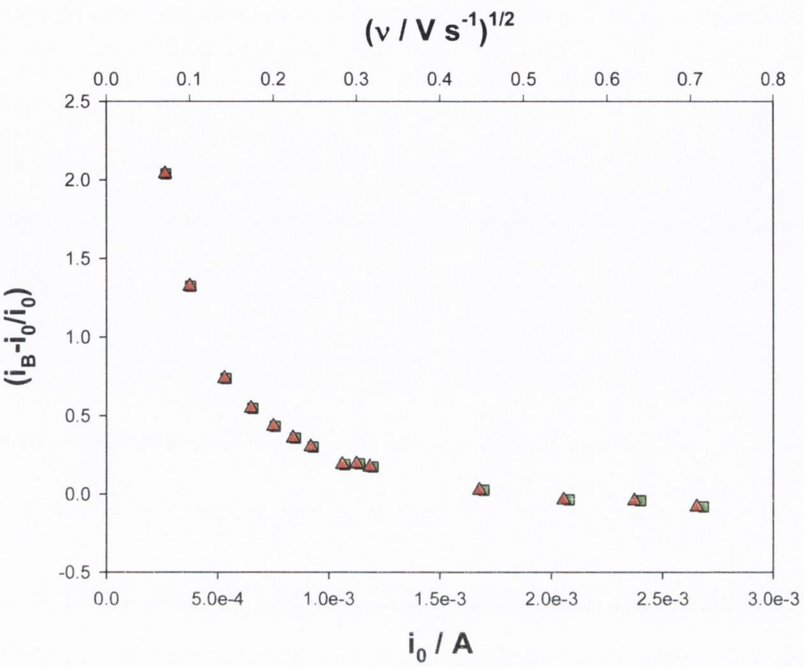

Figure 6.10; Reduced experimental percentage current enhancement (I_B-I_0/I_0) *vs.* I_0 and $\nu^{1/2}$ obtained at a platinum macroelectrode for a 0.1 M concentration of $Fe(CN)_6^{3-}$ ions.

In figure 6.10, the variation of percentage current enhancement as a function of I_0 and of scan rate is described. A plot of the inverse square root of the scan rate *vs.* the percentage current enhancement yields a straight line (Figure 6.11, $r^2 > 0.995$).

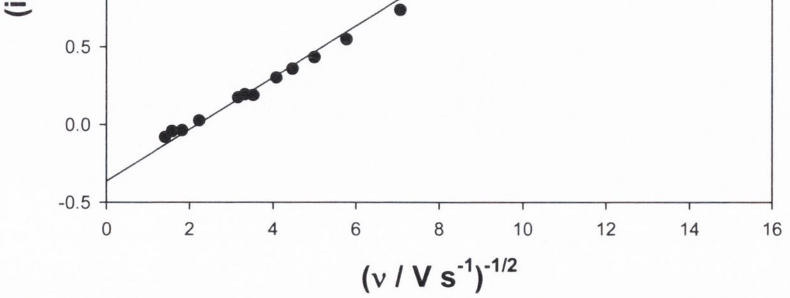

Figure 6.11; Typical plot of percentage current enhancement due to a 1 Tesla field *vs.* inverse square root scan rate, for a 0.1 M concentration of ferricyanide at a platinum macroelectrode.

Some deviations from linearity start to occur at the high scan rates (typically, $\nu \geq$ 100mV/s). Indeed the current enhancement has negative values in some cases and so the magnetic field actually inhibits I_B, when compared to its I_0 analogue. These deviations can be attributed to the perpendicular electrolye flux, but instead of a low concentration or low B value, experimental timescale limits solution convection.

The aim to quantify the exponential dependency of I_B on C^∞ and B was successful and were in excellent agreement with some of the more prominent literature findings. At low scan rates I_B is proportional to $C^{4/3}$ and $B^{1/3}$. At low B values and analyte concentration, deviations from these dependencies are observed. The deviations attributed to the experimental timescale were also outlined. The effect of scan rate on the dependency of (I_B-I_0) on (I_0*B) can be seen in figure 6.12.

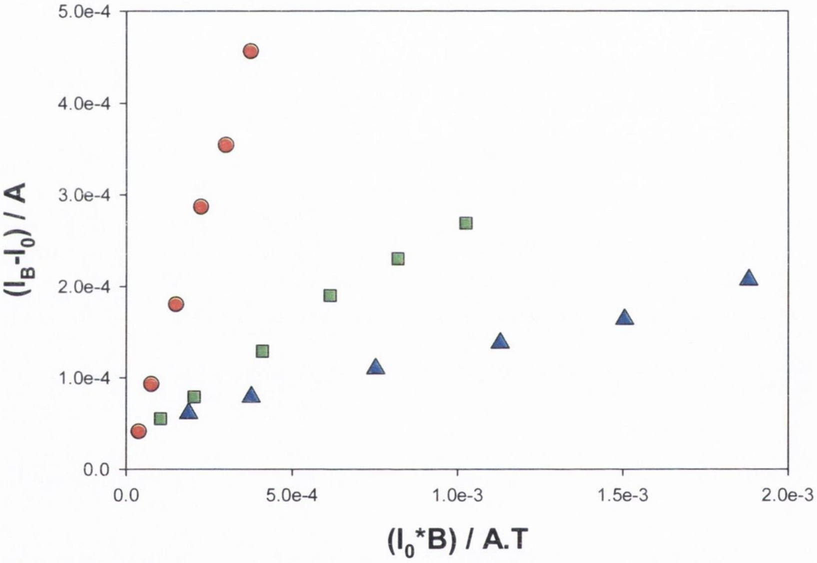

Figure 6.12; Plot of enhancement of voltammetric current $|I_B-I_0|$ for the reduction of 0.1M ferricyanide as a function of I_0*B at a Platinum macroelectrode. Scan rates of 5mV/s (●), 70mV/s (🟩) and 300mV/s (▲).

At a scan rate of, $\nu \geq$ 70mV/s, from the double reciprocal plot in figure 6.13, the slope = 1, therefore, I_B is proportional to C^∞. This dependency of log (I_B) on log C^∞ has increasingly sub-unity values for scan rates greater than 70mV/s.

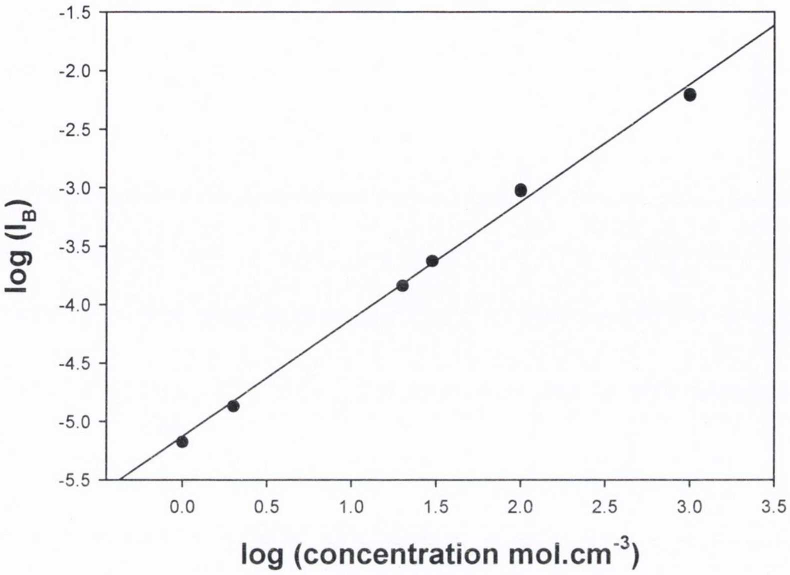

Figure 6.13; Effect of the concentration on the limiting current for the reduction of ferricyanide at a Glassy Carbon macroelectrode. Scan rate, 70mV/s.

These findings were very similar for the three different macroelectrodes for all concentrations of ferricyanide examined. The basic proportionality of $I_B/C^\infty \propto (B.C^\infty)^{1/3}$ was shown to be valid for both macro- and microelectrodes and the deviations from this relationship occurred at low values of B. Low values of C^∞ ($C^\infty \leq$ 2mM) at macroelectrodes deviated from linearity but not at the microelectrode. This, we concluded, was due to the radial diffusion associated with microelectrodes.

6.5 Effect of Magnetic Field Strength on the Reduction Kinetics

The magnetic field had no observable effect on the kinetics of the reduction of ferricyanide. The reduction peak potentials varied with scan rate in the same manner in the absence and in the presence of an applied magnetic field. Instead a homogeneous catalytic system was studied, and the, magnetic field *versus* no field, reaction rates compared.

6.6 *Homogeneous Catalysis*

In this section cyclic voltammetry and rotating disk electrode (RDE) voltammetry were used to study the reduction of methylene blue (MB) to leucomethylene blue (LMB), at a glassy carbon electrode and in the presence of Ferri-/Ferrous Ammonuim Sulphate. The rates for a homogeneous catalytic reaction were easily calculated. The catalysis was performed in a magnetic field varied from 0.1 – 1 Tesla and the rates compared.

Homogeneous catalytic reactions follow the general scheme:

$$\mathrm{O} + e^- \longrightarrow \mathrm{R} \qquad \mathbf{E} \qquad (6.4)$$

$$\mathrm{R} + \mathrm{Z} \xrightarrow{\kappa} \mathrm{O} + \mathrm{Y} \qquad \mathbf{C'} \qquad (6.5)$$

This is a specific reaction and overall is ascribed an EC' mechanism. "E" represents an electron transfer at the electrode surface in equation 6.4, and "C" represents a following homogeneous chemical reaction. Homogeneous catalysis, denoted by the "prime", describes the mediated oxidation of species R, by species Z, regenerating the starting material O. The reverse reaction of equation 6.5 does not occur. The reaction would be second-order due to diffusion of species Z and the rate of electron transfer, κ. However, the rate of equation 6.5 is considered to be pseudo-first-order when species Z is present in large excess ($C_Z^{\infty} >> C_O^{\infty}$). The kinetic parameter of interest is:

$$\lambda = \frac{\kappa C_Z^{\infty}}{v}\left(\frac{RT}{nF}\right) \qquad (6.6)$$

An example of this type of reaction, (equation 6.7), is the mediated oxidation of Ti(III) to Ti(IV):

$$\begin{tikzcd} \mathrm{Ti(IV)} + e^- \arrow[r] & \mathrm{Ti(III)} \arrow[l, bend left, "\mathrm{ClO_3^-},\ \mathrm{NH_2OH}"] \end{tikzcd} \qquad (6.7)$$

The rates of reduction of the hydroxylamine and chloride ion at a mercury electrode are small and so these species are not reduced at the potential required to drive the Ti(III) reduction.

Typical cyclic voltammograms of homogeneous catalytic reactions tend toward a limiting current, i_∞, at sufficiently negative values, which is independent of the scan rate:

$$i_\infty = nFAC_0^\infty \sqrt{D_\kappa C_Z^\infty} \qquad (6.8)$$

Also, the anodic/cathodic peak ratio, $i_{pa}/\ i_{pc}$, is unity and independent of λ. The system examined in this study was the iron mediated oxidation of leucomethylene blue to methylene blue. The catalytic current was used to obtain the pseudo-first-order rate constant of this reaction both in the absence and presence of an applied magnetic field.

The specific catalytic oxidation of LMB by is described by the following two equations; 1) the reduction of methylene blue (MB) to leucomethylene blue (LMB), reaction 6.9, at a glassy carbon electrode and 2) the oxidation of LMB to MB in the presence of Ferri-/Ferrous Ammonuim Sulphate, reaction 6.10:

$$\mathrm{MB} + 2e^- \rightleftarrows \mathrm{LMB} \qquad \mathbf{E} \qquad 6.9$$

$$\mathrm{LMB} + 2\mathrm{Fe}^{3+} \xrightarrow{\kappa} 2\mathrm{Fe}^{2+} + \mathrm{MB} \qquad \mathbf{C'} \qquad 6.10$$

Reaction 6.9 describes the charge transfer process of the two electron reduction of methylene blue to leucomethylene blue. The second equation 6.10, describes the irreversible catalytic reaction between LMB and Fe^{3+}, and this reaction increases the concentration of MB at the electrode surface. The overall reaction scheme is classed the aforementioned EC’ mechanism. When this high concentration of MB is reduced, the current produced is greater than the simple charge transfer current of equation 6.9. The difference in magnitude of these currents is termed the catalytic current and can be defined as the observed current due to the chemical reaction between LMB and the Fe^{3+}. This catalytic current can be quantified, and from a relationship (equation 6.11) developed by Saveant and Vianello [14], the rate constant (κ) for reaction 6.10 can be determined. The reaction rate has been shown, by spectral investigations, to follow pseudo-first order kinetics [15], and indeed is assumed to follow first order kinetics when the concentration of Fe^{3+} is greater than the concentration of MB.

For analysis of the homogeneous catalytic reaction *via* cyclic voltammetry, the following equation was used

$$\frac{(i\infty)_C}{(i_P)_d} = \frac{1}{0.447}\sqrt{\frac{\sigma\kappa C_Z^0}{v}\frac{RT}{nF}} \qquad (6.11)$$

where $(i_\infty)_C$ is the catalytic current, $(i_p)_d$ is the diffusion peak current, σ is a stoichiometric factor, κ is the rate constant, $C^0{}_Z$ is the concentration of Fe^{3+} and ν is the scan rate.

In order to obtain the values required to calculate the catalytic rate constant for reaction 6.9, cyclic and rotating disk voltammetry techniques were employed. The experimental conditions were taken from a paper by Murthy and Reddy [16]. In their paper, the authors claim to have obtained results examining the above system at a platinum electrode. Initially the aim of this study was to repeat and confirm their findings, but after careful experimentation it was discovered that this was not yielding the required results. The reason, we have concluded, is that the charge transfer process of the MB/LMB redox couple at a platinum electrode is too facile to require mediation by the Fe^{2+}/Fe^{3+} redox couple. This can clearly be seen from the voltammogram in figure 6.14. The stoichiometry in equation 6.10 requires two equivalents Fe^{2+}/Fe^{3+} to one equivalent MB/LMB, and this was satisfied. Scan rate, ν = 40 mV/s.

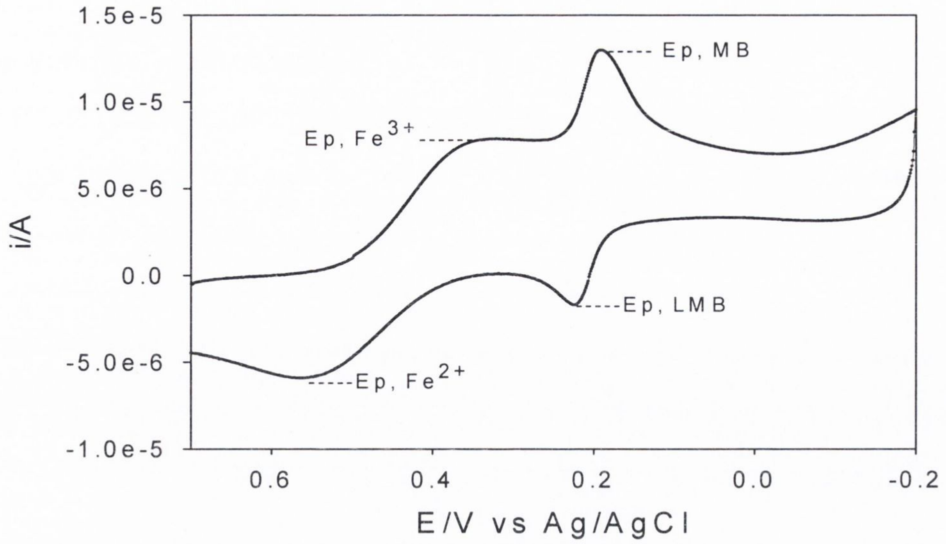

Figure 6.14; Cyclic Voltammogram of 5x10^{-4} mol dm^{-3} MB, 1x10^{-3} mol dm^{-3} Fe^{3+}, in 0.1 mol dm^{-3} H_2SO_4 at a platinum electrode.

A cathodic peak at Ep = +340 mV and anodic peak at Ep = +550 mV correspond to the reduction of Fe^{3+} and oxidation of Fe^{2+} respectively. Ep = 190 mV corresponds to the reduction of MB to LMB, and the oxidation peak at Ep = +224 mV is the reverse conversion of LMB to MB. Clearly there is no mediation of the oxidation of MB to LMB by the Fe^{3+}, but two independent processes can be seen. For this reason the platinum electrode was neglected in favour of the glassy carbon electrode where electron transfer kinetics of the MB/LMB redox couple are known to be sluggish.

Cyclic Voltammetry experiments were performed for four different concentrations of MB-Iron system to quantify the catalytic currents and hence rate constants for reaction 6.10. The cyclic voltammograms of MB (5.0 x 10^{-5} mol dm^{-3}) in 0.1 mol dm^{-3} H_2SO_4 at a glassy carbon electrode are shown in figure 6.15. Scan rate, ν = 40 mV/s. It can be clearly seen from voltammograms {a-d} that there is a change in the anodic and cathodic peaks. In {a} there is no Iron present and both reduction and oxidation peaks corresponding to reaction 6.9 are seen. The cathodic peak current has increased from 2.1 x 10^{-6} A in {a}, when no Fe^{3+} was present, to 1.48 x 10^{-4} A in {d}, when 1 x10^{-2} mol dm^{-3} Fe^{3+} was present. This is due to the chemical reaction between LMB and Fe^{3+} that increases the concentration of MB in the diffusion layer. In {b}, both cathodic and anodic peaks can be seen but the anodic peak has diminished, as the reaction of LMB and Fe^{3+} is irreversible. In {c}, the anodic peak has diminished further and has eventually disappeared in {d}.

The diffusion peak current $(i_p)_d$ is obtained form the voltammogram with no Iron present while the cathodic peak current $(i_p)_c$ is obtained from the voltammogram with Iron present, in which all the LMB has been converted to MB, i.e., the anodic peak is no longer present. The catalytic current $(i_\infty)_c$ is quantified by subtracting $(i_p)_d$ from $(i_p)_c$. Thus the cathodic peak current represents the total current from the charge transfer and the catalytic current. Table 6.1 summarises the values obtained for diffusion peak currents, cathodic peak currents, catalytic currents and rate constants for reaction 6.10 at different scan rates for the 5 x 10^{-5} mol dm^{-3} MB, 1 x10^{-2} mol dm^{-3} Fe^{3+} system.

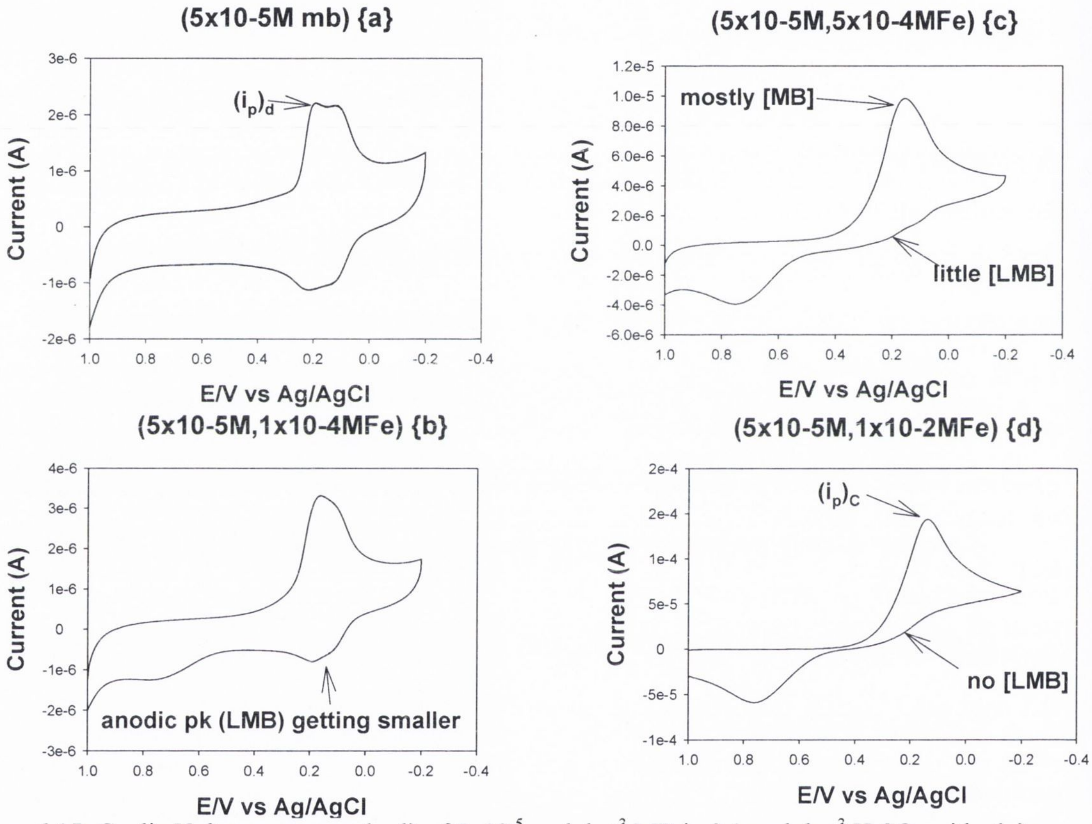

Figure 6.15; Cyclic Voltammograms {a-d} of 5x10^{-5} mol dm^{-3} MB in 0.1 mol dm^{-3} H_2SO_4 with: {a} no Fe^{3+}, {b} 1x10^{-4} mol dm^{-3} Fe^{3+}, {c} 5x10^{-4} mol dm^{-3} Fe^{3+} and {d} 1x10^{-2} mol dm^{-3} Fe^{3+}. The scan rate was ν = 40 mV/s.

Scan rate, ν (mV/s)	**Cathodic peak current, $(i_P)_C$ (A). $5\text{x}10^{-5}$M MB, $1\text{x}10^{-2}$ M Fe^{3+}.**	**Diffusion peak current, $(i_P)_d$ (A), $5\text{x}10^{-5}$M MB**	**Catalytic current $(i_\infty)_C = (i_P)_d - (i_P)_C$ (A)**	$\frac{(i_\infty)_C}{(i_p)_d}$	**Rate Constant, κ (L mol^{-1} s^{-1})**
5	5.49e-5	4.66e-6	5.45e-5	11.7	5.39e+2
10	7.51e-5	6.58e-6	7.44e-5	11.3	1.01e+3
20	1.04e-4	9.92e-6	1.03e-4	10.4	1.71e+3
30	1.23e-4	1.26e-5	1.22e-4	9.7	2.23e+3
40	1.43e-4	1.53e-5	1.42e-4	9.3	2.70e+3
50	1.62e-4	1.83e-5	1.60e-4	8.8	3.03e+3
60	1.70e-4	1.79e-5	1.69e-4	9.4	4.22e+3
70	1.87e-4	2.11e-5	1.85e-4	8.8	4.26e+3
80	1.61e-4	2.21e-5	1.59e-4	7.2	3.27e+3
90	1.93e-4	2.49e-5	1.91e-4	7.7	4.18e+3
100	2.19e-4	2.52e-5	2.16e-4	8.6	5.81e+3
200	2.69e-4	3.83e-5	2.65e-4	6.9	7.55e+3
300	3.01e-4	6.91e-5	2.95e-4	4.3	4.31e+3
400	3.68e-4	7.68e-5	3.60e-4	4.7	6.94e+3
500	3.87e-4	9.56e-5	3.78e-4	4.0	6.15e+3

Table 6.1; Diffusion peak currents obtained for a [MB] 5 x 10^{-5} M and the catalytic currents generated in the presence of 0.01M Fe^{3+}, used to calculate rate constants over a range of scan rates.

The rotating disk electrode (RDE) voltammetric behaviour of MB and of the MB-Fe^{3+} system was studied for the same concentrations investigated using cyclic Voltammetry. The scan rate was kept constant (υ = 20 mV/s), but the rotation speed was varied. The rate constants of reaction 6.10 were determined using the following relationship, developed by Lyons [17]:

$$\Psi = \frac{i_{L,C}}{i_{L,D}} = \sqrt{\kappa \frac{\left[Fe^{3+}\right]_\infty}{D_{MB}}}\,\delta \tag{6.12}$$

$$K = \kappa\,[Fe^{3+}]_\infty \tag{6.13}$$

where $i_{L,C}$ is the catalytic limiting current, $i_{L,D}$ is the diffusion limiting current, $[Fe^{3+}]_\infty$ is the bulk concentration of Fe^{3+} when no LMB remains in the system, D_{MB} is the diffusion coefficient of MB and δ is the diffusion layer thickness. The diffusion layer thickness was calculated using the following equation:

$$\delta = 1.61\ D^{1/3}\ \upsilon^{1/6}\ \omega^{-1/2} \qquad (6.14)$$

where D is the diffusion coefficient, υ is the kinematic viscosity of the solution (~ 10^{-2} $cm^2\ s^{-1}$) and ω is the rotation speed of the electrode in Hertz. The RDE voltammograms (figure 6.16) show the plateau regions at the negative potentials used to determine the catalytic limiting current. The diffusion coefficients were calculated using the slope of the linear graph of $i_{L,D}$ versus $\omega^{1/2}$. Figure 6.17 shows the plot for 5 $x10^{-5}$ mol dm^{-3} MB, from which the diffusion coefficient, $D_{MB} = 8.15 \times 10^{-6}\ cm^2\ s^{-1}$, was obtained. Diffusion peak, catalytic currents and calculated rate constants are summarised in table 6.2.

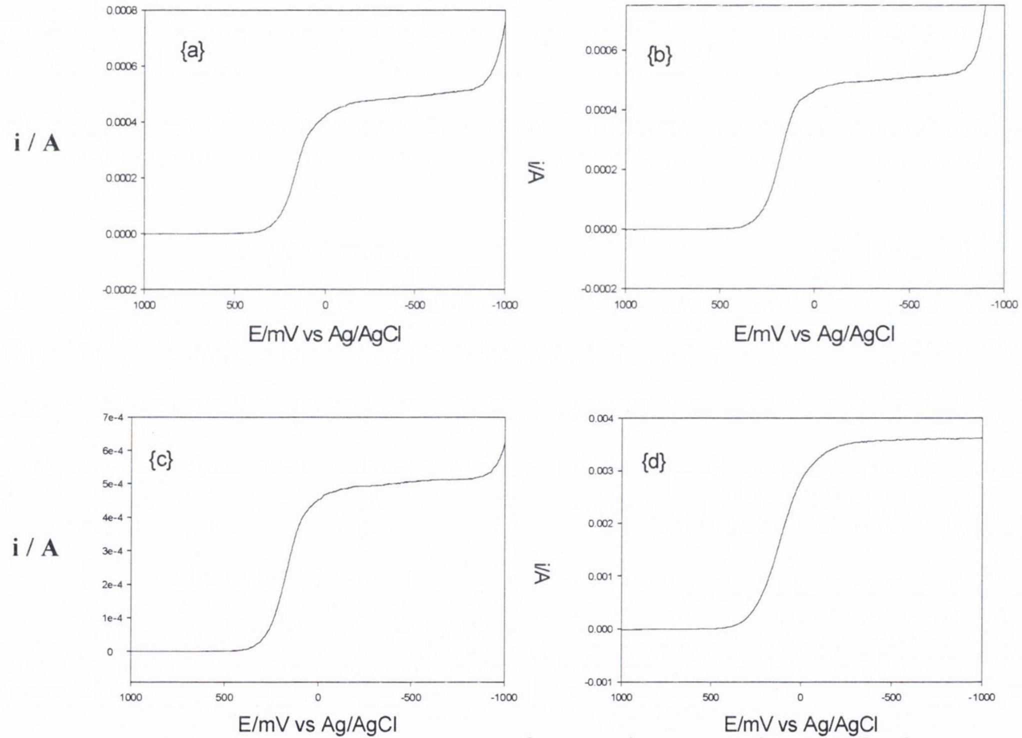

Figure 6.16; RDE Voltammograms of {a} $1x10^{-5}$ mol dm^{-3} MB, $1x10^{-2}$ mol dm^{-3} Fe^{3+}, {b} $5x10^{-5}$ mol dm^{-3} MB, $1x10^{-2}$ mol dm^{-3} Fe^{3+}, {c} $1x10^{-4}$ mol dm^{-3} MB, $1x10^{-2}$ mol dm^{-3} Fe^{3+} and {d} $5x10^{-4}$ mol dm^{-3} MB, $1x10^{-1}$ mol dm^{-3} Fe^{3+} in 0.1 mol dm^{-3} H_2SO_4, 0.1 mol dm^{-3} KCl at a glassy carbon electrode. The catalytic limiting current, $i_{L,C}$, value was obtained form the plateau in the negative potential region. The current increase after the potential of 800 mV is due to hydrogen evolution. The rotation speed was 1000 rpm and the scan rate 20 mV/s.

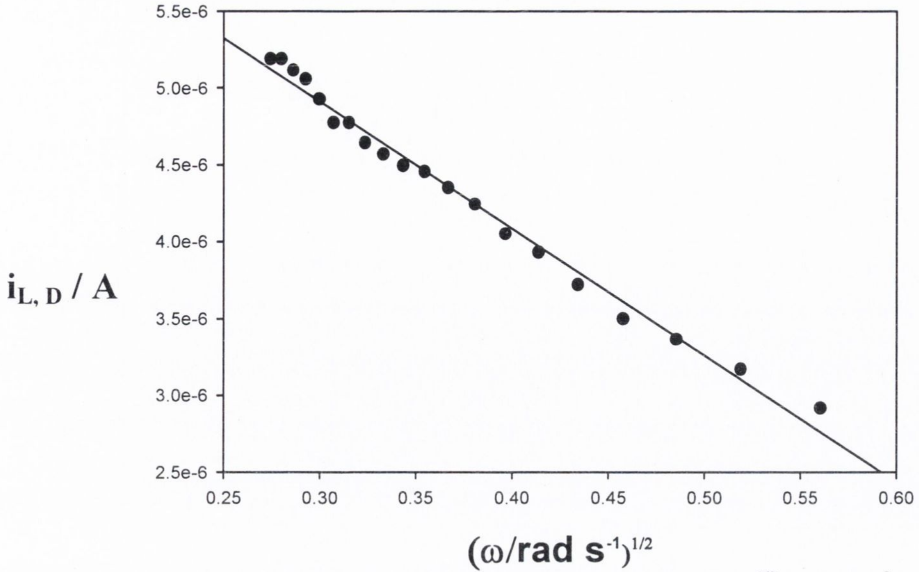

Figure 6.17; A typical plot of diffusion limiting current ($i_{L,D}$) values vs $\omega^{1/2}$ for 5×10^{-5} mol dm^{-3} MB. The slope is proportional to the diffusion coefficient.

$(\omega/\text{Hertz})^{-1/2}$	$\Psi = i_L/i_{L,D}$	κ (L mol^{-1} s^{-1})	$(\omega/\text{Hertz})^{-1/2}$	$\Psi = i_L/i_{L,D}$	κ (L mol^{-1} s^{-1})
1.030	**15.1**	**3.95e+2**	**2.726**	**19.7**	**2.17e+3**
1.262	**15.3**	**4.97e+2**	**2.820**	**20.0**	**1.89e+3**
1.457	**17.1**	**7.15e+2**	**2.914**	**20.2**	**1.99e+3**
1.629	**18.5**	**9.31e+2**	**3.003**	**20.5**	**2.12e+3**
1.784	**19.0**	**1.08e+3**	**3.09**	**20.8**	**2.23e+3**
1.927	**19.2**	**1.18e+3**	**3.175**	**20.7**	**2.29e+3**
2.060	**19.1**	**1.26e+3**	**3.258**	**21.0**	**2.40e+3**
2.185	**19.7**	**1.42e+3**	**3.337**	**21.0**	**2.45e+3**
2.303	**19.6**	**1.48e+3**	**3.416**	**21.0**	**2.53e+3**
2.415	**18.9**	**1.45e+3**	**3.492**	**21.4**	**2.67e+3**
2.523	**19.2**	**1.27e+3**	**3.569**	**21.4**	**2.28e+3**
2.626	**19.4**	**1.65e+3**	**3.642**	**22.0**	**2.95e+3**

Table 6.2; Diffusion peak, catalytic currents and calculated rate constants summarised for a range of rotation speeds.

Values obtained for the $i_{L,C}$ / $i_{L,D}$ ratio which is proportional to $\omega^{-1/2}$ (Figure 6.18), and the rate constant κ for different electrode rotation speeds are shown in Table 6.2.

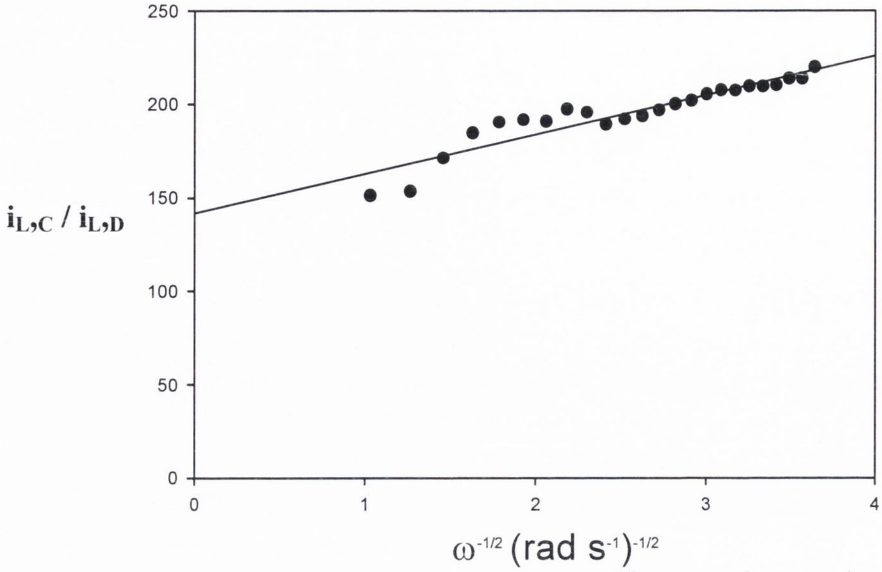

Figure 6.18; Plot of the linear relationship $i_{L,C} / i_{L,D}$ ratio vs $\omega^{-1/2}$ for $5\text{x}10^{-5}$ mol dm^{-3} MB, $1\text{x}10^{-2}$ mol dm^{-3} Fe^{3+}. This shows reasonably good linearity especially at low rpm.

The Cyclic Voltammetry data presented in table 6.1 for the homogeneous catalytic rate constants compare reasonably well with those obtained using RDE Voltammetry in table 6.2. The average rate using Cyclic Voltammetry was 3.86 x 10^3 L mol^{-1} s^{-1}, while the average using RDE Voltammetry was 1.72 x 10^3 L mol^{-1} s^{-1}. This was the case for various concentrations of the MB-Iron system. These rate constants compare very well with those calculated by Murthy and Reddy [16].

6.7 *Effects of an Applied Magnetic Field on Homogeneous Catalysis*

Cyclic voltammetry was employed to analyse the catalysis in the presence of a range of magnetic field strengths [0 – 1 Tesla] and the reaction rates quantified. A series of voltammograms outlining the progression of the catalysis of a 5 x 10^{-4} M MB solution with increasing Fe^{3+} concentrations, in the absence and presence of a 1 Tesla magnetic field, is shown in figure 6.19.

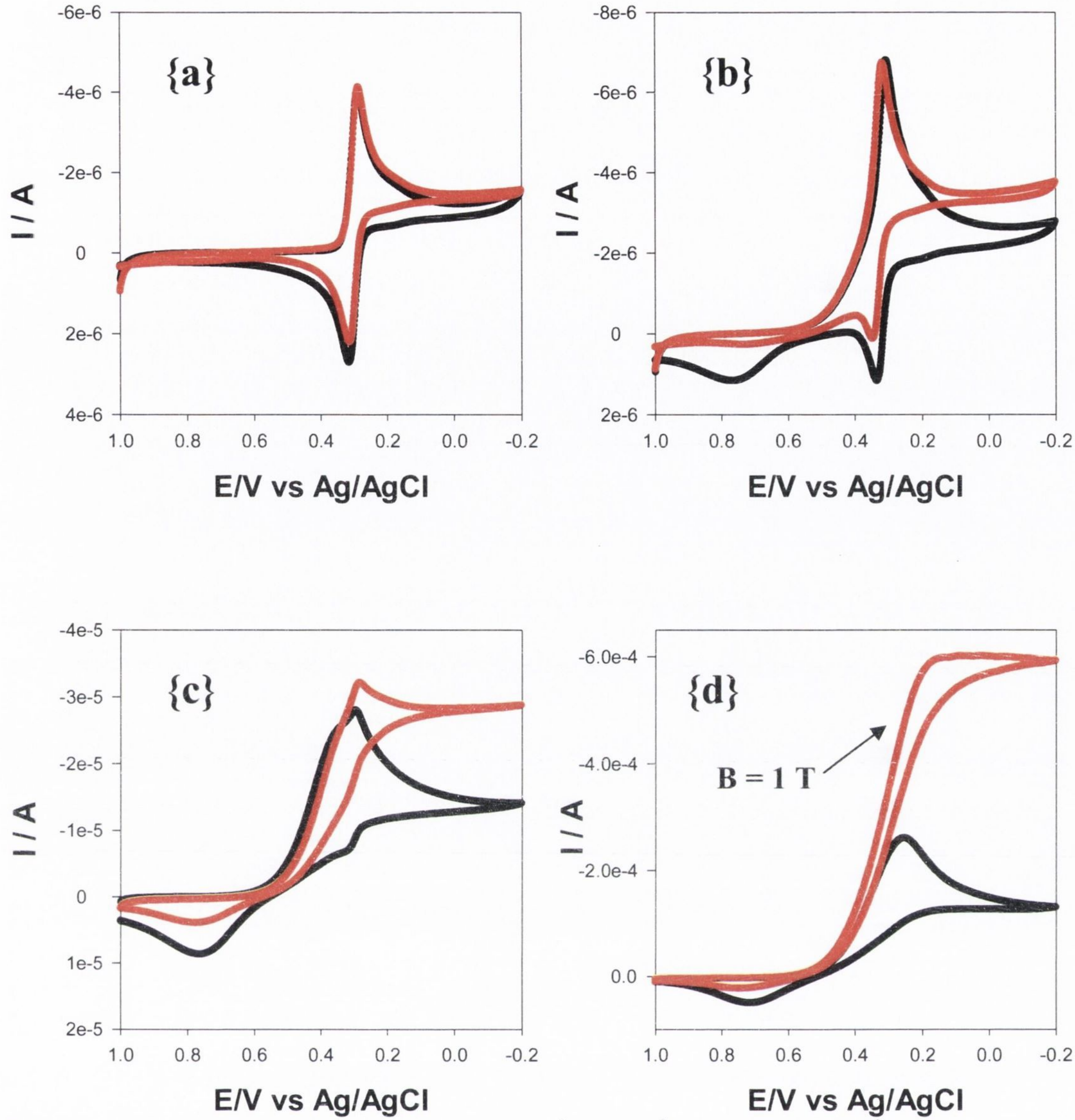

Figure 6.19; Cyclic Voltammograms {a-d} of 5x10^{-4} mol dm^{-3} MB in 0.1 mol dm^{-3} H_2SO_4 with: {a} no Fe^{3+}, {b} 1x10^{-3} mol dm^{-3} Fe^{3+}, {c} 1x10^{-2} mol dm^{-3} Fe^{3+} and {d} 1x10^{-1} mol dm^{-3} Fe^{3+}, in the absence(—) and presence(—) of a 1 Tesla magnetic field. The scan rate was $\nu = 5$ mV/s.

The field induced convection is visibly evident in the voltammogram series. In {b} the concentration of Fe^{3+} is 1 x 10^{-3} M. The anodic peak corresponding to LMB is significantly smaller in the 1 Tesla voltammogram, than in the zero field voltammogram. A greater solution convection, due to the applied field, enables a greater collision incidence of the Fe^{3+} and LMB molecules, and thus, larger amounts of LMB is oxidised to MB. This is reflected in the magnitude of the reaction rates summarised in table 6.3. Equation 6.12 predicts that, $(I_P)_\infty$ / $(I_P)_d$ *vs.* $\nu^{-1/2}$, should be linear and this was also found to be true for all field strengths > 0.2 Tesla, figure 6.20.

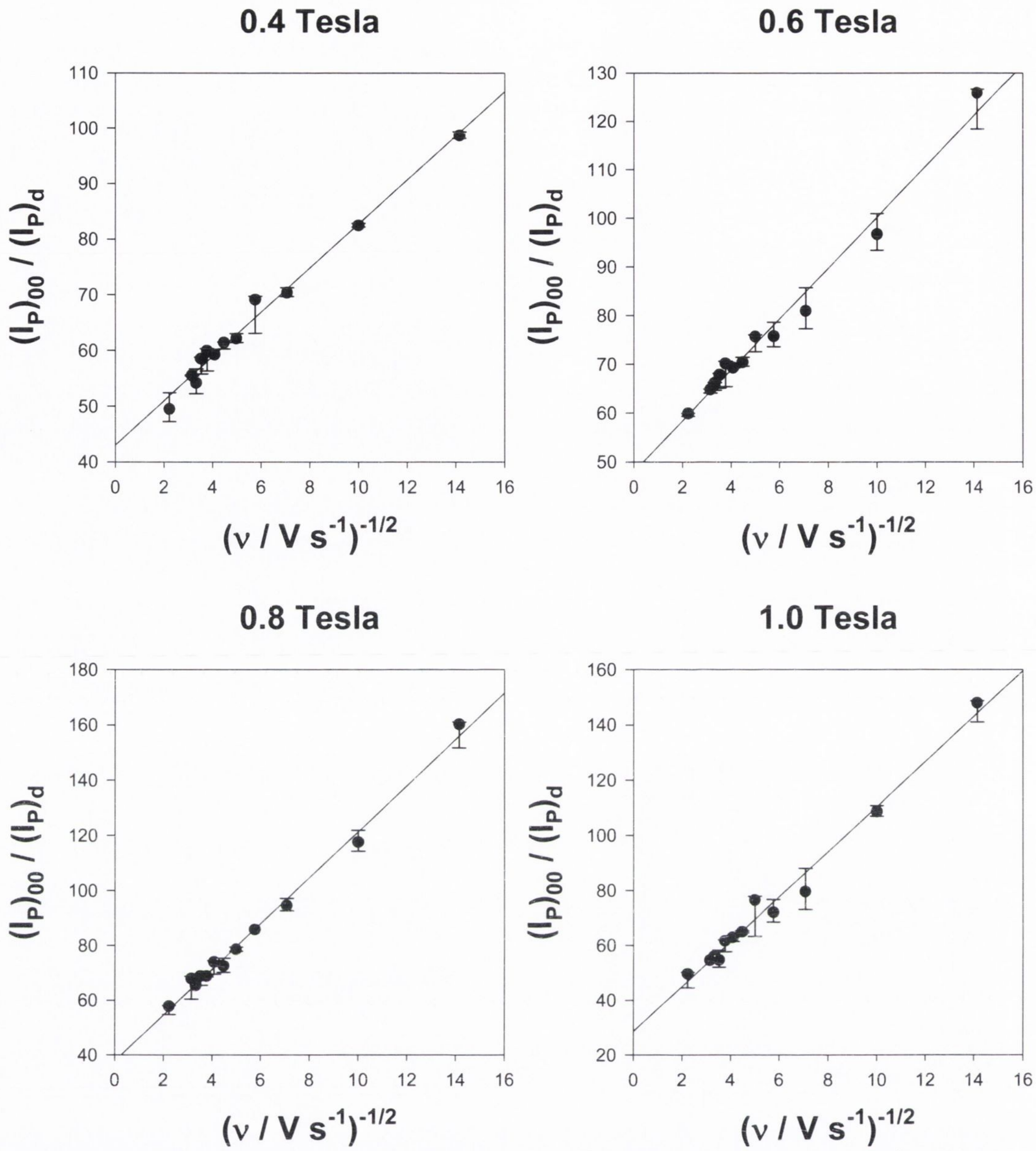

Figure 6.20; Plot, and associated errors, of the linear relationship $(i_P)_\infty / (i_P)_d$ ratio *vs.* $\nu^{-1/2}$ for 5×10^{-4} mol dm^{-3} MB, 1×10^{-1} mol dm^{-3} Fe^{3+}, for four field strengths. The relationship yields good linearity but with some scatter particularly at fast scan rates.

The slopes of the plots were used to calculate the average rate values for the spontaneous oxidation of LMB by Fe^{3+}, as summarised in table 6.3. A final plot of the ratio slopes *vs.* magnetic field strength is shown in figure 6.21. The plot exhibits excellent linearity for ratio type data (large scope for errors), with $r^2 = 0.96$. We again observe the deviation from linearity that occurs between zero and low B values.

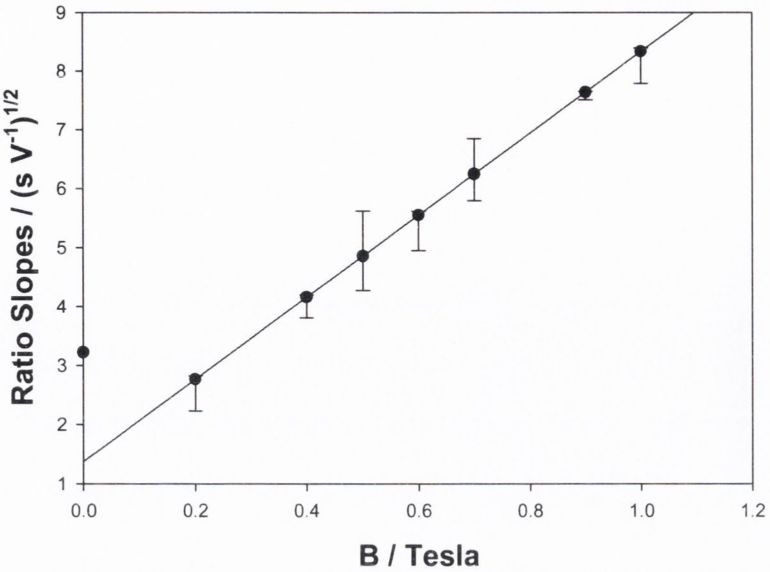

Figure 6.21; Plot, and associated errors, of the slopes of the linear relationship $(i_P)_\infty/(i_P)_d$ *vs.* $v^{-1/2}$ as a function of magnetic field strength for $5\text{x}10^{-4}$ mol dm^{-3} MB, $1\text{x}10^{-1}$ mol dm^{-3} Fe^{3+}. The relationship yields good linearity but with some scatter.

The table is a summary of the average slopes for the ratio for each concentration of MB / Fe^{3+} investigated. From these slopes the average rate was calculated in the absence and presence of the magnetic field, and then compared.

	Ratio slope / $(\text{s V}^{-1})^{1/2}$		**Average Rate (L^{-1} mol s)**	
Conc/ mol L^{-1}	**B = 0 Tesla**	**B = 1 Tesla**	**B = 0 Tesla**	**B = 1 Tesla**
$5\text{x}10^{-4}$ MB, 0.1 Fe^{3+}	**3.22 ± 0.55**	**8.05 ± 0.14**	**$8.24\text{x}10^{2}\pm0.14$**	**$5.14\text{x}10^{3}\pm0.93$**
$1\text{x}10^{-4}$ MB, 0.01 Fe^{3+}	**1.26 ± 0.25**	**2.15 ± 0.45**	**$1.27\text{x}10^{3}\pm0.25$**	**$3.65\text{x}10^{3}\pm0.77$**
$5\text{x}10^{-5}$ MB, 0.01 Fe^{3+}	**1.36 ± 0.27**	**1.66 ± 0.30**	**$1.46\text{x}10^{3}\pm0.39$**	**$2.17\text{x}10^{3}\pm0.65$**
$1\text{x}10^{-5}$ MB, 0.001 Fe^{3+}	**1.02 ± 0.33**	**1.42 ± 0.36**	**$9.3\text{x}10^{2}\pm0.43$**	**$1.04\text{x}10^{3}\pm0.62$**

Table 6.3; Slopes of the $(i_P)_\infty/(i_P)_d$ ratio *vs.* $v^{-1/2}$, and the homogeneous catalytic rate constants compared in the presence and absence of the magnetic field.

It must be stressed that the enhanced rate constants obtained in the presence of the magnetic field were due to an increase in solution convection and not due to any kinetic effects on electron transfer.

6.8 Effect of an Applied Magnetic Field on PMB-GC modified electrode activity

The redox activity shown by a PMB-GC modified electrode is dependent on the porosity of the polymer matrix to the supporting electrolyte. Oxidation and reduction processes in the film require counter ions to keep the localised charge balanced. With the convective effects of a 1 Tesla magnetic field elucidated for solutions, a brief study was performed quantifying the effect of the 1 Tesla field on the activity of PMB-GC electrode. Figure 6.22, shows typical voltammetric responses of the film in the absence and presence of the magnetic field.

Each comparison figure contains four runs each for the non-field and field voltammograms, to highlight the reproducible nature of the films. The film activity is inhibited by the 1 Tesla magnetic field. There is a slight negative shift in the oxidation peak of the film as the field strength increased at low scan rates, implying a more facile electron transfer process. This shift was negligible at higher scan rates and overall the $E^0_{MB/LMB}$ values remained similar as a corresponding and equal negative shift was observed for the polymer reduction peak. A brief summary of the current decrease is shown in Table 6.4.

Scan Rate mV s^{-1}	**Average % current decrease** B = 1 Tesla
20	11.1 ± 0.4
50	12.7 ± 0.5
70	8.33 ± 0.6
100	8.7 ± 0.6
200	9.3 ± 0.5

Table 6.4; Average percentage current decrease observed for the PMB/GC oxidation peak observed in a 1Tesla magnetic field in 0.1M phosphate buffer + 0.1M KCl for a range of experimental scan rates.

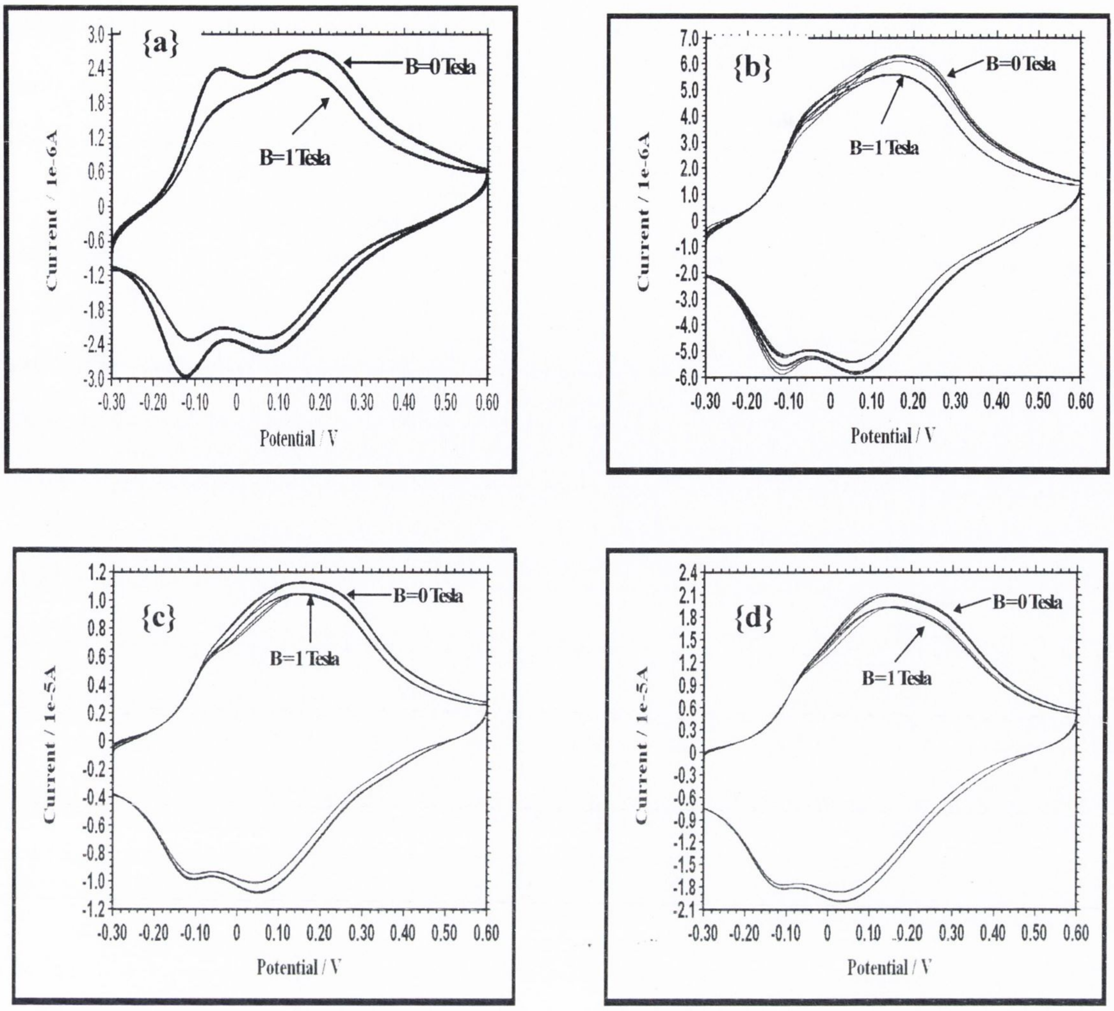

Figure 6.22; Cyclic voltammograms of PMB (L = 6.33±0.55 x 10^{-8} cm) modified GC electrode in 0.1M phosphate buffer and 0.1M KCl, in the absence and presence of a 1 Tesla magnetic field. Scan rates were; **{a}** 20mV/s, **{b}** 50mV/s, **{c}** 100mV/s, **{d}** 200mV/s.

The only trend observed is that the current decreases in the presence of the 1 Tesla magnetic field. Convection is expected to be limited in an environment like a polymer matrix and so a decrease in the redox activity of the film, due to disrupted diffusion of counterions, is not unreasonable.

6.9 Conclusions

The aim of this chapter was to extensively quantify the effects, *via* cyclic voltammetry, that a magnetic field has on analyte ions in solution. The magnetic field was set up so that the main force acting on the solution was the Lorentz force. The dependency of I_B on the magnetic field strength and on solution concentration was elucidated. The relationships were found to be $I_B \propto B^{1/3}$ and $I_B \propto C^{4/3}$. These relationships held true for macroelectrodes and a microelectrode. Deviations were found to occur at low concentrations and low magnetic field strengths. The magnetic field had no affect on the redox peak potentials of the analyte species in solution.

The homogeneous catalytic reaction between leucomethylene blue and ferric ammonium sulphate was examined using cyclic voltammetry and RDE. The effect of an applied magnetic field on the rate constant was investigated and all rates were then compared. The magnetic field caused convection in the solution, effectively narrowing the depletion layer at the electrode surface, and the homogeneous catalytic rate constant was enhanced.

Finally, the effect of an applied magnetic field on the charge carried by a polymethylene blue modified electrode was studied. The charge carried by the PMB/GC electrodes was inhibited in the presence of the magnetic field. Convection in the polymer matrix was not conducive to the efficient ion mobility, needed to maintain electroneutrality, within the polymer.

6.10 References

[1] J. P. Chopart, J. Douglade, P. Fricoteaux, A. Oliver, *Electrochim. Acta.*, **36**, 459, 1991.

[2] R. Aogaki, K. Fueki, T. Mukaibo, *Denki Kagagu*, **44**, 89, 1976.

[3] O. Aoboubi, J. P. Chopart, J. Douglade, A. Olivier, C. Gabrielli, B. Tribollet, *J. Electrochem. Soc.*, **137**, 1796, 1990.

[4] N. Leventis, M. Chen, X. Gao, M. Canalas, P. Zhang, *J. Phys. Chem. B*, **102**, 3512, 1998,.

[5] J. Lee, S. R. Ragsdale, X. Gao, H. S. White, *J. Electroanal. Chem.*, **422**, 169, 1997.

[6] S. Legeai, M. Chatelut, O. Vittori, J. P. Chopart, O. Aaboubi, *Electrochim. Acta*, **50**, 51, 2004.

[7] O. Aaboubi, P. Los, J. Amblard,J. P. Chopart, A. Olivier, *J. Electrochem. Soc.*, **150** (2), E125, 2003.

[8] T. Z. Fahidy, *Electrochim. Acta*, **35**, 929, 1990.

[9] P. L. DeVries, *"A First Course in Computational Physics"*, John Wiley & Sons: NY, Chapter 4, p 205, 1994.

[10] J. Lee, X. Gao, L. D. A. Hardy, H. S. White, *J. Electrochem. Soc.*, **142**, L90, 1995.

[11] S. R. Ragsdale, K. M Grant, H. S. White, *J. Am. Chem. Soc.*, **120**, 13461,1998.

[12] O. Devos, O. Aaboubi, J. P. Chopart, E. Merienne, A. Olivier, C. Gabrielli, B. Tribollet, *Pol. J. Chem.*, **71**, 1160, 1997.

[13] O. Aaboubi, J. P. Chopart, A. Olivier, P. Los, *Energy. Convers. Manage.*, **43**, 373, 2002.

[14] J. M. Saveant, E. Vianello, *Electrochim. Acta*, **10**, 905, 1965.

[15] D. E. Nicodem, M. DeMenezes, *Solar Energy*, **26**, 365, 1981.

[16] A. S. N. Murthy, K. S. Reddy, *Electrochim. Acta*, **28**, 1677, 1983.

[17] M. E. G. Lyons, unpublished work, Trinity College Dublin.

CHAPTER 7

CONCLUSIONS AND FUTURE WORK

7.1 General Conclusions

Chapter 3 was the first results chapter and started with detailed analysis of the solution phase electrochemistry of methylene blue, examined *via* cyclic voltammetry and RDE voltammetry. The reduction of MB involves the gain of two electrons and a proton to form leucomethylene blue. MB is known to form dimers and larger aggregates in solution due to molecular forces such as hydrogen bonding and Van der Waals interactions. The amount of dimerisation that occurs in solution increases with bulk concentration and can be quantified in terms of monomer fraction. The diffusion coefficient and the electron transfer rates for MB were found to vary substantially as a function of monomer species present in solution.

MB is also known to adsorb strongly and rapidly to electrode surfaces and at low concentrations conforms to a Langmuir adsorption isotherm. Adsorption in high bulk MB concentrations was also analysed and an adsorption isotherm was constructed. From the isotherm a maximum surface coverage for a MB monolayer was elucidated. When correlated to solution monomer fraction, different orientations of the adsorbed species were discussed.

In the latter part of Chapter 3, MB was electropolymerised onto a GC electrode and the properties of the films were investigated. The polymerisation was examined as a function of initial MB solution concentration and number of polymer growth cycles. The properties of the resultant polymer films varied in the amount of charge carried by the polymer modified electrode. Finally, charge transport in the polymer film was quantified in terms of the charge transfer diffusion coefficient, and of the electroneutrality required counterion motion, using theoretical and experimental techniques.

The polymer modified GC electrodes were used in the redox catalysis of four biologically important analytes, as detailed in Chapter 5. The redox catalysis occurred throughout the polymer film as diagnosed by the Albery-Hillman model, and the kinetic parameters associated with this catalysis were quantified using the Michaelis-Menten model. The PMB/GC electrodes exhibited little catalytic properties towards the oxidation of these analytes. This is supported by the fact that the polymer film exhibited low affinity for values for each of the analytes - quantified by the kinetic parameter k_C. However the polymer films exhibited permselective properties when explored using the DVP technique. This enabled the accurate detection of the catecholamines DA, NE, and EP in the presence of AA. The following three paragraphs give the structure of Chapter 5.

Diffusion coefficients for the analytes at the bare GC and the PMB/GC electrodes were quantified using CV and RDE voltammetry. The amperometric data was analysed using the mass transport corrected Tafel equation, which revealed that the majority of the applied potential was required to drive substrate oxidation. The oxidation kinetics of each analyte were investigated at the RDE *via* linear sweep voltammograms and subsequently *via* Koutecky-Levich analysis.

Calibration curves of AA and the catecholamines, at pH 7, at the modified electrodes were constructed from batch amperometric data. The kinetic parameters, K_m and k_C, were quantified using linear Lineweaver-Burk and Eadie-Hofstee equations. The theoretical analysis of steady-state amperometric responses, for a polymer modified electrode that exhibits Michaelis-Menten kinetics, was applied. Non-linear least square analysis of the amperometric data in tandem with the LB and EH expressions produced reasonable values for the Miahaelis-Menten constant K_m, and the catalytic rate constant k_C. Analyte detection limits were also determined.

Finally, the selectivity of the PMB/GC was investigated using DPV. The ionic association between the cationic PMB redox sites and the anionic AA, coupled with short experimental timescales, made the selective detection of the catecholamines possible in the presence of AA.

The goal of Chapter 6 was to extensively quantify the effects, *via* cyclic voltammetry, that an applied magnetic field has on analyte ions in solution. The dependency of I_B on the magnetic field strength and on solution concentration was found to be $I_B \propto B^{1/3}$ and $I_B \propto C^{4/3}$. These relationships held true for macroelectrodes and a microelectrode. Deviations were found to occur at low concentrations and low magnetic field strengths. The magnetic field had no kinetic effect on the redox behaviour of species in solution.

The homogeneous catalytic reaction between LMB and ferric ammonium sulphate was examined using cyclic voltammetry and RDE voltammetry. The effect of an applied magnetic field on the rate constant was investigated and compard to those found in the absence of the magnetic field. The magnetic field caused solution convection, effectively narrowing the depletion layer at the electrode surface, resulting in enhanced homogeneous catalytic rate constants.

Finally, the effect of an applied magnetic field on the charge carried by PMB/GC electrode was investigated. The charge carried by the polymer films was inhibited in the presence of the magnetic field. Magnetic field induced convection in the polymer matrix was not conducive to the efficient ion mobility required to satisfy electroneutrality within the polymer film.

7.2 Future Work

Future work should be carried out to elucidate definitive structures for the MB adsorbed monolayer electrode coatings. The structures and orientation of the monomer/dimer/oligomers species could then be correlated to solution concentration and pH. The special molecule has remarkable properties which could be manipulated more.

The anion exclusion properties that are exhibited by the PMB/GC electrode could be exploited more in the future. PMB is an ideal polymer for immobilisation of redox species close to the electrode surface and could be coupled to the anion exclusion properties in a DPV experimental setup. For example, some other interferent analyte could be catalysed by the PMB immobilised moiety so that its redox behaviour is observed at a different potential than that of the analyte of interest.

The magnetic field has got potential applications in that it can cause solution convection in a solution that could not be stirred effectively otherwise – with microelectrodes for example. Unfortunately the eagerly anticipated kinetic effects were not observed. This was a disappointing aspect to the magnetic field research performed. Magnetic nanoparticles may be an exciting area of research in the future, especially in drug delivery application.